DEVELOPMENT OF TECHNIQUES TO INVESTIGATE EARLY OVARIAN FOLLICLE GROWTH IN CULTURE



Ava Shaye Harrison
Lady Margaret Hall

Nuffield Department of Women's and Reproductive Health
Medical Sciences Division
University of Oxford

Thesis submitted for the degree of Doctor of Philosophy
Michaelmas Term 2025

ABSTRACT

Early follicle development is dependent on tightly regulated, bidirectional communication between the oocyte and surrounding follicular somatic cells within a complex three-dimensional tissue environment. Disruption of ovarian architecture can impair follicle development and compromise fertility. Whilst existing methodologies have advanced the understanding of early follicle development, many rely on static, terminal histological analyses that limit spatial resolution and preclude longitudinal assessment. The overarching aim of this thesis was to develop and evaluate experimental approaches to support and enable dynamic monitoring of follicles in culture.

The reaggregated ovary (RO) model of follicle reformation was assessed following enzymatic dissociation and separation of cell populations via differential adhesion. ROs supported the re-establishment of follicle-like structures and early developmental transitions in culture; however, comparison with age-matched whole ovaries revealed divergence in growth trajectories, including altered stage distributions, reduced tissue expansion, and absence of advanced follicles. Introduced to facilitate downstream viral manipulation, an extended protocol for RO generation preserved follicle number but impaired oocyte growth and follicular developmental trajectories, highlighting the sensitivity of early follicles to structural perturbation and disruption of oocyte-somatic communication.

To optimise adeno-associated virus (AAV)-mediated gene delivery to primary murine ovarian cells, AAV9 vectors were selected and evaluated to achieve efficient somatic cell labelling whilst maintaining cell viability. In parallel, AAV constructs incorporating CRISPR/Cas9 elements were designed to enable follicular cell-specific reporting as a strategy to identify follicles in tissue.

FolliTracker, a live-imaging and computational analysis workflow, integrated AAV-mediated fluorescent labelling with three-dimensional confocal microscopy and quantitative image analysis. FolliTracker supported non-destructive, longitudinal tracking of follicle-associated features within intact tissue. FolliTracker demonstrated concordance with conventional histology-based methods for tissue volume and mCherry signal, while revealing technical constraints related to imaging depth and follicle segmentation accuracy. Together, this thesis defined the capabilities and limitations of RO-based systems, established optimised viral labelling strategies, and introduced a method for dynamic analysis of early follicle development, providing a foundation for future mechanistic and translational studies in ovarian biology and fertility preservation.

ACKNOWLEDGEMENTS

"Science and everyday life cannot and should not be separated."

— **Rosalind Franklin**, Letter addressed to Ellis Franklin (1940)

It is impossible to compress the gratitude of several years into a handful of paragraphs, but, much like sectioning tissue barely visible to the human eye on a Friday at 8 pm, I shall proceed with conviction and hope for the best.

First and foremost, my deepest thanks go to my family: Paul, Tessa, Madeleine, and Ethan Harrison. To my parents, Paul and Tessa, there is no adequate way to express my gratitude for a lifetime spent believing that the world was mine to explore and that no dream was too ambitious, eccentric, or pluripotent. You fostered a home in which curiosity was celebrated, aspirations nurtured, and every obstacle quietly dismantled before I could even realise it was there. Your unwavering support has followed me through every chapter of my life, and this thesis is as much a testament to you both as to any biological principle.

It is customary, and entirely deserved, to thank those who guided the research itself. My supervisor, Professor Suzannah Williams, offered not just expertise and opportunity, but belief in my ability to pursue complicated questions with even more complicated experiments. I am grateful for her support, generosity, and the invitation to be part of the Williams Group. My secondary supervisor, Dr Karin Hellner, has been a source of wisdom and steady perspective, particularly during those uniquely challenging moments that all DPhil candidates seem to face.

To the Williams Group, past and present – Dr Nilay Kuscu, Dr Tomi Adeniran, Janet Kwan, Olivia Boardman, Dr Antonia Weberling, Emmerson Teas, Dr Ruth Appeltant, and Omar Ammar – thank you for sharing in the science, the learning, and in the daily rituals of lab life. I am also grateful to the Cellular Imaging Core at the Centre for Human Genetics, Dr James Bancroft and Edward Drysdale, whose expertise and technical knowledge provided vital support, and whose camaraderie made the many hours at the confocal microscope all the more enjoyable. To researchers of the Nuffield Department of Women's and Reproductive Health, especially the Thames Office, thank you for every thoughtful discussion, troubleshooting session, celebration, and collective sigh of despair when the fume hoods chose violence.

To the Keble College Senior Common Room and Lady Margaret Hall Senior and Middle Common Rooms: thank you for welcoming me into the magic of Oxford and cultivating experiences that I will cherish for the rest of my life. I also wish to acknowledge my students, both the Lady Margaret Hall pre-clinical medical students and the MSc Clinical Embryology cohort. Teaching is a privilege, and I often felt I learned as much as I tried to impart. Thank you for your trust in your own academic journeys; it has been an honour to accompany you.

No thesis is written alone; it takes a village, an evensong chorus, and occasionally a search party. I am profoundly grateful for the friends who sustained me. Rajwa Mecca and Sofia Medina, your flat became a home in the truest sense: a refuge, a cosy couch, and a place where I could exhale fully. I remain in awe of your strength, intelligence, and generosity. I cannot ever fully articulate my gratitude for you both; this is to be expected, as a 'man' among Middle-earth hobbits and dwarves.

To Amelie Berz, Emily Beaumont (née McCluskey), Pierre Tanguy, Irina Kolegova, Peter Andringa, Lexia Khan, Sarah Macklin, Julia Lawson-Johns, Hannah Eyerman, Michael Furlan, Jeremy Stroud, Joseph Ross and Kitty Howie: thank you for sharing in the highs and for offering an ear, a smile, or a well-timed distraction during the lows. When the waters grew unexpectedly rough, you helped steady the boat, reminding me that I wasn't navigating the currents alone. You each played an invaluable role in this chapter and the ones to come.

I am grateful to the many fellow students whose paths intertwined with mine: brilliant, kind, and endlessly impressive people who shaped Oxford life, from the extravagant college balls, Jericho coffee dates, and the shared urgency of looming deadlines at Rad Cam. To my ski-trip friends, who have long since become simply my friends: thank you for championing adventure and whimsy, and for being genuinely remarkable humans. Although too numerous to list, you know who you are and have provided more moments of happiness than I could ever count. To the Sadler's Gate Mews gals – Netta Claydon, Anna Barton, and Katherine Mullins – thank you for being exceptional flatmates, even better friends, and for sharing a glass of wine during tangents about figure configurations or the phrasing of an introduction. And to the LMHBC and Vesta rowing communities, with special mention to the 'Henley House', thank you for nurturing my love of rowing… and of Pimm's, which I assure future readers is a beverage, not a coping mechanism (though occasionally it has been both).

Finally, a few honourable mentions to the unsung heroes of this doctoral endeavour:

- The various dogs of University Parks and along the Putney embankment, who provided emotional support without ever asking for authorship
- The Lamb and Flag, for crisp pints and countless hours of dimly lit philosophising and pontificating among friends, colleagues, and charming strangers
- Najar's Place, whose chicken tikka and falafel wrap (with everything on it) fuelled many Oxford ventures – academic and otherwise
- UCL Senate House Library, for being the venue where this thesis was coaxed, bribed, and occasionally threatened into existence through sheer will and caffeine-induced hallucinations
- Hans Zimmer, for scoring both my lab work and my existential crises with dramatic flair
- Louis Theroux, whose documentaries kept me sane between solitary culture timepoints at various obscure hours and reminded me that curiosity is, in itself, a companion

Do not fear – you have indeed reached the end of my acknowledgements monologue, the first of many milestones of this thesis. Although not in my nature, concerted effort was made to be more concise elsewhere. In closing, if the last few years have taught me anything, it is that science is rarely linear, occasionally exasperating, unexpectedly hilarious, and always collaborative. I am profoundly grateful to everyone who walked, ran, rowed, or gently nudged me along across the finish line.

Thank you, wholeheartedly.

TABLE OF CONTENTS

ABSTRACT **2**

ACKNOWLEDGEMENTS **3**

TABLE OF CONTENTS **5**

LIST OF TABLES **11**

LIST OF FIGURES **12**

LIST OF ABBREVIATIONS **16**

1. INTRODUCTION **18**

1.1 OVARIAN FUNCTION AND FERTILITY PRESERVATION 18

1.1.1 Biological and societal importance of fertility *18*

1.1.2 Prevalence of infertility, cancer survivorship, and reproductive aging *19*

1.2 THE OVARIAN LANDSCAPE AND EARLY FOLLICLE DEVELOPMENT 24

1.2.1 Architecture of the ovary *24*

1.2.2 Follicle formation and the establishment of the ovarian reserve *25*

1.2.3 Follicle development *27*

1.2.4 Bidirectional communication and regulatory pathways in growing follicles *30*

1.3 INVESTIGATION OF FOLLICLE DEVELOPMENT *IN VITRO* 32

1.3.1 Review of culture approaches to investigate follicle development *32*

1.3.2 Limitations with current systems to support in vitro follicle growth *33*

1.3.3 The reaggregated ovary model *33*

1.4 CURRENT METHODOLOGICAL BARRIERS TO INVESTIGATE EARLY FOLLICLE DEVELOPMENT 36

1.5 EMERGING USE OF VIRAL VECTORS AND GENE DELIVERY IN OVARIAN RESEARCH 38

1.6 FOLLITRACKER: A DYNAMIC METHODOLOGY FOR EARLY FOLLICULAR ANALYSIS 40

1.7 OVERARCHING HYPOTHESIS, AIMS, AND OBJECTIVES 40

2. METHODOLOGY **42**

2.1 Ethics 42
2.2 Mouse colony 42
2.2.1 Mouse breeding *42*
2.3 Ovary collection and processing 42
2.4 Reaggregated ovary generation 43
2.5 Determination of cell viability and number 47
2.6 Reaggregated ovary culture 48
2.7 Histological processing 48
2.7.1 Fixation *48*
2.7.2 Embedding *48*
2.7.3 Sectioning *49*
2.8 Histological staining 49
2.9 Histological assessment of the ovary 50
2.9.1 Volumetric ovarian assessment *50*
2.9.2 Follicle classification *51*
2.9.3 Assessment of follicle number *52*
2.9.4 Quantitative morphometric analysis of ovarian and follicular structures *52*
2.10 Molecular analysis 54
2.10.1 Slide preparation *54*
2.10.2 Immunohistochemistry *55*
2.10.3 Quantification of DAB signal *57*
2.11 Imaging 58
2.11.1 Spinning-disc confocal imaging *58*
2.11.2 Brightfield microscopy *58*

3. FOLLICULAR REFORMATION AND MORPHOLOGICAL INTEGRITY FOLLOWING OVARIAN REAGGREGATION 59

3.1 Introduction 59
3.1.1 Background *59*
3.1.2 Chapter aims *61*
3.2 Methodology 62
3.2.1 Mouse colony *62*

3.2.2 Reaggregated ovary generation *62*

3.2.3 Reaggregated ovary culture *63*

3.2.4 Histological staining *63*

3.2.5 Ovarian tissue and follicle assessment *63*

3.2.6 Imaging *64*

3.2.7 Statistical analysis *64*

3.3 RESULTS 65

3.3.1 Follicle number in reaggregated ovaries remained stable across culture durations but stage composition shifted *65*

3.3.2 Reaggregated ovaries contained fewer follicles than age-matched whole ovaries *65*

3.3.3 Follicle stage distribution shifted during reaggregated ovary culture and diverged from age-matched whole ovaries *68*

3.3.4 Reaggregated ovary volume remained stable during culture but was smaller than age-matched whole ovaries *69*

3.3.5 The extended reaggregated ovary protocol altered follicle dynamics without reducing total follicle number *69*

3.3.6 Theca cell presence was evident in reaggregated ovaries but limited in extended reaggregated ovaries after seven-day culture *70*

3.3.7 Oocyte and follicle size were reduced in ROEx, whilst symmetry was preserved *70*

3.3.8 Follicle growth trajectories diverged between standard and extended reaggregated ovary groups after seven days in culture *71*

3.4 DISCUSSION 73

4. TRANSDUCTION AND TARGETING OF FOLLICULAR PRIMARY MURINE OVARIAN CELLS 80

4.1 INTRODUCTION 80

4.1.1 Background *80*

4.1.2 Chapter aims *84*

4.2 METHODOLOGY 86

4.2.1 Murine ovary collection and dissociation *86*

4.2.2 Viral particles *86*

4.2.3 Transduction and cell culture protocol *87*

4.2.4 Flow cytometry *91*

4.2.5 Statistical analysis *92*

4.3 RESULTS 93

4.3.1 Determination of optimal multiplicity of infection using AAV-EGFP *93*

4.3.2 Determination of transduction efficiency through fluorescent reporter expression in primary ovarian cells following sequential exposure of AAVs *95*

4.4 DISCUSSION 98

5. IMPLEMENTATION AND EVALUATION OF FOLLITRACKER FOR LIVE MONITORING OF FOLLICLE DEVELOPMENT IN TISSUE CULTURE 104

5.1 INTRODUCTION 104

5.1.1 Background *104*

5.1.2 Chapter aims *107*

5.2 METHODOLOGY 109

5.2.1 Murine ovary dissociation *109*

5.2.2 Viral vectors *109*

5.2.3 Transduction of primary ovarian cells *110*

5.2.4 Reaggregated ovary generation *110*

5.2.5 Reaggregated ovary culture and maintenance *112*

5.2.6 Histological processing *112*

5.2.7 Histological staining *113*

5.2.8 Histological ovarian assessment *113*

5.2.9 Molecular analysis *113*

5.2.10 Imaging *114*

5.2.11 FolliTracker image processing and quantitative analysis *115*

5.2.12 Statistical analysis *115*

5.3 RESULTS 117

5.3.1 FolliTracker enabled follicle visualisation in transduced reaggregated ovaries *117*

5.3.2 FolliTracker identified more follicles in viral tissues compared with controls *119*

5.3.3 Viral reaggregated ovaries had more mCherry signalling than control reaggregated ovaries across all culture timepoints *120*

5.3.4 Volume of mCherry signal was positively correlated with follicle number detected by FolliTracker *121*

5.3.5 Tissue volume was similar between both groups at each assessed timepoint with FolliTracker *123*

5.3.6 Total tissue volume was similar between the control group and viral group via histological analysis 123

5.3.7 Follicle number and stage distribution were similar between the control group and viral group 125

5.3.8 Although follicle area was similar between groups, the oocyte areas of follicles from viral reaggregated ovaries was smaller than controls 126

5.3.9 Follicular growth rate was similar between follicles from both control and viral reaggregated ovaries 126

5.3.10 The symmetry of follicles and oocytes did not differ between groups 127

5.3.11 The proportion of AMH-positive follicles were similar across experimental groups following immunohistochemical assessment 128

5.3.12 The intensity of AMH stained follicles was greater in the viral group compared with the control group .. 130

5.3.13 A greater area was positive for mCherry in viral tissues than in control tissues 130

5.3.14 Viral reaggregated ovaries had a greater proportion of mCherry-positive follicles compared with control reaggregated ovaries 132

5.3.15 The proportional expression of mCherry was not correlated to follicle number 133

5.3.16 The number of follicles per reaggregated ovary recorded were not correlated between histology and FolliTracker 134

5.3.17 Total tissue volume was highly correlated between both methodologies 136

5.3.18 The recorded values for the proportion of mCherry-positive area from FolliTracker and immunohistochemical analysis were correlated 136

5.3.19 The proportion of mCherry signal correlated with improved follicle agreement 137

5.4 Discussion 139

6. DISCUSSION 149

6.1 Introduction 149

6.2 Summary of principal findings and key insights 150

6.2.1 Chapter 3: Reaggregated ovary characterisation and protocol selection 150

6.2.2 Chapter 4: AAV-mediated transduction optimisation 152

6.2.3 Chapter 5: FolliTracker assessment and validation 153

6.2.4 Synthesis 153

6.3 Limitations and technical considerations of FolliTracker 154

6.4 Contextualisation within recent advances: Comparison with Yoshida *et al.* (2025) 155

6.5 Methodological refinement and optimisation of FolliTracker 158

6.6 Future directions and translational potential 161

6.7 FINAL REMARKS AND OVERARCHING CONCLUSIONS 163

7. REFERENCES 164

8. APPENDIX 189

8.1 APPENDIX I: PUBLICATIONS AND AWARDS 189

8.1.1 Publications 189

8.1.2 Conference abstracts 189

8.1.3 Awards 215

8.2 APPENDIX II: SUPPLEMENTARY RESULTS FOR CHAPTER 5 216

LIST OF TABLES

Table 2.7.2) Tissue dehydration and clearing protocol for paraffin embedding.....49

Table 2.8) Haematoxylin and eosin staining protocol for paraffin-embedded ovarian tissue.....50

Table 2.9.2) Classification criteria for ovarian follicle developmental stages.....51

Table 2.10.2.1) Tissue deparaffinisation and rehydration protocol prior to immunohistochemical analysis……...55

Table 2.10.2.2) Counterstaining, dehydration, and clearing of tissue sections during immunohistochemical analysis……...56

Table 2.10.3) Semi-quantitative grading criteria for DAB chromogen staining intensity.....57

Table 4.2.3.1) Media composition and viral particle volume used to establish multiplicities of infection in primary murine ovarian cells.....88

Table 5.3.3) Proportion of mCherry-positive volume in reaggregated ovaries via FolliTracker across culture timepoints.....120

Table 5.3.13) Immunohistochemical assessment of mCherry-positive area via DAB staining in reaggregated ovaries following 14 days in culture.....130

Table 5.3.14) Distribution of oocyte mCherry staining intensity grades in reaggregated ovaries following 14 days in culture.....133

Table 6.4) Experimental and methodological comparison between Yoshida *et al.* (2025) and the FolliTracker pipeline.....157

LIST OF FIGURES

Figure 1.1.2.1) Primary causes of infertility…….....20

Figure 1.1.2.2) Pathogenic model, diagnostic criteria, and health consequences of premature ovarian insufficiency……..….22

Figure 1.1.2.3) Fertility preservation strategies and clinical workflow for female patients undergoing gonadotoxic treatment…….…….…….…..23

Figure 1.2.1) Structural and microenvironmental components of the ovary ……..……...25

Figure 1.2.3.1) Representation of early follicle development from the primordial to antral stages…27

Figure 1.2.3.2) The two-cell, two-gonadotrophin model of ovarian steroidogenesis…….28

Figure 1.3.3) Representative images of reaggregated and whole ovaries following culture or transplantation compared with age-matched *in vivo* controls……..…..35

Figure 1.4) Limitations of conventional histology for staging follicles…….....37

Figure 1.5) AAV9-mediated Kitl gene therapy to rescue congenital infertility due to dysfunctional granulosa cells…….....39

Figure 2.3) Dorsal dissection and retrieval of ovaries from a postnatal mouse.....43

Figure 2.4) Generation of reaggregated ovaries and the differential cell adhesion process.....45

Figure 2.9.4) Morphometric parameters of follicular structures.....53

Figure 3.2.2) Experimental timeline for the generation of reaggregated ovaries and extended reaggregated ovaries.....62

Figure 3.3.1.1) Histological comparison of ovarian and follicle morphology and development in whole and reaggregated ovary models.....66

Figure 3.3.1.2) Quantitative analysis of follicle number and stage distribution in whole and reaggregated ovary models.....67

Figure 3.3.8) Comparative follicle and oocyte growth parameters in reaggregated ovary models following standard and extended cultures.....72

Figure 4.1.1) Schematic representation of the adeno-associated virus infection and transgene expression pathway.....81

Figure 4.2.2) Viral construct designs for transduction in primary murine ovarian cells with AAV-SaCas9 and AAV-DS.....87

Figure 4.2.3.1) Experimental workflow for determining optimal multiplicity of infection in primary murine ovarian cells.....88

Figure 4.2.3.2) Experimental workflow for assessing transduction efficiency of sequential co-transduction with AAV-Cas9 and AAV-DS in primary murine ovarian cells.....90

Figure 4.3.1.1) Representative gating strategy and EGFP fluorescence profiles for multiplicity of infection optimisation following transduction with AAV-EGFP.....94

Figure 4.3.1.2) Cell viability and EGFP expression across increasing multiplicities of infection in primary murine ovarian cells.....95

Figure 4.3.2.1) Transduction efficiency in primary murine ovarian cells with AAV-SaCas9 and AAV-DS... 96

Figure 4.3.2.2) Flow cytometric quantification of cell viability and fluorescent reporter expression following sequential transduction of AAV-Cas9 and AAV-DS.....97

Figure 5.2.4) Experimental workflow for generating viral reaggregated ovaries and accompanying live-imaging analysis using FolliTracker.....111

Figure 5.3.1.1) Composite confocal images of live control and viral reaggregated ovaries during culture …….....117

Figure 5.3.1.2) FolliTracker imaging and volumetric reconstruction of live reaggregated ovaries during culture.....118

Figure 5.3.2) Quantification and visualisation of follicles in reaggregated ovaries via FolliTracker.....119

Figure 5.3.3) Quantitative assessment of mCherry signal volume in reaggregated ovaries via FolliTracker.....121

Figure 5.3.4) Quantitative correlation and volumetric assessment of mCherry signal and tissue size via FolliTracker in reaggregated ovaries.....122

Figure 5.3.6) Histological assessment of tissue volume, follicle number, and stage distribution in reaggregated ovaries following 14 days in culture.....124

Figure 5.3.7) Quantitative assessment of theca cell presence, follicle area, and oocyte area from histological analysis of reaggregated ovaries following 14 days in culture.....125

Figure 5.3.9) Quantitative assessment of granulosa cell density and follicular growth rate from histological analysis of reaggregated ovaries following 14 days in culture.....127

Figure 5.3.10) Quantitative assessment of oocyte and follicle symmetry from histological analysis of reaggregated ovaries after 14 days in culture.....128

Figure 5.3.11) Immunohistochemical assessment of AMH expression in reaggregated ovaries following 14 days in culture.....129

Figure 5.3.13) Immunohistochemical assessment of mCherry expression in reaggregated ovaries following 14 days in culture.....131

Figure 5.3.15) Correlation between proportion of mCherry-positive tissue area and total follicle number following 14 days in culture, as determined by histology-based analysis.....134

Figure 5.3.16) Correlation and agreement of follicle counts obtained via FolliTracker and histological analysis in reaggregated ovaries following 14 days in culture.....135

Figure 5.3.17) Correlation and agreement of total tissue volume quantified via FolliTracker and histological analysis in reaggregated ovaries following 14 days in culture.....137

Figure 5.3.18) Correlation and agreement of proportional mCherry-positive area quantified via FolliTracker and histology-based methodologies, and its relationship with follicle detection concordance……..138

LIST OF ABBREVIATIONS

AAV	Adeno-associated virus
BSA	Bovine serum albumin
Cas9	CRISPR-associated protein 9
CRISPR	Clustered regularly interspaced short palindromic repeats
DAB	3,3′-diaminobenzidine
ddH_2O	Double distilled water
DPBS	Dulbecco's phosphate-buffered saline
DS	Donor strand
ECM	Extracellular matrix
EGFP	Enhanced green fluorescent protein
EtOH	Ethanol
FBL	Follicular basal lamina
FBS	Foetal bovine serum
GC	Granulosa cell
GDF9	Growth differentiation factor 9
H&E	Haematoxylin and eosin
IHC	Immunohistochemistry
KitL	KIT ligand
mAMH	Murine anti-Müllerian hormone
mROSA26	Murine ROSA26 locus
MOI	Multiplicity of infection
MS	Mouse serum
mTOR	Mechanistic target of rapamycin

NBF	Neutral buffered formalin
NGS	Normal goat serum
PBS	Phosphate-buffered saline
PBS-T	Phosphate-buffered saline with Tween-20
pf-GC	Pre-flattened granulosa cell
PGC	Primordial germ cell
PI3K	Phosphoinositide 3-kinase
POI	Premature ovarian insufficiency
RO	Reaggregated ovary
ROEx	Extended protocol reaggregated ovary
ROI	Region of interest
SiR-DNA	Silicon–rhodamine deoxynucleic acid
sgRNA	Single guide ribonucleic acid
SaCas9	*Staphylococcus aureus* Cas9
TC	Theca cell
TCT	Tissue-culture-treated
WO	Whole ovary
ZP	Zona pellucida

1. INTRODUCTION

1.1 Ovarian function and fertility preservation

1.1.1 Biological and societal importance of fertility

Reproduction, whether sexual or asexual, is an imperative and unifying process for all life on Earth, through which genetic information endures, changes, and supports the continuation of species across generations (Cooper, 2000). Reproductive success in females is dependent on the coordinated function of the ovary: 1) to produce mature eggs, herein referred to as oocytes, capable of fertilisation, and 2) regulate the endocrine system for balanced, cyclic sexual hormone secretion (Oktem and Oktay, 2008; Richards and Pangas, 2010). The physiological significance of the ovarian organ extends beyond reproduction, with its associated function contributing to metabolic, skeletal, and cardiovascular health (Benayoun *et al.*, 2025; Maric-Bilkan *et al.*, 2014).

Globally, infertility affects approximately one in six couples of reproductive age and influences physiological, psychological, and social wellbeing (World Health Organisation, 2025a). The implications of infertility are felt beyond the individual, contributing to large-scale demographic change that shapes healthcare demand, economic planning, and strategies for population sustainability (Feng *et al.*, 2025; Scripps and Webb, 2025). Fecundity and reproductive potential are closely associated with personal identity, bodily autonomy, and social standing; as a result, loss of fertility can carry profound emotional and cultural burdens (Bueno-Sánchez *et al.*, 2024; Leyser-Whalen *et al.*, 2012; Xie *et al.*, 2023).

Historically, diverse human cultures and civilisations have developed traditions, folklore, and practices surrounding fertility and reproduction. Thesmophoria, a women-only religious festival in ancient Greece, linked the fertility of women with the fertility of crops and the earth in dedication to

the goddesses Demeter and Persephone (Nilsson *et al.*, 2016). Even within the wider animal kingdom, successful reproductive behaviours, such as the elaborate courting dance of the male blue-footed booby, are essential for the production of offspring (Anchundia *et al.*, 2014; Kemeny, 2014). Fertility and parenthood are linked to social inclusion, perceived purpose, and intergenerational establishment, which impact overall quality of life (Leyser-Whalen *et al.*, 2012; Xie *et al.*, 2023).

According to established biological dogma, the human ovary is constrained by a finite number of germ cells established before birth (Faddy and Gosden, 1996; Tingen *et al.*, 2009). This non-renewable primordial pool is highly susceptible to depletion through natural ageing, disease, or medical intervention (Faddy *et al.*, 1992; Oktem and Oktay, 2008; Pellatt *et al.*, 2007; Richardson *et al.*, 1987; Rooda *et al.*, 2025; Wallace *et al.*, 2003). Thus, the ovary's sensitive 'biological clock' contrasts with the functionality of the male gonad, the testes, where spermatogonia support continuous spermatozoa production throughout adult life (Faddy and Gosden, 1996; Liu *et al.*, 2009; Richards and Pangas, 2010). The concept of a fixed ovarian reserve has therefore shaped scientific understanding, clinical practice, and societal norms surrounding female fertility for decades.

Understanding the mechanisms that govern oocyte growth and survival is central to reproductive and fertility research, reflecting the focus of this thesis. Beyond the scope of this thesis, ovarian-focused research is critical to establish equitable long-term health solutions, inform ethical frameworks in policy governance, and expand societal norms for women (National Academies of Sciences *et al.*, 2025; Regensteiner *et al.*, 2025; Warren *et al.*, 2025).

1.1.2 Prevalence of infertility, cancer survivorship, and reproductive aging

Understanding the current landscape of reproduction and fertility provides the necessary context for the work presented here. The United Nations and World Health Organisation (WHO) recognise reproductive rights are human rights (UNFPA *et al.*, 2014; World Health Organisation, 2025b). It is long established that individuals and couples have the right to freely and responsibly decide the number, timings, and spacing of their offspring (United Nations General Assembly, 1979).

Infertility, defined by the WHO as the failure to achieve pregnancy after 12 months of regular unprotected sexual intercourse, is a global public health crisis that does not discriminate based on socioeconomic status or geopolitical borders (Dhalwani *et al.*, 2013; Liu *et al.*, 2025; World Health Organisation Guideline Development Group for Infertility *et al.*, 2025; Zegers-Hochschild *et al.*, 2009). The source of infertility can be attributed to male-factor only, female-factor only, a combination of both, or idiopathic causes (Figure 1.1.2.1) (Kashir *et al.*, 2010; World Health Organisation Guideline Development Group for Infertility *et al.*, 2025). Female infertility is frequently associated with ovulatory dysfunction, diminished ovarian reserve, tubal disease, endometriosis, or uterine pathology (Becker *et al.*, 2022; World Health Organisation Guideline Development Group for Infertility *et al.*, 2025).

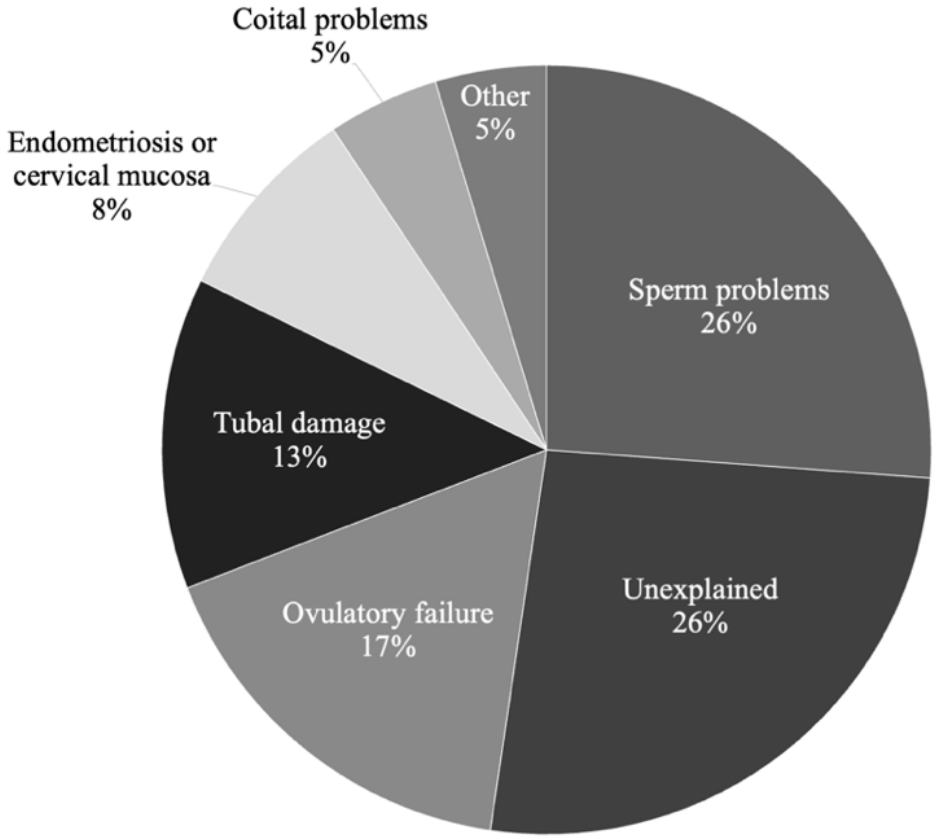

Figure 1.1.2.1) Primary causes of infertility. Approximate proportional contributions of major factors causing infertility, including sperm-related abnormalities (26%), unexplained infertility (26%), ovulatory failure (17%), tubal damage (13%), endometriosis or cervical mucosa factors (8%), coital problems (5%), and other causes (5%). Adapted from Kashir *et al.*, 2010.

The observed global trend of declining fertility rates has resulted in new investment and attention, as evidenced by the recent release of the first WHO guidelines on the prevention, diagnosis, and treatment of infertility (Liu *et al.*, 2025; World Health Organisation Guideline Development Group for Infertility *et al.*, 2025).

Reproductive ageing remains a principal barrier to conception. In many high-income societies, women are having children later in life (Lei *et al.*, 2025). In the UK, the average maternal age at birth of first offspring has risen from ~23 years of age in 1970 to ~31 years of age based on 2021 census data (Office for National Statistics, 2025; Office for National Statistics UK, 2024). Delayed childbearing paired with the decline of reproductive potential at advancing maternal age has further compounded prevalence of infertility. Both 'natural' and assisted reproductive technology (ART)-mediated birth rates decline after the mid-30s, with reduced oocyte quality and increased aneuploidy risk (Valeri *et al.*, 2011; Winstanley *et al.*, 2024; World Health Organisation Guideline Development Group for Infertility *et al.*, 2025).

Premature ovarian insufficiency (POI) is a condition affecting approximately 1% of women, wherein ovarian function ceases before 40 years of age (American College of Obstetricians and Gynecologists, 2014; Coulam *et al.*, 1986; Luborsky *et al.*, 2003). By this logic, approximately 350,000 women in the UK alone are estimated to be at risk of developing this condition (Office for National Statistics UK, 2025). More recent analyses suggest that over 3% of women may be affected or at risk, demonstrating its public health significance (Golezar *et al.*, 2019). POI can be caused by genetic factors (e.g., Turner syndrome), autoimmune mechanisms, iatrogenic exposures, or be idiopathic (Figure 1.1.2.2) (American College of Obstetricians and Gynecologists, 2014; Chon *et al.*, 2021; Mishra *et al.*, 2017; Nie *et al.*, 2024). Turner syndrome, a uniform or mosaic disorder where a single X chromosome is inherited, commonly leads to POI in affected individuals (Chon *et al.*, 2021; Nie *et al.*, 2024).

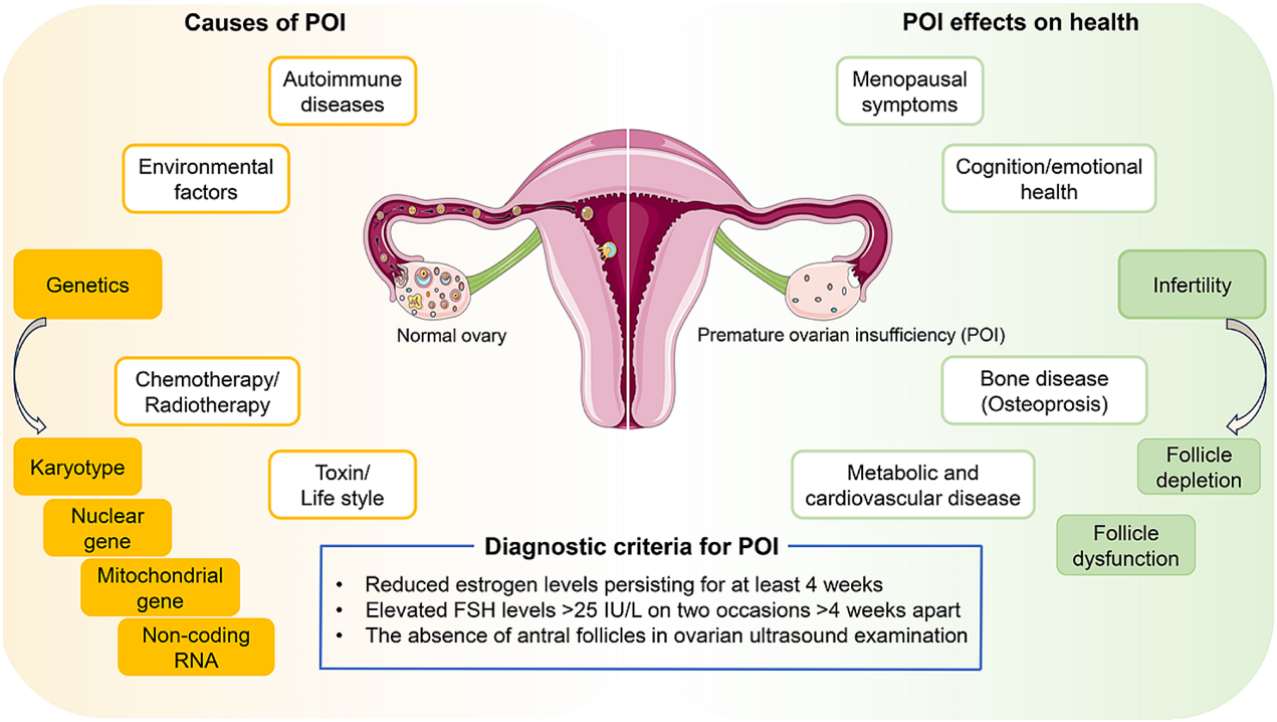

Figure 1.1.2.2) Pathogenic model, diagnostic criteria, and health consequences of premature ovarian insufficiency. Overview of factors contributing to POI and its clinical consequences. Causes of disease include genetic abnormalities, autoimmune disease, environmental factors, toxins, chemotherapy and/or radiotherapy, and lifestyle factors. Diagnostic criteria for POI comprise ≥4 weeks of reduced oestrogen levels, elevated FSH (>25 IU/L on two occasions >4 weeks apart), and the absence of antral follicles on ovarian ultrasound examination. POI can result in infertility, as well as osteoporosis, cardiovascular disease, and induce menopausal symptoms. Images are not to scale. Reproduced from Nie *et al.* (2024) under the terms of the Creative Commons Attribution 4.0 International License (CC BY 4.0). No changes were made. E2, oestradiol; FSH, follicle-stimulating hormone; IU/L, international units per litre; LH, luteinising hormone; POI, premature ovarian insufficiency; RNA, ribonucleic acid.

Iatrogenic POI may arise following the use of gonadotoxic treatments (Chon *et al.*, 2021). Advances in diagnostics and treatment have improved survival outcomes, resulting in a growing population of young cancer survivors at risk of infertility (De Paola *et al.*, 2025; Rahman *et al.*, 2025). In the UK and similar settings, approximately 10% of new cancer diagnoses occur in people aged 25–49, overlapping with the expected female reproductive lifespan (Faddy and Gosden, 1996; Lionis *et al.*, 2025). Although under-25s are a smaller proportional makeup, the five-year cancer survival in this group exceeds 80% in numerous tumour types (e.g., lymphoma) (Xiao *et al.*, 2025). A significant fraction of childhood and adolescent cancer survivors experience acute ovarian failure or POI later in life (Anderson et al., 2018; De Paola et al., 2025; Rahman et al., 2025). These shifts in survival demographics have intensified the demand for a deeper understanding of ovarian function and fertility preservation technologies. Fertility preservation options clinically available include embryo cryopreservation, oocyte vitrification, and ovarian tissue cryopreservation (Anderson *et al.*, 2017; Antonouli *et al.*, 2023).

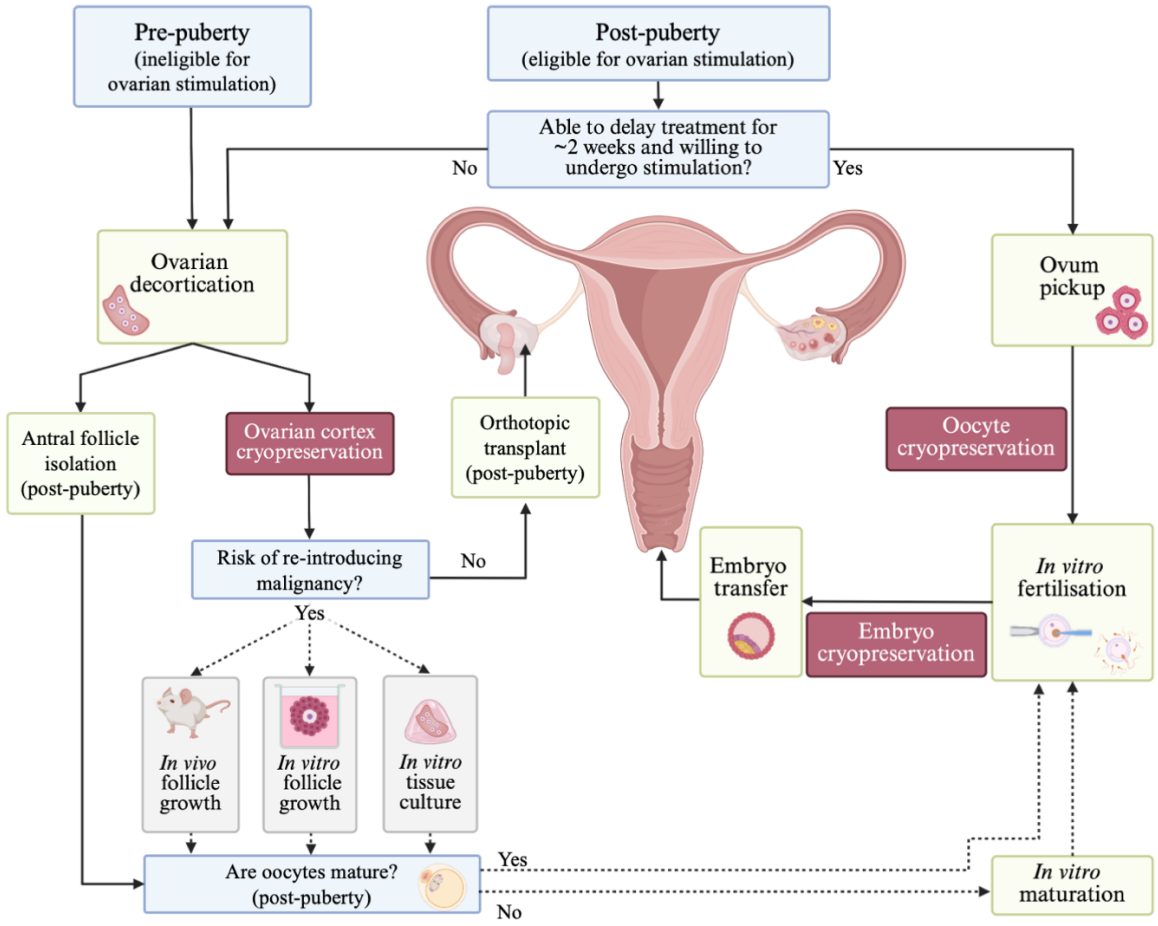

Figure 1.1.2.3) Fertility preservation strategies and clinical workflow for female patients undergoing gonadotoxic treatment. Overview of current and emerging fertility preservation options available to females at risk of treatment-related gonadotoxicity. For pre-pubertal patients, fertility preservation is limited to ovarian tissue cryopreservation, as ovarian stimulation and oocyte retrieval are not clinically feasible; however, oocyte-based approaches are applicable post-puberty. Established clinical approaches (dark pink) include oocyte, embryo, and ovarian cortical tissue cryopreservation. The clinical workflow (blue) outlines the pathway from patient assessment to downstream ART or tissue utilisation strategies (green). Solid lines represent clinically available options, whereas dotted lines and grey boxes represent experimental or investigational strategies. Images are not to scale. Adapted from a BioRender.com template (Lopez, 2025). Created with BioRender.com. ART, assisted reproductive technology.

Oocyte and embryo cryopreservation require controlled ovarian stimulation and transvaginal oocyte retrieval (Anderson *et al.*, 2017; Antonouli *et al.*, 2023) (Figure 1.1.2.3). This approach is restricted to post-pubertal individuals who can safely undergo hormone stimulation and delay cancer treatment for non-hormone-sensitive malignancies for the required 10–14 days, if so required (Cobo *et al.*, 2016; Donnez and Dolmans, 2013). Ovarian cortical tissue cryopreservation is offered to eligible pre- and post-pubertal patients, which can restore endocrine function and fertility following surgical autograft transplantation (Anderson *et al.*, 2017; Antonouli *et al.*, 2023). However, this fertility preservation strategy carries risks associated with surgery, does not guarantee successful pregnancy, and may risk the reintroduction of malignant cells in certain cancers, like haematological cancers (Bastings *et al.*, 2013; Gellert *et al.*, 2018).

The growing intersection between survivorship, ageing, and fertility decline has highlighted the urgent need for robust fertility research and interventions (Benayoun *et al.*, 2025; Feng *et al.*, 2025; De Paola *et al.*, 2025; Xiao *et al.*, 2025). For women with POI due to intrinsic somatic cell dysfunction, some gonadotoxic cancer survivors, and patients with blood-borne or ovarian malignancy, current fertility preservation options may be inadequate or contraindicated (Bastings *et al.*, 2013; Chon *et al.*, 2021; Nie *et al.*, 2024; Rahman *et al.*, 2025). These limitations highlight the need for robust *ex vivo* systems that can support follicle development from the earliest stages, that are safe, scalable, and capable of future clinical translation.

1.2 The ovarian landscape and early follicle development

1.2.1 Architecture of the ovary

The mammalian ovaries are dynamic organs located in the pelvic cavity, with one at either side of the uterus (Gibson and Mahdy, 2023; Oktem and Oktay, 2008; Richards and Pangas, 2010). The two principal roles of the ovary are the cyclical development and release of haploid gametes and the production of sex hormones that support sexual development, secondary sex characteristics, and reproductive function (Oktem and Oktay, 2008; Richards and Pangas, 2010). The ovary consists of several layers. The outermost ovarian layer is the surface epithelium which covers a dense layer of connective tissue called the tunica albuginea (Auersperg *et al.*, 2001; Kinnear *et al.*, 2020; Williams and Erickson, 2012) (Figure 1.2.1). Next, the ovarian cortex is enriched with a highly dense extracellular matrix (ECM) that provides structural support and houses germ cells and other cell types (Kinnear *et al.*, 2020; Ouni *et al.*, 2018; Williams and Erickson, 2012). The innermost region of the ovary, the medulla, is a loose, highly vascularised structure with blood vessels, nerves, and steroidogenic cells (Auersperg *et al.*, 2001; Kinnear *et al.*, 2020; Williams and Erickson, 2012). The follicle, consisting of a single oocyte surrounded by supportive somatic cells, is considered the fundamental reproductive unit of the ovary (Baca and Zamboni, 1967; Gougeon, 1986; Strauss and

Williams, 2019). Primordial follicles are localised towards the cortex, with more advanced follicles distributed towards the medulla in a stage-dependent manner.

1.2.2 Follicle formation and the establishment of the ovarian reserve

Much of this thesis was written with various translational applications to humans in mind. As such, human physiology is focused here with parallels across mammalian species. Ovary development and ovarian reserve establishment occurs during foetal life. Primordial follicles, an oocyte surrounded by a single layer of flattened pre-granulosa cells (fp-GCs), are the earliest and most abundant follicle type that constitute the ovarian reserve (Baker, 1963; Kerr *et al.*, 2013; Yin *et al.*, 2016).

During foetal life, primordial germ cells (PGCs), the precursor for oocytes, first appear in the yolk sac at two weeks post coitum (Heeren *et al.*, 2015; McLaughlin and McIver, 2009; Strauss and Williams, 2019). Through amoeba-like movement, the PGCs migrate to the gonadal ridges at 4–6 weeks' gestation. From female sex differentiation (~8 weeks gestation) until 20 weeks' gestation, PGCs differentiate into oogonia and proliferate into clusters known as germ cell nests, reaching an estimated peak of seven million germ cells (Faddy *et al.*, 1992; Sarraj and Drummond, 2012; Strauss and Williams, 2019; te Velde *et al.*, 1998).

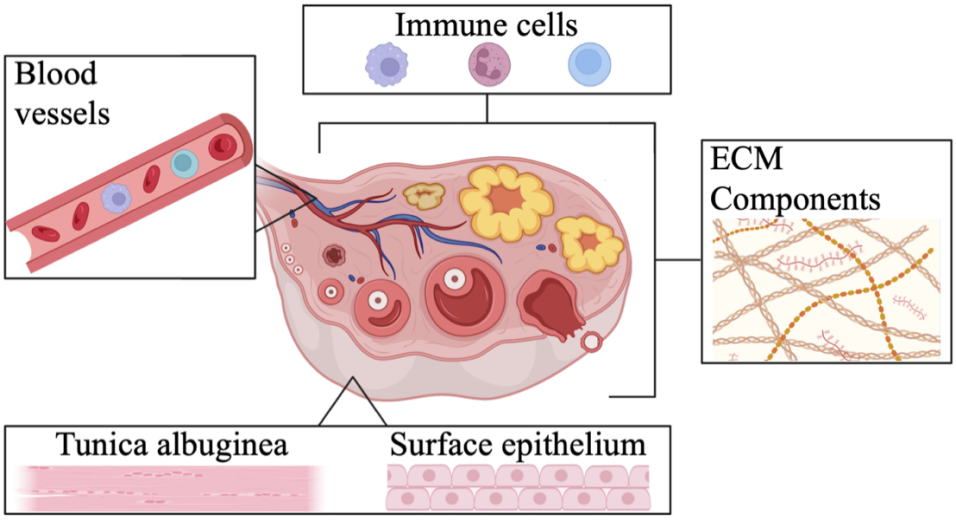

Figure 1.2.1) Structural and microenvironmental components of the ovary. Schematic representation of a human ovary showing follicle development and corpora lutea at various stages within the ovary, surrounded by panels highlighting key stromal elements, including (clockwise from top centre): immune cells (macrophage, neutrophil, and lymphocyte), ECM components, surface epithelium and tunica albuginea, and a blood vessel containing red blood cells and immune cells. Images are not to scale. The figure is intended to provide contextual overview of the ovarian microenvironment rather than a detailed representation of follicle structure. Adapted from Kinner *et al.* (2020). Created with BioRender.com. ECM; extra-cellular matrix.

As proliferation ceases, oogonia enter meiosis I, differentiate into primary oocytes, and arrest at the diplotene stage of prophase I (Kerr *et al.*, 2013; Wang and Pepling, 2021; Wear *et al.*, 2016). Germ cell nest breakdown is accompanied by the invasion of somatic cells, which surround individual oocytes to form primordial follicles (Kerr *et al.*, 2013; Tingen *et al.*, 2009; Wear *et al.*, 2016). Approximately two-thirds of oogonia will not form primordial follicles; without the support of fp-GCs, these germ cells undergo apoptosis (Pepling and Spradling, 2001). At birth, the number of remaining germ cells declines to approximately one million, and by menarche this is further reduced to ~300,000–400,000 oocytes (Faddy *et al.*, 1992; te Velde *et al.*, 1998). The ovarian reserve is the number of remaining oocytes in the ovary, representing the individual's potential for fertility.

The ovarian reserve declines through two principal mechanisms: 1) physiological recruitment of follicles into the growth pathway, followed by ovulation or atresia; and 2) age-related or pathological atresia of dormant follicles. The rate of decline increases with age, particularly after the mid-30s, consistent with modelling of non-growing follicle depletion, until menopause when follicle numbers fall below a critical threshold (Faddy and Gosden, 1996; Hansen *et al.*, 2008; Wallace and Kelsey, 2010). It is now widely accepted that follicle depletion is not absolute at menopause, with approximately 1000 follicles remaining at this stage (Hansen *et al.*, 2008; Wallace and Kelsey, 2010). Further, it is understood that the primordial pool in humans and mice are non-renewable (Bristol-Gould *et al.*, 2006; Kerr *et al.*, 2013). However, it should be acknowledged that this dogma has been challenged; studies have reported mitotically active germline stem cells in adult human ovaries, as well as evidence of adult germ cell pluripotency in certain non-human mammals (Clarkson et al., 2018; Johnson et al., 2004, 2005; Porras-Gomez and Moreno-Mendoza, 2020). Whilst intriguing, these findings have not led to a paradigm shift in biological understanding nor have they produced reproducible results. For the purposes of this thesis, the ovarian reserve is considered a fixed, finite resource whose preservation and utilisation are a central focus to female fertility.

1.2.3 Follicle development

For a mature oocyte capable of fertilisation to be ovulated, the entire follicle must undergo a complex and tightly regulated process of development (Eppig *et al.*, 2002; McLaughlin and McIver, 2009; Wang and Pepling, 2021; Zhao *et al.*, 2023). Following activation, growing follicles exhibit increasing responsiveness to gonadotrophins, although early development remains largely gonadotrophin-independent (Longobardi *et al.*, 2024; Orisaka *et al.*, 2021; Zhang *et al.*, 2023).

1.2.3.1 Primordial follicle quiescence and activation

The dominant population of follicles are of the primordial stage, which are considered dormant (Adhikari and Liu, 2009; Kubo *et al.*, 2025; Zhang and Liu, 2015) (Figure 1.2.3.1). These follicles have three fates: continue quiescence, atresia, or undergo the process of activation. Upon activation, the fp-GCs proliferate and morphologically transition to cuboidal granulosa cells (GCs) (Kubo *et al.*, 2025; Zhao *et al.*, 2021). Follicles with a mixture of flattened and cuboidal GCs are herein referred to as transitional follicles. Although transitional follicles are thought to be 'activated', they may represent a substantial, slow-growing cohort of the resting primordial pool (De Bruin *et al.*, 2002; Gougeon, 1986; Van Wezel and Rodgers, 1996). Primordial follicle activation and early development occur independently of pituitary gonadotrophins and are instead regulated by intra-ovarian signalling pathways (Orisaka *et al.*, 2021; Zhang *et al.*, 2023).

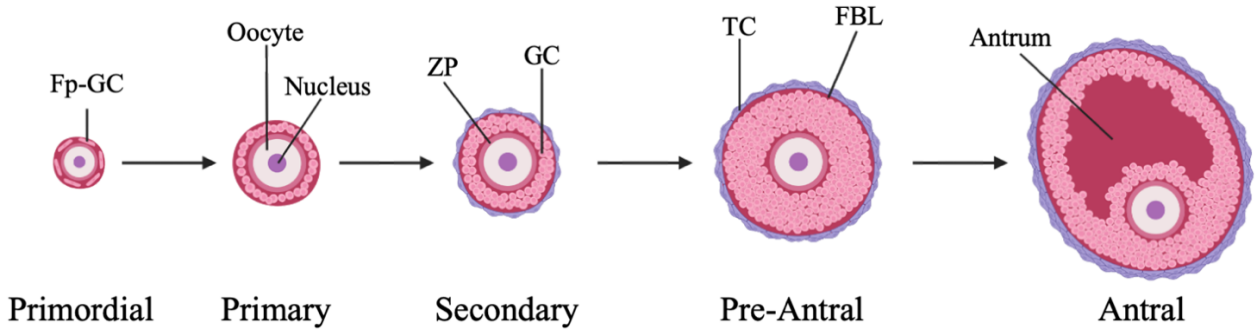

Figure 1.2.3.1) Representation of early follicle development, from the primordial to antral stages. Illustration of follicle development showing primordial, primary, secondary, pre-antral, and antral follicles. A transitional follicle, defined by a mixture of fp-GCs and cuboidal GCs, represents an intermediate stage between primordial and primary follicles and is not depicted. Key structural features, including oocyte, nucleus, GCs, FBL, TCs, ZP, and antral cavity, are labelled at the relevant stages. Images are not to scale. Created with BioRender.com. FBL, follicular basal lamina; GC, granulosa cell; fp-GC, flattened pre-granulosa cell; TC, theca cell; ZP, zona pellucida.

1.2.3.2 Growing follicle development

The primary follicle is defined by having a single, complete layer of cuboidal GCs surrounding the oocyte. During the primordial-to-primary transition, the oocyte increases in volume and the zona pellucida (ZP), a thin specialised glycoprotein layer in between the oocyte and GCs, is established (Baca and Zamboni, 1967; Epifano *et al.*, 1995; Marchais *et al.*, 2022; Strauss and Williams, 2019). GCs continue to proliferate to form a full second layer, the secondary stage. Continued oocyte growth and GC proliferation lead to follicles with multiple GC layers, referred to as pre-antral follicles. Human oocytes reach a terminal size of ~120 µm by the end of the pre-antral stage, concurrent with GC and TC proliferation (Gougeon, 1986; Telfer *et al.*, 2023). Stromal cells adjacent to the follicular basal lamina (FBL) are recruited and differentiate into theca cells (TCs), providing structural support and blood supply access to the follicle, with full steroidogenic differentiation becoming established at the antral stage (Liu *et al.*, 2015; Orisaka *et al.*, 2021; Young and McNeilly, 2010).

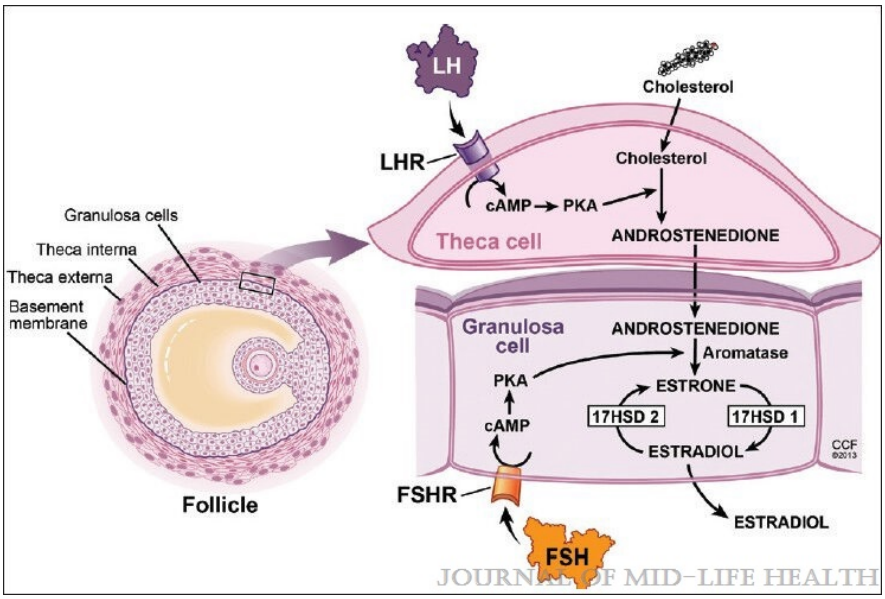

Figure 1.2.3.3) The two-cell, two-gonadotrophin model of ovarian steroidogenesis. Representation of coordinated steroidogenesis within the TC and GC layers of the follicle. LH binds to LHCGR, shown as LHR, on TCs, activating cAMP/PKA signalling and promoting the conversion of cholesterol into androstenedione. The androgen diffuses across the FBL into the adjacent GC, where FSH binds to FSHR and activates cAMP/PKA pathways. In GCs, androstenedione is converted to oestrogens via aromatase, forming oestrone and subsequently 17β-oestradiol via 17HSD1. Oestradiol is then secreted into the follicular environment. The left panel shows a corresponding follicle cross-section highlighting key structural features. Image not to scale. Sourced from Doshi and Agarwal (2013) under the terms of the CC BY-NC-SA 3.0 licence. 17HSD1, 17β-hydroxysteroid dehydrogenase type 1; 17HSD2, 17β-hydroxysteroid dehydrogenase type 2; cAMP, cyclic adenosine monophosphate; FBL, follicular basal lamina; FSH, follicle-stimulating hormone; FSHR, follicle-stimulating hormone receptor; GC, granulosa cell; LH, luteinising hormone; LH(CG)R, luteinising hormone (/choriogonadotropin) receptor; PKA, protein kinase A; TC, theca cell.

1.2.3.3 Gonadotrophin-dependent follicle growth

Growing follicles exhibit increasing responsiveness to pituitary-derived gonadotrophins, follicle-stimulating hormone (FSH) and luteinising hormone (LH), with full dependence emerging at the antral stage (Oktem and Oktay, 2008; Richards and Pangas, 2010). Steroidogenesis is classically described by the two-cell, two-gonadotrophin model: TCs produce androgens in response to LH, which diffuse across the FBL to GCs (Doshi and Agarwal, 2013; Marchais *et al.*, 2022; Millier *et al.*, 1994) (Figure 1.2.3.3). There, aromatase converts androgens to oestrogens in response to FSH, promoting GC proliferation. The onset of antral follicle development is characterised by the presence of an antrum, fluid-filled cavities between GCs, which merge to form a single cavity within the follicular somatic compartment. The antrum consists of a mixture of growth factors, hormones (including progesterone, oestradiol, LH, and FSH), antioxidants, and metabolites that support oocyte maturation (Hennet and Combelles, 2012).

As the follicle grows, so does the antral cavity which separates the surrounding GCs into two distinctive populations: cumulus cells and mural cells (Gilchrist *et al.*, 2004; Marchais *et al.*, 2022; Telfer and McLaughlin, 2012). Cumulus GCs remain close to the oocyte, adjacent to the ZP, and are involved in the completion of meiotic maturation of the oocyte (Gilchrist *et al.*, 2004; Turathum *et al.*, 2021). Mural GCs line the follicular wall and contribute to endocrine function through steroidogenesis and their capacity to differentiate into luteal cells following the LH surge (Christenson *et al.*, 2013; Oktem and Oktay, 2008).

Although a cohort of antral follicles are selected for pre-ovulatory growth, only one follicle will achieve dominance in the typical menstrual cycle (Fauser and van Heusden, 1997; te Velde *et al.*, 1998). The precise mechanisms coordinating dominant follicle selection are not fully understood but are thought to involve differences in sensitivity to FSH, vascularisation, and response to local ovarian feedback loops (Fortune *et al.*, 2004; Webb and Campbell, 2007). Selection occurs in response to an increase in FSH during the late follicular phase to prime the dominant follicle for successful ovulation (Mihm and Evans, 2008; Zeleznik, 2004).

When the dominant follicle matures, the increasing amounts of oestradiol exert a negative feedback response along the hypothalamic-pituitary-gonadal axis, which suppresses the release of FSH and, in turn, the growth of other nondominant follicles (Fortune *et al.*, 2004; Webb and Campbell, 2007; Zeleznik, 2004). However, once oestrogen levels reach a critical threshold, the feedback loop reverses to positive and causes a mid-cycle surge of LH (Holesh *et al.*, 2023; Marchais *et al.*, 2022).

This LH surge triggers the resumption of meiotic activity in the oocyte, cumulus expansion, and follicular rupture, in a process known as ovulation (Marchais *et al.*, 2022; McLaughlin *et al.*, 2018; Turathum *et al.*, 2021). The released oocyte, reaching metaphase II competency, is captured by the fallopian fimbriae and is capable of fertilisation. The remaining GCs and TCs left behind in the ovary differentiate to form the corpus luteum, which secretes progesterone in support of potential early pregnancy until placenta steroidogenesis is established via joint support from the mother and foetus (Bochner *et al.*, 2015; Cable and Grider, 2023; Soygur and Laird, 2021).

1.2.4 Bidirectional communication and regulatory pathways in growing follicles

Follicle development is dependent on bidirectional communication between the oocyte and its surrounding follicular somatic compartment. The exchange of signals is mediated via gap junctions, paracrine and autocrine signalling, and ECM support to ensure coordinated growth between germ and somatic cells (Alam and Miyano, 2019; Albertini *et al.*, 2001; Eppig, 1991; Gilchrist *et al.*, 2004).

Communication within the follicle primarily occurs via paracrine signalling and gap junctions (Alam and Miyano, 2019; Eppig, 1991; Gittens *et al.*, 2005). Paracrine signalling occurs when secreted factors induce changes in neighbouring cells (Alam and Miyano, 2019; Eppig, 1991). Oocyte-derived growth differentiation factor 9 (GDF9) and bone morphogenetic protein 15 (BMP15) stimulate GC proliferation, differentiation, and cumulus expansion (Alam and Miyano, 2019; Gittens *et al.*, 2005; Peng *et al.*, 2013). Gap junctions consist of intercellular channels that permit the direct transfer of ions and small molecules between cells (Alam and Miyano, 2019; Gittens *et al.*, 2005; Oktem and Oktay, 2008). Connexin-based gap junctions link GCs to one another and, via transzonal projections

across the ZP, to the oocyte (Albertini *et al.*, 2001; Gittens and Kidder, 2005; Marchais *et al.*, 2022; O'Connell and Pepling, 2021). Connexin 43 is a key protein in GCs that is widely utilised as a marker of intercellular communication during early follicle development (Chang *et al.*, 2016; Gittens and Kidder, 2005; Thomas *et al.*, 2024). If connexin 43 is absent, gap junctional communication between GCs fails and lead to impaired follicle growth (Gittens and Kidder, 2005; Zhu *et al.*, 2024).

A wide range of intracellular signaling pathways regulate follicle dormancy, activity, and growth, forming an interconnected network that is still being actively characterised (Telfer *et al.*, 2023). These pathways include, but are not limited to, the evolutionarily conserved phosphoinositide 3-kinase (PI3K)/Akt/mechanistic target of rapamycin (mTOR) and Hippo pathways, alongside additional regulators such as transforming growth factor-β and mitogen-activated protein kinase signalling pathways (Telfer *et al.*, 2023). The PI3K/Akt/mTOR signaling cascade, with respect to mTOR especially, integrates growth factor, nutritional, and stress signals to modulate cell proliferation, metabolism, and autophagy within the GCs and oocytes (Cheng *et al.*, 2015; Dupont *et al.*, 2012; Grosbois and Demeestere, 2018; Hao, Li, *et al.*, 2024; Yaba *et al.*, 2008). Pharmacological modulation with rapamycin (mTOR inhibitor) or MHY1485 (mTOR activator), alters GC proliferation and activation in both *in vitro* and *in vivo* settings (Cheng *et al.*, 2015; Hao, Liu, *et al.*, 2024; Yaba *et al.*, 2008). The Hippo pathway has been implicated in culture-induced activation of primordial follicles following ovarian fragmentation, in part through Yes-associated protein (YAP)-mediated transcription (Grosbois and Demeestere, 2018; Kawamura *et al.*, 2013).

Whilst the precise role of these pathways in follicle development remains an active area of research, they demonstrate how biochemical and mechanical cues shape early follicle trajectories. The finely tuned balance of local signals, systemic factors, and tissue architecture is necessary to support development. Experimental culture systems that aim to model early follicle growth *in vitro* must acknowledge and be accountable for this complexity, such as techniques that involve tissue fragmentation, dissociation, and/or reaggregation, as explored here.

1.3 Investigation of follicle development *in vitro*

1.3.1 Review of culture approaches to investigate follicle development

In vitro growth of ovarian follicles has emerged as an important research tool and prospective future alternative to existing fertility preservation techniques, with particular focus for patients for whom standard methods are unavailable or unsafe. Broadly, culture strategies can be grouped into three categories: 1) ovarian tissue culture, 2) isolated follicle culture (including three-dimensional matrices), and 3) reaggregated ovary (RO) or organoid culture.

Whole ovary (WO) culture preserves the native architecture of the organ, including its vasculature and stromal networks (Lo *et al.*, 2019; Morgan *et al.*, 2015). However diffusion limitations, challenges in maintaining long-term viability, and difficulties in imaging deep tissue regions constrain this model. Cortical strip culture, involving the maintenance of thin ovarian cortex slices *in vitro*, has been widely employed to investigate follicle activation and growth from as early as the primordial stage (Bjarkadottir *et al.*, 2021; McLaughlin *et al.*, 2018; Walker *et al.*, 2021). The thinner cortical tissue slices promote nutrient uptake and gas diffusion in culture. Isolated follicle culture, typically within three-dimensional systems, with or without matrices (e.g., alginate or synthetic hydrogels), offer a more controlled microenvironment and has enabled the development of fully grown oocytes from the pre-antral stage in multiple species (Francés-Herrero *et al.*, 2023; Xu *et al.*, 2009, 2021).

In a landmark study, human primordial follicles were grown *in vitro* through to competent (metaphase II) oocytes through a multi-step culture system, where primordial and unilaminar follicles were cultured in cortical tissue then dissected and further grown in an isolated follicle culture (McLaughlin *et al.*, 2018). Further protocol optimisation is required for future clinical application as only nine metaphase II oocytes emitted polar bodies were obtained from an initial pool of 385 follicles.

Complex three-dimensional systems including ovarian organoids, chimeric ovarian constructs, and ROs have been developed to model early follicle formation and growth, including cross-species chimeras for mechanistic investigation (Dipali *et al.*, 2024; Eppig and Wigglesworth, 2000; Gittens

and Kidder, 2005; Lo *et al.*, 2019; Porras-Gomez and Moreno-Mendoza, 2020; Sheikh *et al.*, 2023). ROs form a key focus in this thesis and are discussed in more detail below.

1.3.2 Limitations with current systems to support *in vitro* follicle growth

Despite substantial progress, current *in vitro* models for follicle culture and ovarian tissue research face key limitations in their ability to recapitulate early follicle development. Ovarian culture systems, whether cortical fragments, WOs, or reconstituted tissues, offer unique opportunities to interrogate primordial and early growing follicles but can introduce substantial artefacts.

Tissue fragmentation and dissociation can accelerate primordial activation and alter growth dynamics, often at the cost of premature depletion of follicles (Kerr *et al.*, 2013; McLaughlin *et al.*, 2018; O'Connell and Pepling, 2021; Telfer and Andersen, 2021; Zhao *et al.*, 2021). Fragmentation has been linked to activation of Hippo/YAP signalling and modulation of PI3K and mTOR pathways, promoting granulosa proliferation and oocyte growth (Dupont *et al.*, 2012; Grosbois and Demeestere, 2018; Guo and Yu, 2019; Kawamura *et al.*, 2013; Yang *et al.*, 2022). While these effects can be harnessed experimentally, *in vitro* follicle development is not an exact mirror of *in vivo* processes (Bjarkadottir *et al.*, 2021; Cheng *et al.*, 2024; Lo *et al.*, 2019; Xiao *et al.*, 2015).

1.3.3 The reaggregated ovary model

The RO model represents a powerful tool to interrogate follicle formation and early development in a controlled, three-dimensional context. Initially described by Eppig and Wigglesworth (2000), this approach involves the dissociation of ovarian ECM into a heterogeneous suspension of cells comprised of germ cells, GCs, and other stromal cells. Following cell culture, the heterogeneous cell population is recombined into a tissue pellet for culture or transplantation (Eppig and Wigglesworth, 2000; Lo *et al.*, 2019; Porras-Gomez and Moreno-Mendoza, 2020; Sheikh *et al.*, 2023).

ROs and related chimeric ovaries can re-establish follicle formation and communication between germ and somatic cells. Previously, this model has been used to investigate oocyte-somatic

communication, cross-species follicle formation, and the rescue of defective phenotypes (Eppig and Wigglesworth, 2000; Gittens and Kidder, 2005; Hikabe *et al.*, 2016; Li *et al.*, 2024; Porras-Gomez and Moreno-Mendoza, 2020; Zhang *et al.*, 2024). By separating germ cells and somatic cells via differential adhesion and recombining them in specific ratios or from alternative sources (e.g., xenogeneic combinations of mouse and rat material), ROs enable direct investigation of the follicular microenvironments and its influence on oocyte development (Eppig and Wigglesworth, 2000; Porras-Gomez and Moreno-Mendoza, 2020; Sheikh *et al.*, 2023).

Lo *et al.* (2019) provided a pivotal analysis of murine ROs derived from postnatal ovaries, assessing follicle development from transplanted ROs (beneath the kidney capsule), cultured ROs, as well as cultured ovaries from postnatal day 2 (P2) and P6 mice (Figure 1.3.3). Stage distribution and growth dynamics differed from ROs to intact WOs of the same experimental condition, with follicle growth accelerated in cultured ROs (Lo *et al.*, 2019). Cultured RO follicles also exhibited morphological differences, including fewer GCs in early stage follicles, incomplete FBL formation, and limited theca recruitment (Lo *et al.*, 2019). These findings are broadly consistent with reports that *in vitro* systems, whilst more experimentally tractable, can alter the tempo and fidelity of follicle development (Cheng *et al.*, 2024; McLaughlin *et al.*, 2018; Telfer and McLaughlin, 2012).

In addition to the RO model, ovarian organoids and organoid-like models, where stem-cell-derived or primary ovarian cells self-organise, are utilised to recapitulate and investigate aspects of ovarian architecture (Bagheri *et al.*, 2024; Li *et al.*, 2024; Zhang *et al.*, 2024). These models reinforce the observation that the timing and coordination of oocyte-somatic communication is vital for follicle development. However, challenges persist between models with incomplete volumetric growth, limited TC recruitment, reduced reproducibility, and difficulty in standardisation across laboratories (Lo *et al.*, 2019; Telfer and McLaughlin, 2012; Wu *et al.*, 2023; Zhang *et al.*, 2024).

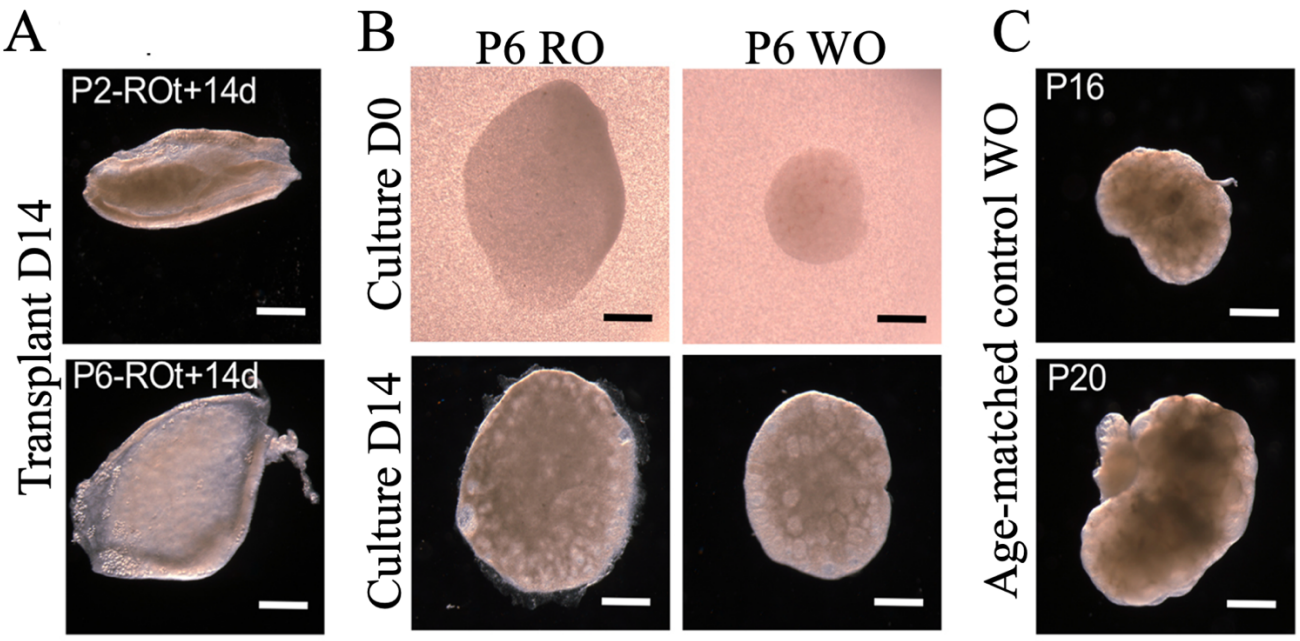

Figure 1.3.3) Representative images of reaggregated and whole ovaries following culture or transplantation compared with age-matched *in vivo* controls. Examples from Lo *et al.* (2019) study illustrate how the RO model recapitulates ovarian tissue growth while diverging from intact WOs. ROs were generated by enzymatically dissociating ovaries from P2 or P6 mice into a heterogenous suspension of primary cells. Germ cell and somatic cell populations were separated in culture via differential adhesion. Cell populations were then recombined to form a tissue pellet, the RO. Follicular growth was assessed following culture or transplantation. **A)** ROs derived from P2 (top) and P6 (bottom) murine ovaries following 14 days of transplantation beneath the kidney capsule. **B)** Comparative images of a P6 RO and a P6 WO at the start of culture (D0; top) and after 14 days *in vitro* (D14; bottom). **C)** Age-matched control WOs collected a P16 (top) and P20 (bottom), served as an *in vivo* comparator for P2-ROt-14d and P6-derived tissues cultured or transplanted for 14 days, respectively. Scale bar represents 500 µm. Adapted from Lo *et al.* (2019), under the Creative Commons Attribution 4.0 International licence. Panels were cropped and rearranged, with statistical graphs omitted. Terminology has been adjusted to reflect this thesis. D(0/14), day (0/14); P(2/6/16/20), postnatal day (2/6/16/20); RO, reaggregated ovary; ROt+14d, RO transplanted for 14 days; WO, whole ovary.

The RO model is particularly attractive for future clinical translation to support fertility preservation in patients with dysfunctional ovarian somatic cells or malignancy. In principle, it could allow the replacement of diseased or dysfunctional somatic cells with healthy counterparts, whilst retaining the patient's own oocytes (Sheikh *et al.*, 2023). An RO-based approach could 'rescue' oocyte development and maturity for subsequent *in vitro* maturation (Bastings *et al.*, 2013; Prasad *et al.*, 2016). However, to realise this potential, it is essential to understand how structural manipulations during RO generation impact follicle assembly, communication, and growth trajectories, as well as develop methods for dynamic, data-rich assessment of follicle health in these tissue constructs. This forms a core focus of the present thesis.

1.4 Current methodological barriers to investigate early follicle development

A central limitation with the assessment of early follicle development lies in the methodology. Histology and immunohistochemistry (IHC) are considered gold-standard methods for analysing early follicle development. Histology-based methodology preserves cross-sectional tissue architecture, cellular morphology, and supports the localisation of proteins (Adeniran *et al.*, 2021; Harrison *et al.*, 2025). Conventional histology typically involves embedding tissue with wax, slicing tissue into ~5 μm sections, staining or immunolabelling sections, and then two-dimensional visualisation via brightfield or fluorescence microscopy (Adeniran *et al.*, 2021; Harrison *et al.*, 2025).

Follicles are commonly staged and scored using the largest cross-section, as identified by the presence of the oocyte nucleus as a substitute for the entire follicle structure (Figure 1.4) (Adeniran *et al.*, 2021; Harrison *et al.*, 2025; Uslu *et al.*, 2017). However, a 5 μm section cannot encapsulate the full three-dimensional follicle. Only visible follicular cells present within the selected cross-section are assessed, whilst cells in adjacent sections are ignored (Harrison *et al.*, 2025). The orientation of follicles within the tissue cannot be controlled and is unknown during the embedding process; thus, the plane of cross-sectional assessment may variably intersect the follicle, leading to inconsistent representation of GC morphology. As a consequence, transitional follicles and primordial follicles are at particular risk of incorrect classification, where accurate staging relies on subtle differences in GC shape and arrangement (Harrison *et al.*, 2025).

In previous work of the Williams Group, a whole-mount immunolabelling and optical tissue clearing protocol for human ovarian tissue was developed that enabled the three-dimensional visualisation of follicles as early as the primordial stage (Harrison *et al.*, 2025). The method combined nuclear staining (DAPI, 4′,6-diamidino-2-phenylindole), oocyte-specific labelling (DEAD-box helicase 4), and FBL labelling (laminin) with imaging of optical z-stacks across three orthogonal planes (XY, XZ, YZ) in cleared ovarian tissue.

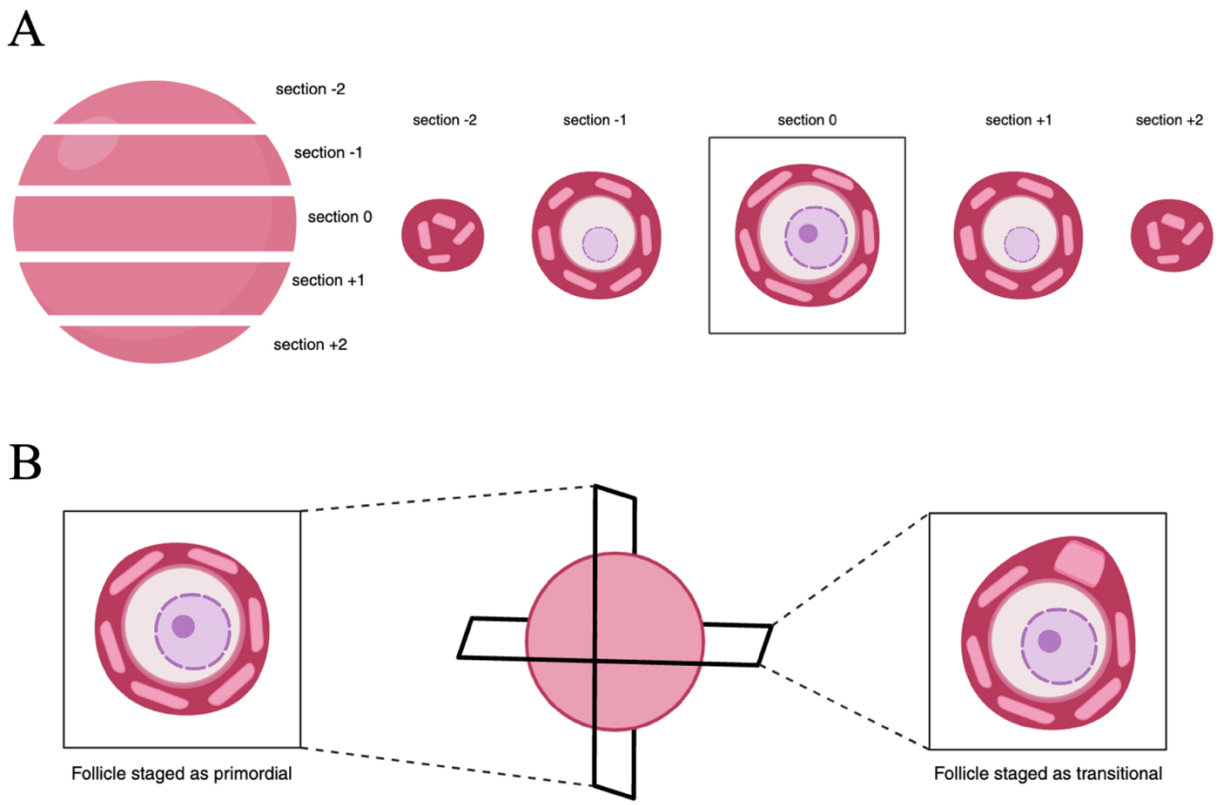

Figure 1.4) Limitations of conventional histology for staging follicles. Illustrations of how two-dimensional histological analysis can misrepresent the true three-dimensional structure of primordial and transitional follicles, as discussed in the text. **A)** Serial sections through a primordial follicle embedded within ovarian tissue. Only the largest follicle cross-section containing the oocyte nucleus (section 0) is typically used for staging and quantitative analysis, whereas neighbouring sections (section -2; section -1; section +1; section +2) are excluded. This leads to the loss of comprehensive information on three-dimensional follicle architecture. **B)** Example of sectioning-orientation artefact. As follicles cannot be visualised prior to embedding and sectioning of tissue, the angle of sectioning cannot be controlled. The same follicle section along one axis (y-axis) yields a largest cross-section consistent with a primordial follicle (left), whereas sectioning along a different axis (x-axis) yields a largest cross-section containing a single cuboidal GC and would be staged as a transitional follicle (right). Images are not to scale. Adapted from Harrison *et al.* (2025), under the Creative Commons Attribution 4.0 International licence. Created with BioRender.com. GC, granulosa cell.

Harrison *et al.* (2025) found that 58% of follicles initially classified as 'primordial' by two-dimensional assessment were reclassified as 'transitional' following three-dimensional analysis. Follicle and oocyte diameters did not differ between primordial and transitional stages. Thus, stage determination relied on observed GC morphology, emphasising that accurate classification of early follicles is dependent on comprehensive evaluation of GC characteristics across three dimensions (Harrison *et al.*, 2025).

Routine research and clinical assessment of ovarian tissue is still overwhelmingly reliant on two-dimensional histology and terminal endpoints. This introduces several challenges, including the generation of static snapshots. Each tissue piece can be fixed and analysed only once, so each timepoint represents a different set of follicles. This prevents continuous, longitudinal tracking of individual follicles and disregards follicle-to-follicle heterogeneity, whilst decreasing total data

output. High inter-sample variability and low throughput is a second limitation. Follicle numbers, stage distributions, and response to culture conditions can vary between tissue pieces and between donors (Anderson *et al.*, 2017; Bjarkadottir *et al.*, 2021; Walker *et al.*, 2021). Manual sectioning and scoring are labour-intensive and introduce artifacts generated from methodological processing, as well as user-specific differences in processing or interpretation. Lastly, the loss of three-dimensional spatial information can impact global context of follicle health, signalling, and lead to misclassification. There is therefore a clear need for adaptable, scalable *in vitro* methodologies that support early follicle growth and can capture the full complexity of development with dynamic, data-rich imaging and analysis.

1.5 Emerging use of viral vectors and gene delivery in ovarian research

Adeno-associated viral vectors (AAVs) have emerged as versatile tools for gene delivery in biology, characterised by low immunogenicity and cytotoxicity compared to lentiviral or adenoviral systems (Ahmadi *et al.*, 2023; Arjomandnejad *et al.*, 2023; Ran *et al.*, 2015). A key advantage of AAVs pertains to the delivery of episomal DNA, which does not randomly integrate into the host genome, reducing the risk of mutagenesis (Ahmadi *et al.*, 2023; Asmamaw Mengstie, 2022). In the ovarian context, Kanatsu-Shinohara *et al.* (2022) investigated AAV-mediated gene therapy in infertile mice (transgenic heterozygous *Kitl* knockout) (Figure 1.5). Vectors carrying the murine Kitl gene were delivered systemically, taking advantage of the ability of AAV serotype 9 (AAV9) to traverse the FBL to reach follicular GCs. This intervention restored follicle development beyond the primordial stage, as treated mice produced healthy offspring without detectable AAV integration (Kanatsu-Shinohara *et al.*, 2022). Such studies demonstrate the capability for AAV9s to modulate follicular GCs and rescue impaired fertility, without genetic modifications to the next generation.

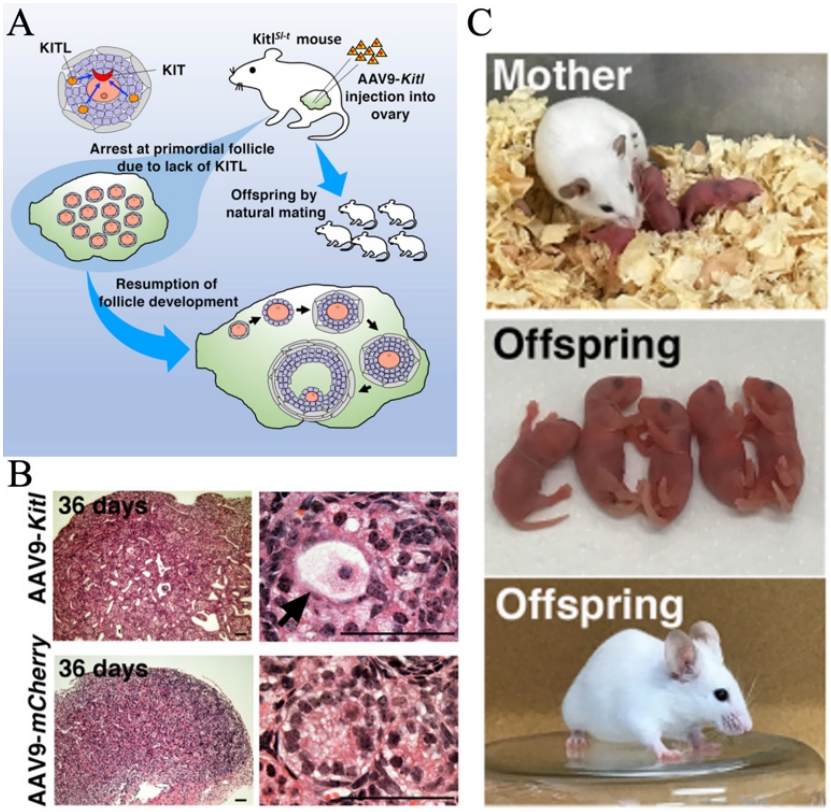

Figure 1.5) AAV9-mediated Kitl gene therapy to rescue congenital infertility due to dysfunctional granulosa cells. Schematic and representative images demonstrating the use of AAV9-based gene delivery to overcome primordial follicle arrest caused by the loss of KitL signalling in Kitl mutant female mice. **A)** Graphical overview of the experimental strategy. **B)** Histological sections of Kitl mutation ovaries 36 days after intra-ovarian injection with AAV9-Kitl (upper panels) or a control AAV9-mCherry vector (lower panels). In AAV9-Kitl-treated ovaries, growing follicles contain growing oocytes (arrow), whereas control ovaries predominantly contain arrested primordial follicles. **C)** Photographs of a rescued Kitl mutant mother and her offspring obtained after AAV9-Kitl treatment, illustrating restoration of fertility without detectable transmission of the therapeutic vector to the next generation. Adapted from Kanatsu-Shinohara *et al.* (2022), and reproduced under the Creative Commons Attribution 4.0 International licence. AAV9, adeno-associated virus serotype 9; KitL, KIT ligand.

Beyond therapeutic applications, AAVs serve as powerful tools for delivering fluorescent reporters, enabling targeted visualisation and assessment of cells *in vitro* or *in vivo*. Fluorescent proteins such as enhanced green fluorescent protein (EGFP) and mCherry have long been used as reporters of gene expression in live imaging (Hickey *et al.*, 2022; Nackenhorst *et al.*, 2022). When driven by ubiquitous promoters, fluorescent reporters are expected to elicit a bright signal if present in the cell (Adeniran *et al.*, 2021; Harrison *et al.*, 2025). Alternatively, signals driven by cell-type-specific promoters, such as the murine anti-Müllerian hormone (mAMH) promoter, can enable visualisation of targeted cells like follicular GCs (Bristol-Gould *et al.*, 2005; Morgan *et al.*, 2015).

In the present thesis, AAV vectors were employed as tools to label specific ovarian cell populations, GCs, in murine ROs. By integrating optimised AAV constructs, the selection of appropriate promoters, and fluorescent reporters, a method was established in which follicles can be

simultaneously visualised and quantified over time. This directly motivated the development of FolliTracker, a dynamic, real-time imaging system that combines AAV-mediated fluorescent labelling, live confocal microscopy, and computational analysis to track follicle growth longitudinally.

1.6 FolliTracker: A dynamic methodology for early follicular analysis

FolliTracker is a dynamic imaging and analysis workflow developed to address the limitations associated with tracking and assessing early follicle development in culture, as outlined above. Built on the murine RO model, FolliTracker integrates three core components:

- AAV-based, cell-type-specific labelling of ovarian follicular cells using fluorescent markers;
- Live confocal imaging of ROs over multiple days in culture, enabling three-dimensional visualisation of early follicles within tissue;
- A customisable, computational pipeline to track follicle and ovarian parameters across numerous timepoints

By combining optimised RO culture protocols (Chapter 3), viral transduction strategies (Chapter 4), and three-dimensional imaging and analysis workflows (Chapter 5), FolliTracker enabled non-destructive, longitudinal assessment of follicle formation within intact RO tissues. This approach addressed the fundamental limitation of conventional histological methods, its terminal and static nature, whilst preserving three-dimensional architecture.

1.7 Overarching hypothesis, aims, and objectives

It was hypothesised that the RO model could recapitulate key aspects of early follicle formation and development *in vitro*, but that structural disruption associated with dissociation and reaggregation would alter early follicular dynamics relative to intact ovarian tissue. Furthermore, it was hypothesised that the integration of optimised viral gene delivery and live imaging approaches would

enable non-destructive, longitudinal assessment of follicle development, providing complementary and biologically informative outputs alongside conventional end-point methodologies.

The overarching aim of this thesis was to develop and validate an integrated experimental and analytical framework to investigate early follicle development *in vitro*, combining RO culture, targeted gene delivery, and live imaging-based analysis.

To address this aim, the following objectives were defined:

- To characterise follicle reformation, developmental dynamics, and structural integrity following ovarian tissue reaggregation (Chapter 3)
- To optimise and evaluate AAV-mediated gene delivery in primary murine ovarian cells (Chapter 4)
- To develop and assess a live imaging and computational workflow, FolliTracker, for longitudinal follicle tracking within intact RO tissues (Chapter 5)

2. METHODOLOGY

2.1 Ethics

Approval for all experiments involving mice was granted by the Local Ethical Review Panel at the University of Oxford under the project license held by Prof. Suzannah Williams (PP1638762), in accordance with the United Kingdom Animals (Scientific Procedures) Act 1986.

2.2 Mouse colony

The colony contained male C57BL/6 mice, purchased from the Biomedical services at the University of Oxford, UK, and female CD-1 mice purchased from Charles River, UK. Hybrid mating (CD-1 x C57BL/6) was completed in-house to generate the first filial generation (F1). The specified use of F1 mice is further described below and in relevant Chapters.

2.2.1 Mouse breeding

Mice were maintained on a 12 hour (hr) light and 12 hr dark cycle with water and food provided *ad libitum* at the Biomedical services, University of Oxford, UK. CD-1 x C57BL/6 mice were set up in trios, containing one male (8–10 weeks of age) and two female mice, at (6 weeks of age). Litters were expected every 3 weeks as gestation is 19–21 days on average. Following parturition, females experience a 24 hr window of fertility due to post-partum oestrus.

2.3 Ovary collection and processing

Mice were euthanised under Schedule 1 by cervical dislocation, with death confirmed by cessation of circulation and/or rigor mortis. To retrieve ovaries, sacrificed mice were placed ventrally, with the dorsal region exposed and moistened with Oosafe® laboratory surface disinfectant (OODSF-10000, SparMED ApS, Denmark) to facilitate dissection.

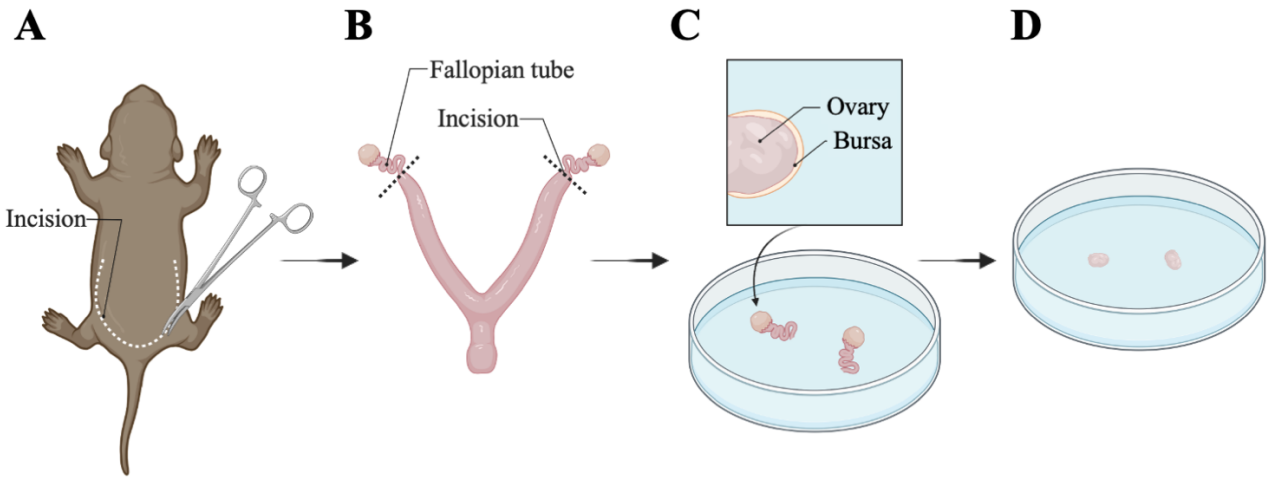

Figure 2.3) Dorsal dissection and retrieval of ovaries from a postnatal mouse. A) A 'U'-shaped surgical incision was made along the dorsal surface above the base of the tail to expose the reproductive tract. **B)** The uterine horns and attached fallopian tubes were isolated. Each ovary, enclosed within the ovarian bursa, was dissected from the surrounding tissue. **C)** Ovaries and accompanying structures were rinsed in dissection media. **D)** Excess bursal and tubal tissues were trimmed to obtain clean ovaries for downstream processing. Images are not to scale. Created with BioRender.com.

A large 'U'-shaped incision was made above the medial base of the tail, continuing cranially along the lateral aspect of the lumbar region using blunt forceps (Narrow pattern, 11002-12, Fine Science Tools, Germany) and Bonn scissors (114185-09, Fine Science Tools) (Figure 2.3A). The incision penetrated through the skin and body wall to reveal anatomical structures, including the ovaries as identified below the kidneys. Each ovary was dissected out of the body cavity, with any accompanying ovarian bursa and portion of the fallopian tube, and rinsed with dissection medium containing sterile phosphate buffered saline (PBS; 1282-1680, Fisher Scientific, UK) with 1 mg/mL of bovine serum albumin (BSA; A9647-100G, Sigma-Aldrich, UK) warmed to 37°C (Figure 2.3B,C). Under a stereomicroscope (M125, Leica Microsystems, Milton Keynes, UK) with fresh dissection medium, ovaries were finely dissected to trim any excess bursa and fallopian tubal structures using fine forceps (Dumont #5, Fine Science Tools) and a 30Gx ½" Agani™ needle (37617, Terumo, Japan) (Figure 2.3D). Dissected ovaries were then washed twice with fresh dissection medium.

2.4 Reaggregated ovary generation

The protocol for RO generation was adapted from Lo *et al.* (2019), based on the original Eppig and Wigglesworth study (2000). For each RO, approximately 5–8 ovaries were used from P6 mice, unless otherwise stated.

Following ovarian collection and processing (Chapter 2.3), finely dissected ovaries were transferred to a 35mm Falcon® petri dish (351008, Scientific Laboratory Supplies (SLS), UK) containing 2 mL of Trypsin-EDTA solution (1x; 0.5 g/L porcine trypsin and 0.2 g/L EDTA in Hank's Balanced Salt Solution; T3924-100ML, Sigma-Aldrich) supplemented with 0.02% deoxyribonuclease I (DNase I; DN25-100MG, Sigma-Aldrich) (Trypsin/EDTA/DNase I). The ovaries were incubated (5% CO_2 and 95% atmospheric air; MC0-15AC, SANYO, Japan) for 30 min in 37ºC (Figure 2.4A). To aid enzymatic digestion and generate a single cell suspension, the solution containing the ovaries was mechanically agitated by gentle pipetting after 15 min of incubation and every 5 min thereafter until 30 min of incubation had elapsed. To neutralise enzymatic activity, 1 mL of warm, equilibrated cell culture media [medium 199 (M199; 31150-022, Gibco, UK) supplemented with 10% (v/v) foetal bovine serum (FBS; FB-1090/500, Biosera, UK), 31.3 mM sodium DL-lactate (L1375, Sigma-Aldrich), and 100 IU/mL penicillin and 10 mg/mL streptomycin (pen/strep; P0781, Sigma)] was added to the solution with dissociated ovaries. The suspension was then transferred to a Corning® 15 mL polyethylene terephthalate (PET) centrifuge tube (430053, SLS). A further 2 mL of cell culture media was added to rinse the petri dish and collect any remaining cells then transferred to the same 15 mL centrifuge tube. The suspension was then centrifuged at 663 x *g* for 5 min (Medifuge Centrifuge; 75008800, Thermo Scientific), supernatant discarded, and resuspended in 3 mL of warm cell culture medium. The cell suspension was then transferred to a 35 mm tissue-culture-treated (TCT) Falcon® petri dish (351001, SLS) and incubated overnight (5% CO_2 and 95% air atmosphere, 37ºC).

Differential adhesion to the TCT petri dish enabled the separation of somatic and germ cell populations (Figure 2.4B). Viable somatic cells (e.g., GCs) adhered to the bottom of the dish. The non-adhered cells floated in the medium, including germ cells and non-viable somatic cells. Non-adhered cells were carefully collected, without dislodging adhered cells, and transferred to a new TCT petri dish. The volume was adjusted to 3 mL of fresh, warm cell culture media and the dish was incubated (37ºC, 5% CO_2) for a further 5–6 hr. The monolayer of remaining adhered somatic cells were vigorously washed with warmed PBS/BSA solution twice.

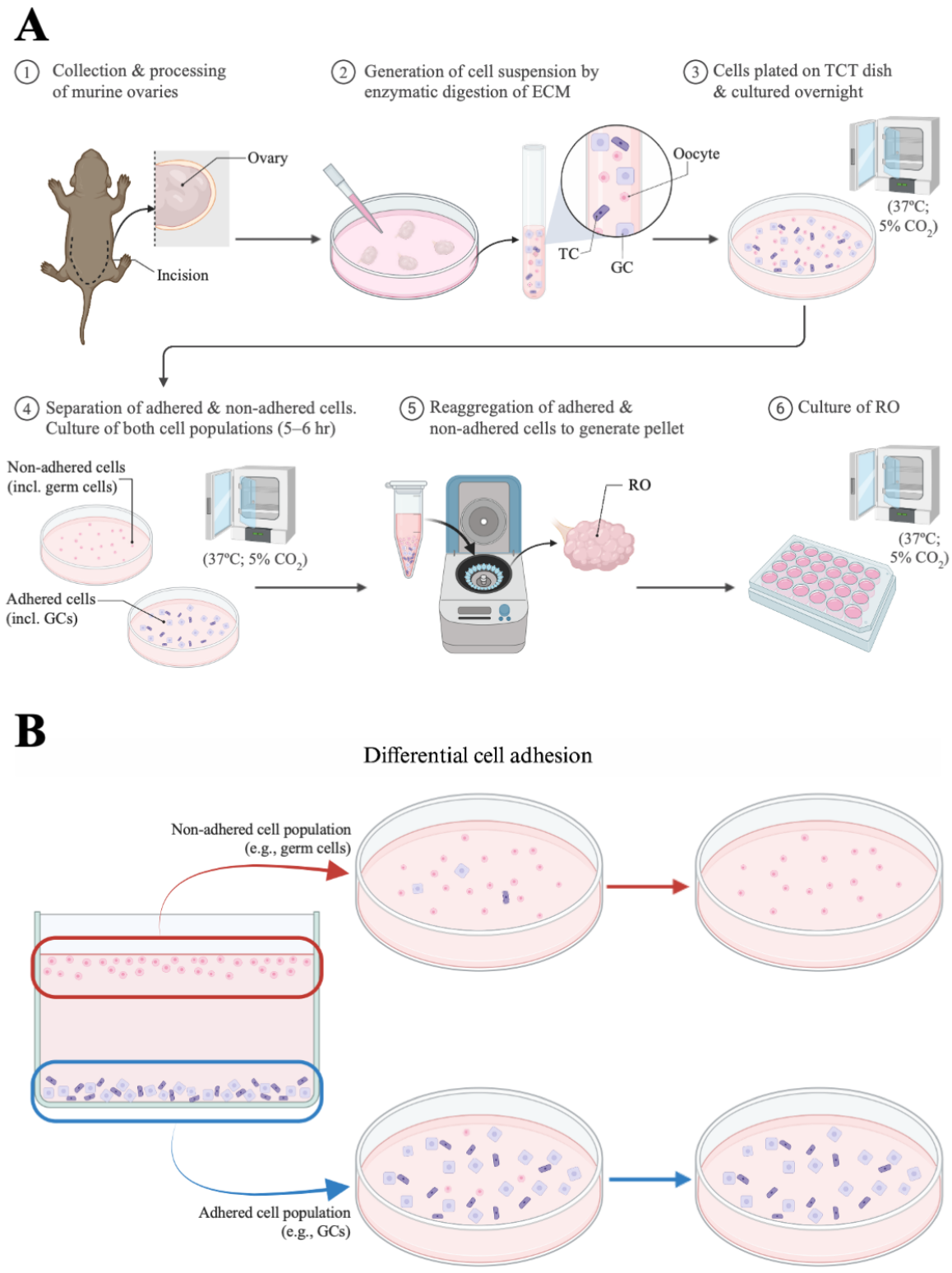

Figure 2.4) Generation of reaggregated ovaries and the differential cell adhesion process. A) Process for generating ROs from dissociated primary murine ovarian cells. Step 1: Ovaries were collected and processed. Step 2: The ECM was enzymatically digested to generate a heterogeneous cell suspension containing somatic and germ cells. Step 3: The cell suspension was plated onto a TCT dish and incubated overnight to promote cell adherence. Step 4: Adhered and non-adhered cell populations were separated, washed, and plated onto a new TCT dish, respectively. Both cell populations were cultured for an additional 5–6 hr. Step 5: Both cell populations were recombined and centrifuged to form an RO pellet. Step 6: ROs were placed on Transwell® membranes and cultured under standard RO culture conditions. Media was replaced every other day. Incubation occurred at 37ºC (5% CO_2). **B)** Illustration of the differential cell adhesion process used to separate viable somatic and germ cell populations twice. Somatic cells (e.g., GCs) adhered to the TCT dish surface, whilst non-adhered cells (incl. germ cells) remained suspended in the medium and were subsequently collected into a separate dish. Non-adherent cells, including oocytes, are removed prior to viral exposure; however, complete removal is not always achieved during the differential adhesion process, and some non-adherent cells may persist or loosely associated somatic cells may be dislodged. Images are not to scale. Created with BioRender. ECM, extracellular matrix; GC, granulosa cell; RO, reaggregated ovary; TC, theca cell; TCT, tissue-culture treated.

After washing, the PBS/BSA solution and any dislodged cells were discarded and replaced with 2 mL of warmed Trypsin/EDTA/DNase I. The adhered cells were incubated (37ºC, 5% CO_2) with Trypsin/EDTA/DNase I for 5 min. Following incubation, the base of the dish was tapped to dislodge any adhered cells prior to neutralisation of enzymatic activity with 1 mL of cell culture media. The somatic cell suspension was transferred to a new 15 mL centrifuge tube. A further 2 mL of cell culture media rinsed the petri dish, to collect any remaining cells, and was then transferred to the same tube. The somatic cells were centrifuged at 663 x *g* for 5 min. The supernatant was discarded and cells were re-suspended in 3 mL of fresh, warm cell culture media. The suspension was then transferred to a new TCT petri dish and incubated (37ºC, 5% CO_2) for 5–6 hr.

After incubation, adhered and non-adhered cells were collected and/or washed as described above. The adhered and non-adhered cell populations were transferred to separate 15 mL tubes and centrifuged for 663 x *g* for 5 min. The supernatant of each tube was then discarded and re-suspended in 200 µL of cell culture media. Cell viability and number were then determined as described in Chapter 2.5. To generate ROs, a mixture of somatic cells and germ cells was required. All somatic cells in suspension, approximately 200 µL total, were transferred to a microfuge tube (Multiply-Pro 0.5 mL Biosphere®; 72.735.100, SARSTEDT, Germany). The non-adhered cells (inclusive of germ cell population) were then added to the same microfuge tube to constitute a third (i.e., 100 µL) of the total RO cellular component. To promote cell adhesion, 35 µg/mL of phytohemagglutinin (L-PHA) [L-PHA (Lectin from *Phaseolus vulgaris*; L1668, Sigma-Aldrich) in PBS] was added to the mixed cell population. The cells were then centrifuged at 10,000 x *g* for 30 sec, the tube rotated 180º, then centrifuged for an additional 30 sec to form a pellet, herein referred to as an RO. The RO was then placed on a polycarbonate Transwell® membrane (6.5 mm diameter, 0.4 µm pore size; 3413, Corning Incorporated, USA) in a Costar® 24-well TCT plate (3526, Corning Incorporated) containing 250 µL Waymouth/10%FBS medium [Waymouth MB752/1 medium (W1625, Sigma-Aldrich) supplemented with 10% (v/v) FBS] for overnight culture and incubation (37ºC, 5% CO_2).

An additional 250 µL of media was placed on top of the RO. Media was removed until there was only a thin layer of media covering the RO. The RO was then gently 'nudged' to the edge of the membrane to promote 'rounding up' of the pellet. Waymouth/10%FBS media was prepared and equilibrated a minimum of 4 hr prior to use. Sterilised double distilled water (ddH_2O) with pen/strep was added into the inter-well spaces of the plate to mitigate evaporation.

2.5 Determination of cell viability and number

Cell number and viability were determined either automatically (v2.103; TC20™Automated Cell Counter, Bio-Rad, UK) with dual-chamber cell counting slides (1450011, Bio-Rad) or manually using a haemocytometer (BS748, Weber Scientific International Ltd., UK). Both methods utilised trypan blue (T8154-20ML, Sigma) solution. A 10 µL aliquot was removed from the cell suspension, placed in a new microtube with 10 µL of trypan blue dye, and mixed through agitation. Trypan blue dye penetrates the cell membrane to stain dead cells blue. Viable cells remain unstained. Subsequently, 10 µL of the cell and dye mixture was loaded into the haemocytometer or dual-chamber cell counting slide. With the automatic method, cell viability (%) and count (cells/mL) were analysed.

For the manual method, the number of live (unstained) and dead (blue) cells were counted in each quadrant (four quadrants with 16 squares each) in the haemocytometer grid. The average number of cells per quadrant was recorded. The portion of viable cells was recorded using the equation below:

$$Viable\ cells\ (\%) = \left(1 - (Number\ of\ blue\ cells\ \div Number\ of\ total\ cells)\right) \times 100$$

To calculate total cell number the following equation was used:

$$\frac{Cells}{190\ \mu L} = \begin{array}{c}\text{Average number of cells per quadrant}\\ \times \\ \text{10,000 (volume factor for the haemocytometer)}\\ \times \\ \text{2 (due to the 1:1 dilution with trypan blue)}\\ \times \\ \text{0.2 (as cells are re-suspended in 0.2 mL)}\\ \times \\ \text{0.95 (because 10 µL was removed for assessment)}\end{array}$$

2.6 Reaggregated ovary culture

Following overnight culture, the RO and accompanying Transwell membrane were moved to a new well containing 300 µL of Waymouth media with 5% (v/v) mouse serum (Waymouth/5%MS) [Waymouth media supplemented with 5% (v/v) mouse serum (MS; MO-340/50, Biosera), 2.5 IU/10 µL recombinant follicle stimulating hormone (rFSH; GONAL-f® (follitropin alfa), Merck Seromo, Italy), 1% (v/v) insulin,-transferrin-selenium solution (ITS; 41400-045, Gibco), 100 IU/mL penicillin and 100 µg/mL streptomycin (pen/strep), and 25 µg/mL of ascorbic acid (352680050, Acros Organics, Belgium) dissolved in minimal essential medium (MEMα; 22561054, Gibco)]. This was considered day 0 (D0) of culture. A Pasteur pipette was used to gently 'nudge' the RO to the centre of the membrane. Excess media was aspirated until only a thin layer of film covered the RO. The plate was incubated (5% CO_2) at 37ºC. Equilibrated media was replaced fresh every other day.

2.7 Histological processing

2.7.1 Fixation

Tissue samples were fixed in Form-Acetic solution comprised of 5% (v/v) acetic acid (1.00063.1011, Merck Life Science UK Ltd., UK) in 10% neutral buffered formalin (NBF; 11699408, VWR International, UK) as described by Adeniran *et al.* (2021). Samples were immersed in fixative that was at least ten times the volume of the tissue. Tissue was fixed at room temperature (RT) on a rocker for 24 hr. Following fixation, tissues were washed and stored in 70% ethanol (EtOH) at 4ºC until processing.

2.7.2 Embedding

Prior to embedding, tissue samples were serially dehydrated in increasing concentrations of EtOH for 15 min at RT (Table 2.7.2). Initially, the tissue pieces were incubated in 1:10 parts eosin (Eosin Y; HT110333, Sigma) to 70% EtOH solution for 15 min to visualise the samples. Dehydrated tissue pieces were then washed in xylene for 20 min at RT thrice to optically clear the sample.

Tissues were quickly transferred from xylene to melted paraffin wax (Histoplast; 6674060, Thermo Scientific) within plastic moulds via wide-bore tips (E1011-9618, StarLab, Germany). Once tissues were centred, labelled cassettes were attached to the moulds. Samples were incubated for 2 hr total at 62ºC, after which the wax blocks were allowed to cool to RT overnight and then stored at RT.

Table 2.7.2) Tissue dehydration and clearing protocol for paraffin embedding. Tissue pieces were incubated in increasing concentrations of EtOH following by serial xylene washes, all performed at RT.

Process	Reagent	Incubation time
Dehydration	(1:10) Eosin : 70% EtOH	15 min
	80% EtOH	15 min
	95% EtOH	15 min
	100% EtOH I	15 min
	100% EtOH II	15 min
	100% EtOH III	15 min
Clearing	Xylene I	20 min
	Xylene II	20 min
	Xylene III	20 min

EtOH, ethanol; RT, room temperature.

2.7.3 Sectioning

The embedded samples, in paraffin wax blocks, were sectioned at 5 µm with a RM2245 semi-motorised rotary microtome (Leica Biosystems). Sectioned wax sections were floated on a water bath (38ºC– 42ºC) and mounted onto positively charged glass slides (SuperFrost^{TM} Plus; 631-0108, VWR International). Slides were stored at RT and baked at 62ºC for 1 hr prior to staining.

2.8 Histological staining

Haematoxylin (Gills #2 haematoxylin; GHS232, Sigma-Aldrich) and eosin (H&E) staining protocol was performed to visualise ovarian tissue samples for determination of follicle classification and number (Table 2.8). Xylene wash was used to deparaffinise sections thrice before rehydration by decreasing concentrations of EtOH and H_2O. Haematoxylin stain enabled the visualisation of the cell nucleus by staining the nuclei purple. Excess haematoxylin staining was removed via acid alcohol (70% EtOH supplemented with 1% (v/v) HCl) immersion. Sections were briefly exposed to eosin solution to stain cytoplasm and ECM components pink.

Following staining, sections were dehydrated in increasing concentrations of EtOH, cleared in xylene twice, and mounted with DPX medium (06522, Sigma-Aldrich) on coverslips (#1.5, 630-1845, VWR International) overnight to dry.

Table 2.8) Haematoxylin and eosin staining protocol for paraffin-embedded ovarian tissue. Summary of the H&E staining process, including sequential deparaffinisation, rehydration, staining, dehydration, and clearing prior to mounting. All steps were performed at RT. Samples were stained with haematoxylin to visualise cell nuclei and eosin to visualise cytoplasmic and ECM components.

Process	Reagent	Incubation Time
Deparaffinisation	Xylene I	8 min
	Xylene II	4 min
	Xylene III	4 min
Rehydration	100% EtOH I	3 min
	100% EtOH II	3 min
	90% EtOH	2 min
	70% EtOH	2 min
	50% EtOH	3 min
	Tap water	3 min
Staining	Haematoxylin	2 min*
	Running tap water	5 min*
	Acid alcohol (1% HCl in 70% EtOH)	1– 2 sec
	Running tap water	5 min
	80% EtOH	1 min
	Eosin	1–2 sec
Dehydration	95% EtOH	30 sec
	100% EtOH I	45 sec
	100% EtOH II	1 min
	100% EtOH III	2 min
Clearing	Xylene I	8 min
	Xylene II	8 min

*Incubation time unless otherwise stated. ECM, extracellular matrix; EtOH, ethanol; H&E, haematoxylin and eosin; HCl, hydrochloric acid; RT, room temperature.

2.9 Histological assessment of the ovary

All follicle-based analyses were performed on randomised sample groups and blinded. Unblinding only occurred following completion of follicle counting and classification using ImageJ/FIJI (ImageJ; v.2.1.0/1.53c; National Institutes of Health, Bethesda, MD, USA).

2.9.1 Volumetric ovarian assessment

Ovarian volume was determined using the Cavalieri principle (planimetry method) from serial tissue sections, as previously described (Forabosco and Sforza, 2007; Gundersen and Jensen, 1987).

All measurements were performed on the same H&E-stained sections used for follicle counting. In brief, for each tissue, 5 µm sections were sampled at regular intervals (e.g., every fifth section). The area of each section was manually established via the freehand selection tool in ImageJ while blinded to sample identity. The region of interest (ROI) encompassed the entire RO tissue boundary. Area (μm^2) was extracted directly and then calculated for volume estimation (μm^3):

$$\mathcal{V} = \mathrm{T} \sum_{i=1}^{n} \mathrm{A}_i \qquad with \qquad \mathrm{T} = \frac{t}{ssf}$$

V represents total volume, expressed as μm^3 or converted to mm^3, *n* is the number of sampled sections, and A_i is each cross-sectional area (μm^2). *T* represents *t* (section thickness of 5 µm) divided by the section sampling fraction (*ssf*, which was 1/5 as every fifth section was sampled). For internal consistency, two parallel phase measurements (A/B) were performed per specimen as an internal validation mechanism to confirm comparable estimates of total RO volume.

2.9.2 Follicle classification

Ovarian follicles were classified into development stages according to established criteria, as seen in Table 2.9.2 (Adeniran *et al.*, 2021; Grasa *et al.*, 2015; Pedersen and Peters, 1968). Follicles were included in classification if oocyte nucleus was visible and considered 'normal', thus containing non-pyknotic, non-shrunken oocyte and non-pyknotic GCs (Walker *et al.*, 2021).

Table 2.9.2) Classification criteria for ovarian follicle developmental stages. Morphological criteria used to classify murine ovarian follicles based on oocyte and GC characteristics. Follicles were categorised according to the number and morphology of surrounding GCs and the presence of an antral cavity. Classification was performed only on follicles containing visible, morphologically normal oocytes with non-pyknotic nuclei.

Stage	Definition
Primordial	Oocyte surrounded by a single layer of fp-GCs
Transitional	Oocyte surrounded by a mixture of fp-GC(s) and cuboidal GC(s)
Primary	Complete layer of cuboidal GCs surrounding the oocyte
Secondary	Two complete layers of cuboidal GCs surrounding the oocyte
Pre-antral	Greater than two complete layers of cuboidal GCs with interspersed fluid filled areas surrounding the oocyte
Antral	Greater than two completed layers of cuboidal GCs surrounding the oocyte with a large antral cavity

(fp-)GC, (flattened pre-)granulosa cell.

2.9.3 Assessment of follicle number

Follicles were only counted if oocyte nucleus was present following H&E analysis. Total follicle numbers counted per ovary via the cell counter tool and nuclear diameter were both assessed using the ImageJ software. Follicle numbers were corrected with the Abercrombie correction factor (Abercrombie, 1946). The formula for calculating the corrected total follicle number is below:

$$Total\ follicle\ number = count\ of\ follicles\ \times\ Abercrombie\ correction\ factor$$

Where:

$$Count\ of\ follicles = number\ of\ follicles\ counted\ \times\ sampling\ number$$

$$Abercrombie\ correction\ factor = \frac{Thickness\ of\ sections\ (\mu m)}{Average\ nuclear\ diameter\ (\mu m) + Section\ thickness\ (\mu m)}$$

2.9.4 Quantitative morphometric analysis of ovarian and follicular structures

Quantitative morphometric analyses were performed on ovarian sections to assess size, symmetry, and cellular composition of follicles and other components (Figure 2.9.4). Analyses were conducted using ImageJ software. All parameters were measured at a consistent image magnification (20x) and an appropriate zoom level applied in ImageJ for each individual follicle. All measurements were calibrated using the corresponding image scale bar (µm). Identical brightness and contrast adjustments were applied across all comparator groups to ensure image consistency. In accordance with standard practice, only follicles sectioned through the largest cross-section, identified by the presence of visible oocyte nuclei, were included for analysis (Figure 2.9.4A).

All measurements were performed across biological replicates. Data from ImageJ were exported to Microsoft Excel (v16.103.2; Microsoft® 365, Microsoft Corporation, Redmond, USA) and GraphPad Prism (v10.3.1; GraphPad Software, La Jolla, USA) for data collection and statistical analysis. Statistical analyses are described in detail within the methods section of each corresponding chapter.

2.9.4.1 Follicular and oocyte symmetry

Follicular and oocyte symmetry were evaluated to assess morphological regularity and potential distortion across experimental conditions. The major and minor diameters (µm) were measured manually via the straight line tool at fixed orientations of 0º (x-axis; major diameter) and 90º (y-axis; minor diameter) of each oocyte (Figure 2.9.4B) and follicle (Figure 2.9.4C). Symmetry was expressed as the ratio of diameters (minor diameter ÷ major axis) for both oocytes and follicles, with a theoretical value of 1.0 indicative of ideal symmetrical morphology. Follicular diameters extended to the FBL for consistency across developmental stages and irrespective of TC presence.

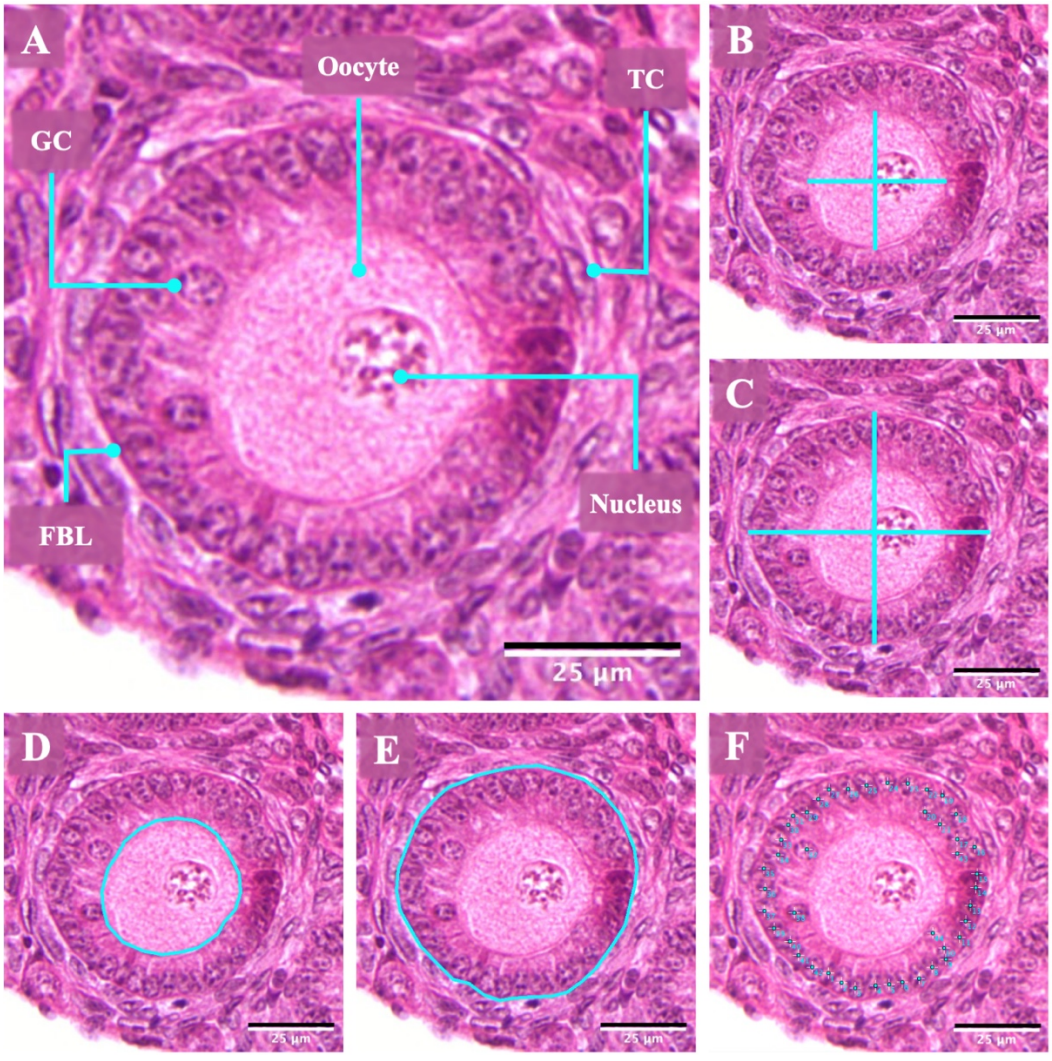

Figure 2.9.4) Morphometric parameters of follicular structures. Representative brightfield image of an H&E-stained primary follicle from a murine ovary (20x). All panels (A–F) shown the same follicle with cyan overlays indicating measurement or annotation of morphometric parameters. **A)** Identification of key follicular structures: oocyte, oocyte nucleus, GC, TC, and FBL. **B)** Oocyte diameters (major = x-axis; minor = y-axis) used to calculate oocyte symmetry as the ratio of minor to major axis. **C)** Follicle diameters (major = x-axis; minor = y-axis) extending to the FBL, used to calculate follicle symmetry (minor : major axis). **D)** Oocyte and **E)** follicle area, delineated by the parameter of each respective structure. GC area was calculated by subtracting oocyte area from follicle area. **F)** GC count based on manual quantification of visible GCs using the ImageJ cell counter tool. GC density was determined by dividing the number of GCs by the corresponding GC area. All parameters were quantified in ImageJ. Scale bar represents 25 µm. FBL, follicular basal lamina; GC, granulosa cell; H&E, haematoxylin and eosin; TC, theca cell.

2.9.4.2 Follicular and oocyte area

Follicular and oocyte areas (μm^2) were quantified via the polygon selection tool to assess relative growth across timepoints and between experimental conditions. The oocyte boundary was manually traced along the perimeter corresponding to the zona pellucida or its expected position (Figure 2.9.4D). Follicle area was defined by tracing along the edge of the FBL (Figure 2.9.4E). GC area was calculated by subtracting the oocyte area from the total follicle area, representing the GC compartment.

2.9.4.3 Granulosa and theca cell analysis

GC and TC parameters were assessed to evaluate cellular composition and follicular organisation. GCs, including fp-GCs, were identified based on characteristic morphology and their presence in the follicular somatic cell compartment surrounding the oocyte. Individual GCs were manually counted using the cell counter tool (Figure 2.9.4F). GC density was calculated as the number of GCs per unit GC area (cells/μm^2).

TCs were identified based on characteristic cell morphology and their location within the outer cellular layer beyond the FBL. TCs were recorded as present (1) or absent (0) for each follicle, as appropriate to the developmental stage. TC presence was expressed as a mean decimal value (0.0–1.0) to represent the proportion of expectant follicles in which TCs were observed per sample.

2.10 Molecular analysis

2.10.1 Slide preparation

Prior to any molecular analysis, slides with 24 hr Form-Acetic fixed murine tissue sections were baked for 1 hr at 62ºC to remove excess wax, as stated above (Chapter 2.7.3).

2.10.2 Immunohistochemistry

Baked slides were immersed in xylene and decreasing concentrations of EtOH and ddH_2O at RT (Table 2.10.2.1). A Tris-based buffer (pH 9.0) [100x Vector antigen unmasking solution (H3301, Vector Laboratories Inc., USA) in ddH_2O] was used for antigen retrieval after rehydration, unless otherwise stated.

Table 2.10.2.1 Tissue deparaffinisation and rehydration protocol prior to immunohistochemical analysis. Sequential deparaffinisation and rehydration steps were performed on baked tissue slides before antigen retrieval. Samples were first immersed in xylene to remove paraffin, followed by serial graded EtOH and ddH_2O washes to rehydrate sections, all performed at RT.

Process	Reagent	Incubation time
Deparaffinisation	Xylene I	4 min
	Xylene II	3 min
	Xylene III	3 min
Rehydration	100% EtOH I	1 min
	100% EtOH II	1 min
	90% EtOH	1 min
	80% EtOH	1 min
	70% EtOH	1 min
	ddH_2O I	1 min
	ddH_2O II	1 min
	ddH_2O III	1 min

ddH_2O, double distilled water; EtOH, ethanol; RT, room temperature.

Slides in antigen retrieval buffer were exposed to 10 min of microwave heating [700W for 1 min then 70 W for 9 min] followed by 20 min of cooling at RT. Sections were washed twice in ddH_2O for 2 min each. To block endogenous peroxidase activity, samples were immersed in 3% H_2O_2 [30% H_2O_2 stock (31642, Sigma) in PBS] for 5 min at RT. Slides were then washed in PBS for 5 min twice. Prior to incubation in blocking solution, a hydrophobic PAP pen (Advanced PAP pen (2 mm tip width); Z672548, Sigma-Aldrich) was used to trace around tissue sections on dry slides. Sections were blocked in either 5% normal goat serum (NGS; S-1000-20, Vector Laboratories Inc.) in PBS with 0.05% Tween20 (PBST) (Tween20; BP337-100, Fisher Scientific) or 5% rabbit serum (R9133, Sigma-Aldrich) in PBST solution for 1 hr at RT. Next, sections were incubated overnight at 4ºC in 1º antibody diluted in corresponding blocking solution, specified in each relevant Chapter. Negative control sections were incubated in blocking solution.

The following day, slides were moved to RT for 20 min prior to three washes of PBST for 3 min each. Sections were incubated in 2º antibody, diluted in the appropriate blocking solution, for 1 hr at RT. As specified in later Chapters, 2º antibody was either biotinylated goat anti-rabbit IgG (VECTASTAIN® Elite® ABC-HRP kit; PK6101, Vector Laboratories Inc.) or biotinylated rabbit anti-goat IgG (BA-5000, Vector Laboratories Inc.).

Slides were then washed in PBST for 3 min, thrice. To amplify antigen signal based on the avidin-biotin-peroxidase complex system, the VECTASTAIN® Elite® ABC-HRP kit (PK6101, Vector Laboratories Inc.) was used according to manufacturer's instructions. In brief, slides were incubated in working solution for 30 min at RT then washed for 5 min in PBS three times. A chromogen DAB substrate (3,3'-diaminobenzidine) kit (SK-4100, Vector Laboratories, Inc.) was used to produce a brown staining reaction to visualise signal in tissues. Slides were immersed into ddH_2O to stop the DAB reaction then counterstained with haematoxylin to visualise nuclei (Table 2.10.2.2). Sections were then dehydrated and cleared in increasing concentrations of EtOH and xylene, respectively. Slides were mounted with DPX medium.

Table 2.10.2.2) Counterstaining, dehydration, and clearing of tissue sections during immunohistochemical analysis. Sequential counterstaining, dehydration, and clearing of tissue sections following DAB chromogen reaction. Sections were counterstained with haematoxylin to visualise nuclei, dehydrated through serial graded EtOH concentrations, and cleared in xylene prior to mounting. All procedures were performed at RT.

Process	Reagent	Incubation time
Counterstaining	Haematoxylin	2 min*
	Running tap water	5 min*
	Acid alcohol (1% HCl in 70% EtOH)	1–2 sec
	Running tap water	5 min
Dehydration	50% EtOH	1 min
	70% EtOH	1 min
	90% EtOH	1 min
	100% EtOH I	1 min
	100% EtOH II	1 min
Clearing	Xylene I	3 min
	Xylene II	3 min
	Xylene III	4 min

*Incubation time unless otherwise stated. DAB, 3,3′-diaminobenzidine; EtOH, ethanol; HCl, hydrochloric acid; RT, room temperature.

2.10.3 Quantification of DAB signal

Quantification of DAB signal was performed using ImageJ following the colour deconvolution (haematoxylin and DAB), as described by Ruifrok and Johnston (2001). ROIs were manually defined to identify the entire tissue and follicular structures from ROs across experimental groups, as well as representative background tissue regions of control ROs. Mean intensity and integrated density values were extracted for each ROI with 255 arbitrary units (AU) representing the absence of DAB staining. GC-layer intensity was calculated from other intensity (I) and area (A) parameters, as followed:

$$I_{GC} = \frac{\left(I_{follicle} \times A_{follicle}\right) - \left(I_{oocyte} \times A_{oocyte}\right)}{\left(A_{follicle} - A_{oocyte}\right)}$$

Normalised DAB intensity for each follicle was then derived relative to the mean background of paired control sections according to:

$$Normalised\ intensity = \frac{\left(I_{background} - I_{GC}\right)}{I_{background}}$$

Normalised intensity values were used to assign follicles into semi-quantitative staining grades (Table 2.10.3), as adapted previously (Varghese *et al.*, 2014).

Blinding to experimental condition was not feasible due to the requirement to use paired control sections to define background intensity for normalisation in certain analyses. Quantitative measurements were generated using standardised, algorithm-based ImageJ outputs from manually defined ROIs in accordance to consistent morphological parameters (e.g., follicle and oocyte boundaries), rather than subjective scoring, thereby minimising the risk of observer bias.

Table 2.10.3) Semi-quantitative grading criteria for DAB chromogen staining intensity. Ovarian tissue structures were classified into staining grades based on normalised DAB chromogen intensity values derived from ImageJ analysis. Thresholds were adapted from Varghese *et al.* (2014) to categorise staining as negative or positive, with grades ranging from 0 (no detectable staining) to 3 (strong staining). The duration of DAB exposure was consistent across all comparators. Normalisation against paired control background values was used to correct for inter-experimental variation and ensure batch-to-batch comparability.

Staining status	**Negative**	**Positive**		
Grade	0	1	2	3
Normalised intensity	< 0.1	$0.1 \leq x < 0.2$	$0.2 \leq x < 0.3$	≥ 0.3

DAB, 3,3′-diaminobenzidine; ROI, region of interest.

2.11 Imaging

2.11.1 Spinning-disc confocal imaging

High-resolution live imaging of ROs was performed using the Olympus SpinSR SoRa spinning-disc confocal microscopy (Yokogawa CSU-W1 SoRa; Olympus Corporation, Tokyo, Japan). Images were acquired using CellSens software (Olympus Corporation). ROs were imaged within a temperature- and atmosphere-controlled chamber (37ºC, 5% CO_2; 95% humidity) to preserve tissue viability. Imaging and associated expertise were provided by the Cellular Imaging Core at the Centre for Human Genetics, University of Oxford.

Z-stack images were captured using the 20x objective (NA 0.8) with a 0.5 µm optical step size to provide high-resolution sampling through the tissue, enabling image reconstruction comparable to standard ~5 µm microtome sections. Excitation was achieved using 405 nm (SiR-DNA), 488 nm (EGFP), and 561 nm (mCherry) diode lasers, with emission collected via appropriate single-pass filter sets (DAPI/Alexa 488/Alexa 568) and recorded using a Hamamatsu ORCA Fusion BT camera. Acquisition settings (exposure time, laser power, and gain) were standardised across sessions to permit comparison.

2.11.2 Brightfield microscopy

Dissection of ovarian tissue was performed under the M125 stereomicroscope attached to a Lumenera 5-3 camera (Teledyne Vision Solutions, Birmingham, UK) with the accompanying Infinity Analyse software (Teledyne Vision Solutions).

Imaging of sectioned tissue stained with dyes or chromogens were captured with a Leica microscope (DM2500, Leica Microsystems) with the Lumenera Infinity 5 camera (Teledyne Vision Solutions) via the Infinity Analyse software (Teledyne Vision Solutions). Light intensity and exposure were adjusted as appropriate within each imaging session.

3. FOLLICULAR REFORMATION AND MORPHOLOGICAL INTEGRITY FOLLOWING OVARIAN REAGGREGATION

3.1 Introduction

3.1.1 Background

Early follicle development is highly sensitive to the spatial and temporal relationship between the oocyte and its surrounding supportive somatic cells (Gilchrist *et al.*, 2004; Gittens *et al.*, 2005; Wear *et al.*, 2016). *In vivo*, germ cells and fp-GCs, later cuboidal GCs, establish intimate contact during foetal life and maintain this association throughout the dominant follicle's progression to ovulation (Richards and Pangas, 2010; Shirafuta *et al.*, 2024; Wear *et al.*, 2016; Williams and Erickson, 2012). This arrangement supports bidirectional communication via paracrine signalling, gap junctions, and ECM cues which coordinate oocyte growth, granulosa proliferation, and follicular survival (Alam and Miyano, 2019; Albertini *et al.*, 2001; Eppig, 1991; Gittens *et al.*, 2005; Marchais *et al.*, 2022). Any *in vitro* system that disrupts or delays the re-establishment of this germ-to-somatic cell contact therefore risks altering the trajectory of follicle development (Lo *et al.*, 2019; Sheikh *et al.*, 2023).

The RO model offers a unique approach to study follicle formation and early growth within a controlled three-dimensional tissue structure. In this system, ovaries are enzymatically dissociated into a heterogeneous suspension of cells (including germ cells, somatic cells, and stromal elements) which are subsequently reaggregated to form a new ovarian-like construct (Eppig and Wigglesworth, 2000; Lo *et al.*, 2019; Porras-Gomez and Moreno-Mendoza, 2020; Sheikh *et al.*, 2023).

ROs and chimeric variants have been used to investigate how different somatic environments influence primordial activation, cell-to-cell communication, and the role of the oocyte (Eppig *et al.*, 2002; Eppig and Wigglesworth, 2000; Hikabe *et al.*, 2016; Li *et al.*, 2021; Zhang *et al.*, 2024). Lo *et al*. (2019) provided important insights into the murine RO model by demonstrating that, although total follicle numbers can be broadly preserved in transplanted ROs, stage distribution and growth dynamics diverged greatly from intact age-matched *in vivo* WOs. Further, cultured ROs showed accelerated early growth but limited later-stage progression (Lo *et al.*, 2019).

Oocytes that fail to acquire or maintain appropriate pre-granulosa support *in vivo* undergo apoptosis, contributing to follicular atresia (Mork *et al.*, 2012; Pepling and Spradling, 2001; Telfer and Andersen, 2021; Tingen *et al.*, 2009). In the RO model, dissociation deliberately disrupts these interactions, placing germ and somatic cells into separate suspension prior to reaggregation into a tissue pellet (Eppig and Wigglesworth, 2000; Lo *et al.*, 2019). The success of reaggregation may, therefore, depend not only on the composition of the cell suspension and subsequent culture conditions, but also on the duration for which germ and somatic cells remain separated prior to reformation. If dissociation is prolonged, oocytes could become more vulnerable to stress, loss, or inappropriate interactions. Simultaneously, somatic cells may organise into configurations that are less conducive to oocyte encapsulation. Even if the absolute number of follicles appears preserved, aspects of follicle quality (e.g., stage distribution, oocyte and follicle size, granulosa organisation, theca recruitment, and growth efficiency) may be compromised. These features are particularly important for downstream applications that depend on healthy follicle architecture, including the dynamic imaging and tracking of follicles discussed in later chapters.

The RO generation protocol described by Lo *et al*. (2019), adapted from Eppig and Wigglesworth (2000), has not been systematically evaluated with respect to how variations in the duration of cell culture affect follicle reformation and growth. Understanding these effects is important when adapting the RO protocol, including modifications such as the extended RO generation (ROEx) protocol, for specialised downstream applications.

Later chapters of this thesis explore AAV-mediated gene delivery (Chapter 4) with a live imaging/computational workflow (Chapter 5) within ovarian tissues. Both benefit from extended exposure of primary cells to viral culture. Practically, an extended protocol necessitated testing as to determine whether extended germ and somatic cell separation prior to reaggregation would compromise the ability of cells to reform follicles with appropriate architecture. In the ROEx protocol, dissociated ovarian cells remained in suspension or on plates for longer than in the standard RO method, thereby increasing the window for potential cell stress, selective loss, or reorganisation.

In conclusion, this chapter aimed to position the RO as a tractable model for studying early follicle reformation, whilst critically evaluating how protocol impacted outcomes. Establishing the structural and developmental consequences of the ROEx was necessary before adding experimental tools, such as AAV-mediated labelling and FolliTracker-based imaging, in subsequent chapters.

3.1.2 Chapter aims

It was hypothesised that ovarian reaggregation would support follicle reformation but alter developmental dynamics relative to intact ovaries, and that prolonged germ–somatic cell separation would further impact follicle organisation and development. The aim of this Chapter was to evaluate the RO as a model of early follicle development *in vitro* and to determine how extended dissociation prior to reaggregation (ROEx) influenced follicular outcomes.

To address this aim, the following objectives were defined:

- To assess total follicle number in ROs across early culture timepoints and compare with WOs
- To examine follicle stage distribution and how this changed over culture and relative to WOs
- To evaluate ovarian tissue volume as a measure of structural integrity and growth
- To determine the effect of extended dissociation on follicle number and stage distribution
- To assess selected morphological features of follicle development, including oocyte and follicle size, symmetry, and TC presence

3.2 Methodology

3.2.1 Mouse colony

Ovaries used to make ROs were collected and isolated from culled P6 mice (Chapter 2.3). Age-matched *in vivo* WO controls of P6, P9, and P13 pups were cervically dislocated and their ovaries isolated (Chapter 2.3).

3.2.2 Reaggregated ovary generation

ROs were generated as previously described (Chapter 2.4). Tissues from the ROEx group had an extended cell suspension plating protocol of 24 hr, as opposed to the standard 5–8 hr incubation period (Figure 3.2.2). The subsequent generation process, including the mixture of somatic and germ cells and centrifugation to form a pellet of reaggregated ovarian cells, was performed as previously reported.

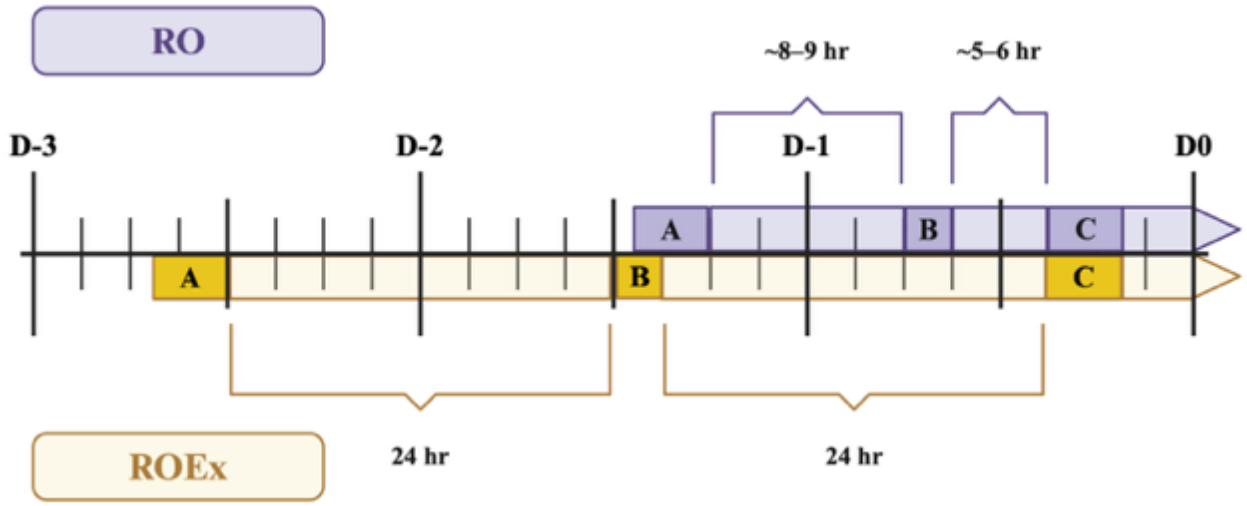

Figure 3.2.2) Experimental timeline for the generation of reaggregated ovaries and extended reaggregated ovaries. A) Murine ovaries were collected, enzymatically digested to dissociate the ECM, and used to establish a heterogeneous cell suspension of primary somatic and germ cells. **B)** Differential cell adhesion was performed to separate somatic and germ cell populations. **C)** Somatic and germ cells were recombined to generate an RO or ROEx pellet, respectively. ROs were incubated overnight between steps A–B, with a ~5–6 hr incubation period between steps B–C. ROEx tissues underwent the extended protocol which incorporated 24 hr incubation periods between A–B and B–C. D-3, D-2, and D-1 indicate days prior to the start of the culture experiment, signified by D0 and the final arrows. All incubation was completed at 37ºC with 5% CO_2. Created with BioRender.com. D (-3/-2/-1/0), day (-3/-2/-1/0); ECM, extracellular matrix; RO, reaggregated ovary; ROEx, extended reaggregated ovary.

3.2.3 Reaggregated ovary culture

Uncultured (D0) RO and ROEx tissues did not undergo overnight culture following RO generation. ROs and ROEx tissues cultured for three (D3) or seven days (D7) were maintained according to the culture protocol described in Chapter 2.6 until the predetermined endpoint.

Histological processing of all tissues in the RO, ROEx, and WO groups was performed as described in Chapter 2.7, including fixation, embedding, and sectioning. WO (P6, P9, P13) tissues were fixed immediately following ovarian dissection and cleaning, while RO and ROEx D0 tissues were fixed immediately following RO generation.

3.2.4 Histological staining

To visualise ovarian tissue for determination of follicle classification, number, and other follicular-related measurements, tissues were stained with haematoxylin (Gills #2 haematoxylin, Sigma-Aldrich) and eosin (Chapter 2.8).

3.2.5 Ovarian tissue and follicle assessment

Tissue volume was calculated using the Cavalieri principle (planimetry method), as previously reported (Chapter 2.9.1).

Follicle classification, number, and associated follicle-based analyses were performed blind with randomised sample groups. Unblinding only occurred following completion of follicle counting and classification via ImageJ (v.2.1.0/1.53c).

Follicle classification followed the criteria described in Chapter 2.9.2. Total follicle counts per ovary were corrected with the Abercrombie factor (Abercrombie, 1946) (Chapter 2.9.3).

3.2.6 Imaging

Dissection of ovarian tissue was performed under the M125 stereomicroscope and brightfield microscopy images taken with a Leica microscopy (DM2500, Leica Microsystems) (Chapter 2.11.2).

3.2.7 Statistical analysis

Statistical analysis was performed using GraphPad Prism. Data normality was assessed using the Shapiro–Wilk test to determine the use of parametric or non-parametric methods. Data was generated from RO (D0, *n*=5; D3, *n*=6; D7, *n*=5), ROEx (D0, *n*=5; D3, *n*=5; D7, *n*=5), and WO tissues (P6, *n*=3; P9, *n*=5; P13, *n*=4).

Differences in mean total follicle number across culture timepoints (D0, D3, D7) were analysed using either Welch's t-test or Mann-Whitney U test. Follicle stage distributions were assessed by two-way ANOVA, with Tukey's test used for between-group comparisons (e.g., RO versus ROEx) and Šídak's test used for subgroup comparisons (e.g., RO versus age-matched WO).

Where multiple t-tests were performed, *p*-values were adjusted to account for multiple comparisons using the Holm-Šídák method as implemented by GraphPad Prism, and adjusted *p*-values (adj. *p*) are reported. Comparisons of follicle and oocyte areas between RO and ROEx groups were analysed using unpaired t-tests with Welch's correction for unequal variance, or Mann-Whitney U tests when data were non-normally distributed. Follicle and oocyte symmetry were compared using Welch's t-tests and Mann-Whitney U tests, respectively. The presence of TCs was reported descriptively due to limited numbers of primary follicles (*n*=2) in the ROEx group, which precluded statistical testing. Follicle and granulosa area growth trajectories relative to GC number were fitted using simple linear regression, with $r^2>0.6$ considered biologically relevant as reported by Lo *et al.* (2019). Differences in regression slopes and y-intercepts between groups were compared using analysis of covariance.

Data are presented as mean ± SD unless otherwise stated. Significance was defined as $p\leq0.05$.

3.3 Results

3.3.1 Follicle number in reaggregated ovaries remained stable across culture durations but stage composition shifted

Representative H&E sections are shown in Figure 3.3.1.1A. Uncultured ROs (D0) appeared less morphologically consolidated compared to cultured samples, reflecting the absence of an overnight culture period that facilitates compaction and rounding of the reaggregated tissue. It was first necessary to establish the total follicle number across culture timepoints before comparing ROs with samples of other experimental groups. The number of follicles in uncultured ROs (n=5; 492.1 ± 627.9) did not significantly differ to ROs cultured for three (n=6; 91.81 ± 31.09) or seven days (n=5; 82.55 ± 44.67) (Figure 3.3.1.2A). No difference was observed between ROs cultured for three (91.81 ± 31.09) versus seven days (82.55 ± 44.67). Despite similar totals, two-way ANOVA analysis showed a significant interaction between follicle stage and culture duration (p<0.01), indicating that the effect of culture duration was follicle stage-dependent. Follicle stage alone also influenced follicle number (p<0.05), whilst the factor of culture duration alone was not significant. Uncultured ROs were found to contain more primordial follicles than either RO D3 and RO D7 groups (All comparisons, adj. p<0.05) and primary follicles (D0 vs. D3, adj. p<0.05; D0 vs. D7, adj. p<0.05) increased with time in culture (Figure 3.3.1.2B). Secondary follicles were rarely observed and appeared in only one sample in the RO D7 group.

3.3.2 Reaggregated ovaries contained fewer follicles than age-matched whole ovaries

As murine age impacts follicle development *in vivo*, age-matched WOs were included as a comparator group, P6 ovaries (n=3) were compared with uncultured ROs, P9 ovaries (n=5) with the RO D3, and P13 ovaries (n=4) with RO D7 (Figure 3.3.1.1A). When comparing mean total follicle number, a two-way ANOVA found a significant interaction between ovary condition (RO versus WO) and age/culture duration (p<0.05). Ovary condition had the most significant impact on follicle number (p<0.0001), while age/culture duration alone had no significant effect.

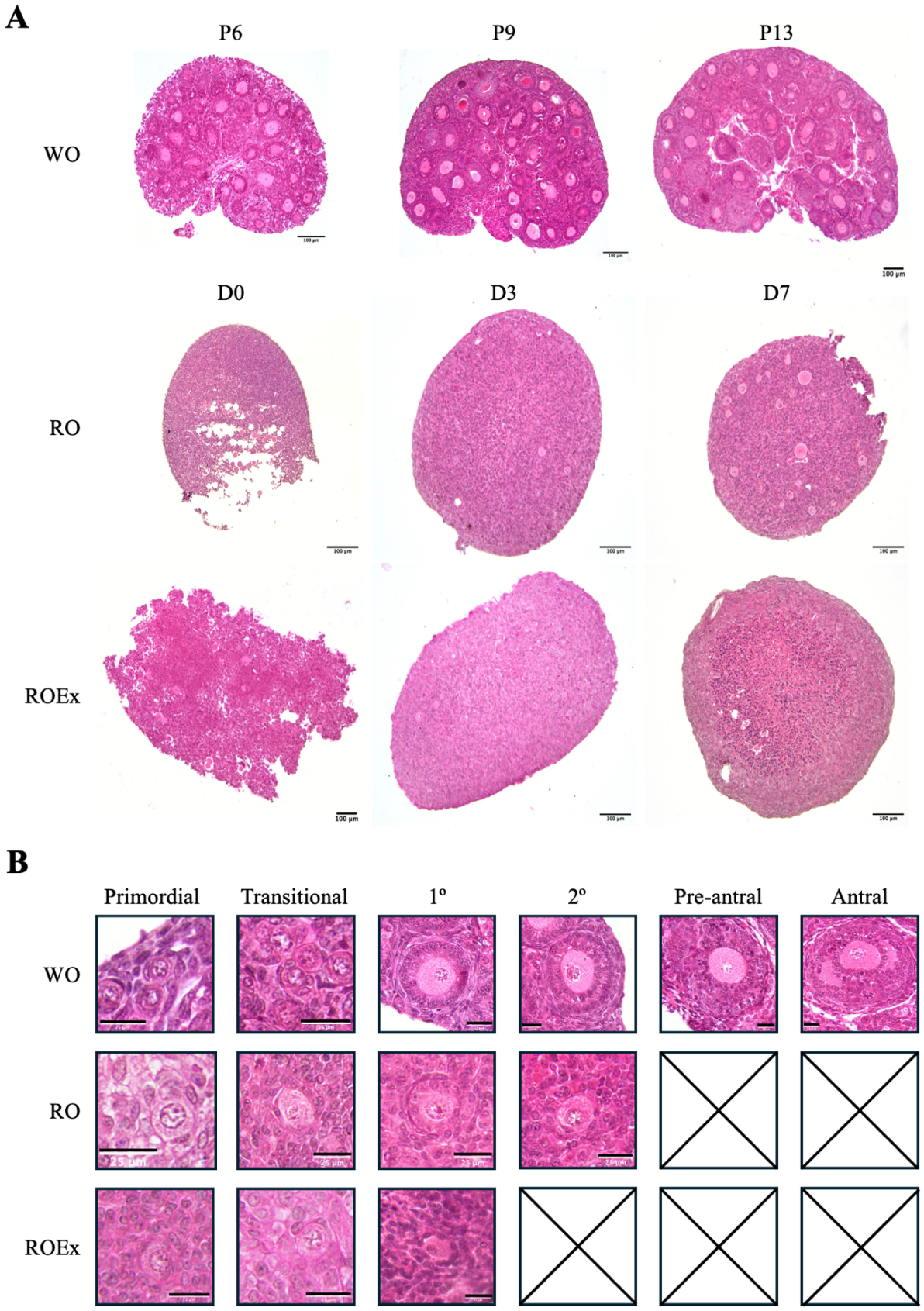

Figure 3.3.1.1) Histological comparison of ovarian and follicle morphology and development in whole and reaggregated ovary models. A) Representative murine tissue sections stained with H&E at various postnatal ages (WO: P6, P9, P13) or culture timepoints (D0, D3, D7) following reaggregation (RO or ROEx). Scale bar represents 100 µm. **B)** Representative images of follicles from histological sections stained with H&E of each experimental group at the various stages of development. Scale bar represents 25 µm. WO: P6 (*n*=3), P9 (*n*=5), P13 (*n*=4); RO: D0 (*n*=5), D3 (*n*=6), D7 (*n*=5); ROEx: D0 (*n*=5), D3 (*n*=5), D7 (*n*=5). 1º, primary; 2º, secondary; D(0/3/7), culture day (0/3/7); H&E, haematoxylin and eosin; P(6/9/13), postnatal day (6/9/13); RO, reaggregated ovary; ROEx, extended protocol reaggregated ovary; WO, whole ovary.

Total follicle number was comparable between ROs and age-matched P6 WOs (Figure 3.3.1.2A). In contrast, older WOs contained significantly more follicles than cultured ROs: P9 group versus RO D3 (adj. p<0.05) and P13 group versus RO D7 group (adj. p<0.05).

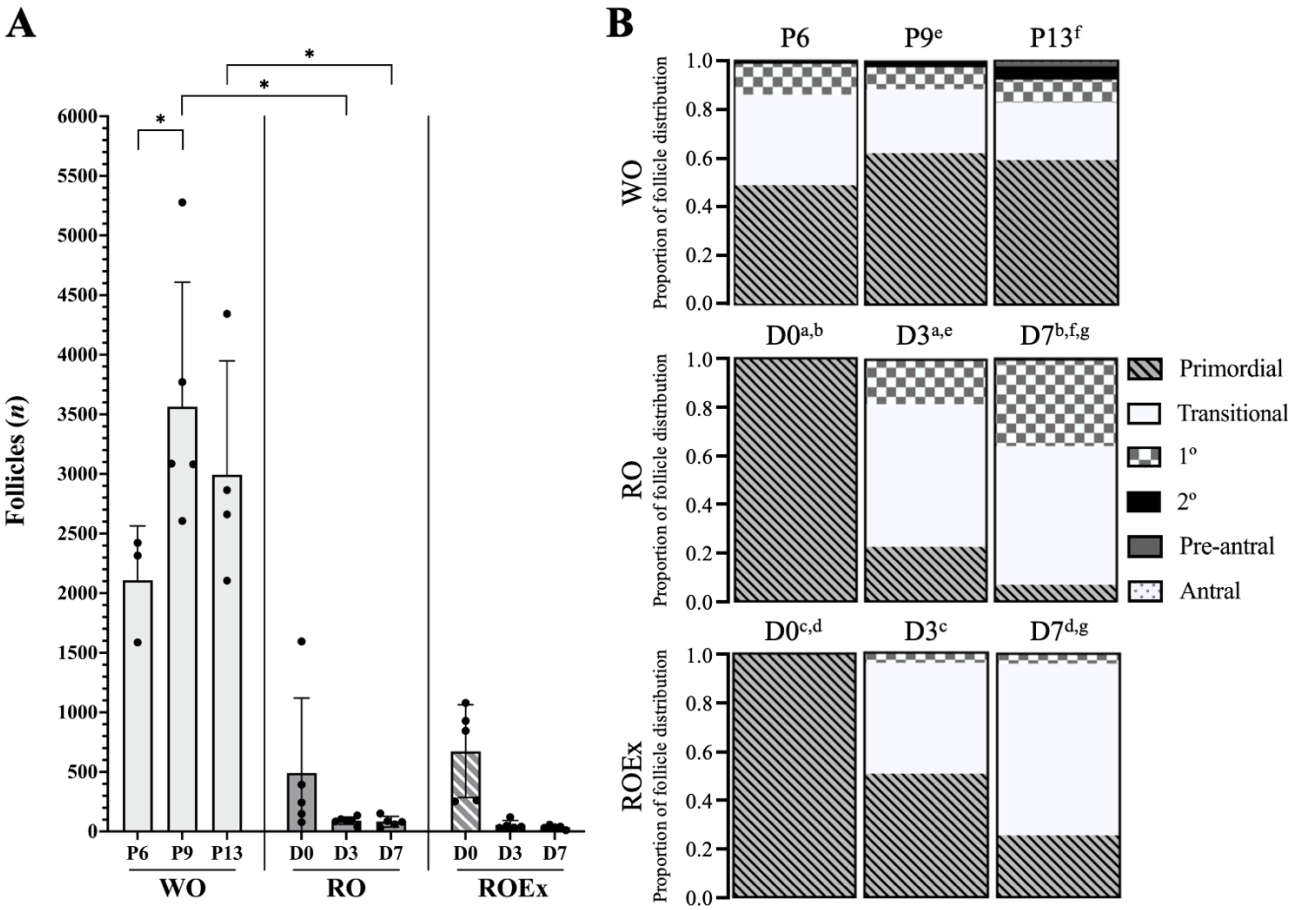

Figure 3.3.1.2) Quantitative analysis of follicle number and stage distribution in whole and reaggregated ovary models. A) Total follicle number (mean ± SD) was compared within each respective experimental group (WO, RO, ROEx) across age or culture duration. RO total follicle number was also compared with age-matched control (WO) or extended protocol (ROEx) count following the same culture period. Significance between comparators was determined using the Welch's t-test (for normal data distribution) and the Mann-Whitney U test (for non-normal data distribution). Where there is no asterisk symbol, there was no significant difference seen comparators. **B)** Proportional distribution of follicle development in each experimental condition across time points: WO (mean; P6 [primordial, 49.0%; transitional, 37.1%; 1º, 12.5%; 2º, 1.3%; pre-antral, 0.7%], P9 [primordial, 62.4%; transitional, 26.3%; 1º, 8.9%; 2º, 2.3%], P13 [primordial, 59.4%; transitional, 23.6%; 1º, 9.2%; 2º, 5.5%; pre-antral, 1.6%; antral, 0.6%]), RO (mean; D0 [primordial, 99.8%; transitional, 0.2%], D3 [primordial, 22.6%; transitional, 59.1%; 1º, 18.3%], D7 [primordial, 6.9%; transitional, 57.1%; 1º, 35.2%; 2º, 0.8%]), ROEx (mean; D0 [primordial, 99.7%; transitional, 0.3%], D3 [primordial, 50.5%; transitional, 45.3%; 1º, 4.2%], D7 [primordial, 25.4%; transitional, 70.6%; 1º, 4.0%]). Multiple unpaired t-tests (for normal data distribution) and multiple Mann-Whitney U tests (for non-normal-data distribution) as expressed by an adj. *p*-value. The choice of statistical test for each comparison was determined by data normality as assessed by the Shapiro-Wilk test. Proportional distribution of follicular stages was compared within the same experimental condition at different time-points or between the RO with the age-matched WO/culture-duration-matched ROEx. Where there is no letter, there were no significant differences between comparators. a: primordial (adj. $p<0.001$), transitional (adj. $p<0.001$), primary (adj. $p<0.05$); b: primordial (adj. $p<0.0001$), transitional (adj. $p<0.01$), primary (adj. $p<0.05$); c: primordial (adj. $p<0.05$), transitional (adj. $p<0.05$); d: primordial (adj. $p<0.05$), transitional (adj. $p<0.05$); e: transitional (adj. $p<0.05$), secondary (adj. $p<0.05$); f: primary (adj. $p<0.05$); pre-antral (adj. $p<0.05$); g: primary (adj. $p<0.05$). WO: P6 (n=3), P9 (n=5), P13 (n=4); RO: D0 (n=5), D3 (n=6), D7 (n=5); ROEx: D0 (n=5), D3 (n=5), D7 (n=5). 1º, primary; 2º, secondary; D(0/3/7), culture day (0/3/7); P(6/9/13), postnatal day (6/9/13); RO, reaggregated ovary; ROEx, extended protocol reaggregated ovary; SD, standard deviation; WO, whole ovary. *$p\leq0.05$.

3.3.3 Follicle stage distribution shifted during reaggregated ovary culture and diverged from age-matched whole ovaries

To assess whether culture influenced the distribution of follicle stage, the proportion of primordial, transitional, and primary follicles were compared across ROs cultured for 0, 3, or 7 days (Figure 3.3.1.1B). Two-way ANOVA analysis found a strong interaction between follicle stage and culture duration ($p<0.0001$), as well as follicle stage alone ($p<0.0001$), whilst culture duration alone did not.

Uncultured ROs had a greater proportion of primordial follicles than either the D3 (adj. $p<0.001$) or D7 groups (adj. $p<0.0001$) (Figure 3.3.1.2B). However, the uncultured RO group had a smaller fraction of transitional (versus D3, adj. $p<0.001$; versus D7, adj. $p<0.01$) and primary follicles (versus D3, adj. $p<0.05$; versus D7, adj. $p<0.05$) compared with cultured groups. The distribution of follicular stages was similar between ROs cultured three days and seven days. Notably, secondary follicles were observed only in the D7 group.

When ROs were compared to age-matched WOs via a two-way ANOVA, follicle stage and the interaction of age/culture duration with stage exerted a strong effect (RO D0 versus WO P6; RO D3 versus WO P9; RO D7 versus WO P13; all comparisons were $p<0.0001$). Ovarian condition did not appear to influence proportion of follicles independently of stage and age/culture duration. At baseline, uncultured ROs resembled the fractional makeup of P6 WOs with respect to primordial and transitional follicles, although WOs contained more advanced follicles absent in the uncultured RO (Figure 3.3.1.2B). After three days in culture, ROs had a higher proportion of transitional follicles than P9 WOs (adj. $p<0.05$), while other stages were similar. By D7, follicle distributions diverged further, with ROs showing enrichment of primary follicles (adj. $p<0.05$), whereas P13 WOs contained follicles up to the antral stage. These findings indicated that, whilst early follicle proportions in uncultured ROs were similar to age-matched ovaries, the trajectory of stage progression diverged during culture.

3.3.4 Reaggregated ovary volume remained stable during culture but was smaller than age-matched whole ovaries

RO volume was similar irrespective of culture duration (mean ± SEM; D0, 0.059 mm^3 ± 0.024 mm^3; D3, 0.085 mm^3 ± 0.016 mm^3; D7, 0.062 mm^3 ± 0.006 mm^3). In contrast, WO volume significantly increased with age ([P6, 0.079 mm^3 ± 0.004 mm^3; P9, 0.15 mm^3 ± 0.012 mm^3; $p<0.01$], [P9, 0.155 mm^3 ± 0.012 mm^3; P13, 0.332 mm^3 ± 0.023 mm^3; $p<0.01$]).

Two-way ANOVA showed that ovary condition (RO versus WO; $p<0.0001$), age/culture duration alone ($p<0.0001$), and their interaction ($p<0.0001$) significantly contributed to volume variation. The RO D3 group was smaller than the WO P9 group (adj. $p<0.05$) and D7 ROs were smaller than P13 WOs (adj. $p<0.01$). In contrast, uncultured ROs had comparable volumes to P6 WOs. These data indicate that RO volume was stable across culture, but failed to expand in parallel with WOs.

3.3.5 The extended reaggregated ovary protocol altered follicle dynamics without reducing total follicle number

Having established the baseline developmental characteristics of ROs, the next was to examine whether extending the duration of germ-somatic cell separation during RO generation (the ROEx protocol) would alter follicular outcomes. The mean total follicle number (mean ± SD) was greater in uncultured ROEx (D0; $n=5$) samples (673.6 ± 389.0) when compared with ROEx D3 ($n=5$; 54.54 ± 37.92; $p<0.01$) or ROEx D7 ($n=5$; 34.59 ± 16.71; $p<0.01$). Follicle number did not significantly differ between ROEx groups cultured for three (54.54 ± 37.92) versus seven days (34.59 ± 16.71).

A two-way ANOVA revealed culture duration alone significantly influenced follicle count across RO and ROEx groups ($p<0.001$), whilst protocol alone and the interaction between both factors did not contribute significantly to source of variation. Total follicle number was similar between RO and ROEx groups at each time point. Analysis of follicle distribution demonstrated that at D0, ROs and ROExs had similar proportions of primordial and transitional follicles. However, significant differences emerged following culture of tissues. At D3, ROs had a smaller proportion of primordial

follicles than the ROEx group (adj. $p<0.05$). After seven days in culture, ROs had a larger proportion of primary follicles than in ROExs (adj. $p<0.01$).

To determine whether the extended protocol influenced tissue growth over time, ROEx volume was assessed across culture timepoints. Volume (mean ± SEM) did not differ between uncultured ROEx tissue (D0, 0.176 mm^3 ± 0.076 mm^3) and tissues cultured for three (D3, 0.143 mm^3 ± 0.016 mm^3) or seven days (D7, 0.086 mm^3 ± 0.006 mm^3), respectively. However, ROEx D7 tissues were significantly smaller than D3 tissues ($p<0.01$).

3.3.6 Theca cell presence was evident in reaggregated ovaries but limited in extended reaggregated ovaries after seven-day culture

To assess follicular morphology, the presence of TCs was evaluated in relevant follicles. In the RO D7 group, 56.82% of follicles had a visible TC layer. In contrast, only two primary follicles were identified in the ROEx D7 group with one having a discernible TC layer (50.00%). Due to the very low number of follicles at these stages in the ROEx group, statistical analysis was not feasible.

3.3.7 Oocyte and follicle size were reduced in ROEx, whilst symmetry was preserved

To assess how the generation protocol affected follicle size, oocyte and follicle areas were compared between RO and ROEx groups after seven days of culture. Transitional follicles in the RO group had a greater oocyte area (447.4 μm^2 ± 158.3 μm^2) than those in the ROEx group (282.8 μm^2 ± 177.8 μm^2; $p<0.0001$) (Figure 3.3.8A). Similarly, follicle area was larger in ROs (992.0 μm^2 ± 312.8 μm^2) compared with ROExs (673.5 μm^2 ± 355.7 μm^2; $p<0.0001$) (Figure 3.3.8B). Although follicle numbers were maintained, follicle expansion was impaired in the ROEx group. To further investigate follicle development and oocyte competence, symmetry of both oocytes and follicles was examined. Despite the reduction in size, both oocyte symmetry (RO D7 with 1.064 ± 0.1607 vs. 1.013 ± 0.1474 with ROEx D7) and follicle symmetry (RO D7, 1.012 ± 0.0797; ROEx D7, 0.9390 ± 0.1271) were similar.

To further examine coordination between oocyte and somatic compartment growth, the relationship between oocyte area and granulosa area was assessed (Figure 3.3.8E). Oocyte area increased with granulosa area in both groups, with significant positive associations observed in RO D7 (r^2=0.2532, p<0.0001) and ROEx D7 (r^2=0.3552, p<0.001). The slope of this relationship differed significantly between groups (p<0.05), indicating altered scaling between oocyte and granulosa compartments under the extended protocol.

3.3.8 Follicle growth trajectories diverged between standard and extended reaggregated ovary groups after seven days in culture

To assess the growth rates of follicles in ROs in the standard protocol compared to the extended protocol, follicle area and granulosa area were assessed relative to GC number. As expected, both measures increased with GC number, consistent with progressive follicular expansion. Linear regressions were fit to follicles ranging from the transitional to secondary stages, consisting of 2–46 GCs in ROs and ROExs after seven days in culture. Follicle area increased rapidly per GC in both groups, with strong fits to the linear model (RO D7, r^2=0.8385; ROEx D7, r^2=0.7044) (Figure 3.3.8D). However, follicles in the RO group displayed a significantly steeper trajectory of GCs per follicle area compared with the ROEx group (p<0.05). Growth trajectories of GC per granulosa area were similar between both groups (RO D7, r^2=0.8585; ROEx D7, r^2=0.8075), but differences were observed between y-intercepts (p<0.05), demonstrating a shift in baseline GC area organisation (Figure 3.3.8C).

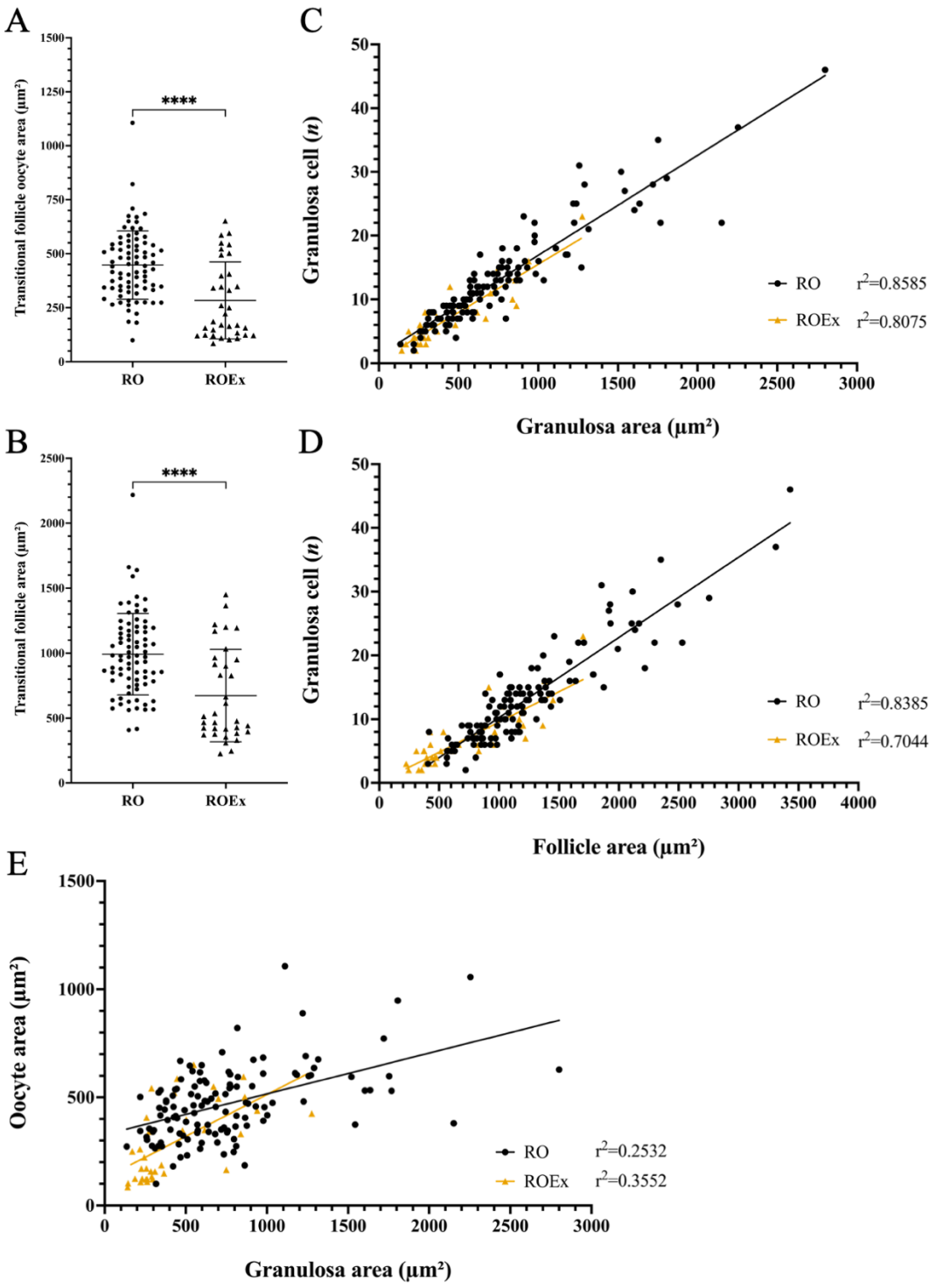

Figure 3.3.8) Comparative follicle and oocyte growth parameters in reaggregated ovary models following standard and extended cultures. **A)** Comparison of oocyte area (µm²) of transitional stage follicles between RO D7 (represented by circles) and ROEx D7 (represented by triangles). **B)** Comparison of follicle area (µm²) of transitional follicles between RO D7 (represented by circles) and ROEx D7 (represented by triangles). **C)** Relationship between GC number and granulosa area (µm²), and **D)** GC number and follicle area (µm²) across all follicle stages in RO D7 (black circles) and ROEx D7 (yellow triangles). Separate regression lines were fitted for each group, with corresponding r² values shown. The slopes were found to differ significantly between groups ($p<0.05$). **E)** Relationship between oocyte area (µm²) and granulosa area (µm²) across all follicle stages in RO D7 (black circles) and ROEx D7 (yellow triangles). Separate regression lines were fitted for each group, with corresponding r² values shown. The slopes were found to differ significantly between groups ($p<0.05$). Oocyte and follicle sizes are expressed as mean ± SD, and differences were analysed using the Mann-Whitney U test (for non-normally distributed data). Growth trajectories were assessed using simple linear regression, with $r^2>0.6$ considered biologically relevant (Lo *et al.*, 2019). RO D7 ($n=5$); ROEx D7 ($n=5$). D7, culture day 7; GC, granulosa cell; RO, reaggregated ovary; ROEx, extended protocol reaggregated ovary; SD, standard deviation. *$p\leq0.05$; **$p<0.01$; ***$p<0.001$; ****$p<0.0001$.

3.4 Discussion

The aim of this Chapter was to investigate the RO as a model for early follicle reformation *in vitro* and to evaluate how modifications to the generation protocol (ROEx) influenced follicular dynamics. Experimental findings demonstrated that while total follicle number was preserved across culture duration in ROs, the distribution of follicle stage shifted with a depletion of primordial follicles and enrichment of transitional and primary follicles.

Compared with age-matched WOs, ROs contained fewer follicles overall and diminished developmental potential. Volume analysis further revealed that ROs maintained structural stability throughout the seven day culture period, whilst volumetric expansion was characteristic of the intact WOs over time. Notably, an apparent increase in total follicle number was observed between P6 and P9 WOs. Whilst this was not biologically expected, follicle assembly is thought to be established in the early postnatal murine ovary (~P6–P7) (Bristol-Gould *et al.*, 2006; Tanimoto *et al.*, 2021; Tomic *et al.*, 2002). This observation is most likely attributable to the small sample size and the sensitivity of morphological classification, rather than a true increase in follicle number. Introduction of the extended generation protocol did not significantly reduce mean total follicle number compared with ROs with both follicle and oocyte symmetry maintained between groups. However, follicle stage distribution, as well as oocyte and follicle growth was altered in the ROEx group, with reduced growth trajectory. To the author's knowledge, this represents one of the first systematic assessments of follicle reformation and development after the reaggregation process across early culture timepoints. Here, the impact of extended germ–somatic cell separation on follicle formation and growth was tested. In doing so, it established oocyte-somatic coordination as a critical determinant of developmental efficiency *in vitro* for the chosen RO model.

The first observation was that total follicle number remained broadly stable across culture timepoints in the RO; however, follicle number was variable in uncultured ROs. It should be noted that oocytes without clear fp-GCs were classified as primordial follicles and were prevalent in the RO D0 group.

Germ cells require support from somatic cells to establish a follicle, as demonstrated by germ cell apoptosis in foetal ovaries when fp-GCs are absent (Mork *et al.*, 2012; O'Connell and Pepling, 2021; Pepling and Spradling, 2001; Telfer and Andersen, 2021; Tingen *et al.*, 2009; Wear *et al.*, 2016; Yang *et al.*, 2022). This may explain the numerically larger number of total follicles in the uncultured ovary. Total follicles in the RO did not differ significantly overtime, but variation between follicle number was present between individual ROs. However, while total numbers remained stable, the distribution of follicle development stages shifted.

Uncultured ROs contained more primordial follicles than either D3 or D7 tissues, whilst transitional and primary follicles increased over the same period. These data suggest that follicle activation occurred in culture, shifting the pool toward more advanced stages. A study by the Williams group found that, whilst total follicle number was consistent, cultured ROs generated from P6 mice had less primordial follicles after 14 days than those transplanted (Lo *et al.*, 2019). However, the Lo *et al.* (2019) study grouped primordial and transitional follicles in the same category for analysis. The transition of quiescent primordial follicles to activated primary follicles is associated with numerous pathways to coordinate and regulate gene expression in mice (Dharma *et al.*, 2009; Kerr *et al.*, 2013; Pepling and Spradling, 2001; Shirafuta *et al.*, 2024; Wear *et al.*, 2016; Zhao *et al.*, 2021). The observed redistribution is consistent with increased follicle activation during culture. While this has previously been linked to ovarian fragmentation disrupting Hippo signalling (Kawamura *et al.*, 2013), as well as activation of the PI3K/Akt/mTOR pathways (Dupont *et al.*, 2012; Grosbois and Demeestere, 2018; Guo and Yu, 2019; Zhang and Liu, 2015; Zhao *et al.*, 2021); however, present data do not directly assess these molecular mechanisms. An alternative explanation is that reaggregation alters the spatial organisation and local density of primordial follicles, which may influence spatial dynamics (Da Silva-Buttkus *et al.*, 2009). Spatial analyses in the neonatal murine ovary have shown that primordial follicles exert a localised inhibitory effect on neighbouring follicles, with interfollicular proximity associated with increased activation (Da Silva-Buttkus *et al.*, 2009). Thus, the increased proportion of activating follicles in ROs may reflect reduced local

inhibitory signalling attributed to altered follicle density, as opposed or in addition to changes in intracellular signalling pathways.

Although not found to be significantly different between RO D0 and WO P6 groups, follicle numbers were significantly lower in ROs cultured for three and seven days compared with P9 and P13 WOs, respectively. Lo *et al.* (2019) similarly reported that ROs generated from P6 mice and cultured for 14 days had fewer follicles than age-matched P20 WOs. Notably, transplanted ROs developed follicle populations more comparable to *in vivo* ovaries, suggesting systemic cues and vascularisation may assist with restoring typical follicle dynamics (Lo *et al.*, 2019). The dynamic widening of follicle distribution hints at limitations of using age-matched WOs as comparators, since development does not follow parallel progression.

Analysis of stage distribution patterns further supported the proposed developmental divergence. While WOs maintained a broader and balanced range of follicular stage development, including progression to antral follicles by P13, ROs plateaued at the secondary stage after seven days in culture. This pattern is consistent with the general observation that culture systems promote follicle activation; however, follicle progression may not be sustained (Cheng *et al.*, 2024; Hikabe *et al.*, 2016; Lo *et al.*, 2019; McLaughlin *et al.*, 2018; Schallmoser *et al.*, 2022; Sheikh *et al.*, 2023; Telfer and Andersen, 2021; Xu *et al.*, 2021; Yang *et al.*, 2022). The concept of reaggregation-induced developmental lag provided a useful framework: cultured ROs activated and expanded early follicles, but their developmental outcomes diverged progressively from intact ovaries over time.

The absence of advanced follicles in ROs likely reflected limitations of the *in vitro* environment and the model, rather than insufficient gonadotrophin stimulation alone. While early follicle development is largely gonadotrophin-independent, progression to later stages *in vivo* is supported by coordinated endocrine, stromal, and vascular factors (Adhikari and Liu, 2009; Cheng *et al.*, 2024; Honda *et al.*, 2007; Lo *et al.*, 2019; McGee and Hsueh, 2000). Although recombinant FSH was included in culture media, *in vitro* systems such as the RO lack endocrine signalling and tissue-level interactions present

in vivo (Kuscu *et al.*, 2025; Lo *et al.*, 2019; Sheikh *et al.*, 2023; Telfer and McLaughlin, 2012; Van Wezel and Rodgers, 1996). This limitation has been addressed in murine and human systems through multistep culture protocols involving follicle isolation and optimised media composition (Bagheri *et al.*, 2024; Cheng *et al.*, 2024; McLaughlin *et al.*, 2018; Xiao *et al.*, 2015). The use of mouse serum (MS) rather than FBS to supplement media was chosen based on previous evidence that species-specific factors may enhance murine follicle development in culture (Kuscu *et al.*, 2025).

The extended RO generation protocol (ROEx) was investigated to assess the impact of prolonged separation of adhered (e.g., viable somatic cells) and unadhered (e.g., germ cells) cell populations. Despite the extended period of separation, total follicle number remained similar between RO and ROEx groups. Across timepoints, follicle number also remained similar between protocols. However, much like the RO group, the ROExs had a reduction of total follicle count between D0 compared with D3 tissues. A two-way ANOVA confirmed that culture duration alone was the primary factor of this decline in total follicle number, whilst generation protocol had no significant effect. Thus, these findings indicate that the extended protocol did not deplete follicle pools, but may influence follicle development. ROEx tissues did not demonstrate volumetric expansion over time, with a reduction in volume observed by D7.

Stage distribution diverged between the RO and ROEx groups. Uncultured ROs and ROEx contained similar proportions of primordial and transitional follicles. However, differences became apparent following time in culture. At D3, ROExs had a higher proportion of primordial follicles than ROs, suggesting impairment or delay in follicle activation. Further, D7 ROs had a larger proportion of primary follicles than ROEx tissues, consistent with the observed accelerated follicle development in the standard RO protocol. Although follicle numbers were conserved between groups, the timing of activation and follicular development appeared to be altered in the ROEx generation protocol.

Follicle development is highly sensitive to oocyte-granulosa cell communication *in vitro* (Alam and Miyano, 2019; Albertini *et al.*, 2001; Honda *et al.*, 2007; Telfer and Andersen, 2021; Wu *et al.*, 2023).

Activation of the PI3K/Akt and mTOR pathways support the primordial-to-primary transition (Grosbois and Demeestere, 2018; Kawamura *et al.*, 2013; Yang *et al.*, 2022; Zhang and Liu, 2015; Zhao *et al.*, 2021). In the ROEx group, where oocytes are separated from their supportive somatic cells for a longer period, these signals may be less effectively re-established upon reaggregation. This may have contributed to the observed persistence of primordial follicles, decreased accumulation of primary follicles, and absence of secondary follicles in the ROEx group. This raises the question of whether, whilst follicle quantity was preserved, aspects of developmental quality were compromised.

It is known that regulation of follicle development is the direct consequence of the environment supporting this growth (West-Farrell *et al.*, 2009; Xu *et al.*, 2021). ROs can support follicular formation, but the reaggregation process may impact subsequent development following reformation (Eppig and Wigglesworth, 2000; Lo *et al.*, 2019; Sheikh *et al.*, 2023). Transitional follicles were the only subgroup of 'activated' follicles that could be compared due to the low number of pooled primary follicles (n=2) present in the ROEx group. Analysis of size metrics showed that the ROEx protocol may have constrained follicle and oocyte growth. After seven days in culture, transitional follicles from ROs had a larger oocyte area and larger follicle area compared with ROExs. Thus, the results showed that the extended protocol may negatively impact follicle and oocyte expansion, with evidence of altered scaling between oocyte and granulosa compartments. In the Sheikh *et al.* study (2023), follicle area, oocyte area, and GC area of primary follicles were reduced in ROs generated from older ovarian cells (3-weeks, 6-weeks, 3-months) compared with ROs from younger ovaries (8-days) following transplantation of 21 days. This suggests that both composition of cells and communication impact efficiency of growth in the RO. Despite the smaller follicle and oocyte area in transitional follicles in the ROEx group, follicle and oocyte symmetry was preserved with ratios approximating 1.0 across groups. Symmetry could be considered an indicator of uniform somatic encapsulation and support bidirectional/paracrine signalling between oocytes and GCs (Albertini *et al.*, 2001; Gittens *et al.*, 2005).

Theca recruitment was descriptively reviewed, wherein approximately half of the primary/secondary follicles in ROs and ROExs displayed a visible TC after seven days in culture. Lo *et al.* (2019) observed that FBL thinning and stromal organisation influenced TC recruitment in ROs, with transplanted ROs more effectively re-establishing TC organisation than cultured (2019). Walker *et al.* (2021) reported variability in follicle integrity, including TC development, in human ovarian tissues following culture. The contribution of theca support is essential for advanced follicle development and steroidogenic function (Honda *et al.*, 2007; Xu *et al.*, 2021; Young and McNeilly, 2010). All of which suggested that *in vitro* follicle development may impair the capacity for TC recruitment, potentially impeding follicle progression in the RO and ROEx groups.

Progressive follicular expansion in both groups (RO D7 and ROEx D7) had an r^2 value >0.6, which was considered biologically meaningful as it reflected a strong positive association between follicle size and GC expansion. However, the trajectory of follicle growth was significantly reduced in the ROEx D7 group. This would suggest that the extended protocol reduced the efficiency of scaling follicle area with increasing GC number. Although the granulosa area per GC regression slopes did not differ, the differing y-intercepts would support an altered baseline organisation of GC area in the ROEx compared to the RO. Lo *et al.* (2019) found P2 ROs (transplanted and cultured) had slower growth trajectories compared to *in vivo* WO, but this difference was not evident when compared with the P6 group. This finding would further support a developmental 'lag' linked to the *in vitro* environment. Sheikh *et al.* (2023) found that 8-day ROs had a steeper growth trajectory compared with older ROs (3-weeks, 6-weeks, 3-months) when assessing the relationship between follicle area and granulosa area with GCs, demonstrating that age of somatic cell impacted oocyte-granulosa interactions with varying levels of efficiency for follicle expansion. This aligns with the suggestion that the extended separation in the ROEx group may compromise the germ-somatic cell coordination required for optimal growth. Shallower trajectories and reduced y-intercepts may indicate impaired scaling dynamics of follicular development. Misalignment in oocyte-somatic signalling can lead to

developmental inefficiencies and result in limited progression to later developmental stages (Alam and Miyano, 2019; Paulino *et al.*, 2022).

This study provided the first systematic assessment of follicle reformation of ROs during the early culture period, offering insight into how reaggregation shapes initial follicular reformation and development. Across timepoints, cultured ROs preserved overall follicle number but demonstrated a redistribution from primordial to transitional and primary stages, indicating that activation occurs *in vitro* within the first 72 hrs. When compared to age-matched WOs, ROs contained fewer follicles and displayed limited progression beyond the secondary stage, consistent with a reaggregation-induced developmental lag and highlighting the absence of systemic cues in culture. Introduction of the extended protocol (ROEx) maintained follicle quantity, but showed signs of altered quality with limited stage distribution, reduced oocyte and follicle expansion, and dampened growth trajectories; demonstrating the sensitivity of early follicle development to the prolonged separation of germ and somatic cells. These findings establish ROs as a tractable system for investigating early follicle formation, while revealing potential limitations in advanced-stage progression and the importance of optimised reaggregation processes to improve developmental fidelity.

4. TRANSDUCTION AND TARGETING OF FOLLICULAR PRIMARY MURINE OVARIAN CELLS

4.1 Introduction

4.1.1 Background

Understanding early follicle development increasingly requires novel tools that enable precise manipulation without compromising follicular integrity, including signalling, metabolic exchange, and structural organisation. The preceding chapter demonstrated that the efficiency of follicle reformation following dissociation was dependent on the time-sensitive re-establishment of germ–somatic cell contact, and that the standard reaggregation protocol better supported more advanced stages of follicular development. These observations have direct methodological implications: any gene delivery strategy intended to interrogate or manipulate GC function must perform reliably and sensitively in primary ovarian cells, particularly within timeframes relevant to the re-establishment of somatic networks. Chapter 4 therefore aimed to address a foundational requirement for subsequent experimental work: the optimisation of a reporter system in primary ovarian cells that can be integrated into RO models for the study of follicle development.

AAVs have emerged as a promising gene delivery system, despite the relatively low cargo capacity (Ahmadi *et al.*, 2023; Ran *et al.*, 2015). Unlike many other viral vectors, AAVs do not integrate DNA randomly into the host genome, which minimises the risk of disrupting typical cellular functions (Ahmadi *et al.*, 2023) (Figure 4.1.1).

AAV infection begins with viral capsid attachment to the host cell surface. For AAV9, the primary receptor is terminal N-linked galactose on cell-surface glycans, stabilised by proteinaceous secondary receptors that differ among serotypes, which contributes to the non-uniform tropism observed across tissues (Dhungel *et al.*, 2021). Following binding, AAVs are internalised via endocytosis and transported to the nucleus after release from the endosome (Ahmadi *et al.*, 2023; Dhungel *et al.*, 2021). Within the nucleus, the single-stranded viral DNA is typically converted to double-stranded episomal DNA, which is subsequently transcribed into mRNA and exported for translation into protein. The persistence of viral DNA in the host nucleus varies between cell types, particularly between dividing and non-dividing cells, influencing both gene expression and signal longevity (Muhuri *et al.*, 2022).

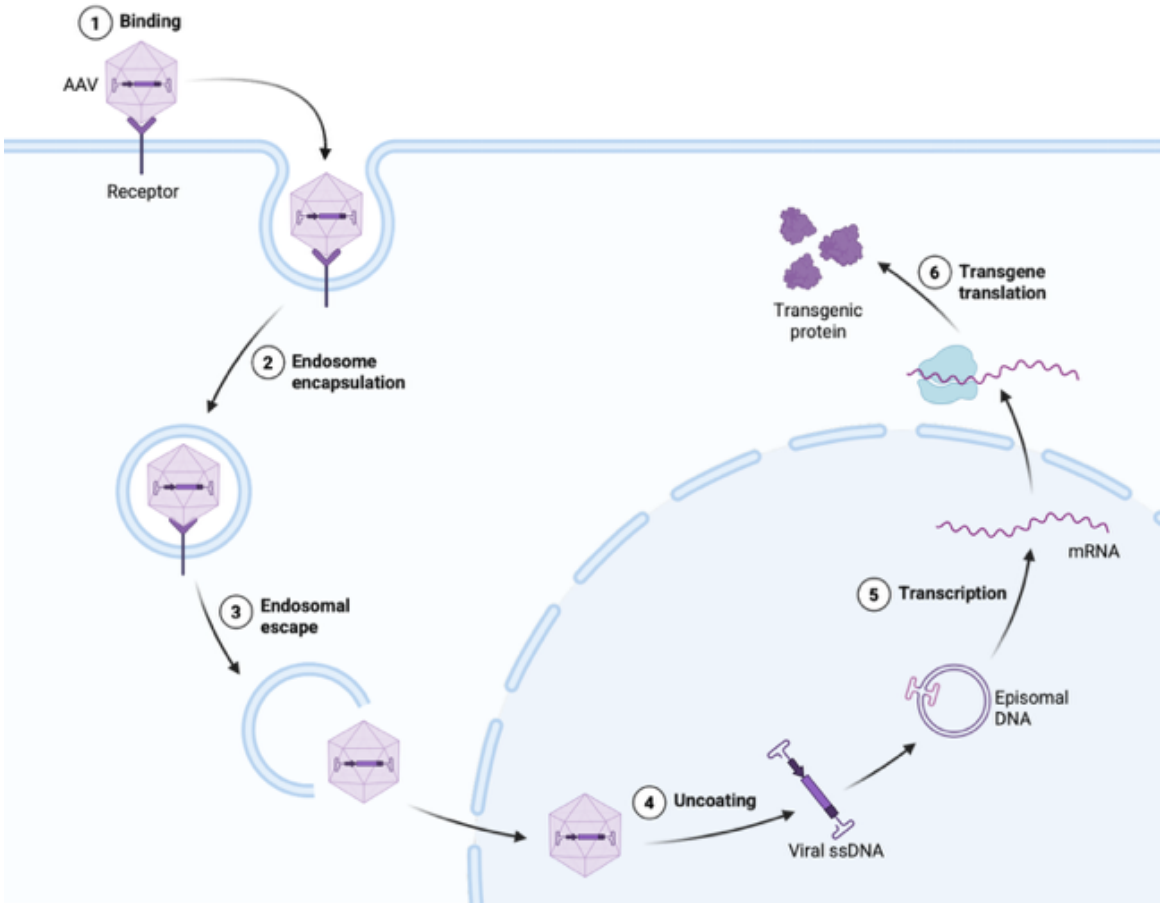

Figure 4.1.1) Schematic representation of the adeno-associated virus infection and transgene expression pathway. Overview of the AAV infection process illustrating six key steps of typical viral entry, processing, and transgene expression within the host cell. (1) *Binding:* AAV particles attach to specific cell-surface receptors. (2) *Endosome encapsulation:* The virus is internalised into an endosome via receptor-mediated endocytosis. (3) *Endosomal escape:* AAV particles escape into the cytoplasm prior to endosomal degradation. (4) *Uncoating:* The viral capsid disassembles, releasing viral ssDNA. (5) *Transcription:* The viral genome converts to episomal double-stranded DNA, serving as a template for transcription into mRNA. (6) *Transgene translation:* mRNA is translated into the encoded transgenic protein. Images are not to scale. Figure sourced from BioRender.com (2025) and created using BioRender.com. AAV, adeno-associated virus; mRNA, messenger ribonucleic acid; (ss)DNA, (single-stranded) deoxyribonucleic acid.

AAV9 was selected as the candidate vector for optimisation due to its favourable combination of low immunogenicity, episomal persistence, and broad tropism across epithelial and mesenchymal tissues (Ahmadi *et al.*, 2023; Arjomandnejad *et al.*, 2023). AAV tropism is highly context-dependent, for example, receptor availability and cell-cycle status influence episomal persistence (Walkey *et al.*, 2025; Zincarelli *et al.*, 2008). Primary ovarian cells are heterogenous and sensitive to culture perturbation; these factors combine to produce a unique and experimentally unpredictable environment for transduction. The absence of systematic data on AAV9 performance in dissociated primary murine ovarian cells represents a major methodological gap. In the *in vivo* Kanatsu-Shinohara *et al.* study (2022), AAV9s were selected for their ability to transcytose the follicular FBL following intravenous injection in mice. In this study, transgenic ($Kitl^{Sl\text{-}t}$/$Kitl^{Sl\text{-}t}$) mice were congenitally infertile and were successfully treated with an intravenous injection of AAV9 particles carrying the murine Kitl gene. This intervention was reported to have restored oogenesis and follicle development beyond the primordial stage (Kanatsu-Shinohara *et al.*, 2022). Mutant mice in the treatment group produced healthy offspring through natural mating, without evidence of AAV genome integration in the F1 generation, demonstrating effective use of AAV-mediated gene therapy to restore fertility caused by defective follicular somatic cells (Kanatsu-Shinohara *et al.*, 2022).

The multiplicity of infection (MOI) represents the number of viral particles per cell transduced. Primary ovarian cells exhibit heterogeneous activity and are known to be sensitive to both serum composition and mechanical stress (Alam and Miyano, 2019; Hao, Li, *et al.*, 2024; Kuscu *et al.*, 2025; De Roo *et al.*, 2020; Zhang *et al.*, 2018). High MOIs can saturate endosomal processing pathways or impose structural burden on cells, whilst low MOIs risk insufficient delivery of vector genomes to achieve detectable expression (Dan and Kang-Zheng, 2025; Ellis *et al.*, 2013). Although AAVs are generally less cytotoxic than other viruses, optimisation must balance expression efficiency with preservation of viability and cell morphology (Ahmadi *et al.*, 2023; Ellis *et al.*, 2013). As this chapter focused on dissociated cells, compromising follicular organisation was not a consideration which supported the assessment of viability and MOI compatible with downstream RO applications.

Fluorescent markers, such as EGFP and mCherry, are indispensable tools in research to track gene expression and observe cellular processes in a wide range of tissue and organ systems, including ovarian tissue culture and folliculogenesis (Ellis *et al.*, 2013; Kanatsu-Shinohara *et al.*, 2022; Morgan *et al.*, 2015). Fluorescent reporters support non-invasive observation via fluorescent microscopy to monitor instantaneous gene expression in live cells. EGFP is valued for its brightness and photostability, whilst mCherry is particularly beneficial for multicolour experiments due to its distinctive red emission (Kato *et al.*, 1999; Wu *et al.*, 2009). When driven by an ubiquitous promoter, fluorescent signals can be utilised to assess AAV transduction efficiency within ovarian tissue and follicles (Kanatsu-Shinohara *et al.*, 2022).

Alternatively, a conditional promoter can be selected to drive expression of a marker for cell-specific purposes, such as to identify ovarian follicles. AMH is a marker of ovarian function with expression largely restricted to GCs of growing ovarian follicles from the primary stage, observed in mice as early as P4 (Dharma *et al.*, 2009; Gruijters *et al.*, 2003; Visser *et al.*, 2006; Weenen *et al.*, 2004). Murine AMH (mAMH) expression in transgenic ovaries has been found to be restricted to GCs which supports mAMH as a promising candidate for follicle identification via cell-specific fluorescent expression (Bristol-Gould *et al.*, 2005; Lécureuil *et al.*, 2002). However, it has been reported that transgene expression under the control of the AMH gene promoter, as detected via IHC, was not found to be ubiquitously expressed across GCs with reduced detection in aging ovaries (Lécureuil *et al.*, 2002; Wang, Yang, *et al.*, 2024).

Another potential promoter candidate, Forkhead box L2 (FOXL2) is expressed at earlier follicular stages, such as the primordial stage, but declines during follicle development (Nicol *et al.*, 2020). In contrast, Cyp19α1 promoter-driven expression is associated with differentiated GCs of preovulatory follicles and luteal cells, indicating specificity for more mature antral follicles rather than earlier gonadotrophin-responsive follicles (Lv *et al.*, 2019; West-Farrell *et al.*, 2009). The FSH receptor is highly expressed in GCs across multiple stages of follicle development, and has more recently been reported in oocytes, suggesting it may represent a potential candidate as a follicle-specific marker

(Chen *et al.*, 2025; Heckert *et al.*, 1998). However, it has been concluded that the murine FSH promoter contains two SF-1-like binding sites with variable activity and lacks conventional elements such as a TATA box (Gromoll and Simoni, 2005; Levallet *et al.*, 2001). Thus, this promoter could introduce regulatory uncertainty inappropriate for initial validation.

The CRISPR/Cas9 genome-editing system can support more precise, targeted modifications to the genome. Applications of which have been beneficial to the study of gene function in ovarian cells, as well as research into the development of therapeutic interventions for infertility and other reproductive disorders (Ge *et al.*, 2016; Mizuno *et al.*, 2018). In the context of ovarian research, transgenic murine models with fluorescent reporters have been implemented to investigate follicular development (Zhao *et al.*, 2021).

To facilitate the insertion of genomic materials in wild type primary cells, AAVs have been used to deliver the necessary CRISPR components (Gaj *et al.*, 2017; Ge *et al.*, 2016; He *et al.*, 2022; Mizuno *et al.*, 2018). To streamline the delivery process and reduce the number of experimental steps, a single AAV can carry both the Cas9 protein and corresponding sgRNA sequences (Xiao *et al.*, 2019). Moreover, this method reduces the risk of off-target effects, a common challenge in genomic-editing studies (Liao *et al.*, 2024).

4.1.2 Chapter aims

It was hypothesised that AAV9-mediated transduction would enable efficient delivery and expression of exogenous genetic material in primary murine ovarian cells *in vitro* without substantially compromising cell viability, and that the use of a cell-type-specific promoter would allow selective identification of GCs within a heterogeneous population.

The aim of this Chapter was to evaluate AAV9-mediated gene delivery in primary murine ovarian cells and determine whether fluorescent reporter systems could be used to assess transduction efficiency and enable cell-type-specific targeting.

To address this aim, the following objectives were defined:

- To determine the optimal MOI for AAV9-mediated transduction by assessing cell viability and EGFP expression across increasing MOIs
- To quantify transduction efficiency following sequential co-transduction of AAV vectors by measuring mCherry and EGFP expression in primary ovarian cells

4.2 Methodology

4.2.1 Murine ovary collection and dissociation

F1 pups (P6–P7) were culled and ovaries isolated (Chapter 2.3). Dissected ovaries underwent enzymatic digestion into a heterogeneous suspension of cells.

4.2.2 Viral particles

All AAVs were produced and packaged by VectorBuilder. Viral particles were stored in -80ºC until ready for use. The AAV9 virus ubiquitously driving EGFP expression (VB010000-9394npt, VectorBuilder; viral titre of ~2×10^{11} genome copies (GC)/mL), herein referred to as AAV-EGFP, was used to determine optimal MOI for transduction in primary murine ovarian cells.

The two custom AAV9 vectors utilised in the sequential transduction efficiency experiments were designed by me, with review and consultation from Dr Christian Babbs (MRC Weatherall Institute of Molecular Medicine, University of Oxford, UK). Both AAV vectors were designed specifically for this study to achieve CRISPR/Cas9-mediated gene knock-in with follicular cell-type-specific visualisation in primary murine ovarian cells.

The first vector, AAV-Cas9 virus (VB231004-1799hyg, VectorBuilder, Illinois, USA; viral titre of ~2×10^{12} GC/mL), encoded for an sgRNA (97 bp) targeting the mROSA26 locus (Figure 4.2.2A). The U6 promoter (249 bp), a RNA polymerase III promoter, drove the expression of the sgRNA, followed by a 5 bp terminator sequence. To accommodate AAV packaging constraints, *Staphylococcus aureus* Cas9 (SaCas9; 3,345 bp) was used and driven by the ubiquitous EF1α short promoter (EFS; 232 bp), with transcription terminated by a poly-A tail (208 bp). The total genome size was 4,515 bp.

The second vector, AAV-Donor Strand (AAV-DS; VB231004-1797awt, VectorBuilder; viral titre of ~2×10^{12} GC/mL), was designed as a donor construct for homology-directed repair (HDR) at the mROSA26 locus (Figure 4.2.2B). The vector contained left (818 bp) and right (817 bp) homology arms flanking an EGFP cassette (720 bp) driven by the mAMH promoter (180 bp), followed by the

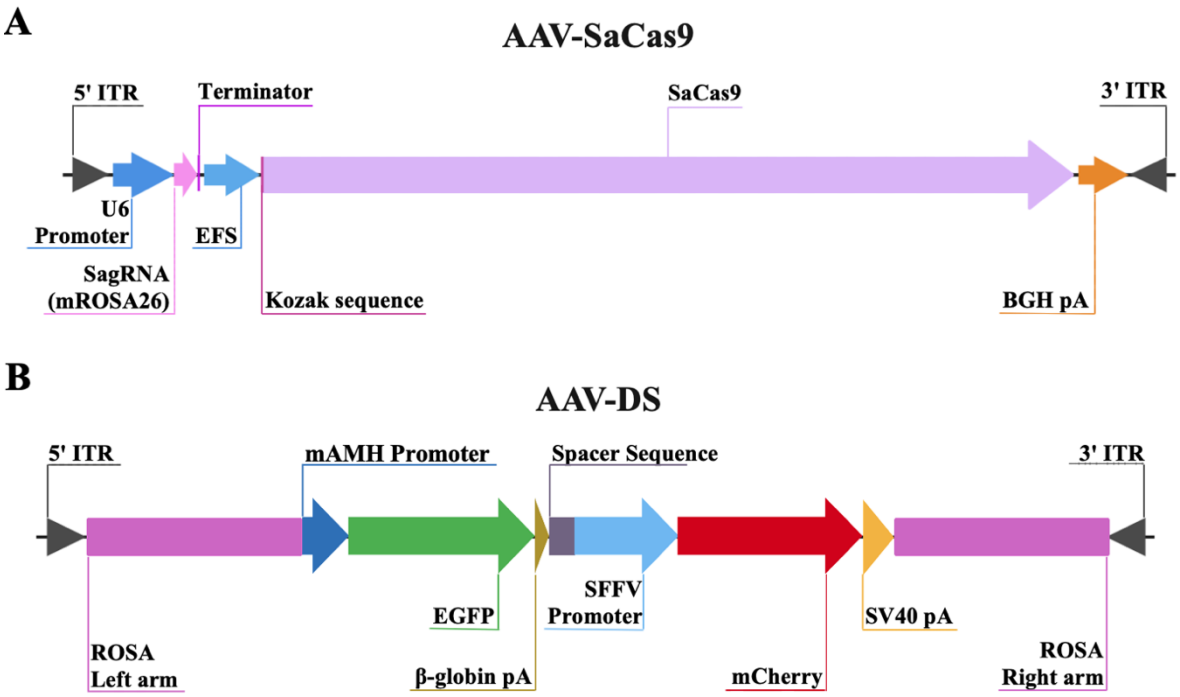

Figure 4.2.2) Viral construct designs for transduction in primary murine ovarian cells with AAV-SaCas9 and AAV-DS. A) Linear diagram of the AAV-SaCas9 construct (VB231004-1799hyg; VectorBuilder) illustrating the U6 promoter driving the sgRNA targeting mROSA26, followed by a short terminator, and the SaCas9 nuclease expressed from the EFS promoter with an upstream Kozak sequence. Transcription terminates at the BGH pA. **B)** Linear diagram of the AAV-DS construct (VB231004-1797awt; VectorBuilder) designed to support HDR at mROSA26 locus. The vector contains ROSA left and right homology arms flanking dual expression cassettes: 1) the mAMH promoter driving EGFP followed by the β-globin pA; and 2) a cassette comprising a spacer sequence, the SFFV promoter, and mCherry terminated by the SV40 pA. Both viral genomes are flanked by AAV2 5′ and 3′ ITRs. Only viral DNA components are shown (not to scale); plasmid backbone elements used for bacterial propagation and selection are omitted. AAV, adeno-associated virus; BGH, bovine growth hormone; DNA, deoxyribonucleic acid; DS, donor strand; EGFP, enhanced green fluorescent protein; EFS, short EF1α promoter; HDR, homology-directed repair; ITR, inverted terminal repeat; mAMH, murine anti-Müllerian hormone; mROSA26, murine ROSA26 locus; pA, polyadenylic acid tail; (Sa)Cas9, (*Staphylococcus aureus*) CRISPR-associated protein 9; SFFV, spleen focus-forming virus promoter; sgRNA, single-guide ribonucleic acid; SV40, simian virus 40.

β-globin poly-A signal (56 bp). A second cassette comprised a spacer sequence (102 bp), the ubiquitous Spleen Focus Forming Virus (SFFV) promoter (402 bp), and mCherry fluorescent reporter terminated by an SV40 poly-A signal (122 bp).

4.2.3 Transduction and cell culture protocol

Prior to transduction, a representative mixture of 10 µL of primary ovarian cells were removed to determine cell number and viability via an automated cell counter (Chapter 2.5).

4.2.3.1 Determination of optimal multiplicity of infection with the AAV-EGFP vector

To determine the optimal MOI, ~10,000 viable primary ovarian cells were transferred to each well of 24-well TCT plate and appropriately labelled (Figure 4.2.3.1). Each well contained 500 µL of warm, cell culture media. To mitigate evaporation, 250 µL of sterile ddH_2O with 1% Pen/Strep was added to the inter-well spaces of the plate. The plate was placed in an incubator (37ºC, 5% CO_2) for 24 hr.

Following incubation, spent media was aspirated and discarded. Each control and experimental group received fresh cell culture media containing viral particles corresponding to the appropriate MOI (Table 4.2.3.1). The 24-well plate was gently swirled and placed in the incubator for 24 hr. The following day, all non-viral and virus-containing media across groups were aspirated, replaced with 500 µL of fresh cell culture media, and allowed to incubate for a further 24 hr.

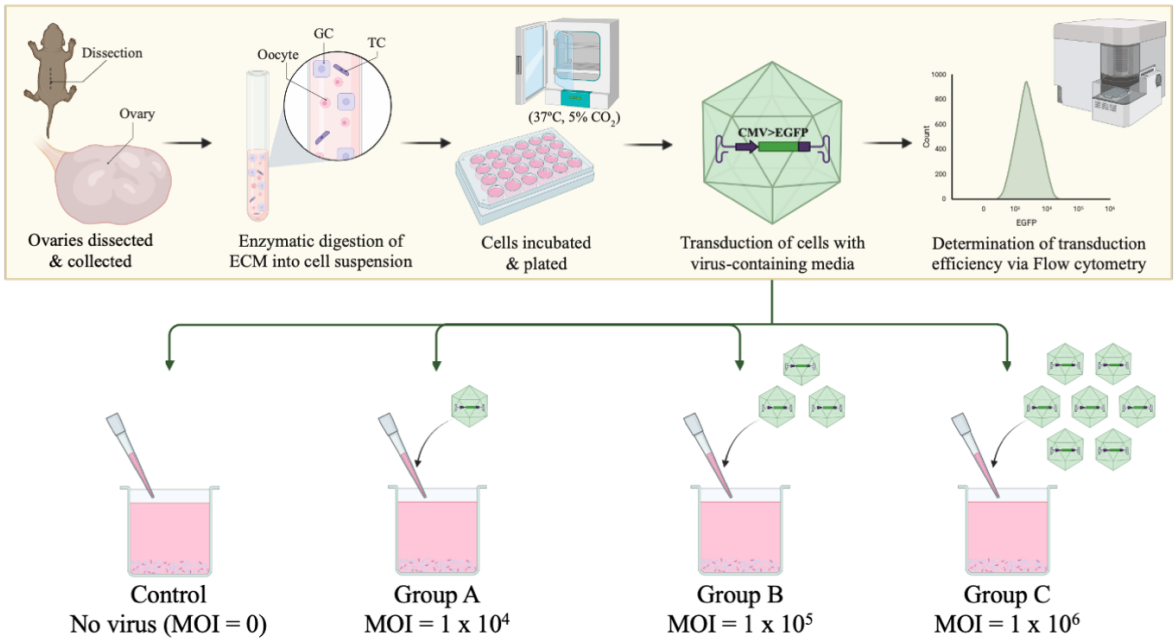

Figure 4.2.3.1) Experimental workflow for determining optimal multiplicity of infection in primary murine ovarian cells. Ovaries were dissected, enzymatically digested to dissociate the ECM into a heterogeneous cell suspension with cell types including GCs, TCs, and oocytes. Following plating and incubation (37ºC;, 5% CO_2), cultures were exposed to AAV-EGFP viral particles at increasing MOIs: control (no virus, MOI = 0), group A (MOI = 1×10^4), group B (MOI = 1×10^5), and group C (MOI = 1×10^6). After incubation, cells were collected and assessed by Flow cytometry (Cytek® Northern Lights Flow cytometer [N7-00021]) to quantify EGFP MFI and proportion of EGFP-expressing cells to determine the optimal MOI. Images are not to scale. Created with BioRender. AAV, adeno-associated virus; CMV, cytomegalovirus; CO_2, carbon dioxide; ECM, extracellular matrix; EGFP, enhanced green fluorescent protein; GC, granulosa cell; MOI, multiplicity of infection; TC, theca cell.

Table 4.2.3.1) Media composition and viral particle volume used to establish multiplicities of infection in primary murine ovarian cells. Summary of media preparation for control and experimental groups during AAV-EGFP transduction. Viral particle volumes corresponding to each MOI were mixed with cell culture media to a total of 500 µL per well prior to incubation. All groups maintained under identical culture conditions.

	Control	A	B	C
MOI, GC per cell	0	1×10^4	1×10^5	1×10^6
Volume of viral particles, µL	0.0	0.5	5.0	50.0
Volume of cell culture media, µL	500.0	499.5	495.0	450.0
Total volume of media, µL	500.0	500.0	500.0	500.0

AAV, adeno-associated virus; EGFP, enhanced green fluorescent protein; GC, genome copies; MOI, multiplicity of infection.

Following incubation, spent media from each well was aspirated and washed once with 500 µL of warmed DPBS. The DPBS was discarded and replaced with 250 µL of warmed Trypsin/EDTA/DNase I. The plate was incubated for 5 min at 37ºC to dislodge adhered cells. The enzymatic digestion reaction was terminated by adding 250 µL of fresh, warmed cell culture media to obtain a heterogeneous cell suspension. Cells from each group were transferred to a separate 15 mL tube. A further 500 µL of cell culture media was added to each well to collect any remaining cells, then transferred to the corresponding tube to prevent any cross over between groups.

4.2.3.2 Co-transduction of AAV-Cas9 and AAV-DS

To assess the transduction efficiency of the designed vectors, ~200,000 viable primary ovarian cells were transferred to a new 35mm TCT petri dish (Figure 4.2.3.3). Each dish was topped up with fresh, warmed cell culture media for a total of 1.5 mL per dish. To promote somatic cell adhesion to the bottom of the dish, cells were left undisturbed to incubate (37ºC, 5% CO_2) for 3–5 hr. Once thawed, the AAV-Cas9 viral aliquot (100 µL; MOI = 1×10^6) was gently mixed to fresh, warm, equilibrated cell culture media. Old, spent medium was aspirated and discarded. The virus-containing media, totalling 1.5 mL, was gently transferred to the TCT petri dish to not disturb the adhered ovarian cells. The control group was replenished with 1.5 mL of fresh cell culture media. Adhered cells were then left to incubate (37ºC, 5% CO_2) for 12 hr.

Following incubation, the thawed AAV-DS viral aliquot (100 µL; MOI = 1×10^6) was gently mixed to fresh, warm, equilibrated cell culture media. The virus-containing media was gently transferred to the TCT petri dish. The control group was replenished with 1.5 mL of fresh cell culture media. Adhered cells from both groups were then left undisturbed for a further 12 hr in an incubator (37ºC, 5% CO_2). Following incubation, spent media (viral and non-viral media) was aspirated, discarded, and replaced with 1.5 mL fresh cell culture media. The cells were left undisturbed to incubate (37ºC, 5% CO_2) for approximately 36 hr.

Following incubation, spent media from each dish was aspirated and washed once with 2 mL of warmed DPBS. The DPBS was discarded, replaced with 2 mL of warmed Trypsin/EDTA/DNase I, and each dish was incubated for 5 min at 37ºC to dislodge adhered cells.

The enzymatic digestion reaction was terminated by adding 1 mL of fresh, warmed cell culture media to obtain a heterozygous cell suspension. Cells from the AAV-Cas9/AAV-DS co-transduced group were transferred to a 15 mL tube. A further 1 mL of cell culture media was added to the original tissue culture dish to collect any remaining cells and transfer the cells to the 15 mL tube. This process was repeated with the control group to a separate 15 mL tube to prevent any cross over between groups.

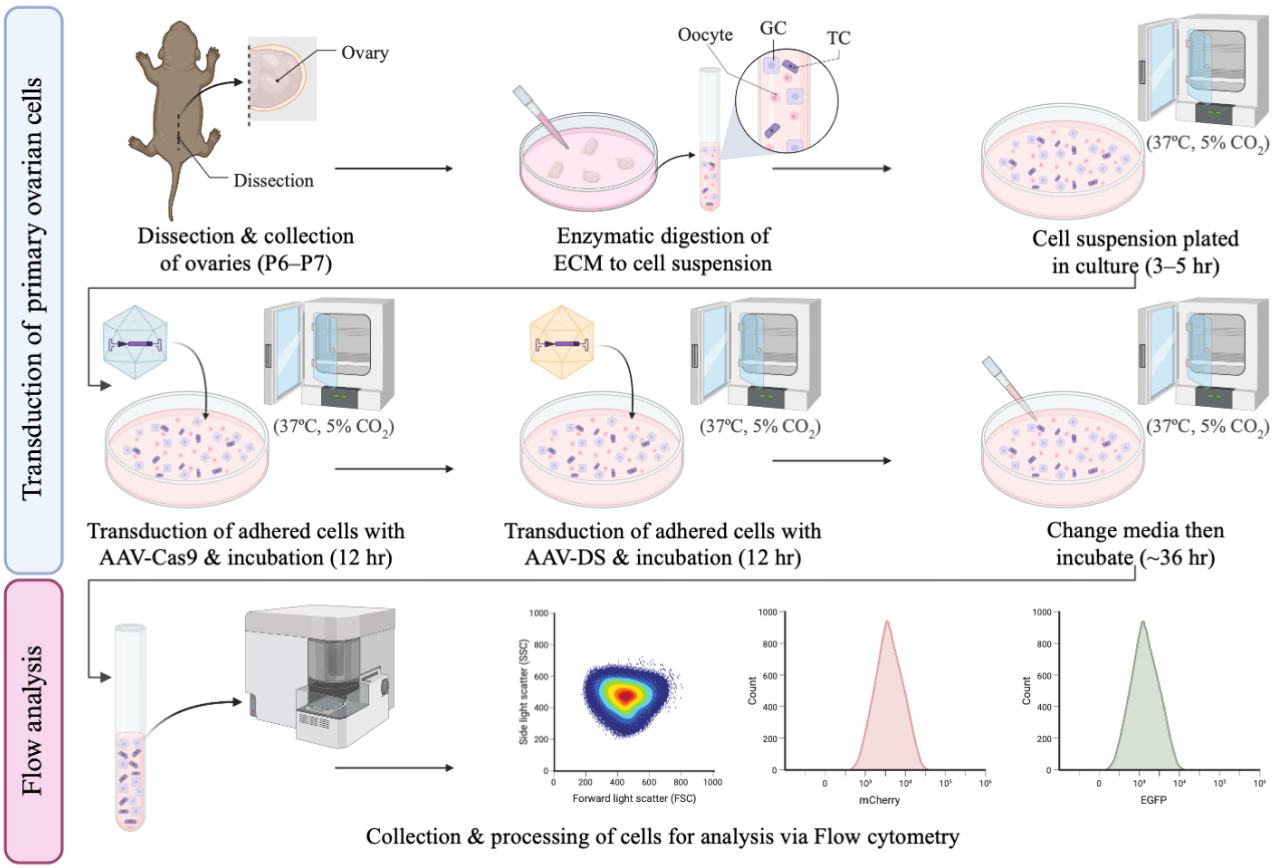

Figure 4.2.3.2) Experimental workflow for assessing transduction efficiency of sequential co-transduction with AAV-Cas9 and AAV-DS in primary murine ovarian cells. Ovaries from P6–P7 mice were dissected and enzymatically digested to dissociate the ECM into a heterogeneous cell suspension containing GCs, TCs, and oocytes. Following plating and incubation (37ºC, 5% CO_2), adhered cells were first transduced with AAV-Cas9 (MOI = 1×10^6) via virus-containing media and incubated for 12 hr. Cells were subsequently transduced with AAV-DS (MOI = 1×10^6) through media change and incubated for a further 12 hr. Media was replaced with fresh, non-virus-containing medium. Cells were further incubated for approximately 36 hr before collection. Transduced cells were processed for Flow cytometric analysis (Cytek® Northern Lights Flow cytometer [N7-00021]) to quantify viability dye, mCherry, and EGFP fluorescence intensity and proportions of positive cells. Images are not to scale. Created with BioRender. AAV, adeno-associated virus; Cas9, CRISPR-associated protein 9; CO_2, carbon dioxide; DS, donor strand; ECM, extracellular matrix; EGFP, enhanced green fluorescent protein; GC, granulosa cell; MOI, multiplicity of infection; P(6/7), postnatal day (6/7); TC, theca cell.

4.2.4 Flow cytometry

To assess transduction of viral vectors and expression of exogenous fluorescent markers in primary murine ovarian cells, Flow cytometry was employed.

4.2.4.1 Sample preparation

The samples underwent temperature-controlled (4ºC) centrifugation (Heraeus Multifuge X3R Centrifuge, Thermo Scientific) at 600 x *g* for 5 min (9 acceleration; 6 deceleration). Following centrifugation, the supernatant was removed, leaving approximately 100 µL of liquid above the pellet. The tube was flicked to re-suspend cells in left over DPBS with 5–10 mL of DPBS added to the tube. Samples completed another round of temperature-controlled centrifugation. The supernatant was removed and discarded after the centrifugation was complete.

4.2.4.2 Cell viability stain

The cells were resuspended with 100 µL of 1:500 Zombie Aqua™ Fixable Viability Kit (lyophilized Zombie Aqua™ dye and anhydrous DMSO; 423101, BioLegend, San Diego, California, USA) in DPBS. Zombie Aqua dye was prepared and stored in accordance to the manufacturer's instructions.

Once resuspended with 1:500 Zombie Aqua in DPBS, cells were removed from light and incubated at RT in atmospheric conditions for 20 min. Following incubation, cells were washed with 2 mL of FACs buffer, comprised of 5% FBS in DPBS. Samples underwent temperature-controlled (4ºC) centrifugation at 600 x *g* for 5 min (9 acceleration; 6 deceleration). The supernatant was removed following centrifugation.

4.2.4.3 Single cell fixation

Samples were fixed with 800 µL of 4% paraformaldehyde in PBS (PFA; SC-281692, Santa Cruz Biotechnology, Dallas, Texas, USA) for 10 mins at 4ºC, then washed and resuspended in 5–10 mL of DPBS before centrifugation. A fourth and final round of temperature-controlled centrifugation was completed with the samples at the same settings as previously recorded (Chapter 4.2.4.1, 4.2.4.2).

The supernatant was removed and discarded following the completion of centrifugation. Samples were resuspended in 300 µL of FACs buffer and transferred to an appropriately labelled, new 12x75mm test tube (Flow tube; 2523749, Beckman Coulter™, Brea, California, USA). Tubes were stored in 4ºC and used within 5 hr of fixation.

4.2.4.4 Flow cytometry use and gating

Flow cytometry was performed using a Cytek® Northern Lights Flow cytometer (N7-00021, Cytek Biosciences, Wuxi City, China) equipped with a 405 nm violet laser, 488 nm blue laser, and 640 nm red laser. Total events recorded with the Flow cytometer ranged from 3,000–10,000 using SpectroFlo® software (v3.3.0; Cytek Biosciences, China). Flow cytometry gating to analyse viable primary murine ovarian cells (EGFP- and/or mCherry-positive) was performed using FlowJo software (v10.10.0; Ashland Oregon, USA). Gating was determined based on exclusion via previously performed control solutions.

4.2.5 Statistical analysis

Statistical analysis was performed using GraphPad Prism (v10.3.1). The Shapiro-Wilk test was used to determine the normality of the data.

For the determination of optimal MOI with AAV-EGFP, differences in viability and transduction efficiency, as determined via proportion of cells and mean fluorescence intensity (MFI; expressed in arbitrary units, shown as AU), were analysed using the two-tailed unpaired t-test with Welch's correction, with p-values interpreted in the context of multiple testing.

For the determination of transduction efficiency following co-transduction of AAV-Cas9 and AAV-DS, cell viability, EGFP expression, and mCherry expression between the control group and viral group (via both MFI and proportion of cells) was analysed using a two-tailed unpaired t-test with Welch's correction.

Data was presented as mean ± SD and significance was defined as $p \leq 0.05$.

4.3 Results

4.3.1 Determination of optimal multiplicity of infection using AAV-EGFP

Before using sequential AAV vectors to induce targeted gene expression, the optimal MOI for primary murine ovarian cells was assessed using AAV-EGFP. Viability and EGFP expression were assessed via Flow cytometry (Figure 4.3.1.1).

The control group (MOI = 0) was not exposed to any viral particles, whilst groups A (MOI = 1×10^4), B (MOI = 1×10^5), and C (MOI = 1×10^6) were exposed to media containing AAV-EGFP. No difference in cell viability was observed between groups via MFI values (control, 24,220 AU ± 3,538 AU; group A, 23,361 AU ± 3,817 AU; group B 22,403 AU ± 3,474 AU; group C, 34,905 AU ± 6,416 AU) (Figure 4.3.1.2A). However, a significantly lower proportion of viable cells was observed in group C (95.5% ± 0.008%) compared to all other groups ([control group, 98.9% ± 0.006%; $p<0.01$]; [group A, 98.1% ± 0.007%; $p<0.05$], [group B, 98.5% ± 0.002%; $p<0.05$]) (Figure 4.3.1.2B).

MFI of EGFP expression was not statistically different between groups (control, 9,945 AU ± 732.1 AU; group A, 9,516 AU ± 1,180 AU; group B, 10,510 AU ± 1,474 AU; group C, 170,622 AU ± 113,474 AU) (Figure 4.3.1.2C). Group C had a larger proportion of EGFP expressing cells (63.7% ± 10.2%) versus other respective groups ([control, 0.3% ± 0.1%; $p<0.01$], [group A, 2.5% ± 1.4%; $p<0.01$], [group B, 15.4% ± 6.7%; $p<0.01$]) (Figure 4.3.1.2D).

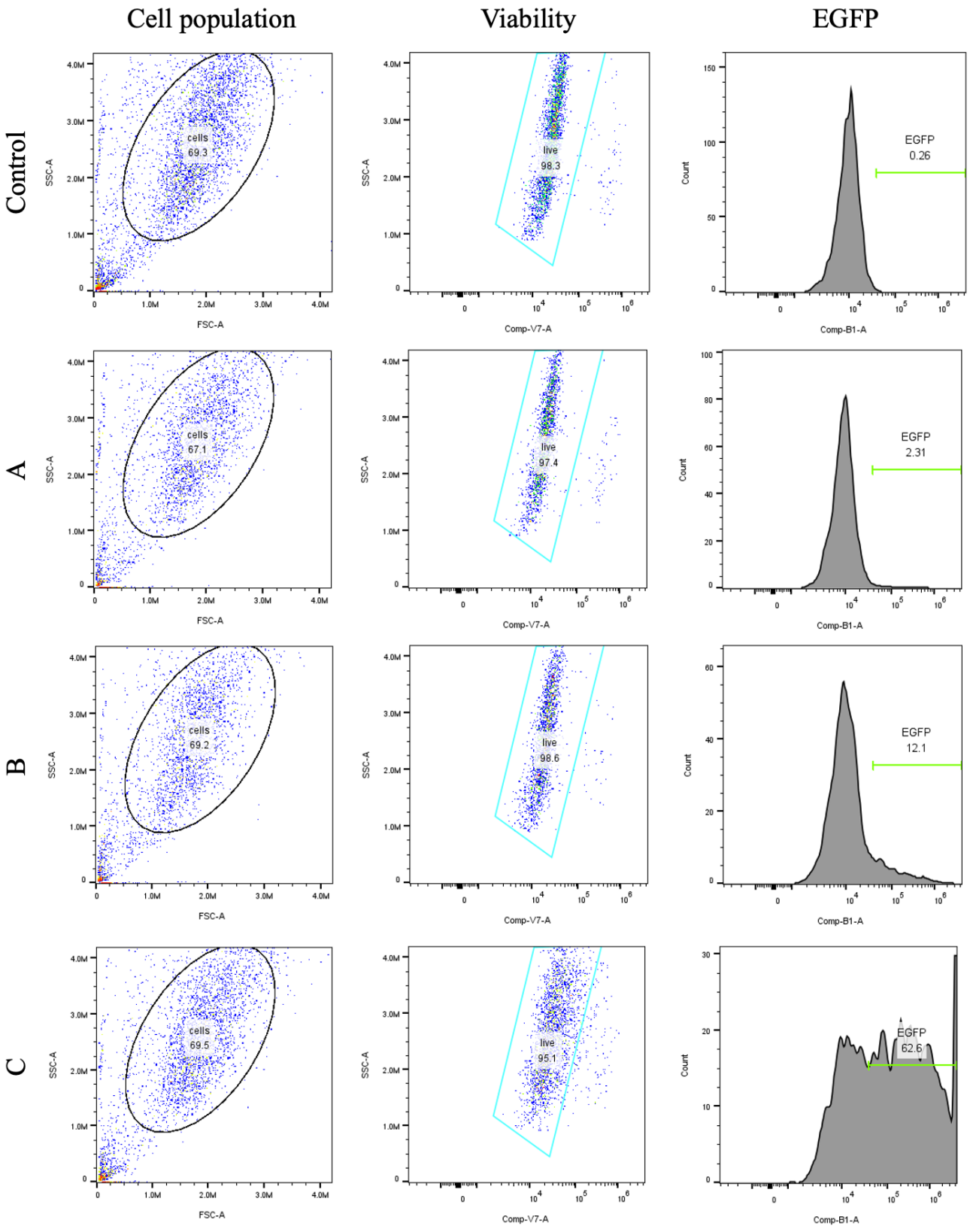

Figure 4.3.1.1) Representative gating strategy and GFP fluorescence profiles for multiplicity of infection optimisation following transduction with AAV-EGFP. Representative Flow cytometry plots from one of three replicates per experimental group: Control (no virus; MOI = 0), group A (MOI = 1×10^4), group B (MOI = 1×10^5), and group C (MOI = 1×10^6). Left panels (Cell population) display the forward and side scatter gating of total primary murine ovarian cell populations (FSC-A versus SSC-A). Middle panels (Viability) show viable-cell gating using exclusion of non-viable events (Comp-V7-A, violet laser, versus SSC-A). Right panels (EGFP) show fluorescence intensity histograms in the EGFP detection channel (Comp-B1-A, blue laser) demonstrating EGFP-positive cells. Gating thresholds were determined from negative controls and applied consistently across all groups. Flow cytometry was performed using a Cytek® Northern Lights Flow cytometer (N7-00021) and analysed using SpectroFlo® software (v3.3.0), with plots generated from FlowJo® software (v10.10.0). AAV, adeno-associated virus; EGFP, enhanced green fluorescent protein; FSC-A, forward scatter area; MOI, multiplicity of infection; SSC-A, side scatter area.

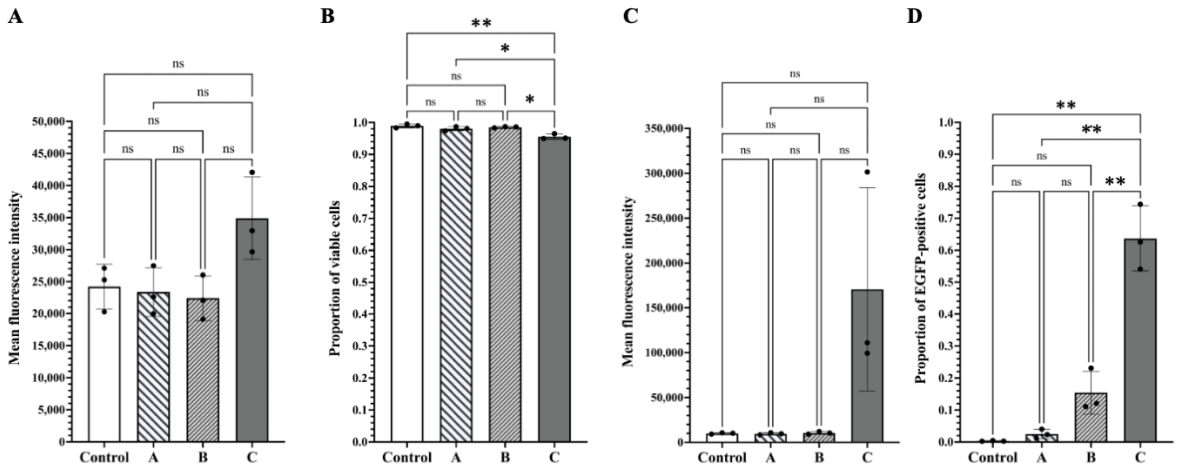

Figure 4.3.1.2) Cell viability and EGFP expression across increasing multiplicities of infection in primary murine ovarian cells. Flow cytometric assessment of primary murine ovarian cells transduced with AAV-EGFP in increasing MOI: control (no virus; MOI = 0), group A (MOI = 1×10^4), group B (MOI = 1×10^5), and group C (MOI = 1×10^6). Each group represents three biological replicates. **A)** MFI of the viability dye and **B)** proportion of viable cells across experimental groups as detected via Comp-V7-A (violet laser). **C)** MFI of EGFP fluorescence and **D)** proportion of EGFP-positive cells across groups as detected via Comp-B1-A (blue laser). Statistical significance was determined using two-tailed unpaired t-tests with Welch's correction. Data are presented as mean ± SD. Flow cytometry was performed using a Cytek® Northern Lights Flow cytometer (N7-00021) with FlowJo® software (v10.10.0). EGFP, enhanced green fluorescent protein; MFI, mean fluorescence intensity; MOI, multiplicity of infection; NS, not significant; SD, standard deviation. *$p\leq0.05$; **$p<0.01$.

4.3.2 Determination of transduction efficiency through fluorescent reporter expression in primary ovarian cells following sequential exposure of AAVs

Primary murine ovarian cells were sequentially co-transduced with AAV-Cas9 (MOI = 1×10^6) then AAV-DS (MOI = 1×10^6) (Figure 4.3.2.1). Cell viability, mCherry expression, and EGFP expression were assessed via Flow cytometry, comparing the transduced group with the unexposed control group. Cell viability was similar between the control and viral groups in terms of MFI (control, 23,507 AU ± 2,966 AU; viral, 36,591 AU ± 10,026 AU) and proportion of viable cells (control, 96.53% ± 1.27%; viral, 94.27% ± 2.23%) (Figure 4.3.2.2A, B).

mCherry expression was significantly greater in the viral group, with MFI of 16,536 AU ± 1,152 AU compared with 9,740 AU ± 577 AU for the control group ($p<0.01$) (Figure 4.3.2.2C). The viral group demonstrated a higher proportion of mCherry-positive cells (32.0% ± 5.1%) versus the control group (1.7% ± 0.5%; $p<0.01$) (Figure 4.3.2.2D). In addition, EGFP expression was significantly increased in the viral group with a MFI of 9,634 AU ± 459 AU compared to 7,871 AU ± 399 AU for the control group ($p<0.01$) (Figure 4.3.2.2E). The proportion of EGFP-positive cells was higher in the viral group than the control group (15.2% ± 4.8% vs. 1.6% ± 0.6%, respectively; $p\leq0.05$) (Figure 4.3.2.2F).

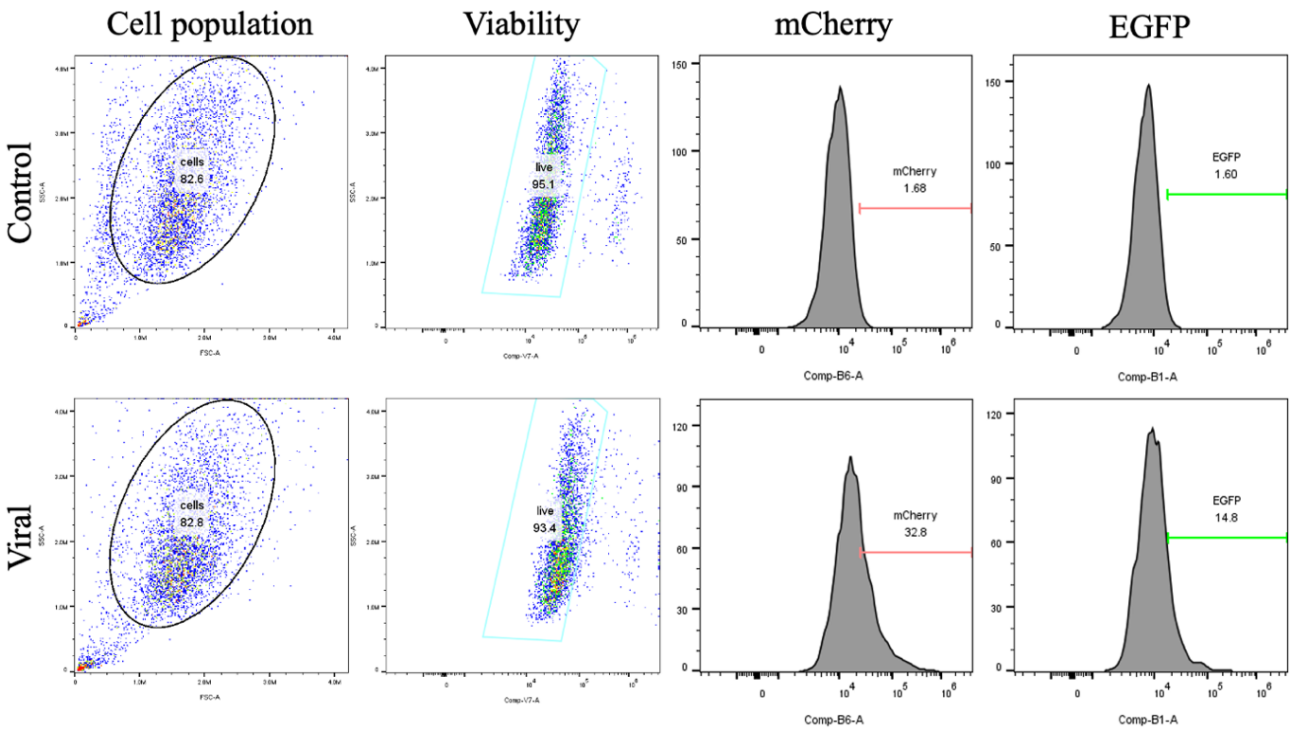

Figure 4.3.2.1) Transduction efficiency in primary murine ovarian cells with AAV-SaCas9 and AAV-DS. Representative Flow cytometry plots from one of three replicates of primary murine ovarian cell suspensions per experimental condition: control (MOI = 0) and viral (co-transduced with AAV-SaCas9 and AAV-DS, each at MOI = 1×10^6). Gating thresholds for viability and fluorescence channels were applied consistently across all samples. Left panels (Cell population) show forward- and side-scatter gating of total ovarian cell populations (FSC-A versus SSC-A). Middle-left panels (Viability) show viable-cell gating based on exclusion of non-viable events (Comp-V7-A versus SSC-A). Middle-right panels (mCherry) and right panels (EGFP) display fluorescence-intensity histograms for mCherry (Comp-B6-A) and EGFP (Comp-B1-A), respectively. Flow cytometry was performed on a Cytek® Northern Lights Flow cytometer (N7-00021) and analysed using SpectroFlo® (v3.3.0), with plots generated in FlowJo® (v10.10.0). AAV, adeno-associated virus; DS, donor strand; EGFP, enhanced green fluorescent protein; FSC-A, forward scatter area; MOI, multiplicity of infection; SSC-A, side scatter area; SV40, simian virus 40.

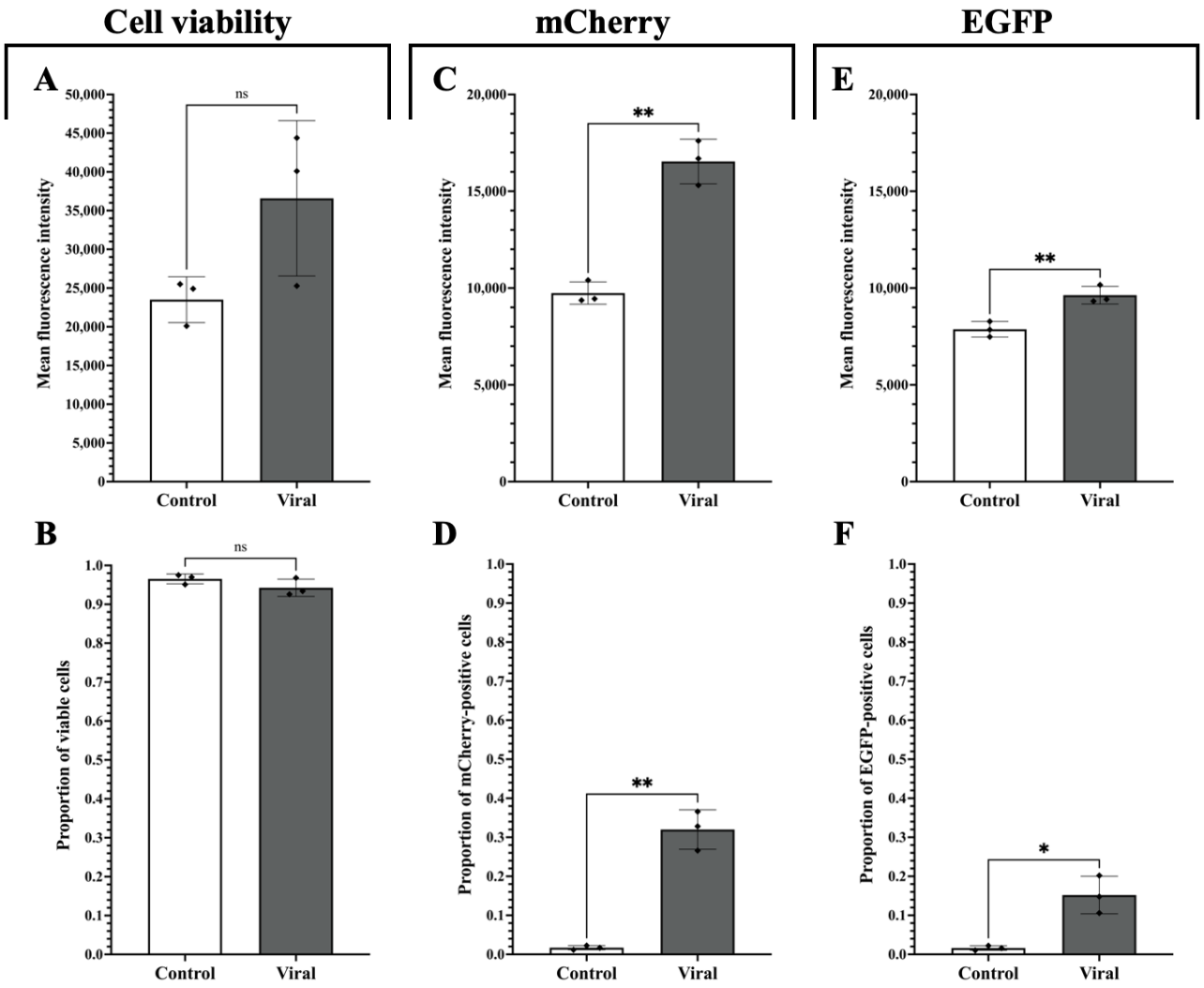

Figure 4.3.2.2) Flow cytometric quantification of cell viability and fluorescent reporter expression following sequential transduction of AAV-Cas9 and AAV-DS. Primary murine ovarian cell suspensions were allocated to control (no virus; MOI = 0) or viral groups (co-transduced with AAV-Cas9 and AAV-DS, each at MOI = 1×10^6). Gating thresholds for viability and fluorescence channels were applied consistently across all samples. Bar groups show quantitative comparisons of MFI and proportion of positive cells for each parameter between control and viral groups. **A)** MFI of the viability dye. **B)** Proportion of viable cells. **C)** MFI of mCherry fluorescence. **D)** Proportion of mCherry-positive cells. **E)** MFI of EGFP fluorescence. **F)** Proportion of EGFP-positive cells. Statistical significance was determined using two-tailed unpaired t-tests with Welch's correction. Data are presented as mean ± SD. Flow cytometry was performed using a Cytek® Northern Lights Flow cytometer (N7-00021) and analysed using SpectroFlo® software (v3.3.0), with plots generated from FlowJo® software (v10.10.0). Unpaired t-test with Welch's correction performed for all analyses. Data are presented as mean ± SD with individual data points overlaid. AAV, adeno-associated virus; Cas9, CRISPR-associated protein 9; DS, donor strand; EGFP, enhanced green fluorescent protein; MFI, mean fluorescence intensity; MOI, multiplicity of infection; NS, not significant; SD, standard deviation. *$p \leq 0.05$; **$p < 0.01$.

4.4 Discussion

The aim of this Chapter was to develop and optimise techniques for AAV-mediated transduction of primary murine ovarian cells *in vitro*. The findings demonstrated the identification of an optimal MOI and successful expression of fluorescent reporters following sequential co-transduction, without substantial compromise to cell viability.

An MOI of 1×10^6 viral particles per cell provided the highest transduction efficiency within the manufacturer's recommended range (MOI: 1×10^4–1×10^6). At time of writing, no published studies had recorded the optimal MOI for the transduction of AAV9s to primary murine ovarian cells *in vitro*. Previous studies have demonstrated that recommended viral titres vary between primary versus immortalised cells (Ellis *et al.*, 2013; Halbert *et al.*, 1995), cell and tissue type (Westhaus *et al.*, 2020), as well as the selected AAV serotype (Ellis *et al.*, 2013; Kanatsu-Shinohara *et al.*, 2022; Westhaus *et al.*, 2020; Yao *et al.*, 2023). Importantly, whilst no significant differences in viability MFI were observed between groups, viral group C demonstrated a higher proportion of EGFP-expressing cells compared to the control group and other viral groups. This result emphasised the importance of optimising MOI to achieve a balance between transduction efficiency and maintenance of cellular integrity, which is a key consideration for applications such as in gene therapy and fertility preservation (Kanatsu-Shinohara *et al.*, 2022; Zwi-Dantsis *et al.*, 2025).

A reduction in proportion of viable cells was observed in the group C compared to other comparators. This is consistent with previous reports indicating that viral transduction can induce cytotoxic effects leading to a reduction of cell viability and an immune response (Arjomandnejad *et al.*, 2023; Dharma *et al.*, 2009; He *et al.*, 2022; Hu *et al.*, 2024). However, the slight reduction of cell viability for a markedly higher transduction rate, suggested that a trade-off is inherent and to be expected. Despite the favourable safety profile, it should be noted that high-dose systemic AAV delivery has been associated with patient fatalities in clinical settings (Duan, 2023; Suoranta *et al.*, 2022). The quantity of available viral particles was a limiting factor for our study with ~10,000 cells seeded per group per

experiment. Future studies should further explore the balance of transduction efficiency and viability in the heterogeneous primary ovarian cells with higher viral titres and in larger population sizes.

AAV vectors were designed to enable the 'knock-in' of the genes in the donor strand via the established CRISPR/Cas9 genome-editing system (Gaj *et al.*, 2017; Ge *et al.*, 2016; He *et al.*, 2022; Mizuno *et al.*, 2018). AAV9 vectors were selected due to their demonstrated efficiency in transducing a range of cell types in both *in vitro* and *in vivo* systems (Armbruster *et al.*, 2016; Pankajakshan *et al.*, 2011; Zincarelli *et al.*, 2008). The Kanatsu-Shinohara *et al.* study (2022) reported that AAV9s could penetrate the FBL, with preference for GCs, without infecting the oocyte. This is an important consideration for future *in vitro* tissue studies wherein the follicle structure remains intact.

The AAV-Cas9 vector encoded for both the Cas9 protein and sgRNA for the mROSA26 locus. The utility of SaCas9 for genome editing across challenging primary cell types has been demonstrated previously in the literature (Ran *et al.*, 2015; Xiao *et al.*, 2019; Zhang *et al.*, 2021). The mROSA26 locus has been used extensively in transgene studies including other gene 'knock-in' experiments (Chu *et al.*, 2016; Soriano, 1999a; Zhang *et al.*, 2021). The mROSA26 locus was selected as a well-characterised safe harbour site for stable transgene expression (Chu *et al.*, 2016; Soriano, 1999b).

The co-delivery of SaCas9 and sgRNA in a single vector simplified and improved efficiency of the transduction process by reducing the number of experimental steps and materials required (Xiao *et al.*, 2019; Zhang *et al.*, 2021). However, the packaging limitations associated with the AAV remained a concern with less flexibility provided compared to dual delivery systems. A single sgRNA design was prioritised to minimise off-target effects, acknowledging that this may limit 'knock-in' efficiency (Cordeiro *et al.*, 2015; Iyer *et al.*, 2020; Jang *et al.*, 2018; Kanatsu-Shinohara *et al.*, 2022; Komatsu *et al.*, 2018). As presented in this chapter, the single-sgRNA approach was prioritised to minimise off-target effects whilst establishing baseline transduction efficiency in primary ovarian cells. The trade-off between 'knock-in' efficiency and genomic safety represents a key consideration for future optimisation, particularly if this system is adapted for potential therapeutic applications. Subsequent

iterations could explore dual-sgRNA designs or alternative genome-editing approaches to enhance precision, such as using base editors to maintain the compact AAV cargo load.

The AAV-DS vector enabled identification of transduced ovarian cells and, more specifically, GCs through the expression of two fluorescent reporter genes. mCherry, a bright red monomeric fluorescent protein widely used in ovarian and follicle research (Cordeiro *et al.*, 2015; Komatsu *et al.*, 2018; Iyer *et al.*, 2020; Kanatsu-Shinohara *et al.*, 2022), was driven by the ubiquitous SFFV promoter (402 bp) and served as an indicator of overall transduction efficiency.

The last major component of the AAV-DS construct surrounded the desired gene insertion with homology arm sequences that flanked the mROSA26 cleavage site to facilitate homology-directed repair. Whilst CRISPR/Cas9-mediated HDR can support targeted insertion, its efficiency is inherently limited (Ahmadi *et al.*, 2023; Liao *et al.*, 2024). However, this limitation is most prevalent in non-dividing cells with the follicular cells of interest, GCs, differentiate during follicle development (Niu and Spradling, 2020; Shao *et al.*, 2022).

Flow cytometry analysis demonstrated successful transduction of primary murine ovarian cells with AAV-Cas9 and AAV-DS vectors at an MOI of 1×10^6, evidenced by significant mCherry and EGFP expression in the viral group. Cell viability, assessed by MFI and proportion of viable cells, remained comparable between control and viral groups, indicating that the transduction process did not cause substantial cytotoxicity. These results suggest that the AAV vectors used were effective in delivering the desired genetic material without compromising cell viability, which is particularly important for live *in vitro* tissue and *in vivo* models.

A major finding of this study was the significant increase in the proportion of mCherry- and EGFP-expressing cells in the viral group compared with the control group. mCherry expression, used as an indicator for transduction efficiency, had a significantly higher proportion of mCherry-positive cells in the viral group (32.00% ± 5.05%) compared with the control group (1.7% ± 0.5%). In a study by Muhuri *et al.* (2022), GFP expression of iPSCs (measured by relative fluorescent units) was found to

be greater 96 hrs following AAV9-GFP transduction (MOI = 1×10^6) than 48 hrs. Thus, maximum levels of MFI may not have been reached at the point of assessment in this study.

It is important to contextualise that total (100%) transduction efficiency with AAV-mediated gene delivery in primary cells is neither expected nor necessarily desirable. Unlike lentiviruses or adenoviral vectors, AAVs demonstrate more modest infection rates in exchange for reduced cytotoxicity and immunogenicity (Ellis *et al.*, 2013; Zincarelli *et al.*, 2008). Whilst increasing viral titre can improve transgene expression, excessive MOI can induce apoptosis and cellular dysregulation (Dan and Kang-Zheng, 2025). The slight reduction in viability observed with group C (MOI = 1×10^6) in this Chapter may support this understanding. In immortalised cell lines, higher transduction rates are more achievable and demonstrate improved cellular resilience, but primary ovarian cells require more conservative optimisation to preserve mechanical and functional integrity (Ellis *et al.*, 2013; Halbert *et al.*, 1995).

mCherry signal may indicate successful delivery and potential genomic integration (Ahmadi *et al.*, 2023). However, it is possible that transgenic expression is present without genomic-editing. AAV-delivered DNA may persist as episomal elements rather than integrating into the host genome, meaning transgene expression may be transient, particularly in dividing cells (Muhuri *et al.*, 2022; Wang, Gessler, *et al.*, 2024).

EGFP expression was increased in the viral group compared with controls (15.2% ± 4.8% vs. 1.6% ± 0.6%; $p<0.05$). Notably, the proportion of EGFP-positive cells was numerically lower than mCherry-positive cells (32.0% ± 5.1%) which supports conditionality of the mAMH promoter driving EGFP versus the ubiquitous SFFV promoter driving mCherry. These findings suggest successful delivery and expression of the follicular cell-specific marker, with integration remaining to be confirmed. Furthermore, these results align with previous studies demonstrating the successful application of AAV vectors in primary cells, particularly in the context of transgene expression and gene-editing (Kanatsu-Shinohara *et al.*, 2022; Ran *et al.*, 2015). Future studies to confirm genome

integration, for example via qPCR (quantitative polymerase chain reaction), would be useful to confirm both transgene integration and comparative mAMH expression at a pre-determined timepoint. However, this was out of the scope of the current study.

It was observed that approximately 15% of cells expressed EGFP, representing roughly half the proportion of mCherry-positive cells. This difference is consistent with the expected behaviour of a cell-type-specific reporter within a heterogeneous primary cell population, rather than indicating a technical artefact.

First, the primary ovarian cell suspension was enriched for somatic cells, including GCs, following enzymatic digestion and differential adhesion, which selectively removed ECM components, oocytes, and non-adherent or non-viable cells. Given that P6 murine ovaries contain a measurable proportion of growing follicles (~15% primary and more advanced stages; Chapter 3), the adhered population subjected to transduction would be expected to include a considerable fraction of AMH-expressing GCs. As AMH expression is restricted to growing follicles, this enrichment would increase the baseline proportion of cells capable of driving EGFP expression under the mAMH promoter.

Second, AAV9 vectors have been reported to preferentially transduce GCs within ovarian tissue (Kanatsu-Shinohara *et al.*, 2022). This tropism would result in enrichment mCherry-positive cells within GC populations relative to the broader heterogeneous cell population. Consequently, a subset of transduced cells would be expected to co-express EGFP in a manner consistent with the proportion of AMH-expressing GCs, explaining why EGFP-positive cells comprised a substantial, but lower, fraction of the total mCherry-positive population.

Third, endogenous autofluorescence in primary murine cells, particularly in the blue-green spectrum, may contribute to low-level background signal in the EGFP detection channel (Baek *et al.*, 2025; Barroso *et al.*, 2023; Dittmar *et al.*, 2011; Hickey *et al.*, 2022). Although gating thresholds were established using control samples, the possibility of minor false positive events cannot be excluded, which may modestly inflate the apparent proportion of EGFP-positive cells.

Finally, it is recognised that *in vitro* culture and viral transduction may perturb oocyte–GC signalling dynamics (Eppig, 1991; Gilchrist *et al.*, 2004; Haery *et al.*, 2019; Sheikh *et al.*, 2023), potentially influencing AMH expression and downstream reporter activity. These factors, alone or in combination, support the interpretation that the observed proportion of EGFP-positive cells reflects the biological characteristics of the experimental system, despite differing from *in vivo* expectations.

In conclusion, this chapter demonstrated successful AAV-mediated gene delivery to primary murine ovarian cells *in vitro*, with significant mCherry and EGFP expression in the viral group. The optimisation of MOI was found to strike a balance between the achievement of detectable transduction and maintenance of cell viability which is crucial for research and therapeutic applications in mammalian ovarian cells. These results contribute to the development of efficient *in vitro* models for ovarian follicle research, where real-time monitoring of gene expression is essential. These findings also lay the groundwork for future experiments aimed at enhancing transduction efficiency in larger ovarian cell populations and exploring the long-term effects of transduction in primary cells. Furthermore, the results described in this Chapter provided the foundation for the FolliTracker methodology explored in Chapter 5, demonstrating immediate translational value.

5. IMPLEMENTATION AND EVALUATION OF FOLLITRACKER FOR LIVE MONITORING OF FOLLICLE DEVELOPMENT IN TISSUE CULTURE

5.1 Introduction

5.1.1 Background

In Chapter 3, follicle quantification and staging in ovarian tissues relied on the static, terminal histological analysis which required the sacrifice of individual ROs, ROEx, and WOs at each assessed timepoint. Histological-based assessment revealed that follicle stage distribution shifted over time; primordial follicles declined, whilst the proportion of transitional and primary follicles increased in culture. However, these findings are snapshots of different sample populations without continuous data and inferred follicle growth trajectories.

Traditional approaches to early follicle assessment have relied primarily on fixed-tissue histology, where follicles are analysed from single two-dimensional sections, often selected on the basis of capturing the oocyte nucleus (Conchello and Lichtman, 2005; Harrison *et al.*, 2025; Soygur and Laird, 2021). While this has been indispensable for staging and morphological assessment, it imposes fundamental constraints; follicle architecture is inherently three-dimensional, histological processing can induce artefacts, and development must be inferred from static snapshots (Harrison *et al.*, 2025). As demonstrated in published studies, fixation of tissue and two-dimensional analysis can result in

misclassification of follicle stage, inaccurate quantification of GCs, and morphological artefacts (Adeniran *et al.*, 2021; Harrison *et al.*, 2025; Uslu *et al.*, 2017). Even in optimally processed tissue, subtle changes in somatic organisation and oocyte-granulosa spacing can be challenging to interpret without dynamic context (Harrison *et al.*, 2025). Together, these issues highlight the need for methodologies capable of observing follicles within tissue in real time that preserve both structure and function.

Advances in tissue clearing and whole-mount imaging have extended the depth at which ovarian tissue can be visualised to reveal structures, such as complex stromal networks and intact pre-antral follicles in three dimensions (Faire *et al.*, 2015; Feng *et al.*, 2017; Harrison *et al.*, 2025; Kagami *et al.*, 2018; McKey *et al.*, 2020; Rinaldi *et al.*, 2018). However, these techniques remain terminal; although they improve spatial resolution, they cannot capture follicle growth trajectories, temporal changes in GC organisation, or the changes of follicle-stroma interactions. Moreover, Chapter 3 established that follicle morphology and developmental dynamics can diverge markedly between *in vivo* tissue and *in vitro* RO models, further emphasising the need for live data readouts. The present chapter aims to address these limitations by introducing FolliTracker, an integrated experimental–analytical workflow for longitudinal tracking of follicles in intact tissues using live imaging and computational analysis.

The development of FolliTracker was largely built upon the technical foundation established in Chapter 4. Sequential AAV-mediated co-transduction (MOI of 1×10^6 for both vectors) achieved ~32% mCherry and 15% mAMH-driven EGFP expression in the adhered cell population following enzymatic digestion of primary murine ovarian cells (Chapter 4.3). The minimal reduction in cell viability demonstrated that transduction at the selected MOI (1×10^6) could be achieved without significant cytotoxicity, thereby establishing that virally delivered fluorescent markers were tolerated by primary murine ovarian cells. However, the Chapter 3 and Chapter 4 experiments were conducted over a maximum of 7 days and 72 hr, respectively. The present chapter extends this work by

investigating the transduction, viability, and follicular dynamics within intact transduced RO tissues over a 14-day culture period.

The rationale for FolliTracker relied on two key methodological requirements. First, labelled cells must remain viable and structurally competent throughout imaging. Confocal microscopy can introduce phototoxicity and thermal load (Oreopoulos *et al.*, 2014). Imaging intervals, z-stack pitch, excitation intensity, and fluorophore selection therefore required careful consideration to preserve physiological relevance. Second, early follicles occupy a complex three-dimensional microenvironment within ROs. As follicles grow, they morphologically change and cells differentiate which can introduce differential autofluorescence and scattering.

To address these challenges, the FolliTracker workflow integrates three components: 1) live spinning-disc confocal imaging of fluorescently labelled cells within ROs; 2) computational segmentation and quantification of follicle units across time; and 3) AAV-mediated fluorescent reporter delivery necessary to support this workflow. The computational layer focused on reproducibility and interpretability, as opposed to high-complexity modelling. Segmentation was performed on z-stack images semi-autonomously, using a combination of intensity thresholding, morphological operations, and connectivity criteria to extract follicles from within defined tissue boundaries.

By enabling repeated imaging of the same RO tissues and, thus, follicles over time, FolliTracker captured developmental kinetics rather than static morphology. This addresses the practical limitation that conventional histology and IHC cannot track the follicles in tissue across multiple timepoints.

More broadly, dynamic follicle monitoring has implications for fertility preservation, toxicology, and reproductive endocrinology; however, these are beyond the scope of this chapter. Understanding the temporal profile of follicle activation is essential for evaluating the effects of chemotherapeutic agents, ovarian cryopreservation protocols, and *in vitro* follicle maturation systems. Although these applications are not tested here, they highlight the motivation for live-imaging approaches that are not static but repeatable.

FolliTracker is not intended to replace histological quantification, but to provide a complementary, non-static readout of follicular data within intact tissue. As such, concordance between methods is expected in selected measures, such as volumetric assessment. Initial thresholds have been applied to gather absolute follicle counts with FolliTracker; however, the sampling principles are fundamentally different between FolliTracker and histology-based methodologies. This chapter established a practical workflow for repeated, dynamic imaging of follicles within intact ROs over 14 days in culture. FolliTracker supported the measurement of follicle-associated signals in tissues.

5.1.2 Chapter aims

It was hypothesised that AAV-mediated fluorescent labelling combined with live confocal imaging would enable longitudinal identification and quantification of developing follicles within intact RO tissues, and that this approach would produce biologically meaningful outputs that correlated with conventional histology-based measures for selected parameters, while highlighting methodological differences in follicle detection.

The aim of this Chapter was to establish and evaluate FolliTracker as a live-imaging and computational workflow for monitoring follicle development *in vitro*, and to determine whether this approach could provide reliable, repeatable, and biologically relevant measurements while preserving tissue integrity and follicular development.

To address this aim, the following objectives were defined:

- To implement the FolliTracker workflow for longitudinal live imaging and segmentation of follicles within intact RO tissues
- To assess the ability of FolliTracker to detect and quantify follicle-associated signals across culture timepoints

- To evaluate concordance between FolliTracker-derived outputs and conventional histology/IHC measurements, particularly for tissue volume and mCherry-associated metrics
- To determine whether AAV-mediated fluorescent labelling affected follicle number, developmental stage distribution, and morphological parameters
- To examine relationships between fluorescence signal (mCherry/EGFP) and follicle detection to assess factors influencing methodological agreement
- To identify technical limitations and key areas for optimisation across the transduction, imaging, and computational analysis pipeline

Together, these objectives were designed to determine the feasibility, validity, and limitations of FolliTracker as a method for dynamic follicle tracking *in vitro*, and to define its role as a complementary tool to conventional histological assessment.

5.2 Methodology

5.2.1 Murine ovary dissociation

F1 pups (C57BL/6 x CD-1) at P6–P7 were cervically dislocated and their ovaries isolated (Chapter 2.3). Dissected ovaries underwent enzymatic digestion into a heterogeneous cell suspension. Cell number and viability via an automated cell counter (Chapter 2.5).

5.2.2 Viral vectors

All AAVs were produced and packaged by VectorBuilder (Chicago, Illinois, USA) and stored at -80ºC until required. The two recombinant constructs utilised in this study were designed primarily by me, with review and consultation from Dr Christian Babbs (MRC Weatherall Institute of Molecular Medicine, University of Oxford, UK), as discussed in Chapter 4.

5.2.2.1 AAV9-Cas9

The AAV-Cas9 vector (VB231004-1799hyg, VectorBuilder) encoded SaCas9 under the control of the EFS promoter, together with a U6-driven sgRNA targeting the murine ROSA26 locus. The vector carried a total titre of approximately 2×10^{12} GC/mL. This construct was designed to enable site-specific cleavage at the ROSA26 safe-harbour site to facilitate precise donor-strand integration.

5.2.2.2 AAV-Donor Strand

The donor-strand vector (VB231004-1797awt, VectorBuilder) contained homologous arms flanking the ROSA26 integration site. Two independent fluorescent marker cassettes were incorporated, including EGFP, driven by the -180 bp *mAMH* promoter for GC-specific expression, as described previously in Chapter 4.2.2 (Arango *et al.*, 1999; Bristol-Gould *et al.*, 2005). The second fluorescent marker was mCherry, driven by the SFFV promoter for ubiquitous labelling of transduced cells. The donor strand construct also had a viral titre of approximately 2×10^{12} GC/mL. Together, with AAV-Cas9, this vector supported ubiquitous and follicular cell-targeted fluorescent expression of primary murine ovarian cells.

5.2.3 Transduction of primary ovarian cells

The MOI (1×10^6 GC/cell) used for this study was determined in Chapter 4.3. Primary murine ovarian cells were prepared with ~200,000 viable cells seeded onto 35 mm TCT dishes in 1.5 mL of pre-warmed cell culture medium (Figure 5.2.4). Cultured cells were incubated at 37ºC with 5% CO_2 for 3–5 hr to support differential adhesion.

Following incubation, the non-adherent cell population (containing germ cells) was gently transferred into a new dish containing fresh pre-equilibrated medium. The remaining adherent somatic cell population received 1.5 mL of fresh medium containing thawed AAV-SaCas9 virus. Viral aliquots were thawed at 4ºC for at least 1 hr before use and mixed gently with cell culture medium immediately prior to addition. The control group received an equal volume of non-viral medium. All dishes were swirled gently to ensure even coverage and returned to the incubator, undisturbed for 12 hr.

This process was then repeated. Spent medium was aspired and discarded after the incubation period. The original non-adhered cell population was again transferred to a new dish containing fresh medium. The original adherent cell population was replenished with medium containing AAV-DS. The control group received non-viral medium. All cultures were maintained under identical conditions for a further 12 hr. This two-stage approach promoted sequential exposure to AAV-SaCas9 and AAV-DS vectors for adhered cells, whilst non-adhered cells were not exposed to AAVs.

5.2.4 Reaggregated ovary generation

After completion of the final incubation step, all cell populations were prepared for RO generation, as previously described (Chapter 2.4). In brief, spent media from the adherent somatic cell population was discarded and washed twice. Adherent population were incubated for 5 min in Trypsin/EDTA to dislodge cells into a floating cell suspension. Once neutralised with 2 mL of cell culture media, the somatic cell population was transferred to a new PET tube. Following the collection of the non-adherent germ cell population into a new PET tube supplemented with fresh media, both tubes underwent centrifugation at 663 x *g* for 5 min.

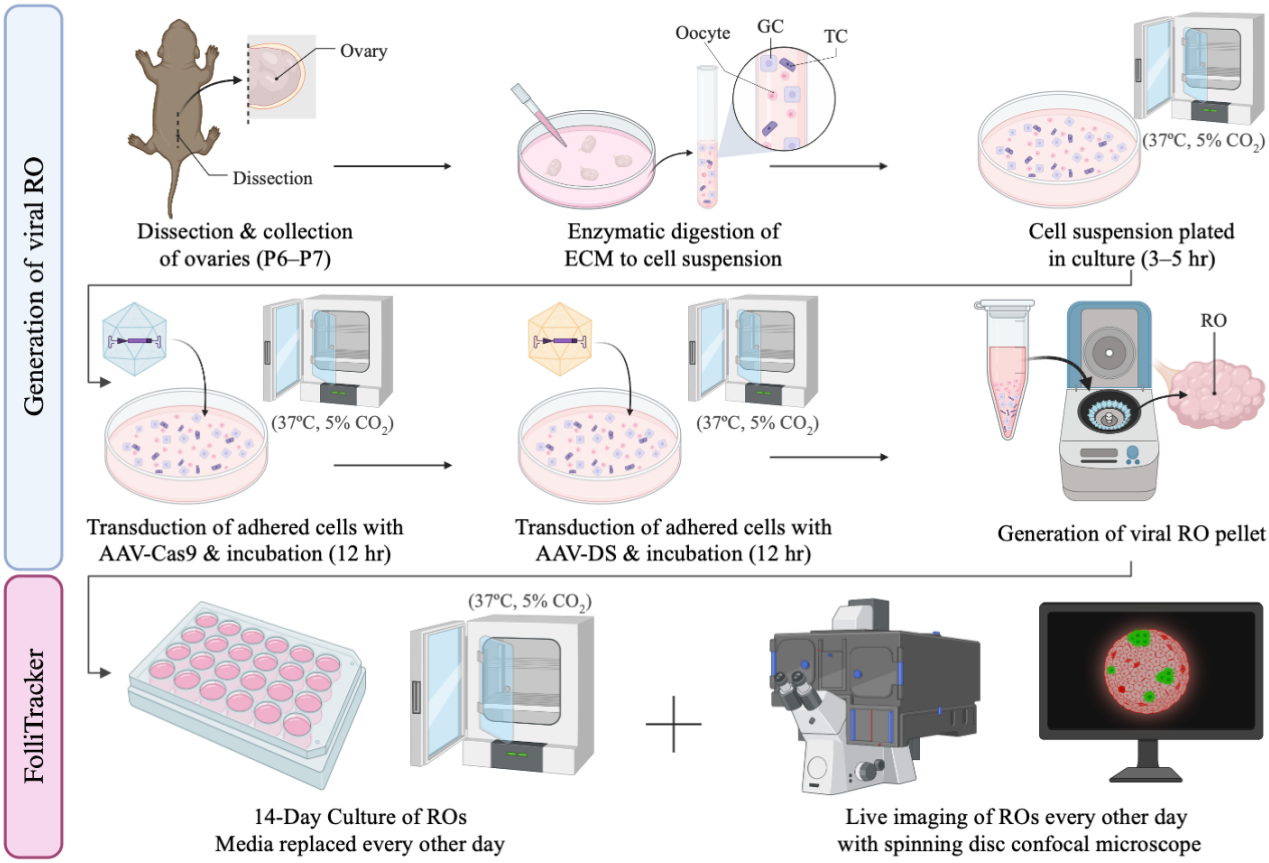

Figure 5.2.4) Experimental workflow for generating viral reaggregated ovaries and accompanying live-imaging analysis using FolliTracker. Ovaries from dissected P6–P7 mice and enzymatically digested to dissociate ECM, resulting in a heterogeneous suspension of primary ovarian cells including GCs, TC, and oocytes. The dissociated cells were plated onto TCT dishes and incubated for 3–5 hr to promote differential cell adhesion. Non-adherent cells, including oocytes, are removed prior to viral exposure; however, complete removal is not always achieved during the differential adhesion process, and some non-adherent cells may persist or loosely associated somatic cells may be dislodged. Adhered somatic cells were first transduced with AAV-Cas9 (MOI = 1×10^6) and incubated for 12 hr, followed by a second transduction with AAV-DS (MOI = 1×10^6) and a further 12 hr incubation under identical conditions. After the final incubation, the transduced somatic and non-adhered germ cell populations were recombined at a 2:1 ratio with L-PHA (35 µg/mL) to promote aggregation and centrifuged to form viral RO pellets. Viral ROs were cultured for 14 days on Transwell® membranes with media replaced every other day. Live imaging was conducted every second day and the midpoint of culture via the Olympus SpinSR SoRa spinning-disc confocal microscopy (Olympus Corporation) to monitor follicle growth in real time. All incubation steps were performed at 37ºC (5% CO_2). Images are not to scale. Created with BioRender. AAV, adeno-associated virus; Cas9, CRISPR-associated protein 9; CO_2, carbon dioxide; DS, donor strand; ECM, extracellular matrix; GC, granulosa cell; L-PHA, Phaseolus vulgaris lectin; MOI, multiplicity of infection; P(6/7), postnatal day (6/7); RO, reaggregated ovary; TC, theca cell; TCT, tissue-culture-treated.

Consistent with (Chapter 2.4), the supernatant was discarded with the somatic and germ cell fractions then resuspended together in a microfuge tube at a 2:1 ratio with 35 µg/mL L-PHA to promote aggregation. The cell mixture was gently pipetted to ensure homogeneity then centrifuged at 10,000 x *g* for 30 sec. Next, the tube was rotated 180º and centrifuged at 10,000 x *g* for an additional 30 sec to form a pellet, herein referred to as an RO. A well was filled with 600 µL of Waymouth/10%MS media of a glass-bottomed 24-well plate (µ-Plate 24-well ibiTreat, ibidi GmbH, Gräfelfing, Germany) to enable optical access for imaging. Each RO was transferred onto a Transwell membrane (0.4 µm pore polyester insert, Corning) in a single well with enough media (100–200 µL) to cover the pellet. The ROs were incubated overnight, as previously described (Chapter 2.4).

5.2.5 Reaggregated ovary culture and maintenance

ROs were cultured as described previously (Chapter 2.6) with adaptations to support live imaging. On day 0 (D0) of culture, medium was replaced with fresh Waymouth/5%MS in sterile conditions. Waymouth/5%MS media was used for the remainder of the 14-day culture period, with media replaced every other day prior to imaging. When media was to be changed, ROs were carefully removed from the Transwell insert, placed in a new well with 600 µL of fresh media mixed with 4 µmol SiR-DNA stain (SC007; Spirochrome Ltd, Stein am Rhein, Switzerland), and incubated (37ºC, 5% CO_2) for 1–2 hr prior to confocal imaging. SiR-DNA was used as a live nuclear counterstain to permit consistent volumetric segmentation of intact RO tissues across culture timepoints, without spectral overlap with EGFP or mCherry signals.

Once imaging was completed, each RO was transferred to a new Transwell membrane and placed in the existing well. Approximately, 100–200 µL of media was supplemented on top of the membrane, as needed, to ensure RO coverage. On D7 and D14 of culture, the samples were removed from the Transwell membrane and incubated with SiR-DNA for imaging but culture media was not replaced.

5.2.6 Histological processing

The histological processing of ROs was executed as reported in Chapter 2.7 or modified; fixed ovarian tissues were transferred into 70% EtOH and then embedded in Histogel (Epredia™ HistoGel™ Specimen Processing Gel, HG-4000-012, Fisher Scientific) to encapsulate and suspend the small RO tissues for easier handling and processing. The tissues were dehydrated in a graded series of EtOH, cleared in xylene, and embedded in paraffin wax with assistance from the Histology Facility, Kennedy Institute of Rheumatology, University of Oxford.

Individual ROs were tracked across experimental batches and analytical modalities to enable direct within-sample comparison between methods. Due to tissue size and processing constraints, not all ROs could be assessed across all modalities. Detailed batch identifiers and RO-level inclusion/exclusion information is provided in Appendix II (Table AII.5.2.6).

5.2.7 Histological staining

To visualise RO tissue for determination of follicle classification, number, and other follicular-related measurements, tissues were stained with haematoxylin (Gills #2 haematoxylin, Sigma-Aldrich) and eosin in accordance with the protocol in Chapter 2.8.

5.2.8 Histological ovarian assessment

Histological evaluation of D14 ROs was undertaken to assess overall tissue morphology, volume, and follicular parameters. Analyses were conducted using H&E-stained sections, with all image processing and measurements performed using ImageJ (v2.1.0/1.53c; National Institutes of Health, USA). All assessments were completed whilst blind to experimental group.

Where applicable, stitched image montages were generated using the pairwise-stitching plugin (Preibisch *et al.*, 2009) to ensure complete reconstruction of each RO at 20x magnification. RO tissue volume and other morphometric parameters were assessed as previously described (Chapter 2.9).

5.2.9 Molecular analysis

IHC assessment was undertaken on fixed sections from D14 ROs to assess mCherry and AMH signal. Sections used for IHC were derived from the same RO tissues analysed histologically, with non-H&E serial sections processed in parallel to preserve spatial and morphological integrity. Tissue sections from ROs were processed for IHC, with protocols conducted as described in Chapter 2.10.

In brief, sections were deparaffinised, rehydrated, and underwent antigen retrieval using either Tris-based unmasking solution (pH 9.0; Vector Laboratories, H-3301) for anti-AMH or citrate buffer (pH 6.0; Vector Laboratories; H-3300) for anti-mCherry. Endogenous peroxidase activity was quenched using 0.3% H_2O_2, and non-specific binding was blocked for 1 hr at RT in PBST with 5% NGS (Vector Laboratories, S-1000).

Primary antibodies were applied overnight at 4ºC: anti-AMH (1:500; rabbit mAb, ab27221, Abcam) and anti-mCherry (1:100; rabbit mAb, ab213511, Abcam). The secondary antibody for both was goat anti-rabbit IgG (Vectastain ABC Elite Kit, PK-6101, Vector Laboratories) and applied at 1:200 for 1 hr at RT, followed by DAB detection and haematoxylin counterstain for visualisation of the nucleus. Negative controls were present on the adjacent section with the primary antibody replaced with blocking solution. Wild type P13 mouse ovarian sections acted as the positive control for anti-AMH.

EGFP immunostaining was attempted but omitted from analysis due to non-specific and inconsistent antibody binding.

Quantification of DAB signal was performed as previously described in Chapter 2.10.3. One control section from experiment E3 displayed artefactual background staining and was handled via sensitivity analysis, as detailed in Appendix II.

5.2.10 Imaging

5.2.10.1 Spinning-disc confocal imaging

High-resolution live imaging of ROs was performed using the Olympus SpinSR SoRa spinning-disc confocal microscopy (Olympus Corporation) with images acquired using a semi-automated acquisition software from CellSens (Olympus Corporation), as described in Chapter 2.11.1.

5.2.10.2 Brightfield microscopy

Dissection of ovarian tissue was performed under the M125 stereomicroscope (Leica Microsystems) with a Lumenera 5-3 camera (Teledyne Vision Solutions, Birmingham, UK) using Infinity Analyse software (Teledyne Vision Solutions), as described previously (Chapter 2.11.2).

Imaging of sectioned tissues following H&E staining or DAB chromogen was performed using a Leica DM2500 microscope (Leica Microsystems) equipped with the Lumenera Infinity 5 camera via the same software (Chapter 2.11.2). Light intensity and exposure were adjusted as appropriate within each imaging session.

5.2.11 FolliTracker image processing and quantitative analysis

FolliTracker refers to the combined workflow of live imaging and computational segmentation/quantification. Arivis Vision4D (Arivis AG, Germany) on the Helios-Titan workstation was used as the computational environment for implementing the segmentation and quantification workflow at the Cellular Imaging Core (Centre for Human Genetics, University of Oxford). Z-stack datasets were exported from CellSens with brightness standardised to support cross-sample review.

Tissue volumes were defined from the SiR-DNA channel during segmentation. Tissue volumes were generated semi-autonomously using the Arivis machine-learning segmentation tool and manually reviewed to remove artefacts. As histology and FolliTracker sample different representations of follicles (terminal section-based inference versus live signal detection), absolute agreement in follicle number is not expected during initial results. Instead, agreement in tissue-scale metrics and directional trends was used as the primary indicator of methodological validity.

A global intensity threshold of 550 AU was applied to identify mCherry-positive regions within the tissue. EGFP signal overlapping mCherry of $\geq$150 μm was classified as a 'follicle'. Quantitative metrics, including tissue and mCherry-positive volume, were exported as CSV files for analysis.

5.2.12 Statistical analysis

Statistical analyses were performed using GraphPad Prism (v10.3.1). Data normality was assessed using the Shapiro–Wilk test to determine whether parametric or non-parametric methods were used.

Differences in mean follicle number across assessed culture timepoints (D7–14) and between experimental conditions (control versus viral) were evaluated by two-way ANOVA and multiple t-tests. The effects of experimental condition, culture duration, and individual RO variability on mCherry signal volume, proportion of mCherry-positive tissue, and total tissue volume were assessed using two-way ANOVA, with multiple t-tests where appropriate. For multiple comparisons, *p*-values were adjusted using the Holm-Šídák method, and adjusted *p*-values (adj. *p*) are reported.

Comparisons of follicle and oocyte areas, AMH-positive follicle proportion, and AMH normalised DAB intensity between groups were analysed using either an unpaired t-test with Welch's correction for normally distributed data or Mann-Whitney U test for non-normally distributed data. Associations between follicular grade (e.g., AMH or mCherry staining intensity) and experimental condition were assessed by Fisher's exact test.

Relationships between continuous variables (e.g., follicle number and mCherry volume, follicle number and mCherry proportion, or tissue volume) were examined by Pearson's correlation and simple linear regression. Where appropriate, data were Log_{10}-transformed to stabilise variance prior to analysis. Regression slopes and r^2 values were used to assess the strength and direction of associations, with $p \leq 0.05$ considered significant.

Agreement between quantitative measures obtained via FolliTracker and histological analysis was assessed using Bland–Altman plots, with proportional bias evaluated by linear regression of the mean-difference relationship.

Data are presented as mean ± SD and statistical significance was defined as $p \leq 0.05$.

5.3 Results

5.3.1 FolliTracker enabled follicle visualisation in transduced reaggregated ovaries

The FolliTracker imaging-analysis workflow was successfully implemented to monitor follicles in real-time. ROs (control, *n*=8; viral, *n*=5) were imaged via spinning disc confocal microscopy at 5 µm optical z-stacks, capturing the three-dimensional tissue structure across the 14-day culture period (Figure 5.3.1.1), then three-dimensionally visualised via a semi-autonomous software (Figure 5.3.1.2). mCherry expression served as an indicator of co-transduction of AAVs, whereas EGFP expression served as a reporter for mAMH activity. To quantify these fluorescence signals and assess follicle dynamics, subsequent three-dimensional image sets were processed via the FolliTracker computational analysis workflow. Successful longitudinal monitoring was defined as the ability to repeatedly image the same RO, identify follicle-associated signals across timepoints, and extract volumetric and fluorescent signal-based metrics without compromising tissue integrity.

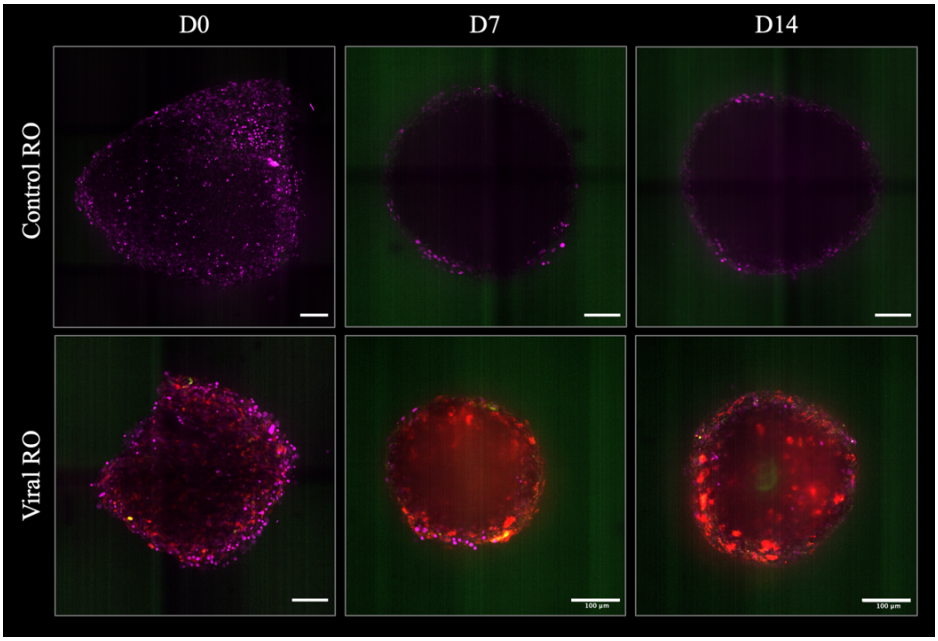

Figure 5.3.1.1) Composite confocal images of live control and viral reaggregated ovaries during culture. Representative confocal micrographs of control (non-viral) and viral ROs on days 0, 7, and 14 of culture. Viral ROs underwent sequential transduction with AAV-Cas9 and AAV-DS prior to reaggregation, whereas control ROs were not exposed to virus-containing media. Images show overlayed fluorescent channels for SiR-DNA (CF640, magenta), mCherry (CF568, red), and EGFP (CF488, green) to represent nuclear staining, somatic cell transduction, and AMH expression, respectively. Each image is comprised of five consecutive 5 µm z-stacks combined from the central optical region of the RO. Overlapping mCherry and EGFP signal may appear yellow, indicating regions of co-expression. All imaging parameters, including laser intensity, exposure, and brightness/contrast adjustments, were applied consistently across samples. Images were acquired via the Olympus SpinSR SoRa spinning-disc confocal microscope (Olympus Corporation) via the CellSens software. Image processing and composite generation were performed with ImageJ. Scale bars represent 100 µm. AAV, adeno-associated virus; AMH, anti-Müllerian hormone; Cas9, CRISPR-associated protein 9; CF, cyanine fluorophore; D(0/7/12/14), culture day (0/7/12/14) DS, donor strand; EGFP, enhanced green fluorescent protein; mCherry, monomeric red fluorescent protein; RO, reaggregated ovary; SFFV, spleen focus-forming virus; SiR-DNA, silicon–rhodamine deoxyribose nucleic acid.

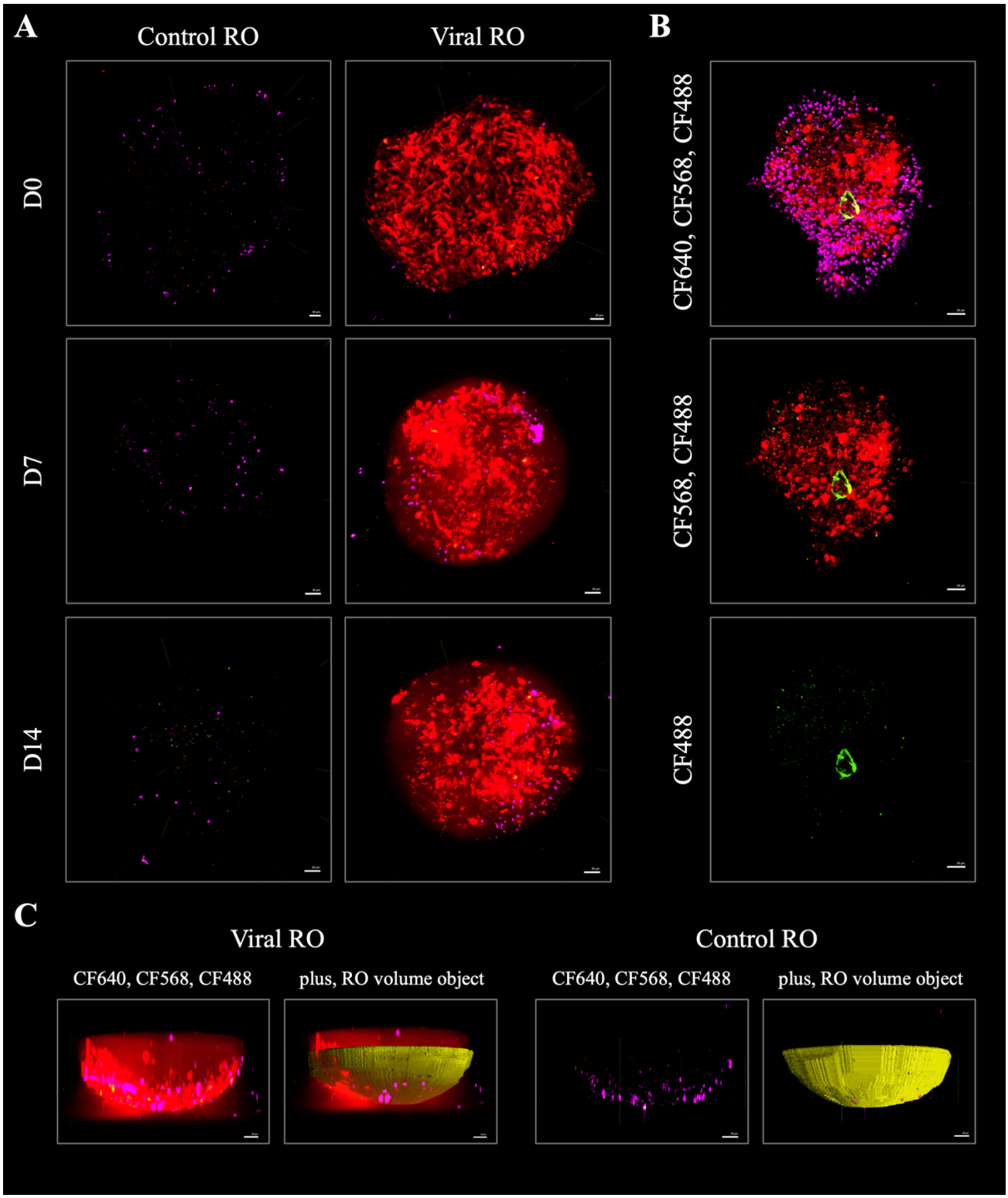

Figure 5.3.1.2) FolliTracker imaging and volumetric reconstruction of live reaggregated ovaries during culture. A) Representative images of control (non-viral) and viral ROs acquired via the live-imaging component of the FolliTracker workflow during culture. Viral ROs underwent sequential transduction with AAV-Cas9 and AAV-DS prior to reaggregation, where control ROs were not exposed to virus-containing media. Fluorescent channels depict SiR-DNA (CF640, magenta), mCherry (CF568, red), and EGFP (CF488, green), representing nuclear labelling, transduction, and AMH expression, respectively. Overlapping mCherry and EGFP signal may appear yellow, indicating regions of co-expression. **B)** Image of a single viral RO at D12 showing individual and merged fluorescent channels. Thresholds were constant, with uniform colour enhancement and brightness adjustment applied across all panels to aid visualisation. **C)** Side view of control and viral ROs. Panels on the left display all fluorescent channels (CF640, CF568, CF488), whilst corresponding right panels (plus, RO volume object) show the fluorescent channels with an overlaid three-dimensional representation of the RO volume. All images parameters, including brightness/contrast adjustments, were applied consistently across samples (A, C). All images were acquired via spinning-disc confocal microscopy (Olympus SpinSR SoRa) and processed with Arivis Vision4D (Arivis AG). Scale bars represent 50 µm. AAV, adeno-associated virus; AMH, anti-Müllerian hormone; Cas9, CRISPR-associated protein 9; CF, cyanine fluorophore; D(0/7/12/14), culture day (0/7/12/14) DS, donor strand; EGFP, enhanced green fluorescent protein; RO, reaggregated ovary; SiR-DNA, silicon-rhodamine deoxyribose nucleic acid.

5.3.2 FolliTracker identified more follicles in viral tissues compared with controls

When assessing follicle number from culture day 7–14 using two-way ANOVA, experimental condition was the primary source of variation (p<0.001). Individual ROs (p<0.01) and the combined effect of time and individual ROs (p=0.05) affected follicle number. Across timepoints, viral ROs consistently had more follicles than controls (Figure 5.3.2A) (D7 [control, 0.125; viral, 10.60]; D8 [control, 0.250; viral, 6.800]; D10 [control, 0.125; viral, 12.00]; D12 [control, 0.375; viral, 9.200]; D14 [control, 0.625; viral, 10.20]; all adj. p<0.01).

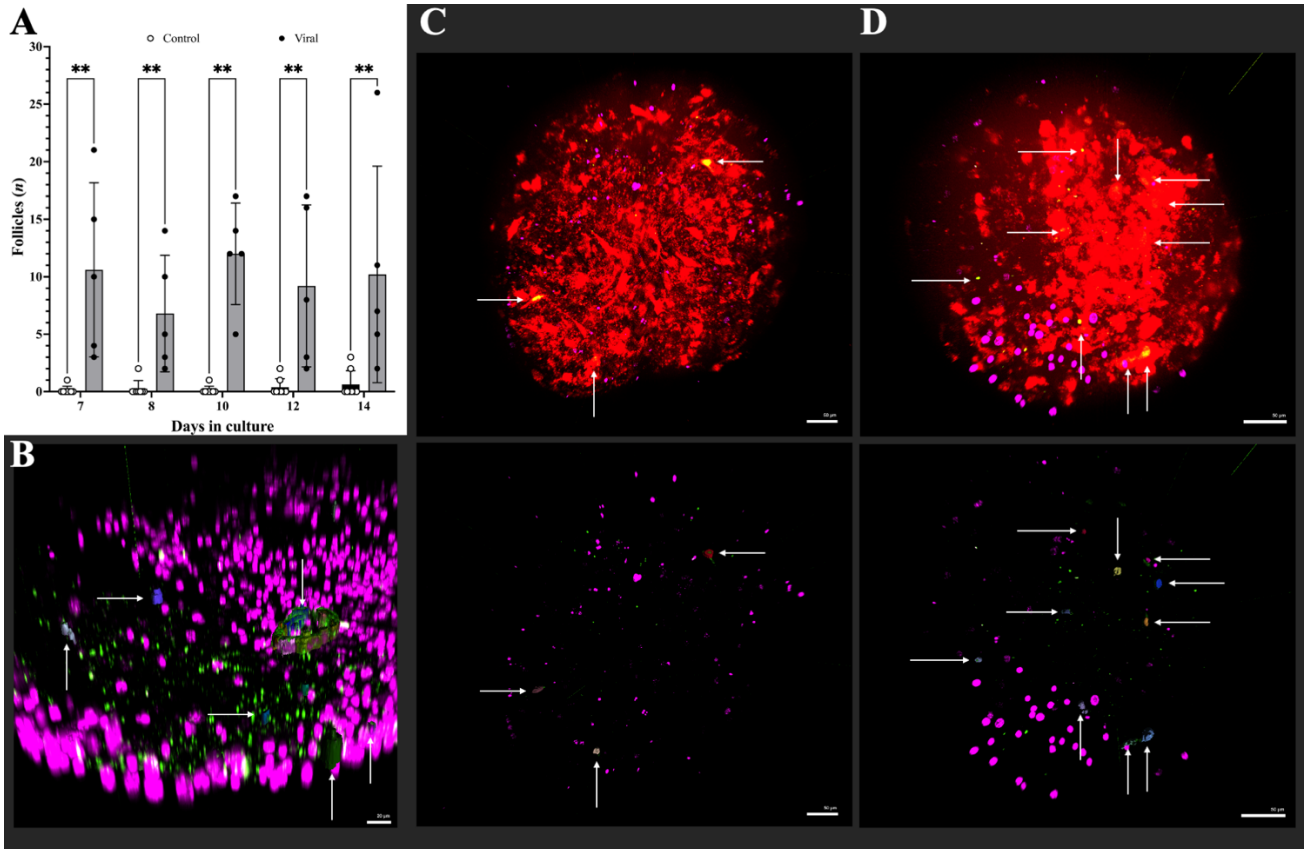

Figure 5.3.2) Quantification and visualisation of follicles in reaggregated ovaries via FolliTracker. Viral ROs underwent sequential transduction with AAV-SaCas9 and AAV-DS prior to reaggregation, whereas control ROs were not exposed to virus-containing media. mCherry fluorescence (CF568, red) reported successful transduction of somatic cells, whilst EGFP (CF488, green), driven by an AMH promoter, was used to identify follicles. Nuclear labelling of SiR-DNA (CF640, magenta) visualised overall tissue structure. **A)** Total follicle number (n) per RO detected by the FolliTracker segmentation criteria, defined by overlapping mCherry and EGFP signal across culture days 7–14. Statistical analyses were performed using multiple t-tests. Data are presented as mean ± SD. **B)** Magnified view of a single viral RO on culture day 12 showing SiR-DNA and EGFP, with three-dimensional objects overlaid within the tissue to represent follicles (white arrows). Brightness was enhanced to support visualisation. **C, D)** Representative viral ROs on culture day 7. Top panels show all relevant fluorescent channels (CF640, SiR-DNA; CF568, mCherry; CF488, EGFP), with follicles appearing yellow where mCherry and EGFP signals overlap (white arrows). Bottom panels show the corresponding SiR-DNA and EGFP channels with segmented three-dimensional follicle objects overlaid (white arrows). Image parameters, including brightness and contrast adjustments, were applied consistently across samples (C, D). All images were acquired via spinning-disc confocal microscopy (Olympus SpinSR SoRa) and processed with Arivis Vision4D (Arivis AG). Scale bars represent 20 µm (B) and 50 µm (C,D). AAV, adeno-associated virus; AMH, anti-Müllerian hormone; Cas9, CRISPR-associated protein 9; CF, cyanine fluorophore; DS, donor strand; EGFP, enhanced green fluorescent protein; RO, reaggregated ovary; SD, standard deviation; SiR-DNA, silicon-rhodamine deoxyribonucleic acid. *p≤0.05; **p<0.01.

5.3.3 Viral reaggregated ovaries had more mCherry signalling than control reaggregated ovaries across all culture timepoints

Two-way ANOVAs revealed that experimental condition significantly affected volume ($p<0.0001$) and proportion of mCherry signal ($p<0.0001$) in ROs across culture duration. Individual ROs ($p<0.05$) and the combination of individual ROs at various timepoints ($p<0.01$) were found to be significant sources of variation for the proportion of mCherry volume. At each culture timepoint assessed, the volume of mCherry signal (Figure 5.3.3A,B) and the proportion of mCherry signal (Table 5.3.3) in transduced ROs was greater compared with control ROs via the FolliTracker analysis. Pooled across timepoints, the average proportion of mCherry signal was greater in the viral group ($n=5$; 1.24% ± 1.40%) compared with the control group ($n=8$; 0.002% ± 0.007%; $p<0.01$) (Figure 5.3.4A).

Table 5.3.3) Proportion of mCherry-positive volume in reaggregated ovaries via FolliTracker across culture timepoints. Viral ROs underwent sequential transduction of AAVs prior to reaggregation, whereas control ROs were not exposed to virus-containing media. mCherry fluorescence reflects successful transduction of somatic cells within the RO. Statistical comparisons between control and viral groups were conducted using multiple t-tests with adjusted p-values reported for each assessed timepoint. Data are presented as mean ± SD. Statistical significance was defined as $p\leq0.05$.

	Control ROs (n=8)	**Viral ROs (n=5)**	**Adj. p-value**
Mean volume of mCherry signal, % ± SD (µm^3)			
Day 0	0.002% ± 0.004% (1,106.06)	0.136% ± 0.073% (49,575.53)	$p\leq0.05$
Day 2	0.00002% ± 0.00003% (11.35)	0.588% ± 0.383% (145,730.94)	$p\leq0.05$
Day 4	0.0003% ± 0.0008% (121.76)	0.652% ± 0.419% (179,904.37)	$p\leq0.05$
Day 6	0.004% ± 0.009% (1,242.49)	1.046% ± 0.933% (212,097.94)	$p\leq0.05$
Day 7	0.000005% ± 0.000009% (1.37)	2.090% ± 2.572% (258,218.39)	$p\leq0.05$
Day 8	0.006% ± 0.016% (1,569.88)	1.678% ± 1.701% (256,899.15)	$p\leq0.05$
Day 10	0.010% ± 0.028% (3,133.23)	1.620% ± 1.440% (258,425.20)	$p\leq0.01$
Day 12	0.0001% ± 0.0002% (36.06)	1.707% ± 2.235% (296,762.43)	$p\leq0.05$
Day 14	0.00002% ± 0.00003% (5.22)	1.612% ± 1.885% (293,366.61)	$p\leq0.05$

AAV, adeno-associated virus; RO, reaggregated ovary; SD, standard deviation.

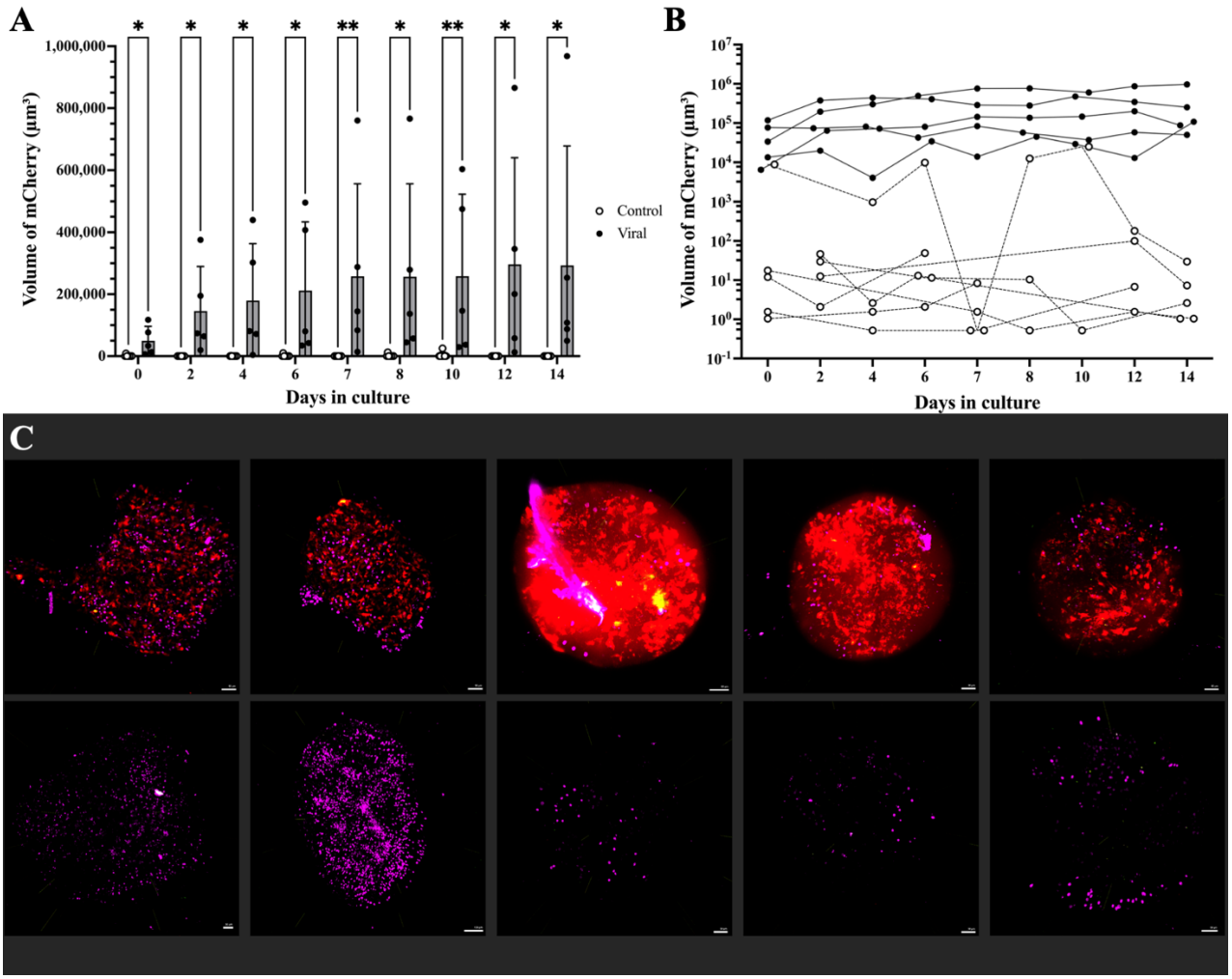

Figure 5.3.3) Quantitative assessment of mCherry signal volume in reaggregated ovaries via FolliTracker. Viral ROs underwent sequential transduction with AAV-SaCas9 and AAV-DS prior to reaggregation, whereas control ROs were not exposed to virus-containing media. mCherry fluorescence (CF568, red) reported successful somatic-cell transduction, whilst EGFP (CF488, green), driven by an AMH promoter, identified follicles. Nuclear labelling with SiR-DNA (CF640, magenta) visualised overall tissue structure. **A)** Volume of mCherry-positive signal (µm³) quantified in control and viral ROs throughout culture. Statistical analyses were performed using multiple t-tests. Data are presented as mean ± SD. **B)** Representation of mCherry-positive signal (µm³) in individual control and viral ROs (culture days 0–14), displayed on a Log_{10} scale y-axis to aid visualisation across the full dynamic range. Values equal to zero are not plotted on the logarithmic scale. **C)** Representative images of viral ROs (top row) and control ROs (bottom row) at key culture timepoints. From left to right: D0 from experimental batch 1, D0 from experimental batch 2, D7 from experimental batch 3, D7 from experimental batch 4, D14 from experimental batch 5. All fluorescent channels (CF640, SiR-DNA; CF568, mCherry; CF488, EGFP) are shown. Image parameters, including brightness and contrast adjustments, were applied consistently across samples. All images were acquired via spinning-disc confocal microscopy (Olympus SpinSR SoRa) and processed using Arivis Vision4D (Arivis AG). Scale bars represent 50 µm. AAV, adeno-associated virus; AMH, anti-Müllerian hormone; Cas9, CRISPR-associated protein 9; CF, cyanine fluorophore; D(0/7/12/14), culture day (0/7/12/14); DS, donor strand; RO, reaggregated ovary; SD, standard deviation. *$p \leq 0.05$; **$p < 0.01$.

5.3.4 Volume of mCherry signal was positively correlated with follicle number detected by FolliTracker

The volume of mCherry signal was strongly correlated with the number of follicles detected by FolliTracker across all timepoints following Log_{10}-transformation ($r^2=0.5155$), with a significant positive association observed ($p<0.0001$) (Appendix II; Figure AII.5.3.4).

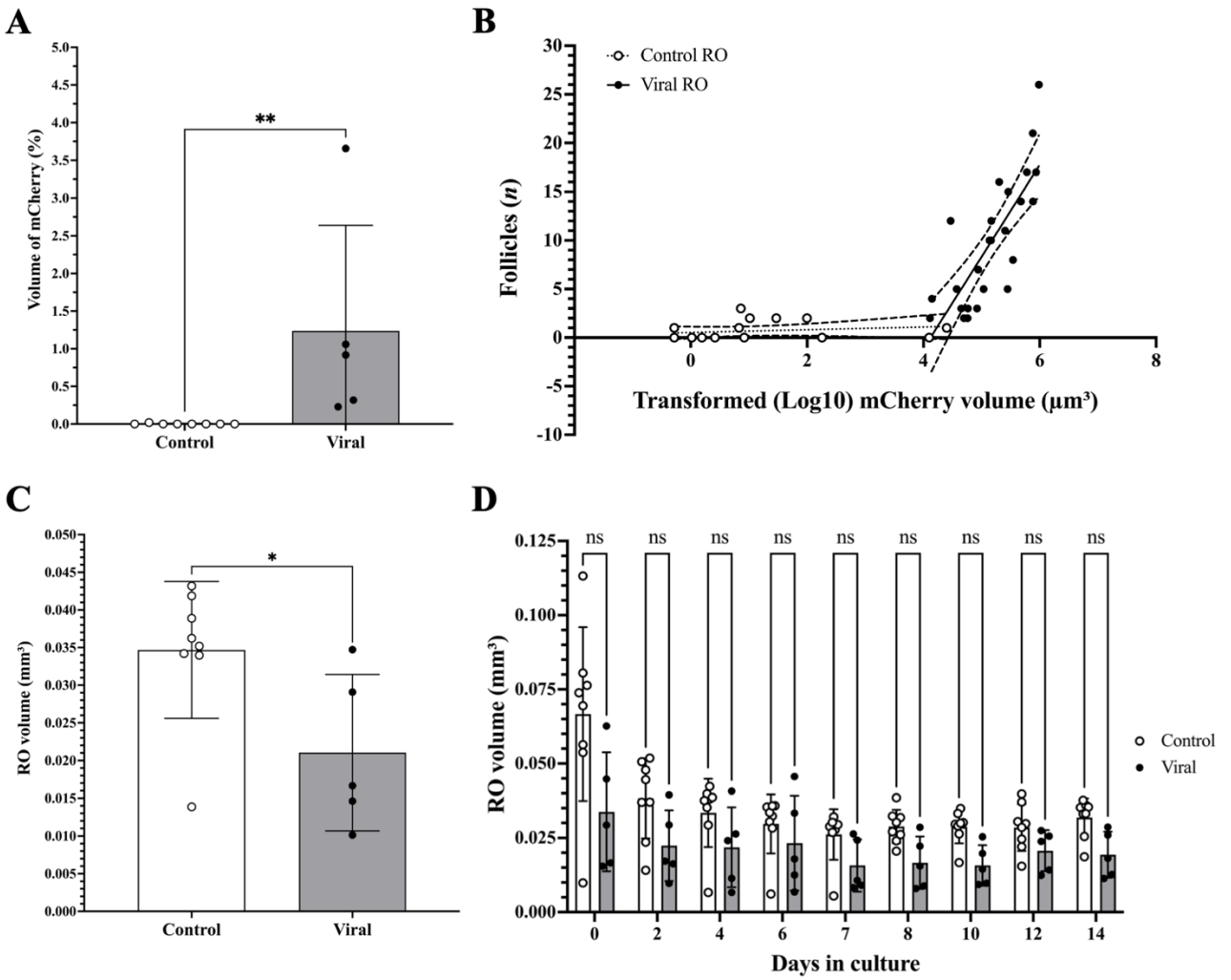

Figure 5.3.4) Quantitative correlation and volumetric assessment of mCherry signal and tissue size via FolliTracker in reaggregated ovaries. Viral ROs underwent sequential transduction of AAVs prior to reaggregation, whereas control ROs were not exposed to virus-containing media. mCherry fluorescence represented successful transduction of somatic cells. **A)** Pooled volume of mCherry-positive signal (%) in control and viral ROs across all assessed timepoints. **B)** Correlation between log-transformed mCherry signal volume (μm^3) and number of follicles detected by FolliTracker in viral ROs (r^2=0.6249; p<0.0001) and control ROs (r^2=0.0422; p=ns). **C)** Total RO volume (mm^3) averaged across all assessed culture timepoints in respective viral and control groups. **D)** Tissue volume (mm^3) at each assessed culture timepoint in control versus viral ROs. Statistical analyses were performed using Mann-Whitney U test (A, C), multiple t-tests (D), and Spearman's correlation (B). Data is presented as mean ± SD; where shown, dashed lines represent 95% CI. AAV, adeno-associated virus; CI, confidence interval; NS, not significant; RO, reaggregated ovary; SD, standard deviation. *p≤0.05; **p<0.01.

A significant positive association between mCherry-positive volume and follicle number was observed in viral ROs (Figure 5.3.4B; r^2=0.6249, p<0.0001), whereas no significant relationship was detected in control ROs (r^2=0.0422). This positive association was consistent between mCherry signal and follicle number in the untransformed viral ROs (r=0.8079; p<0.0001). However, in the untransformed control data, a positive correlation was present (r=0.5885; p<0.0001).

5.3.5 Tissue volume was similar between both groups at each assessed timepoint with FolliTracker

The average tissue volume of the control group across timepoints (n=8; 0.035 mm^3 ± 0.009 mm^3) was greater than the RO group (n=5; 0.021 mm^3 ± 0.010 mm^3; p<0.05) (Figure 5.3.4C). A two-way ANOVA found that the two factors that contributed most significantly to variation of tissue volume was experimental condition (p<0.0001) and the duration of culture (p<0.001). Total tissue volume also differed between individual ROs (p<0.05) and the combination of individual ROs over time in culture (p<0.05).

When assessed at various culture timepoints, tissue volume was similar between groups at individual timepoints (Figure 5.3.4D). Tissue volume was not significantly different between D0 (n=5; 0.034 mm^3 ± 0.020 mm^3) and D14 of viral ROs (0.019 mm^3 ± 0.008 mm^3). In contrast, control ROs became smaller overtime, when tissue volume on culture D0 (n=8; 0.067 mm^3 ± 0.029 mm^3) was compared with D14 (n=8; 0.032 mm^3 ± 0.007 mm^3; p<0.05).

5.3.6 Total tissue volume was similar between the control group and viral group via histological analysis

ROs were preserved in fixative on the final day of culture, D14, and subsequently processed for histological and immunohistochemical analysis (Figure 5.3.6A). Control tissues (n=7) had an average volume of 0.036 mm^3 ± 0.010 mm^3 which did not statistically differ from the volume of viral tissues (n=4; 0.021 mm^3 ± 0.007 mm^3) (Figure 5.3.6E). RO-level inclusion across analytical modalities and experimental batches is detailed in Appendix II.

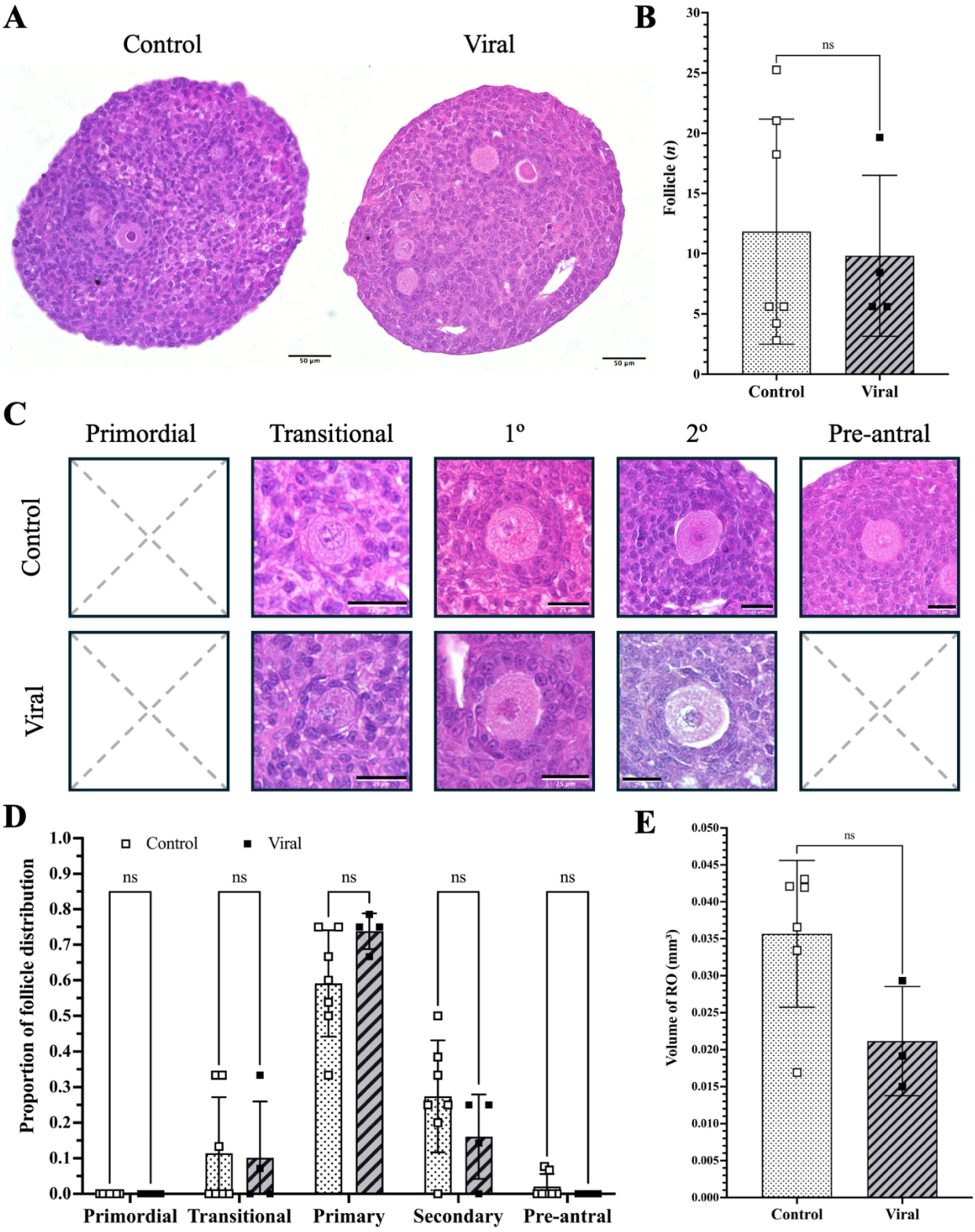

Figure 5.3.6) Histological assessment of tissue volume, follicle number, and stage distribution in reaggregated ovaries following 14 days in culture. Viral ROs underwent sequential transduction with AAVs prior to reaggregation, whereas control ROs were not exposed to virus-containing media. ROs were fixed on day 14 of culture for histological analysis and stained with H&E for tissue and follicle visualisation. **A)** Representative H&E-stained sections of control and viral ROs showing overall tissue morphology. Scale bar represents 50 µm. **B)** Total follicle number per RO in control and viral groups. **C)** Representative micrographs of follicles at distinct early developmental stages in control and viral ROs; morphological distinctions between secondary and pre-antral follicles may appear subtle in RO tissue due to less defined FBL. Follicle classification was performed according to established criteria based on GC layer number (see Chapter 2.9.2). Dashed panels indicate follicular stages absent within the group. Scale bar represents 25 µm. **D)** Proportional distribution of follicle developmental stages in control and viral ROs on culture day 14. **E)** Tissue volume (mm^3) was estimated using the Cavalieri principle from serial histological sections. Statistical analyses were performed using unpaired t-test with Welch's correction (B), multiple Mann-Whitney U tests (D), and Mann-Whitney U test (E). Data is presented as mean ± SD. AAV, adeno-associated virus; FBL, follicular basal lamina; H&E, haematoxylin and eosin; NS, not significant; RO, reaggregated ovary; SD, standard deviation.

5.3.7 Follicle number and stage distribution were similar between the control group and viral group

Total follicle number did not differ between control (n=7; 11.9 ± 9.3) and viral ROs (n=4; 9.8 ± 6.7) (Figure 5.3.6B). The proportional distribution of follicles across developmental stages were recorded per sample (Figure 5.3.6C). A two-way ANOVA revealed that experimental condition (control versus viral) did not affect the distribution of follicular stage.

Primordial follicles were not present in any RO sample assessed following 14 days in culture (0.0% vs. 0.0%), regardless of experimental condition (Figure 5.3.6D). Primary follicles represented the most abundant follicular stage in both groups (control, 59.1%; viral, 73.8%). Pre-antral follicles were only observed in the control ROs (2.1%) and not viral ROs (0.0%), although this difference was not statistically significant.

The proportion of follicles surrounded by TCs was recorded per RO (Figure 5.3.7A). The proportion of follicles with TCs present was similar across experimental groups (control, 75.7%; viral, 86.8%).

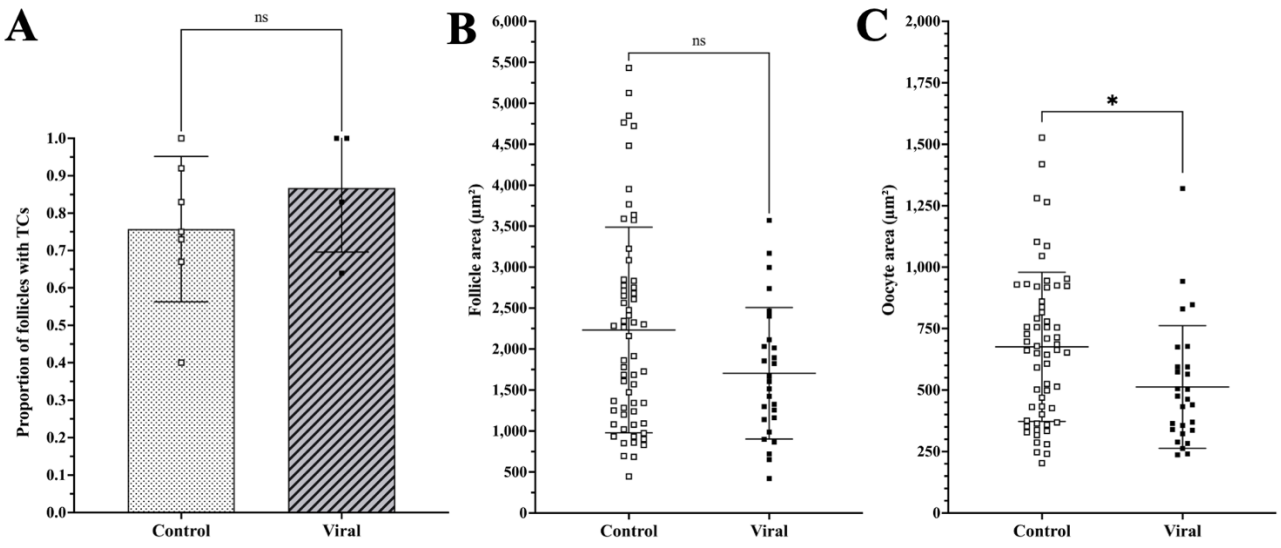

Figure 5.3.7) Quantitative assessment of theca cell presence, follicle area, and oocyte area from histological analysis of reaggregated ovaries following 14 days in culture. Viral ROs underwent sequential transduction with AAVs prior to reaggregation, whereas control ROs were not exposed to virus-containing media. All parameters were quantified from H&E-stained histological sections. **A)** Proportion of follicles surrounded by at least one TC in respective control and viral ROs. **B)** Follicle area (µm^3) per follicle in control and viral ROs. **C)** Oocyte area (µm^3) per follicle in control and viral ROs. Statistical analyses were performed using an unpaired t-test with Welch's correction (A) and Mann-Whiteney tests (B, C). Data is presented as mean ± SD. AAV, adeno-associated virus; H&E, haematoxylin and eosin; NS, not significant; RO, reaggregated ovary; SD, standard deviation; TC, theca cell. *p≤0.05.

5.3.8 Although follicle area was similar between groups, the oocyte areas of follicles from viral reaggregated ovaries was smaller than controls

The area of follicles and oocytes of each follicle identified via histological analysis was recorded. The area of follicles from viral ROs (1,704 $\mu m^2 \pm 802$ μm^2) did not significantly differ to follicles from control ROs (2,232 $\mu m^2 \pm 1,255$ μm^2) (Figure 5.3.7B). However, the oocyte area of follicles from viral tissue was smaller than the control group (513 $\mu m^2 \pm 250$ μm^2 vs. 676 $\mu m^2 \pm 303$ μm^2, respectively; $p<0.05$) (Figure 5.3.7C).

5.3.9 Follicular growth rate was similar between follicles from both control and viral reaggregated ovaries

The density of GCs was assessed by calculating the number of GCs within the GC area of each follicle. GC density was found to be similar between the control group and the viral group (0.018 ± 0.003 vs. 0.019 ± 0.002, respectively) (Figure 5.3.9A).

The growth rate of follicles were compared between the control group and the viral group via simple linear regression. When the relationship between number of GCs and GC area was assessed, growth rate was similar between both the control and viral groups with the r^2 value of both groups larger than 0.6 (control, $r^2=0.9383$; viral, $r^2=0.9671$) (Figure 5.3.9C). The relationship between GC number and total follicle area was similar between groups, with an r^2 value of 0.9307 and 0.9082 for the control group and viral group, respectively (Figure 5.3.9B).

Oocyte area was compared with granulosa area via simple linear regression (Figure 5.3.9D). Significant positive associations were observed in both control ($r^2=0.6793$, $p<0.0001$) and viral groups ($r^2=0.1464$, $p<0.05$). However, the strength of association was reduced in viral ROs, and no significant difference in the relationship between oocyte area and GC area was observed between groups.

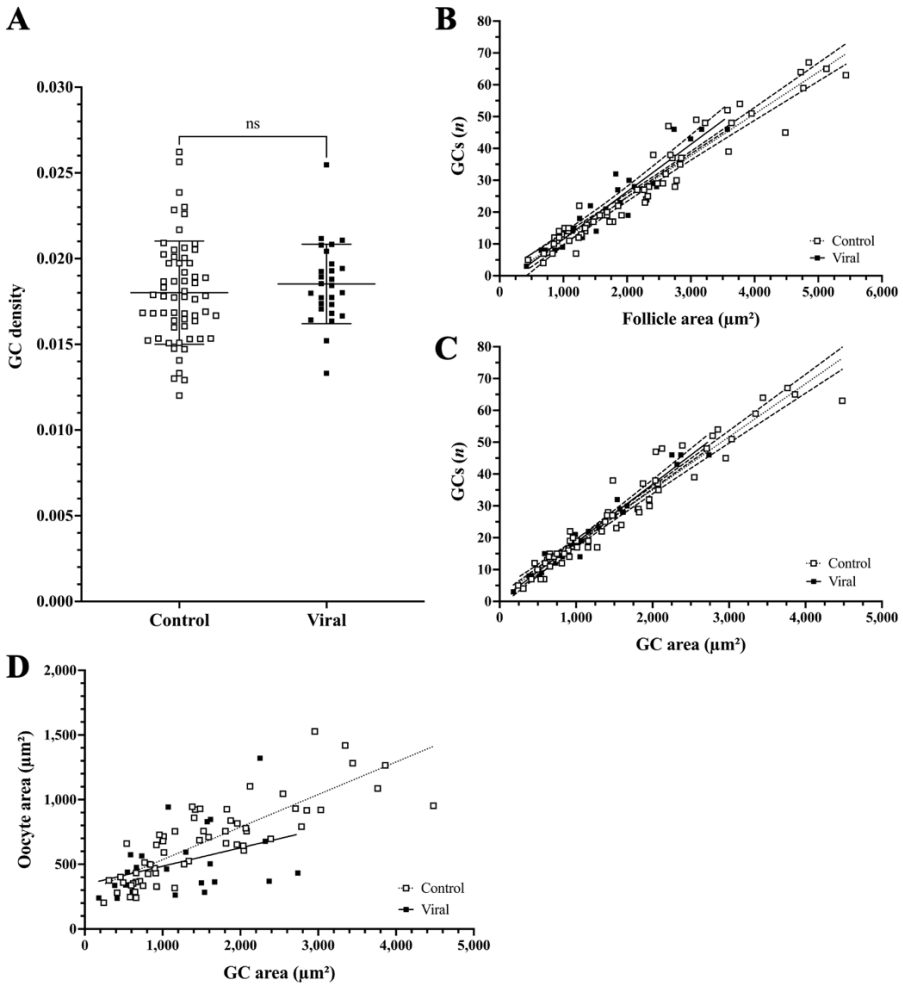

Figure 5.3.9) Quantitative assessment of granulosa cell density and follicular growth rate from histological analysis of reaggregated ovaries following 14 days in culture. Viral ROs underwent sequential transduction with AAVs prior to reaggregation, whereas control ROs were not exposed to viral-containing media. All parameters were quantified from H&E-stained histological sections. **A)** GC density, representing the number of GCs within the follicular GC compartment (µm^2), within follicles of control and viral ROs. Data is presented as mean ± SD. **B)** Correlation between follicle area (µm^2) and number of GCs per follicle. **C)** Correlation between GC area (µm^2) and number of GCs per follicle. **D)** Relationship between oocyte area (µm²) and granulosa area (µm²) in follicles. Statistical analysis of GC density was performed using the Mann-Whitney U test **(A)**, whilst growth rate correlations were assessed by simple linear regression and dashed lines represent 95% CI **(B–D)**. AAV, adeno-associated virus; CI, confidence interval; GC, granulosa cell; H&E, haematoxylin and eosin; NS, not significant; RO, reaggregated ovary; SD, standard deviation.

5.3.10 The symmetry of follicles and oocytes did not differ between groups

The symmetry of oocytes was similar in the control group (0.99 ± 0.10) compared with the viral group (1.01 ± 0.13) when Welch's t-test was employed (Figure 5.3.10A). The oocyte symmetry values from both groups were compared to the theoretical mean of 1.00 to determine if there was significant deviation from perfect symmetry. The oocytes of follicles from the control group (0.99 vs. 1.00) and viral group (1.01 vs. 1.00) were not significantly different from perfect symmetry.

Follicle symmetry did not significantly differ between control and viral ROs (control, 0.98 ± 0.13; viral, 1.05 ± 0.16, respectively; p=0.0521) (Figure 5.3.10B). Follicles in their respective groups were

compared to theoretical mean of 1.00 with a one sample t-test. The symmetry of follicles from the control group were similar to the theoretical mean (0.98 vs. 1.00, respectively). This was consistent when viral symmetry (1.05) was compared to 1.00.

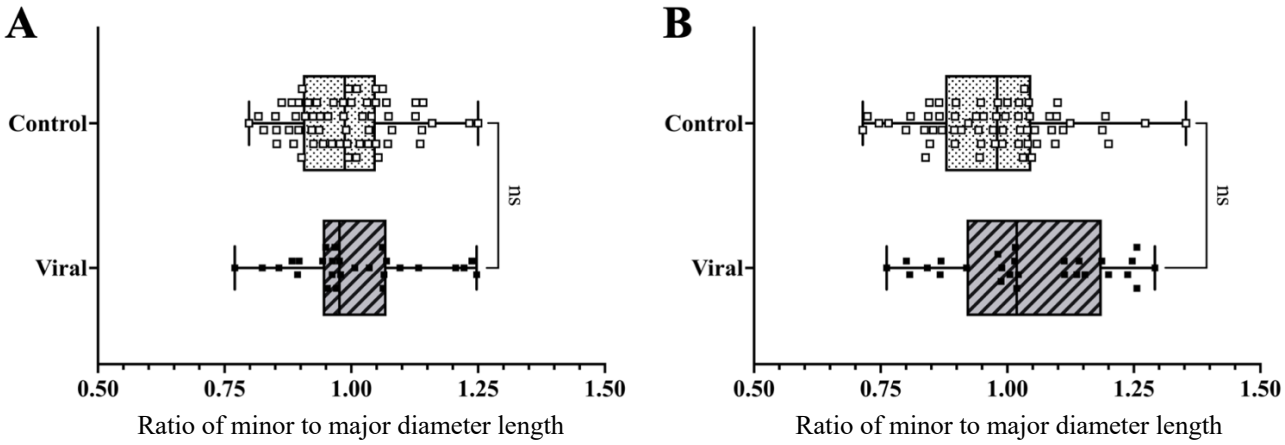

Figure 5.3.10) Quantitative assessment of oocyte and follicle symmetry from histological analysis of reaggregated ovaries after 14 days in culture. Viral ROs underwent sequential transduction with AAVs prior to reaggregation, whereas control ROs were not exposed to virus-containing media. Symmetry values were derived from morphological measurements in H&E-stained histological sections and expressed as the ratio of the minor diameter (y-axis) to the major diameter (x-axis). **A)** Oocyte symmetry in control and viral ROs. **B)** Follicle symmetry in control and viral ROs. Statistical analyses were performed using unpaired t-tests with Welch's correction. Data is presented as mean ± SD. AAV, adeno-associated virus; H&E, haematoxylin and eosin; NS, not significant; RO, reaggregated ovary; SD, standard deviation.

5.3.11 The proportion of AMH-positive follicles were similar across experimental groups following immunohistochemical assessment

As determined via IHC (Figure 5.3.11A), the proportion of follicles that were AMH-positive (normalised DAB intensity score ≥0.1) per RO was not statistically different between the control (n=7; 0.57 ± 0.36) and viral groups (n=4; 0.92 ± 0.17) (Figure 5.3.11C). As DAB normalisation reflected relative optical density, as opposed to absolute protein abundance, increased normalised intensity may reflect differences in background signal rather than absolute antigen abundance.

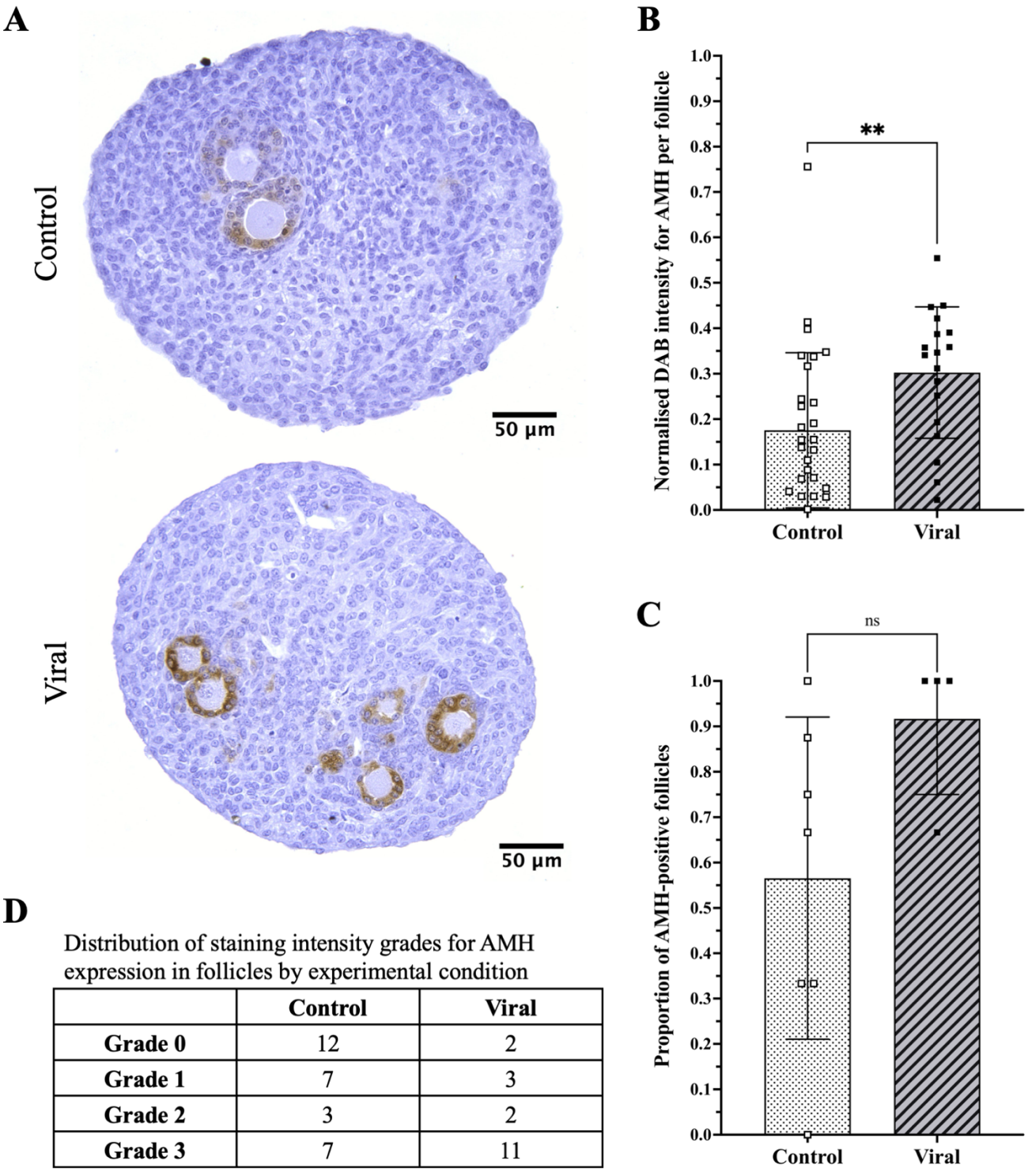

D

Distribution of staining intensity grades for AMH expression in follicles by experimental condition

	Control	Viral
Grade 0	12	2
Grade 1	7	3
Grade 2	3	2
Grade 3	7	11

Figure 5.3.11) Immunohistochemical assessment of AMH expression in reaggregated ovaries following 14 days in culture. Viral ROs underwent sequential transduction with AAVs prior to reaggregation, whereas control ROs were not exposed to virus-containing media. **A)** Representative images of control and viral ROs fixed at the end of culture and processed for IHC to assess AMH expression via DAB (brown) chromogenic staining. **B)** Proportion of AMH-positive follicles (normalised DAB intensity score ≥ 0.1) per RO in each experimental group **C)** Normalised DAB intensity ($AU/\mu m^2$) of AMH staining in follicles from control and viral ROs. **D)** Table showing the number of assessed follicles distributed across AMH staining intensity grades from control and viral ROs, as determined from normalised DAB intensity scores (grade 0, < 0.1; grade 1, 0.1 ≤ x < 0.2; grade 2, 0.2 ≤ x < 0.3; grade 3, ≥ 0.3). A significant association was observed between experimental condition (control versus viral) and follicle grade ($p<0.05$). Statistical analyses were performed using Mann-Whitney U tests (B, C) and Fisher's exact test (D). Data is presented as mean ± SD. AAV, adeno-associated virus; AMH, anti-Müllerian hormone; AU, arbitrary units; DAB, 3,3'-diaminobenzidine; IHC, immunohistochemistry; NS, not significant; RO, reaggregated ovary; SD, standard deviation. *$p\leq0.05$; **$p<0.01$.

5.3.12 The intensity of AMH stained follicles was greater in the viral group compared with the control group

The assessment of follicles via IHC were pooled to evaluate treatment-level trends rather than within-sample variability due to the low total follicle population and uneven representation per RO, as discussed further in the appendix (Appendix II; AII.5.3.12). The normalised DAB intensity for AMH in follicles was greater in the viral group (0.30 AU/μm^2 ± 0.15 AU/μm^2) compared with controls (0.18 AU/μm^2 ± 0.17 AU/μm^2; p<0.01) (Figure 5.3.11B). Follicles were graded (grade 0–3) according to the normalised DAB intensity score (Figure 5.3.11D), as described previously (Chapter 2.10.3). A Fisher's exact test determined there was significant difference between experimental condition (control versus viral) and follicle grade (p<0.05) of AMH intensity.

5.3.13 A greater area was positive for mCherry in viral tissues than in control tissues

IHC and computational analysis was implemented to quantify mCherry-positive tissue area (Figure 5.3.13A), as described (Chapter 2.10.3; Appendix II; Table AII.5.3.13). The average mCherry-positive area per individual RO section via DAB staining was greater in the viral group (n=5; 16,851 μm^2 ± 13,792 μm^2) compared with controls (n=7; 302 μm^2 ± 647 μm^2; p<0.01) (Table 5.3.13). This was consistent when mCherry-positive area proportion was compared between control and viral ROs (0.16% ± 0.29% vs. 20.1% ± 17.5%, respectively; p<0.01) (Figure 5.3.13B). The integrated density, representing the summed DAB staining signal within the defined tissue, of mCherry was assessed (Figure 5.3.13C). Viral tissue had a greater mean integrated density (n=5; 63,794 AU/μm^2 ± 54,875 AU/μm^2) compared with control tissue sections (n=7; 10,096 AU/μm^2 ± 13,209 AU/μm^2; p<0.05).

Table 5.3.13) Immunohistochemical assessment of mCherry-positive area via DAB staining in reaggregated ovaries following 14 days in culture. Viral ROs underwent sequential transduction with AAVs prior to reaggregation, whereas control ROs were not exposed to virus-containing media. Sections were stained for mCherry expression using DAB chromogenic detection to visualise transduction of somatic cell populations within the tissue.

	Control* **(*n*=7)**	**Viral** **(*n*=5)**
Mean area positive for mCherry, μm^2 ± SD (%)	301.5 ± 646.8† (0.16%)‡	16,851 ± 13,792† (20.1%)‡

AAV, adeno-associated virus; DAB, 3,3′-diaminobenzidine; E, experiment; RO, reaggregated ovary; SD, standard deviation.*Batch-level inclusion and processing constraints are detailed in Appendix II; $^{\dagger}p$<0.01 (Mann-Whitney U test); $^{\ddagger}p$<0.01 (Unpaired t-test with Welch's correction).

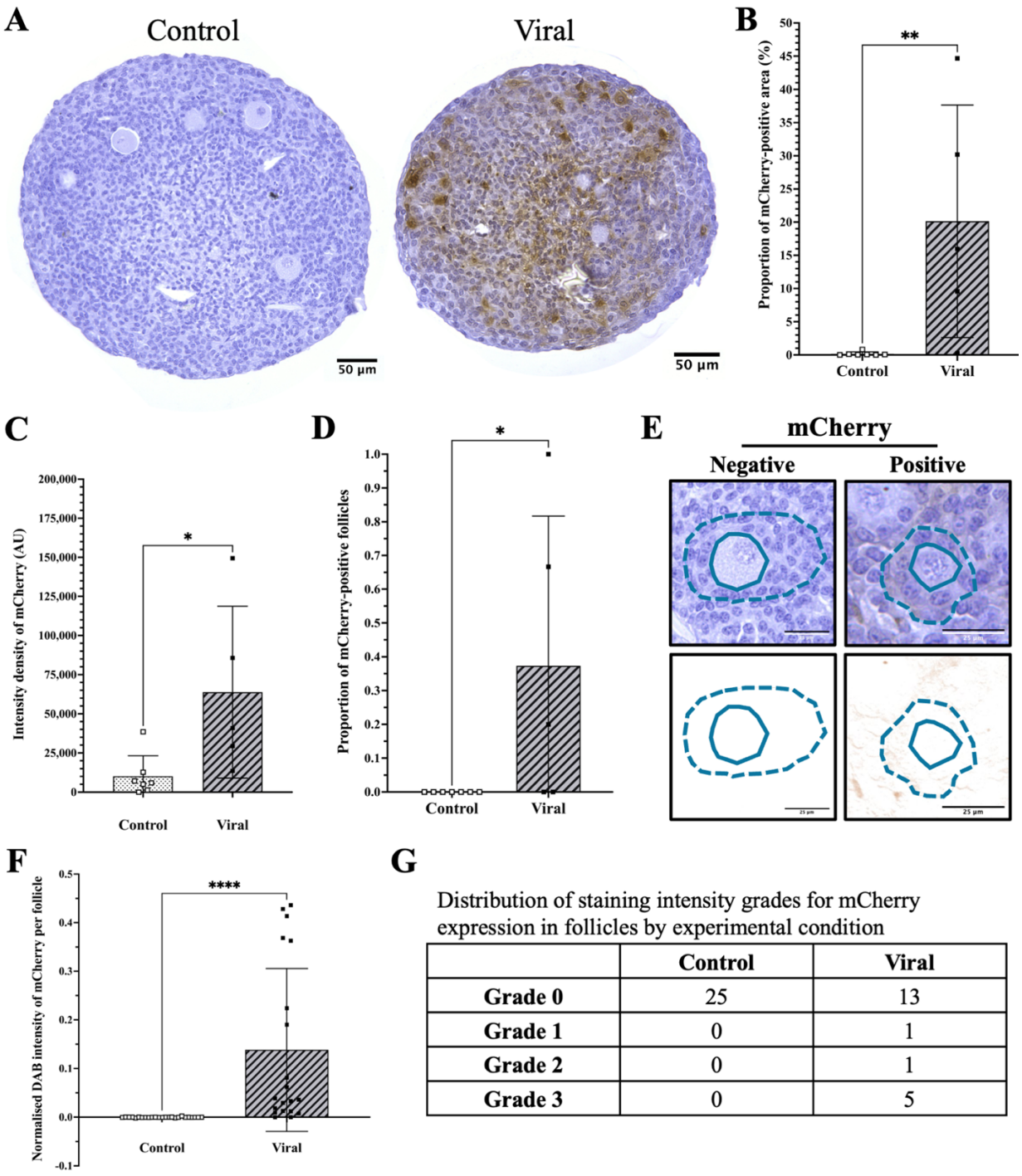

G

Distribution of staining intensity grades for mCherry expression in follicles by experimental condition

	Control	Viral
Grade 0	25	13
Grade 1	0	1
Grade 2	0	1
Grade 3	0	5

Figure 5.3.13) Immunohistochemical assessment of mCherry expression in reaggregated ovaries following 14 days in culture. Viral ROs underwent sequential transduction with AAV-SaCas9 and AAV-DS vectors prior to reaggregation, whereas control ROs were not exposed to virus-containing media. Expression of mCherry, driven by the ubiquitous SFFV promoter, indicated successful viral transduction of somatic cells within the tissue. ROs were fixed at the end of culture and processed for IHC using DAB (brown) chromogenic staining to detect mCherry and haematoxylin to visualise nuclei. **A)** Representative DAB-stained sections of control and viral ROs showing overall tissue morphology and mCherry expression. Scale bar represents 50 µm. **B)** Proportion of total tissue area positive for mCherry signal. **C)** Integrated density (AU) of mCherry DAB staining within the RO tissue section. **D)** Proportion of mCherry-positive follicles per RO. **E)** Representative micrographs of follicles classified as mCherry-negative (left; control RO) and mCherry-positive (right; viral RO) based on normalised DAB intensity thresholds. Top panels show brightfield images following IHC. Bottom panels show the corresponding DAB-only signal following colour deconvolution. Turquoise dashed outlines denote the follicle boundary, and solid outlines denote the oocyte, which was excluded from quantitative analysis. Follicle classification was determined using automated, normalised DAB intensity measurements rather than visual assessment. Scale bar represents 25 µm. **F)** Normalised DAB intensity (AU) of mCherry staining per follicle in control and viral ROs. **G)** Distribution of staining intensity grades for mCherry expression in follicles across experimental groups (grade 0, < 0.1; grade 1, $0.1 \leq x < 0.2$; grade 2, $0.2 \leq x < 0.3$; grade 3, ≥ 0.3). A significant association was observed between experimental condition (control versus viral) and follicle grade ($p<0.01$). Statistical analyses were performed using Mann-Whitney tests (B–D, F) and Fisher's exact test (G). Data are presented as mean ± SD. AAV, adeno-associated virus; AU, arbitrary units; Cas9, CRISPR-associated protein 9; DAB, 3,3′-diaminobenzidine; DS, donor strand; IHC, immunohistochemistry; RO, reaggregated ovary; SD, standard deviation; SFFV, spleen focus-forming virus. *$p\leq0.05$; **$p<0.01$; ***$p<0.001$; ****$p<0.0001$.

5.3.14 Viral reaggregated ovaries had a greater proportion of mCherry-positive follicles compared with control reaggregated ovaries

One control section displayed abnormally high mCherry expression, consistent with potential artefactual signal. Analyses were therefore repeated with and without this section. As results were consistent, the outlier was excluded. Rationale and analyses with the outlier is included in Appendix II (AII.5.3.14). Quantitative classification was driven by normalised integrated signal across the follicular compartment, rather than user-defined visual darkness of DAB staining.

The proportion of mCherry-positive follicles per RO was calculated across the sections which underwent immunohistochemical analysis (Figure 5.3.13D,E). Follicle positivity was defined using normalised DAB intensity thresholds derived from paired control sections. Viral tissues contained a greater proportion of mCherry-positive follicles than control tissues (37.3% ± 44.4% vs. 0.0% ± 0.0%, respectively; $p<0.05$). The average normalised DAB intensity of mCherry was greater in follicles from the viral group (0.138 AU ± 0.167 AU) compared with follicles from the control group (-0.0003 AU ± 0.0007 AU; $p<0.0001$) (Figure 5.3.13F). The follicular grading (Grade 0–3) of normalised DAB intensity for mCherry was implemented to categorise all follicles (Figure 5.3.13G). A Fisher's exact test revealed that there was a significant association between experimental condition (control versus viral) and grade of follicle ($p<0.01$).

Oocytes from both groups were also assessed for mCherry signal via IHC. Oocytes in viral ROs had a greater normalised DAB intensity compared with control oocytes (0.028 ± 0.056 vs. -0.0003 ± 0.0009, respectively; $p<0.01$). However, there was not a significant association between experimental condition and grade of oocyte staining intensity for mCherry (Table 5.3.14).

Table 5.3.14) Distribution of oocyte mCherry staining intensity grades in reaggregated ovaries following 14 days in culture. Viral ROs underwent sequential transduction with AAV-SaCas9 and AAV-DS vectors prior to reaggregation, whereas control ROs were not exposed to virus-containing media. Expression of mCherry, driven by the ubiquitous SFFV promoter, indicated successful viral transduction of somatic cells within the tissue. ROs were fixed at the end of culture and processed for IHC using DAB (brown) chromogenic staining to detect mCherry expression. Oocytes were graded (0–3) based on normalised DAB intensity for mCherry signal (grade 0, < 0.1; grade 1, 0.1 ≤ x < 0.2; grade 2, 0.2 ≤ x < 0.3; grade 3, ≥ 0.3). Statistical comparison between experimental conditions was performed using Fisher's exact test (*p*=NS). Data are presented as oocytes (*n*) per staining grade.

	Control	**Viral**
Grade 0	25	18
Grade 1	0	1
Grade 2	0	1
Grade 3	0	0

AAV, adeno-associated virus; Cas9, CRISPR-associated protein 9; DAB, 3,3′-diaminobenzidine; DS, donor strand; IHC, immunohistochemistry; NS, not significant; RO, reaggregated ovary; SFFV, spleen focus-forming virus.

5.3.15 The proportional expression of mCherry was not correlated to follicle number

As the proportion of mCherry signal largely fell between 0.0% to 1.0%, a Log_{10} transformation was applied to support correlation analysis. Correlation analyses were performed using both transformed and raw datasets. The transformed results included simple linear regression analysis which provided a more accurate reflection of proportional signal intensity changes. Analyses with excluded data is found in Appendix II (Figure AII.5.3.15).

In pooled data, no significant relationship was observed between mCherry signal proportion and follicle number (Figure 5.3.15A). Simple linear regression of transformed data found no significant association was detected (r^2=0.0264) (Figure 5.3.15C). The lack of association was consistent in both control and viral ROs (Figure 5.3.15B,D).

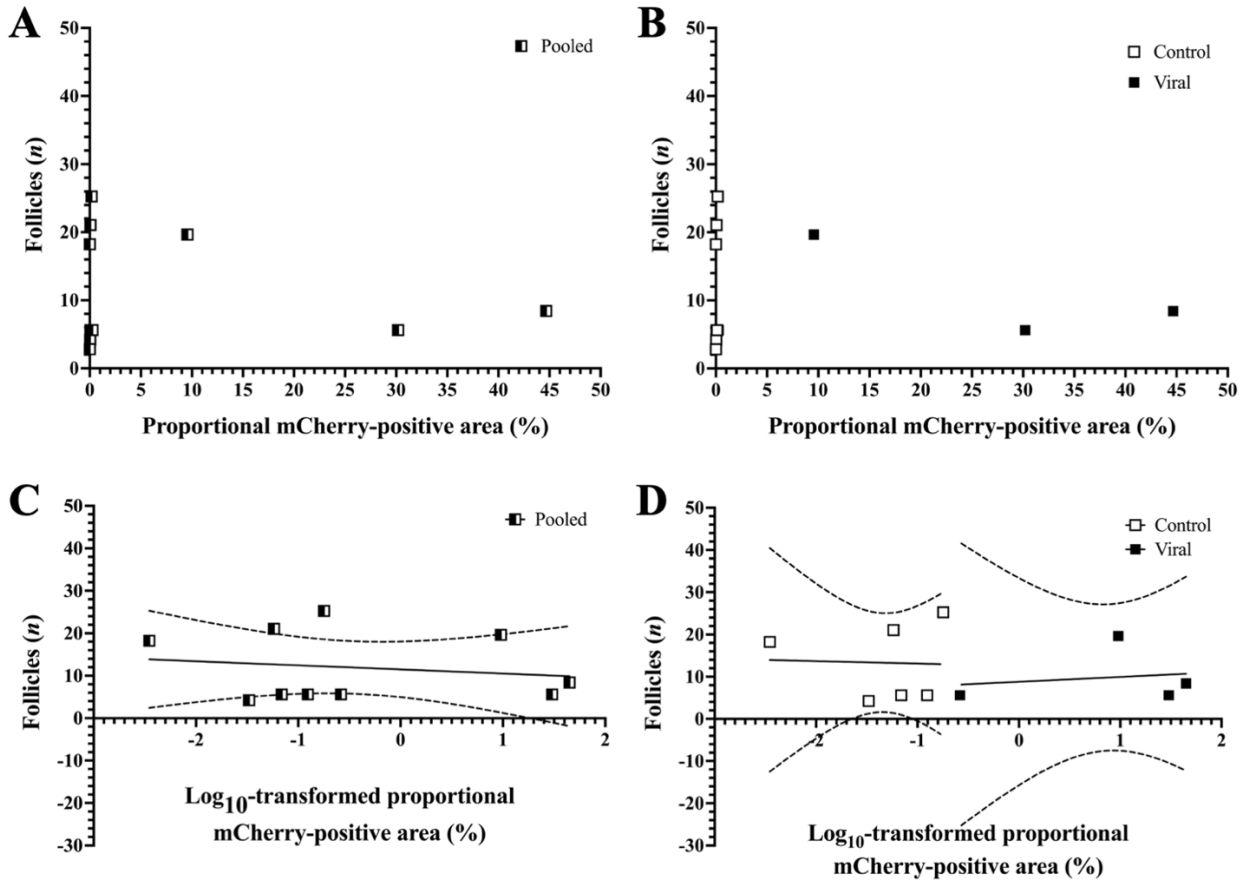

Figure 5.3.15) Correlation between proportion of mCherry-positive tissue area and total follicle number following 14 days in culture, as determined by histology-based analysis. Viral ROs underwent sequential transduction with AAV-SaCas9 and AAV-DS vectors prior to reaggregation, whereas control ROs were not exposed to virus-containing media. Expression of mCherry, driven by the ubiquitous SFFV promoter, indicated successful transduction of somatic cells within tissue. ROs were fixed at the end of culture and processed for histological analysis and IHC using DAB chromogenic staining to detect mCherry expression. Follicle number per RO was quantified using histological analysis of H&E-stained sections. Spearman's correlation between proportional mCherry-positive area (%) and total follicle number in **A)** pooled ROs (r=0.3024) and **B)** separated control (r=0.5946) and viral (r=0.2108) ROs. Simple linear regression of Log_{10}-transformed proportional mCherry-positive area (%) and total follicle number in **C)** pooled ROs (r^2=0.0264) and **D)** separated control (r^2=0.0014) and viral (r^2=0.0301) ROs. In both raw and transformed analyses, no significant association was observed. Data are presented as individual ROs, with best-fit regression lines shown. Dashed lines represent 95% CIs. AAV, adeno-associated virus; Cas9, CRISPR-associated protein 9; CI, confidence interval; DAB, 3,3′-diaminobenzidine; DS, donor strand; IHC, immunohistochemistry; RO, reaggregated ovary; SFFV, spleen focus-forming virus.

5.3.16 The number of follicles per reaggregated ovary recorded were not correlated between histology and FolliTracker

Follicle number was not correlated between histological and FolliTracker analysis (Figure 5.3.16A), with regression analysis confirming a negligible relationship (r^2=0.0010). This was consistent without the Abercrombie correction (Appendix II; Figure AII.5.3.16). Agreement between follicle counts was evaluated using Bland-Altman analysis. FolliTracker tended to underestimate follicle number compared with histological assessment, with a mean bias of -133.6% ± 100.6% (95% limits of agreement (LoA) [-330.9, 63.6%]). Simple linear regression of the Bland-Altman differences against the mean count revealed no significant proportional bias (r^2=0.2814) (Figure 5.3.16B).

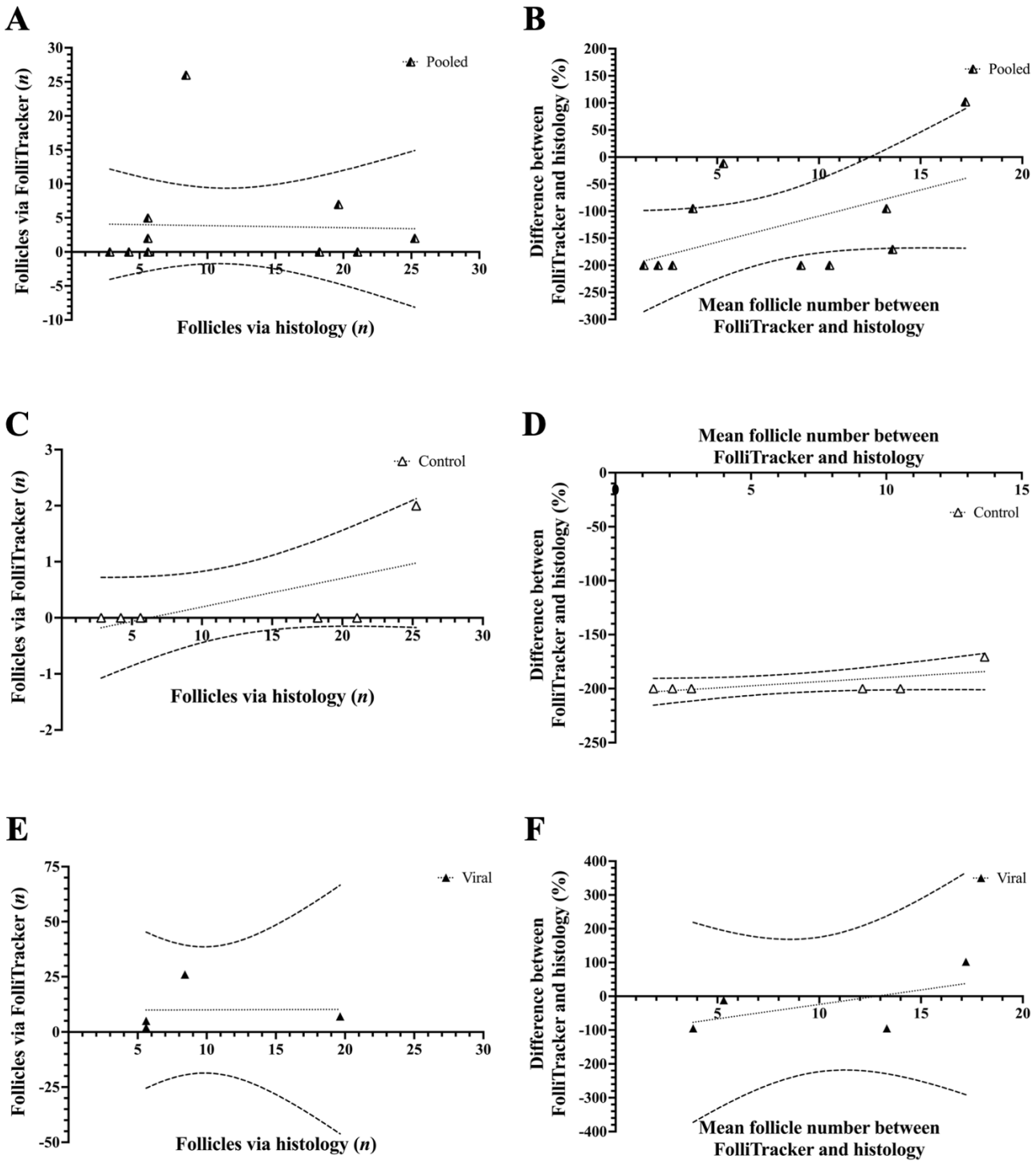

Figure 5.3.16) Correlation and agreement of follicle counts obtained via FolliTracker and histological analysis in reaggregated ovaries following 14 days in culture. Follicle number per RO was quantified independently using histological analysis of H&E-stained sections and via FolliTracker, a live confocal-based imaging and analysis workflow that detects follicles by overlapping mCherry and EGFP fluorescence signals. Viral ROs underwent sequential transduction with AAV-SaCas9 and AAV-DS vectors prior to reaggregation, whereas control ROs were not exposed to virus-containing media. mCherry signal was driven by the ubiquitous SFFV promoter and EGFP signal was driven by the mAMH promoter, a hormone expressed specifically in granulosa cells of developing follicles. Spearman's correlation between follicle counts quantified by histology and by FolliTracker across **A)** pooled data from all ROs (r^2=0.0010), **C)** control ROs only (r^2=0.4022), and **E)** viral ROs only (r^2=0.0002). To evaluate agreement between methods, Bland-Altman analysis was used to assess bias and proportional differences, with simple linear regression of Bland-Altman differences against the mean follicle count determining the presence of proportional bias **(B, D, F)**. Bland-Altman plots show **B)** pooled data with a mean bias of -133.6% ± 100.6% (95% LoA [-330.9, 63.6]; r^2=0.2814), **D)** control data with a mean bias of -195.8% ± 11.09% (95% LoA [-217.5, -174.1]; r^2=0.4611), and **F)** viral data with a mean bias of -24.8% ± 93.3% (95% LoA [-207.7, 158.1]; r^2=0.3449). Data are presented as individual ROs with best-fit regression lines shown. Dashed lines represent 95% CI; mean bias ± SD and 95% LoA are reported in the figure legend and accompanying text. The slope of regression line did not differ significantly from zero in a Bland-Altman analysis, demonstrating no proportional bias (B, D, F). AAV, adeno-associated virus; AMH, anti-Müllerian hormone; Cas9, CRISPR-associated protein 9; CI, confidence interval; DS, donor strand; EGFP, enhanced green fluorescent protein; H&E, haematoxylin and eosin; LoA, limits of agreement; RO, reaggregated ovary; SD, standard deviation; SFFV, spleen focus-forming virus.

As expected, follicle number identified via histology did not demonstrate a strong relationship to follicle number found via FolliTracker in control ROs (r^2=0.4022) (Figure 5.3.16C). FolliTracker-derived follicle counts were lower than those inferred from histology (mean bias, -195.8% ± 11.09%; 95% LoA [-217.5, -174.1]). No significant proportional bias was found (r^2=0.4611) (Figure 5.3.16D). However, follicle number found in viral ROs was also unrelated between methodologies, with regression analysis confirming a negligible relationship (r^2=0.0002) (Figure 5.3.16E). FolliTracker demonstrated a mean bias of -24.8% ± 93.3% (95% LoA [-207.7, 158.1]). No significant proportional bias was found (r^2=0.3449) (Figure 5.3.16F).

5.3.17 Total tissue volume was highly correlated between both methodologies

Total tissue volume was correlated between histological and FolliTracker findings, indicating a strong linear relationship (r^2=0.9229; p<0.0001). (Figure 5.3.17A). Agreement between RO volume findings obtained via FolliTracker and histology was assessed using the Bland-Altman analysis (Figure 5.3.17B). FolliTracker yielded lower values of tissue volume compared to histology, with a mean bias of -8.3% ± 10.4% (95% LoA [-28.61, 11.97]), but no significant proportional bias was found (r^2=0.08847).

5.3.18 The recorded values for the proportion of mCherry-positive area from FolliTracker and immunohistochemical analysis were correlated

When the proportion of mCherry-positive area was compared between histology-based and FolliTracker findings, the results were correlated with a significant positive relationship observed (r^2=0.6475; p<0.01) (Figure 5.3.18A). Proportion of mCherry-positive area is shown with the Log_{10} scale applied for improved visualisation. Linear scale graphs are included in Appendix II (Figure AII.5.3.18).

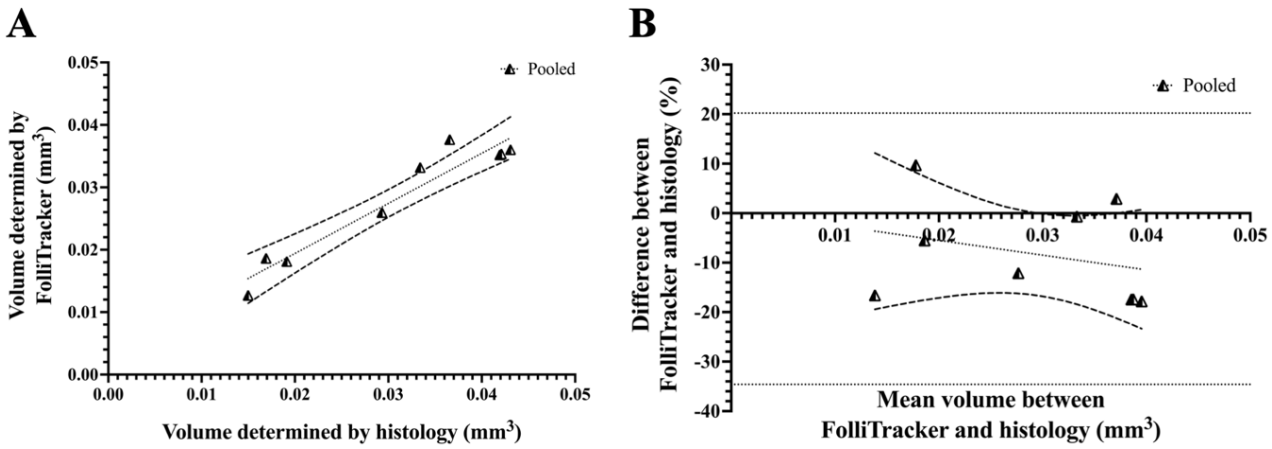

Figure 5.3.17) Correlation and agreement of total tissue volume quantified via FolliTracker and histological analysis in reaggregated ovaries following 14 days in culture. Tissue volume per RO was independently quantified via histological and FolliTracker analysis. Histological volume was determined using the Cavalieri principle (planimetry method) from serial H&E-stained sections. FolliTracker-based volume was obtained from confocal reconstructions using Arivis Vision4D segmentation of the CF640 channel, with all ROs stained using SiR-DNA (4 µmol). Viral ROs underwent sequential transduction with AAVs prior to reaggregation, whereas control ROs were not exposed to virus-containing media. **A)** Spearman's correlation between total tissue volume (mm^3) determined by histology and FolliTracker (r=0.8833; p<0.01), with significant positive relationship observed (r^2=0.9229; p<0.0001). **B)** Agreement between methods was evaluated using Bland-Altman analysis, which identified a mean bias of -8.3% ± 10.4% (95% LoA [-28.61, 11.97], r^2=0.0885). The slope of regression did not differ significantly from zero, showing no significant proportional bias. Data are presented as individual ROs, with best-fit regression lines. Dashed lines represent 95% CI; mean bias ± SD and 95% LoA are reported in the figure legend and accompanying text. AAV, adeno-associated virus; CF, cyanine fluorophore; CI, confidence interval; H&E, haematoxylin and eosin; LoA, limits of agreement; RO, reaggregated ovary; SD, standard deviation; SiR-DNA, silicon-rhodamine deoxyribose nucleic acid.

Agreement between FolliTracker and histology-based methods was determined using Bland-Altman analysis. FolliTracker tended to underestimate the proportion of mCherry signal by -7.2% ± 14.0% (95% LoA [-34.62, 20.21]) when compared with histology (Figure 5.3.18B). Simple linear regression of the Bland-Altman difference against the mean found there was significant proportional bias (r^2=0.9845; p<0.0001).

5.3.19 The proportion of mCherry signal correlated with improved follicle agreement

To evaluate a potential factor of follicle detection concordance between both methods, the proportion of mCherry-positive area from IHC and the follicle agreement of FolliTracker and histology was compared. A strong positive correlation was observed (r=0.8549; p<0.01), indicating that increased mCherry signal was associated with improved concordance between methods (Figure 5.3.18C). Simple linear regression further supported this relationship (r^2=0.6155; slope, 5.182; p<0.01), suggesting that ~33.6% of mCherry expression may represent the threshold for follicle concordance.

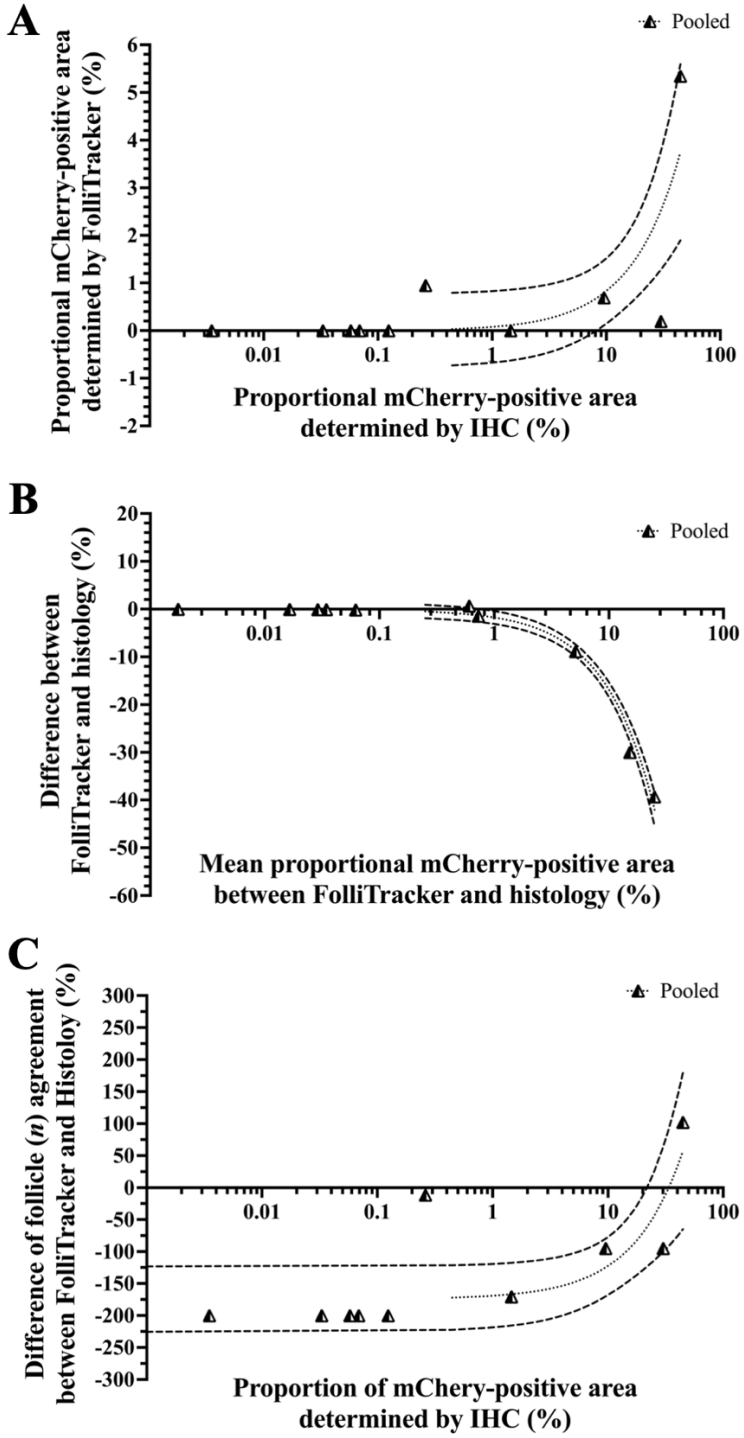

Figure 5.3.18) Correlation and agreement of proportional mCherry-positive area quantified via FolliTracker and histology-based methodologies, and its relationship with follicle detection concordance. Follicle number per RO was quantified independently using histological analysis of H&E-stained sections and via FolliTracker, a live confocal-based imaging and analysis workflow that detects follicles by overlapping mCherry and EGFP fluorescence signals. Viral ROs underwent sequential transduction with AAV-SaCas9 and AAV-DS vectors prior to reaggregation, whereas control ROs were not exposed to virus-containing media. mCherry signal was driven by the ubiquitous SFFV promoter and EGFP signal was driven by the mAMH promoter, a hormone expressed specifically in granulosa cells of developing follicles. ROs were cultured for 14 days, fixed, and processed for histological analysis and IHC using DAB chromogenic staining to detect mCherry expression. **A)** Spearman's correlation between proportional mCherry-positive area (%) determined by IHC and by FolliTracker (r=0.8349; p<0.01), with a significant positive relationship (r^2=0.6475; p<0.01). **B)** Agreement between methods was evaluated using Bland-Altman analysis, which identified a mean bias of -7.2% ± 14.0% (95% LoA [-34.62, 20.21]), as well as proportional bias observed (r^2=0.9845; p<0.0001). **C)** Spearman's correlation between proportional mCherry-positive area determined by IHC and follicle agreement (%) between both methodologies (r=0.8549; p<0.01), with a significant positive relationship observed (r^2=0.6155; p<0.01). Interception at the x-axis suggests that ~33.6% mCherry-positive area represents the threshold at which follicle identification optimally concordant between methodologies. All x-axes are displayed on a Log_{10} scale for improved visualisation. Data are presented as individual ROs with best-fit regression lines shown. Dashed lines represent 95% CI; mean bias ± SD and 95% LoA are reported in the figure legend and accompanying text. AAV, adeno-associated virus; Cas9, CRISPR-associated protein 9; CI, confidence interval; DAB, 3,3′-diaminobenzidine; DS, donor strand; H&E, haematoxylin and eosin; IHC, immunohistochemistry; LoA, limits of agreement; RO, reaggregated ovary; SD, standard deviation; SFFV, spleen focus-forming virus.

5.4 Discussion

This study established and evaluated FolliTracker, a novel live-imaging method designed to quantify and monitor early ovarian follicle development. By integrating AAV-mediated fluorescent labelling, the FolliTracker imaging and computational analysis workflow enabled the longitudinal collection of tissue- and follicle-associated signals within intact RO tissues over a 14-day culture period. This workflow addresses the gap between static histological assessment and dynamic, longitudinal quantification in living ovarian tissue.

FolliTracker-derived tissue volume and mCherry metrics correlated with histology/IHC, whereas follicle counts did not with sources of discordance examined further below. The volume and proportion of mCherry signal recorded by FolliTracker were strongly correlated with histology-based methods, supporting the validity of semi-automated volumetric quantification. Similarly, mCherry expression was strongly correlated to improved follicular agreement, supporting the association between mCherry signal and follicle detection. Although follicle number itself was not correlated between FolliTracker and histology, this divergence likely reflects variable transduction efficiencies and thresholding limitations rather than a permanent discrepancy or bias.

Importantly, viral transduction did not appear to adversely affect follicle number, developmental stage distribution, growth rate, or the presence of a surrounding TC layer. This aligns with previous *in vivo* observations that AAV9-mediated ovarian transduction preserved follicular morphology and stromal integrity without oocyte interference in human and mouse models (Kanatsu-Shinohara *et al.*, 2022; Pépin *et al.*, 2015). Minor differences in oocyte area and AMH intensity may represent physiological variation rather than evidence of dysfunction. Whilst constrained by sample size and tissue depth required for confocal optical sectioning, these findings provided a proof-of-concept for FolliTracker as a potential method for ovarian tissue and follicular assessment. The subsequent sections of this discussion explore these findings in greater depth and contextualise them within the current landscape, highlighting opportunities for refinement and application. Whilst absolute follicle

counts remain conservative under current thresholds, the system reliably tracked relative changes within the same RO across time.

This Chapter developed the FolliTracker workflow from investigations introduced earlier in this thesis. Building upon the transduction optimisation and AAV vector design described in Chapter 4, the present work extended those techniques and insights into a functional imaging method. Investigations into follicle formation and development in ROs of different generation processes (RO versus ROEx) in Chapter 3 established the selected RO generation protocol. Together, these findings demonstrated the technical feasibility and biological tolerance of viral labelling in the cultured RO.

This workflow represents the convergence of three previously independent methodological domains: organoid/RO generation and culture, viral transduction of ovarian somatic cells, and semi-automated three-dimensional quantification. Prior approaches, such as whole-mount or cleared-tissue imaging (Barbato *et al.*, 2023; Feng *et al.*, 2017; Harrison *et al.*, 2025; Rinaldi *et al.*, 2018; Soygur and Laird, 2021) and histological end-point analyses (Barbato *et al.*, 2023; Bjarkadottir *et al.*, 2021; Blevins *et al.*, 2024; Kuscu *et al.*, 2025; Soleimani *et al.*, 2006; Walker *et al.*, 2021), have largely relied on fixed-tissue analysis or semi-quantitative visual inspection of ovarian follicles, limiting temporal insight and increasing variability between samples. Previous studies have incorporated live, time-lapse imaging involving cultured ovarian tissues, but relied on morphological analysis via microscopy with limited early-stage follicle visualisation (Komatsu *et al.*, 2015; Murase *et al.*, 2017), isolated transgenic pre-ovulatory follicles (Thomas *et al.*, 2024), or visualised early-stage follicles *in vivo* via fluorescent contrast agent intravenous injection without specified-labelling and quantification (Bochner *et al.*, 2015).

FolliTracker found consistent differences between control and viral ROs across follicular and mCherry expression analyses. As controls were not exposed to virus-containing media, FolliTracker-based follicle identification was not expected to perform in controls. The control group served as a negative benchmark to assess background segmentation and tissue metrics, rather than a performance

comparator. The decision to only assess follicle number from culture D7 was due to the results described in Chapter 3. AMH expression is known to be relatively restricted to GCs from primary stage follicles and onwards (Dharma *et al.*, 2009; Gruijters *et al.*, 2003; Visser *et al.*, 2006; Weenen *et al.*, 2004). As described in Chapter 3, primary follicles were prevalent proportionally after seven days in culture, but almost absent when assessed on D0 and D3, respectively. In this study, the number of follicles detected in the viral group via FolliTracker was significantly greater compared with the control group at each assessed culture timepoint between day 7–14. This was confirmed with a two-way ANOVA where experimental condition represented the dominant source of variance for follicle number, whilst culture timepoint and interaction between timepoint and individual RO did not contribute significantly. The persistence of this difference across independent samples indicated that transduction was associated with either a greater number of identifiable follicles or enhanced detectability of follicular structures via FolliTracker. Quantification of mCherry fluorescence corroborated these findings. The proportion of mCherry was significantly greater in viral ROs than control ROs at all timepoints. Experimental condition was the predominant source of signal variation with individual ROs over time contributing a modest but significant variance. The differences between ROs likely reflected biological variability in viral uptake. Culture day alone did not influence signal magnitude, speaking to the stability of transgene expressed throughout culture.

The combined results of significantly lower follicle count and lower mCherry signal in control ROs, as determined by FolliTracker, was expected as the control group were not exposed to vectors encoding for ubiquitous mCherry and mAMH-driven EGFP expression. This finding is consistent with control/non-transduced cells in other studies (Baek *et al.*, 2025; Hu *et al.*, 2024), as well as previously reported results (Chapter 4.3). Low-level signal detected in control ROs is consistent with known autofluorescence and background signal in fluorescence imaging and does not affect the overall interpretation of transduction-dependent differences (Baek *et al.*, 2025; Barroso *et al.*, 2023; Dittmar *et al.*, 2011; Hickey *et al.*, 2022). Overall, the significant difference between groups indicated a transduction-associated effect when assessed with FolliTracker.

FolliTracker outputs were compared against well-established histology-based methods to test agreement in follicle detection, tissue volume, and mCherry-associated parameters. Histology remains the prevailing gold standard for quantifying, classifying, assessing ovarian follicles by providing high-resolution imagery of cellular and structural organisation; acting as a comparator for proposed methodologies (Adeniran *et al.*, 2021; Bjarkadottir *et al.*, 2021; Demır *et al.*, 2025; de Koning *et al.*, 2024; Kuscu *et al.*, 2025; Walker *et al.*, 2021). Modernisation of this method to address labour/time-intensity and subjectivity bias have come in the form of automated quantification and classification processes of H&E-stained and immuno-labelled sections (Blevins *et al.*, 2024; Hassan *et al.*, 2024; İnik *et al.*, 2019; Picut *et al.*, 2008; Yin *et al.*, 2025). Yet, a fundamental limitation of the heterogeneity of approaches may lead to inter-laboratory variability and poor cross-study comparability (Adeniran *et al.*, 2021; Tilly, 2003). Alternative methods to assess follicles in tissue have been established but require fixation and optical clearing (Folts *et al.*, 2025; Harrison *et al.*, 2025; Lin *et al.*, 2016), thus analysis is restricted to single static end-points. In contrast, FolliTracker was designed to deliver dynamic, reproducible, three-dimensional data in real-time over a multitude of timepoints.

Tissue volume measurements demonstrated strong concordance between FolliTracker and histological assessment. When corresponding ROs were compared, total tissue volume was highly correlated between the two methods with simple linear regression confirming a significant positive association. Regression analysis found a negligible relationship and demonstrated close approximation between both methods. Bland-Altman analysis found a modest systemic underestimation from FolliTracker with no significant proportional bias. The high level of agreement indicated that FolliTracker was capable of accurately reconstructing total tissue volume from live, confocal z-stacks, despite inherent differences involved in data acquisition between methods. The minor underestimation could be attributed to known technical constraints of live imaging, including limitations of optical penetration depth (Liang *et al.*, 2025; Schneckenburger and Richter, 2021). Utilising conventional assessment as the ‘gold standard’ to interpret these results should be done with

caution as morphology, size, and volume are notably impacted during the fixation and dehydration of tissues (Adeniran *et al.*, 2021; Burton *et al.*, 2014). Nonetheless, the consistency of relationships between methods supported the segmentation and volumetric algorithms used by FolliTracker to capture structural data.

The proportion of mCherry-positive signal derived from FolliTracker correlated strongly with the proportion of chromogenic DAB staining of corresponding RO sections. A robust linear relationship between the two methodologies confirmed a significant positive relationship. Bland-Altman analysis found that FolliTracker yielded lower values of the proportion of mCherry signal relative to IHC. However, significant proportional bias was detected. This may reflect the inherent difference of how fluorescence-based (i.e., FolliTracker) and chromogenic methods (i.e., IHC/DAB) detect and amplify fluorescent/molecular signals from samples. Fluorescence signalling in confocal microscopy can be underrepresented with imaging depth due to scattering, refractive index mismatches, and spherical aberrations that attenuate light paths (Booth, 2007; Dekkers *et al.*, 2019; Lichtman and Conchello, 2005). Comparative analyses of fluorescence confocal microscopy similarly demonstrated reduced signal intensity, especially in thick tissues, and interpretability versus conventional IHC, with the latter known for its stability and morphological fidelity (Nackenhorst *et al.*, 2022; Rizzardi *et al.*, 2012). However, IHC is semiquantitative and highly subjective with a non-linear relationship between staining intensity and protein presence with a propensity to overestimate signal (Adeniran *et al.*, 2021; Taylor and Levenson, 2006; Varghese *et al.*, 2014). Various fixation and processing decisions during IHC can enhance epitope exposure and lead to localised signal amplification, as demonstrated by the Williams group previously (Adeniran *et al.*, 2021). It should be noted that established strategies have been employed here and by others to address this limitation (İnik *et al.*, 2019; Rizzardi *et al.*, 2012; Ruifrok and Johnston, 2001; Taylor and Levenson, 2006; Varghese *et al.*, 2014). Despite the predicted lower yield, the cross-method agreement and similar relative differences between groups were evident when comparing FolliTracker against conventional IHC. This reinforced that FolliTracker could reliably assess fluorescence signal.

The absence of correlation of follicle count between FolliTracker and histological assessment highlights the challenge to align different methodologies at first-pass in an initial study. FolliTracker produced different follicle number estimates compared with histology, a consistent discrepancy across the observed range, suggesting this was unlikely to reflect random error. Several factors contributed to the underestimation from FolliTracker and lack of result congruency. First, variability in viral transduction would have influenced the ability to detect 'follicles' (via EGFP signal overlapping mCherry) with FolliTracker. As assessed via mCherry signal with IHC assessment, transduction efficiency ranged from 0.26% to 44.7% in viral ROs. The heterogeneity demonstrated here is consistent with previously reported outcomes wherein AAV tropism and transduction efficiency vary widely in primary cells and tissues, including both intra- and inter-sample variability (Ellis *et al.*, 2013; Halbert *et al.*, 1995; Walkey *et al.*, 2025; Westhaus *et al.*, 2020). Results reported in this Chapter estimated that a transduction efficiency of ~33.6% would yield more accurate follicle counts. Only two of the five viral RO tissue sections had an average proportion of mCherry-positive area that met/surpassed this value.

Second, the mCherry threshold (set at 550 AU) was determined from calibration of the present dataset with expertise from the researchers at the Cellular Imaging Core Facility. ROs consisted of a heterogeneous population of primary cells wherein endogenous autofluorescence is expected. It should be acknowledged that various techniques have been implemented to utilise well-characterised cell-specific autofluorescence to the advantage of the investigators in alternative studies (Campbell *et al.*, 2022; Roet *et al.*, 2024; Wei *et al.*, 2023). A methodological study has demonstrated that standard mCherry proteins, as utilised here, may generate background signal due to an unintended short isoform which may lead to artificial fluorescence signals (Fages-Lartaud *et al.*, 2022). Further, another study found that recombinant AAV-mediated co-transduction of fluorescent reporters, mCherry and EGFP, resulted in heterogeneous and occasionally discordant expression patterns, wherein IHC assessment exceeded true transduction frequency compared to other molecular assays (Fehrman *et al.*, 2025). These findings suggest the FolliTracker may underestimate follicle number,

while histological assessment may overestimate counts due to reporter-specific artefacts and signal amplification. Despite the numerical discrepancy, a clear correlation was observed between the proportion of mCherry signal and the agreement in follicle number between methodologies. Specifically, higher mCherry signal was associated with closer agreement between FolliTracker and histological follicle counts, with histology used as the reference standard.

Beyond efficacy, the safety of FolliTracker also was assessed. To evaluate whether AAV-mediated fluorescent labelling affected the integrity or developmental progression of follicles in ROs, histological and immunohistochemical parameters were compared between viral and control tissues after the 14-day culture period. Across analyses, transduction did not overtly influence factors, including follicle number, which suggests that FolliTracker was biologically well-tolerated in cultured ROs.

Total tissue volume was comparable between experimental groups which indicated that transduction did not impact tissue formation, accelerate apoptosis, or any other overt cytopathic effects. Average total follicle number was also similar between control and viral ROs, with the distribution of developmental stages unaffected by condition.

Primary follicles predominated in both groups following 14 days in culture (control, 59.12%; viral 73.81%), which was consistent with what was observed for P6 ROs following 14 days of culture or transplantation by Lo *et al.* (2025). Pre-antral follicles were sparse in control tissues and absent in viral ROs, which has been previously observed in RO model studies (Eppig and Wigglesworth, 2000; Lo *et al.*, 2019). In Chapter 3, extended culture duration (ROEx), produced pronounced effects on follicle stage distribution and viability. The proportion of follicles surrounded by TCs was similar between groups (control, 75.7%; viral, 86.8%), suggesting that stromal integrity and TC differentiation were preserved. This is consistent with morphological criteria for healthy follicles and supports the potential of future gonadotrophin-dependent growth (Grasa *et al.*, 2016; Honda *et al.*, 2007; Liu *et al.*, 2015; Lo *et al.*, 2019; Sheikh *et al.*, 2023; Walker *et al.*, 2021; Young and McNeilly,

2010). The absence of notable structural abnormalities, on the follicular and tissue level, are consistent with evidence that support the safety of AAVs in mammalian systems (mouse and human), including ovarian tissues (Baek *et al.*, 2025; Ellis *et al.*, 2013; Kanatsu-Shinohara *et al.*, 2022; Pacak *et al.*, 2008; Pépin *et al.*, 2015; Zincarelli *et al.*, 2008). Previous studies have shown that germ-line and somatic cell populations have demonstrated normal function and genomic stability after AAV exposure in ovarian tissue (Kanatsu-Shinohara *et al.*, 2022; Walkey *et al.*, 2025; Zhao *et al.*, 2020).

Follicle and oocyte morphological parameters further supported absence of cytopathic effect. Follicle area was similar between control and viral groups, but the oocyte area of viral follicles was smaller than those in controls. This reduction was not accompanied by structural irregularity or asymmetry. Slightly smaller oocytes may reflect delayed germ cell cytoplasmic expansion due to the numerically larger proportion of primary follicles in viral ROs. When assessed in relation to GC area, oocyte growth demonstrated a weaker association in viral ROs compared with controls (Section 5.3.9D), suggesting a potential uncoupling of oocyte and GC growth dynamics following transduction. Cultured ROs have previously demonstrated reduced oocyte and follicle areas compared to wild type ovaries (Lo *et al.*, 2019). Variations in follicular parameters have been observed in cultured ovarian tissue when compared to *in vivo* controls, as well (Bjarkadottir *et al.*, 2021; Kuscu *et al.*, 2025; Murase *et al.*, 2017; Walker *et al.*, 2021; Yang *et al.*, 2020). However, the preserved GC density and conserved follicle stage distribution between the control and viral groups support that GC proliferation and recruitment was maintained. The consistent organisation and growth of follicular GCs between viral and control groups indicated that AAV-mediated gene delivery did not introduce obvious morphological degeneration or deleterious development within the 14-day culture period.

When assessed with IHC analyses, the proportion of AMH-positive follicles was not significantly different between control and viral groups. Yet, the mean normalised AMH intensity was greater in viral ROs than in control ROs, which was consistent with the significant association between experimental condition and staining grade found. Elevated AMH expression in viral follicles may reflect leakiness wherein the hormone is overexpressed due to the mAMH promoter driving EGFP

expression. Gene 'knock-in' systems, including those involving CRISPR/Cas9, have the potential for leakiness (Haery *et al.*, 2019; Ling *et al.*, 2024). AMH, typically expressed from the primary to pre-antral stages, is a putative marker of ovarian reserve and positively correlated with follicle growth (Dharma *et al.*, 2009; La Marca and Volpe, 2006; Moolhuijsen and Visser, 2020; Visser *et al.*, 2006; Zhang *et al.*, 2014). The maintenance or modest elevation of AMH in viral ROs may reflect altered regulation of AMH expression under transduction conditions (Lo *et al.*, 2019; Telfer and Zelinski, 2013; Wang *et al.*, 2013). However, under- and overexpression of AMH is a marker of ovarian dysfunction, reflecting the end of the reproductive life-span and PCOS, respectively (La Marca and Volpe, 2006; Pellatt *et al.*, 2007). Thus, further experimentation would be required to elucidate the impact, if any, of FolliTracker to follicular AMH expression in the RO, as *in vitro* and *in vivo* reports on the impact of overexpression are varied (Moolhuijsen and Visser, 2020; Pankhurst *et al.*, 2018; Wang *et al.*, 2013; Zhang *et al.*, 2014). It should be noted that, despite this result, other follicular parameters were consistent between experimental conditions.

From the presented results, the viral transduction of primary murine ovarian cells via FolliTracker preserved follicular integrity, stage distribution, and GC proliferation with minor variations in oocyte size and AMH intensity. The outcomes presented are consistent with previously established definitions of healthy cultured follicles (Adeniran *et al.*, 2021; Bjarkadottir *et al.*, 2021; Kuscu *et al.*, 2025; Lo *et al.*, 2019; Walker *et al.*, 2021), as well as reports of AAV safety and tolerance in mammalian tissues (Ellis *et al.*, 2013; Zincarelli *et al.*, 2008). Immune response and other signs of dysfunction should still be monitored when utilising AAV-mediated gene delivery (Costa-Verdera *et al.*, 2025; He *et al.*, 2022; Suoranta *et al.*, 2022). These findings support future optimisation and expansion of the FolliTracker workflow to improve accuracy of results, without compromising the viability and integrity of samples.

Refinements to FolliTracker system are necessary to improve its accuracy and robustness before it can be established as a formal method. Optimisation was considered at three stages throughout the transduction, imaging, and analytical pipeline. Viral vector design and comprehensive adjustments to

culture media could also serve as areas of interest for methodological improvement. However, these changes could cause significant downstream effects and, thus, would require extensive research and fine-tuning. Practical strategies to build upon the current workflow without altering the overarching aim of this process is discussed further in Chapter 6.

Cross-model validation is essential to solidify the efficacy of FolliTracker. Histology and IHC can provide morphological context, but the inclusion of tools like molecular assays (e.g., RT-PCR/qPCR; confirmation of viral genome integration) and western blotting (establish correlation of fluorescence intensity with true transgene expression levels) to solidify the efficacy of FolliTracker (Kanatsu-Shinohara *et al.*, 2022; Stephens *et al.*, 2018) should be considered. Although beyond the scope of the current study, these methods would aid in defining thresholds for signal detection via quantitative evidence and support comparison across more studies.

In conclusion, this Chapter established FolliTracker as a technically feasible and biologically compatible method for live, dynamic assessment of follicular and tissue-associated parameters in the RO model. Through integration of AAV-mediated fluorescent labelling and three-dimensional data collection, this Chapter demonstrated that live follicle tracking could be achieved without compromising tissue integrity or follicle developmental progression. Minor deviations in oocyte size and AMH intensity were observed, yet overall follicular morphology, growth, and organisation were preserved; demonstrating that viral transduction and confocal imaging were well tolerated under the experimental protocol. These findings support further optimisation of FolliTracker to improve quantification accuracy while maintaining tissue viability.

6. DISCUSSION

"The great tragedy of science — the slaying of a beautiful hypothesis by an ugly fact."

— **T. H. Huxley**, Presidential Address to the British Association (1870)

6.1 Introduction

This thesis developed a novel approach to support and monitor early follicle growth in culture. FolliTracker is an integrated experimental–analytical workflow to enable longitudinal tracking of follicles in tissues. Here, FolliTracker refers to an integrated experimental–analytical workflow, comprising of tissue culture, viral labelling, live imaging, and downstream computational analysis. The work was motivated by fundamental limitations of conventional histology-based approaches which, whilst providing high-resolution morphological data, are terminal, two-dimensional, and capture static snapshots of a highly dynamic developmental process (Adeniran *et al.*, 2021; Harrison *et al.*, 2025).

The current understanding of follicle formation, development, activation, and growth is primarily inferred from cross-sectional observations, as opposed to continuous empirical data of follicles tracked over time. With the growing clinical need for fertility preservation techniques (e.g., women with POI or survivors of haematological cancers) and an increasing understanding that *in vitro* ovarian models diverge from those *in vivo* (Cheng *et al.*, 2024; Lo *et al.*, 2019; Telfer and Andersen, 2021), robust methodologies are critically needed to enable the real-time assessment of follicle development in tissue.

Across three experimental chapters, this research established:

1) Appropriate reaggregation protocols to support follicle reformation and early-stage growth in culture (Chapter 3)
2) AAV-mediated transduction strategies to enable cell-type-specific labelling of primary murine ovarian cells without compromising cell viability (Chapter 4)
3) A live-imaging and computational workflow to generate quantitative, three-dimensional datasets from intact RO tissues over 14 days of culture (Chapter 5)

This discussion synthesizes principal findings across Chapters 3–5, evaluates FolliTracker's biological insights and technical limitations, contextualises the work within recent advancements (particularly the methodologically parallel study by Yoshida *et al.* (2025)), and outlines strategies for technical refinement, as well as future translational applications.

To my knowledge, few existing approaches permit the three-dimensional, live imaging of follicles in reaggregated ovarian tissue with simultaneous volumetric quantification and viral reporter-based labelling across multiple timepoints. By converging tissue culture, viral gene delivery, optical imaging, and computational analysis, FolliTracker provided a potential new tool for the ovarian researcher's methodological arsenal; representing a shift toward dynamic, quantitative investigation of follicles.

6.2 Summary of principal findings and key insights

Throughout this project, a series of experimental models were developed to establish and validate techniques capable of supporting and monitoring early follicle growth in culture.

6.2.1 Chapter 3: Reaggregated ovary characterisation and protocol selection

Morphological analysis in Chapter 3 confirmed that follicles within ROs progressed through early developmental stages whilst retaining expected cellular organisation and integrity, consistent with prior reports (Lo *et al.*, 2019). However, the developmental trajectories of ROs observed *in vitro*

diverged rapidly from age-matched *in vivo* WOs. Proportional distribution of follicles did not differ significantly between uncultured ROs and age-matched P6 WOs. Although, within three days of culture, transitional follicles comprised 59.1% of all follicles in ROs vs. 26.3% in P9 WOs (adj. $p<0.05$); further diverging with 35.2% primary in ROs vs. 9.2% in WO P13 by D7 (adj. $p<0.05$), respectively. Thus, reflecting wider research that *in vitro* conditions promote accelerated follicle activation (De Roo *et al.*, 2020; Telfer and Andersen, 2021; Wang *et al.*, 2013; Zhao *et al.*, 2021). Fragmentation of cultured human ovarian tissue has been found to accelerate primordial activation, more than chemical *in vitro* activation (Hao, Li, *et al.*, 2024), attributed to the disruption of key regulatory signalling cascades like the Hippo pathway (Grosbois and Demeestere, 2018; Kawamura *et al.*, 2013; De Roo *et al.*, 2020). ROs generation involves the complete disruption of cellular communication, including oocyte-granulosa cross-talk, following tissue dissociation. However, the effects of ECM breakdown and cross-talk disruption cannot be separated from alterative factors like altered oxygen diffusion, as all of which may impact the PI3K-Akt and Hippo pathways. In consequence, this work highlighted the limitations of using age-matched *in vivo* WOs as control comparators, especially in longer durations of culture.

The ROEx group did not enhance follicle yield nor developmental progression, instead it produced smaller oocytes and follicles with reduced growth trajectories compared to the standard RO protocol. Disrupted oocyte morphology and growth could suggest that bidirectional oocyte-granulosa communication was deficient (Eppig, 1991; Gilchrist *et al.*, 2004; Marchais *et al.*, 2022). With the modest sample size (ROEx, $n=5$ for each culture timepoint), the reported results should be interpreted as the demonstration of an adverse trend as opposed to a dose-response relationship (extended time in culture to adverse outcomes). Investigations into extending RO protocol were to facilitate viral transduction incubation periods (12 hr vs. 24 hr). However, the standard RO generation for FolliTracker implementation balanced follicle health with promoting transduction efficiency. These analyses contextualised follicle progression within the RO environment and established the biological relevance and limitations of this model.

6.2.2 Chapter 4: AAV-mediated transduction optimisation

Building upon this work, Chapter 4 focused on developing an efficient and biocompatible approach to introduce exogenous fluorescent reporters into a heterogeneous population of primary murine ovarian cells. AAV vectors were selected due to their favourable safety profile (Zwi-Dantsis *et al.*, 2025), capacity for stable transgene expression in non-dividing cells without random insertion of viral DNA (Ahmadi *et al.*, 2023), with serotype 9 selected due to its transduction efficiency and tropism (Kanatsu-Shinohara *et al.*, 2022; Zhao *et al.*, 2020; Zincarelli *et al.*, 2008). Two constructs were designed for a combined approach to follicular cell-specific targeting: 1) a vector encoding SaCas9 and sgRNA targeting mROSA26, and 2) a subsequent vector with two fluorophores (mCherry and EGFP) driven by different promoters (SFFV and mAMH promoter, respectively) and flanked by mROSA26 homology arms.

With systematic optimisation of MOI, timing of exposure, and vectors, an mCherry transduction efficiency of 32.0% ± 5.1% was achieved across three independent experiments at an MOI of 1×10^6 gc/cell, as determined by Flow cytometric analysis (Chapter 4.3.2.2). These MOI estimates, however, relate to viral genome counts rather than infectious units and apply to all viable cells in the heterogenous cell population. EGFP (driven by the mAMH promoter, detailed in Chapter 4.2.2) expression was found in 15.2 ± 4.8% of cells (Chapter 4.2.2.1). The observation that EGFP-positive cells represented approximately half the mCherry-positive population initially appeared suboptimal, but AAV9 vectors have been shown to preferentially transduce GCs (Kanatsu-Shinohara *et al.*, 2022), which may have constituted an enriched fraction of the cell population following differential adhesion. Cell viability remained comparable between control and viral groups (96.5% vs. 94.3%) after sequential AAV exposure, with no significant difference in viability demonstrating tolerance and minimised risk of cytotoxicity. This work demonstrated that AAV-mediated gene delivery could achieve meaningful transduction levels in primary murine ovarian cells without compromising cellular integrity and viability. However, off-target editing, DNA damage, or longer-term genomic stability were not assessed in this Chapter and remain relevant considerations for future work.

6.2.3 Chapter 5: FolliTracker assessment and validation

Comparative analyses between viral and control ROs demonstrated that AAV-mediated gene delivery and repeated confocal imaging over 14 days did not impair follicle development or tissue integrity. Follicle number (control, 11.9 ± 9.3; viral, 9.8 ± 6.7), stage distribution (primary: control, 59.1%; viral, 73.8%), and morphological parameters including TC recruitment (control, 75.7%; viral, 86.8%) remained comparable between groups when assessed with histology (Chapter 5.3.7). Importantly, FolliTracker measurements of total tissue volume correlated strongly with histological assessment (r=0.95; $p<0.001$), and mCherry fluorescence intensity correlated with IHC detection (r=0.89; $p<0.01$), validating the workflow's quantitative accuracy. However, absolute viral follicle counts generated via FolliTracker were poorly concordant with histology, despite moderate linear correlation (r=0.7379), due to systematic underestimation by -24.8% ± 93.3% (95% LoA [-207.7, 158.1]). The strong correlation between mCherry signal and detection accuracy (r=0.85; $p<0.01$) demonstrated that this limitation was technical and addressable, with a ~33.6% of mCherry-positive area via IHC representing a potential threshold for methodology concordance. In Chapter 4, Flow cytometric assessment achieved a transduction efficiency of 32.0%; suggesting the threshold target is feasible. Alternative and supplementary approaches to optimise follicle detection within the FolliTracker workflow will be discussed in depth below (Chapter 6.3).

6.2.4 Synthesis

This thesis established a workflow to integrate tissue culture, AAV-mediated gene delivery, and live confocal imaging to enable dynamic follicle tracking *in vitro.* FolliTracker could provide a complementary approach to conventional histology, offering temporal resolution and longitudinal data that static methods cannot provide, with potential for future application across diverse experimental contexts.

6.3 Limitations and technical considerations of FolliTracker

A key limitation was the variable transduction efficiencies of AAV-mediated transduction in dissociated ovarian cells across viral ROs (range, 0.3%–44.7%; mCherry-positive area via IHC), likely reflecting a combination of biological heterogeneity and variations in dissociation success (Chapter 5.3.13). The heterogeneity directly impacted FolliTracker's follicle detection sensitivity, as demonstrated by the strong correlation between transduction efficiency and concordance with histology ($r=0.85$; $p<0.01$). ROs that achieved ~30% mCherry-positive area or more showed follicle numbers more agreeable to histology, whilst those with <10% yielded substantial underestimation. The limited packaging capacity of AAV also constrained the size of inserted constructs, restricting the potential for multiplexed or more complex genetic reporters.

Another technical consideration concerns the semi-autonomous computational analysis pipeline. Although the Arivis-based segmentation was validated against histological measurements, the workflow required manual verification of object boundaries to correct artefacts or misclassification errors. Consequently, processing remains partially subjective and time-intensive, particularly in large datasets. The accuracy of follicle recognition also depended on the threshold and overlap criteria established for mCherry and EGFP signals; whilst standardised globally to ensure reproducibility, this may have excluded follicles at the margin of detection or with weak signal intensity.

The comparison between FolliTracker and histological methods revealed a systematic underestimation in viral ROs (mean bias for follicle number, -24.8% ± 93.3%) and lack of correlation of follicle number estimates generated by the imaging-computational workflow relative to histology-based counting. This likely reflects both the volumetric resolution limits of the spinning-disc confocal microscopy and the difficulty in distinguishing closely clustered follicles within tissue. As such, while FolliTracker captured dynamic volumetric and fluorescence intensity data, histology remains a more sensitive measure of absolute follicle number and other morphological structures. Additionally, the lack of molecular validation (e.g., qPCR) prevented definitive confirmation and assessment of

genomic integration versus transient episomal transgene expression. In proliferating cells, such as GCs, episomal AAV DNA would be progressively diluted through mitosis (Ahmadi *et al.*, 2023; Muhuri *et al.*, 2022), raising uncertainty about long-term expression stability. Although a trend of mCherry signal drop-off was not observed over the culture period, understanding the stability of expression would have significant implications for long-term tracking applications. From a biological perspective, interpretation of findings must also consider the limitations of the tissue model. ROs lack the full vascular and stromal architecture of the intact ovary. This was evident in Chapter 3 findings and other published studies, where RO follicles exhibited smaller dimensions, incomplete FBL, and limited TC recruitment (Eppig and Wigglesworth, 2000; Lo *et al.*, 2019).

Finally, sample size and experimental variability imposed practical limitations. Variation in dissociation efficiency and reaggregate morphology between replicates may have contributed to variability in follicle yield or transduction efficiency. The limited sample size of ROs (control, n=8; viral, n=5) also reflect the laborious and material-intensive requirements (e.g., sufficient amount of AAVs) associated with generation. Whilst five independent experiments were completed, larger sample cohorts would strengthen conclusions, enable the detection of modest effects, reduce the impact of random variation, and support more thorough investigations.

6.4 Contextualisation within recent advances: Comparison with Yoshida *et al.* (2025)

A recently published study by Yoshida *et al.* (2025) provides important methodological parallels to FolliTracker. Both employ AAV-mediated gene delivery to primary murine ovarian cells, then generate ovarian tissues for culture after reaggregation from transduced cells. Published during the final stages of writing this thesis, the Yoshida study independently validates core methodological principles, with particular emphasis to the AAV serotype selection and reconstituted ovarian tissue (rOvary) culture, whilst pursuing distinct experimental objectives. Yoshida *et al.* (2025) demonstrated the *in vitro* restoration of fertility in congenitally infertile $Kitl^{Sl\text{-}t}/Kitl^{Sl\text{-}t}$ mice, achieving

live births from oocytes grown in culture after AAV-*Kitl* or recombinant KitL treatment. In contrast, FolliTracker prioritised the development of a quantitative imaging method for longitudinal, dynamic follicular assessment. While both approaches utilised AAV transduction and ovarian reconstitution, procedural differences and divergent aims yielded distinct outcomes (Table 6.4).

Several key methodological differences warrant consideration. Firstly, Yoshida *et al.* employed shorter enzymatic (Trypsin/EDTA) digestion which likely preserved established follicular structures in rOvaries (Yoshida *et al.*, 2025), compared to the dissociation of cells requiring *de novo* follicle formation with FolliTracker. This may have resulted in reduced yield in FolliTracker (~10 follicles per RO) compared with the Yoshida protocol (80 secondary follicles per rOvary).

Spatial parameters may have impacted transduction efficiency as Yoshida's 96-well U-bottom (30,000 cells; 200 µL volume; ~940 cells/mm^2) likely achieved a 4.5-fold higher cell density in 10x smaller volume compared to FolliTracker's 35 mm TCT petri dish (200,000 cells; ~2 mL volume; ~208 cells/mm^2). A more confined layout would maximise the likelihood of virus-to-cell contact. The larger surface area of 35 mm generated 30x more space for more dispersed cells. Despite the greater MOI (1×10^6 vg/cell), FolliTracker experienced greater spatial dilution of viral particles than the Yoshida protocol (~6.7×10^5 vg/cell); contributing to more variable transduction efficiencies. These geometric considerations suggest that shifting to a more confined culture setting (e.g., low media volume, U bottom wells) may yield greater improvements in transduction than an increase in MOI.

A major convergence was in the chosen analytical approaches, Yoshida *et al.* (2025) optimised viral concentration based on functional readouts (secondary follicle yield), whilst FolliTracker selected MOI via Flow cytometry. To assess outcomes, Yoshida employed histology and qPCR to validate outcomes and data collection (Yoshida *et al.*, 2025). FolliTracker implemented live confocal imaging with subsequent computational analysis and histological validation, generating datasets inaccessible via Yoshida's static, terminal methodologies. These complementary strategies reflect diverging priorities, functional fertility restoration versus investigation of follicles.

Table 6.4) Experimental and methodological comparison between Yoshida *et al.* (2025) and the FolliTracker pipeline. Overview of key experimental parameters distinguishing the fertility-restoration focus of Yoshida *et al.* from the FolliTracker live-imaging computation framework developed in this thesis. For each parameter, the table compares the Yoshida protocol with the FolliTracker approach, with qualitative summaries of expected experimental impact or readouts.

Parameter	Yoshida *et al.* (2025)	FolliTracker	Impact on outcomes
Experimental aims	Fertility restoration in infertile murine model	Dynamic, longitudinal follicle tracking	Different priorities
Tissue material, age	P0–P5 ovaries	P6 ovaries	Younger tissue may be more plastic; FolliTracker may be more consistent
Dissociation protocol	Collagenase, 30 min Trypsin, 15 min	Trypsin, 30 min Trypsin, 30 min	Partial versus complete dissociation; some follicular structures preserved versus *de novo* formation
Cell separation	None, heterogenous population	Differential adhesion, somatic enrichment	Oocyte-GC communication preserved versus disrupted
Cell seeding	96-well U-bottom plate	35 mm TCT petri dish	Confined geometry versus dispersed culture
Cell density	30,000 cells/well (~940 cells/mm^2)	200,000 cells/dish (~208 cells/mm^2)	Yoshida likely had 4.5x higher density, improved virus-to-cell contact
Culture volume	~200 µL	~2 mL	FolliTracker had 10x dilution of viral particles
Estimated MOI	~6.7×10^5 vg/cell	1×10^6 gc/cell	FolliTracker had 1.5x higher MOI
Transduction optimisation	Functional: Secondary follicle yield	Technical: Transduction (%; Flow cytometry)	Follicle-focused versus cell-focused
Culture medium	α-MEM	Waymouth	Minor metabolic differences
Serum supplement	10% FBS	10% MS	FBS is standard; MS may contain beneficial species-specific factors
Material to final product	~1.3 ovaries per rOvary	~200,000 cells per RO	FolliTracker more restrictive
RO size	~1.0–1.5 mm diameter	~0.34 mm diameter of viral ROs	Optimised for follicle yield versus optical penetration
Follicle yield	~80 secondary follicles per rOvary*	~10 follicles per RO	Reflects methodological and experimental aims
Analysis methods	Histology, qPCR, stereomicroscopy	Live confocal imaging, histology	Static endpoints versus dynamic temporal data
Primary outcome	Live births	Follicle and ovarian morphometrics	Functional versus quantitative developmental assessment

AAV, adeno-associated virus; α-MEM, alpha minimum essential medium; FBS, foetal bovine serum; gc, genome copies; GC, granulosa cell; MOI, multiplicity of infection; MS, mouse serum; P0/P5/P6, postnatal day 0/5/6; qPCR, quantitative polymerase chain reaction; RO, reaggregated ovary; rOvary, reconstituted ovary; TCT, tissue-culture treated; vg, viral genomes. *Terminology of Yoshida *et al.* (2025).

Despite the methodological and experimental differences, both studies converge on critical findings:

1. AAV8 and AAV9 both effectively transduced ovarian somatic cells without oocyte transduction, validating serotype selection;
2. Reaggregated/reconstituted ovarian cultures supported follicle development despite tissue dissociation to overcome limitations of AAV transduction in intact tissues *in vitro*;
3. Transient AAV-mediated gene expression persisted throughout (14+ day) culture period, enabling transient functional compensation

Integration of Yoshida's approach (proof-of-principle for functional *in vitro* fertility restoration with optimised transduction) and the FolliTracker method (dynamic imaging and quantitative workflow for real-time monitoring of ovarian components) could enable both therapeutic applications and mechanistic investigations with novel, data-rich insights. Theoretically, the integrated protocol could utilise high-efficiency AAV8/9-mediated KitL delivery in tissue, whilst FolliTracker simultaneously quantifies the timing and spatial distribution of KitL expression with the appropriate promoter.

6.5 Methodological refinement and optimisation of FolliTracker

Successful sequential transduction of viral vectors is a key technical requirement for FolliTracker, an integrated experimental-computational workflow. The AAV9 serotype has previously demonstrated robust and consistent transgene delivery in murine ovarian tissue (Kanatsu-Shinohara *et al.*, 2022). However, optimised viral transduction presents a rate-limiting step for efficient and uniform viral expression (Ellis *et al.*, 2013; Halbert *et al.*, 1995; Kanatsu-Shinohara *et al.*, 2022; Walkey *et al.*, 2025; Yao *et al.*, 2023; Zincarelli *et al.*, 2008). The MOI selected (1×10^6 gc/cell), as reported in Chapter 4, was the highest concentration tested. Transduction efficiency has been shown to improve in a linear manner until activity is plateaued with excessive viral infection, causing apoptosis and cellular dysregulation (Dan and Kang-Zheng, 2025). However, primary cells do not necessarily behave in a linear manner, such as uptake variability between cell-types (Kanatsu-Shinohara *et al.*, 2022; Walkey *et al.*, 2025; Zincarelli *et al.*, 2008). Given the variable transduction efficiencies in

Chapter 5 (0.3%–44.7%), increasing viral titre could enhance overall labelling consistency in the FolliTracker model within safe physiological limits. However, further increases in viral titre may exacerbate mosaicism, especially if uptake pathways differ between cell types, impacting the applicability of this workflow.

Several chemical and biological interventions could also improve AAV uptake in primary murine cells. Transduction enhancers, such as polycationic polymers and cell-penetrating peptides, promote cell-surface binding and nuclear entry (Cai *et al.*, 2023; Eliyahu *et al.*, 2005; Guo *et al.*, 2016). Polybrene, a cationic polymer, removes the charge repulsion between viral particles and cellular membranes of the target (Najafi *et al.*, 2024), but can reduce viability in delicate primary cells, which could impact germ cells. The LAH4 peptide has been shown to improve expression of transgenes, as well as cross the brain-blood barrier in the central nervous system (Meng *et al.*, 2021). The FBL has been compared to the brain-blood barrier, so this is of considerable interest for future applications (Kanatsu-Shinohara *et al.*, 2022). However, the aforementioned modifications could negatively affect certain cell-types and become harmful at high doses (Meng *et al.*, 2021).

Extending the incubation period of viral exposure in primary murine cells is not recommended here, as Chapter 3 demonstrated that an extended generation (ROEx) protocol was associated with altered follicle-stage distribution and a potential reduction in follicle growth. Collectively, the above strategies offer a logical route to investigate and optimise transduction efficiencies whilst preserving tissue fidelity. Further optimisation of viral serotype, promoter specificity, or delivery timing could enhance uniformity of transgene expression.

Signal quality of a fluorescent protein is dependent on fluorophore stability and spectral compatibility within the heterogeneous population of murine ovarian cells. mCherry is a widely used red fluorescent protein as it is bright and has demonstrated photostability (Fink *et al.*, 2010). The standard mCherry construct, as used here, can produce a short unintended isoform that generates a low excitation spectra (Fages-Lartaud *et al.*, 2022). Furthermore, the mCherry emission spectrum overlaps with cellular

autofluorescence for lipid-rich or apoptotic cells (Cranfill *et al.*, 2016; Fink *et al.*, 2010; Kleeman *et al.*, 2018; Wu *et al.*, 2009). Alternative far-red fluorophores, such as mScarlet3 or mKate2, could offer a promising alternative to reduce endogenous background and improve specificity (Cranfill *et al.*, 2016; Gadella *et al.*, 2023; Jun *et al.*, 2017; Shang *et al.*, 2024). Substituting mCherry for a far-red variant may improve contrast, maintain brightness, and improve spectral separation from EGFP. EGFP is a convenient and commonly used follicular marker, yet murine tissues have been shown to demonstrate endogenous green-blue fluorescence which could interfere with signal detection (Jun *et al.*, 2017; Lifante *et al.*, 2020). This may lead to false 'follicle' readings in FolliTracker. However, various studies have found that the combination of mCherry and EGFP are suitable for assessment (Doherty *et al.*, 2010; Fink *et al.*, 2010; Kleeman *et al.*, 2018). Marker adjustments could enhance the signal specificity in FolliTracker, supporting more accurate segmentation of individual follicles.

Spinning-disc confocal microscopy was utilised to three-dimensionally image ROs live, in real-time. The imaging of live tissues was constrained due to the thickness of the sample. In the present study, all ROs were within ~300 μm thickness, as a compromise between viability and optical accessibility. Light scatters and spherical aberrations increase with depth and cause an attenuation of fluorescent signal (Booth, 2007; Dekkers *et al.*, 2019; Oreopoulos *et al.*, 2014; Richardson and Lichtman, 2015; Schneckenburger and Richter, 2021). Adjusting the imaging strategy could mitigate this limitation without altering sample preparation. Implementing dual-surface imaging, wherein an image is captured from both the top and bottom of each tissue, would support reconstruction of a more complete volume and image of each RO. The Williams group have already employed this strategy using a whole-mount immunolabelling and optical clearing method in human ovarian tissue (Harrison *et al.*, 2025). This could be achieved either by mechanical inversion of samples between acquisitions, which may be technically challenging, or by integrating an opposing objective configuration. Optical clearing presents a long-term solution for enhancing signal penetration, but this is not practiced in live tissue as of yet. However, a recent publication from Ou *et al.* (2024) may signal that live-compatible clearing agents will be available in the not-so-distant future. Dye molecules which absorb

in the blue regions were found to improve optical transparency of live tissue by increasing the refractive index of the medium; achieving near optical transparency in the abdomen of a live mouse (Ou *et al.*, 2024). Ou was able to achieve imaging depths from 500–800 μm beneath the surface epithelial layer (Ou *et al.*, 2024). Nonetheless, dyes and various agents can induce osmotic stress and/or cytotoxicity with prolonged exposure (Folts *et al.*, 2023; Harrison *et al.*, 2025; Ou *et al.*, 2024). Imaging improvements would support signal preservation and enhance spatial and quantitative data.

Computational changes could support the reproducibility and interpretive accuracy of FolliTracker. The use of a fixed mCherry fluorescence threshold (550 AU) as a signal for transduction provided a practical reference for this thesis. However, a fixed threshold may negate variations in background intensity, z-depth, and inter-batch autofluorescence variation. Transitioning to an adaptive or artificial intelligence-assisted thresholding system could more accurately reflect sample heterogeneity and normalise potential outliers within small sample sizes. Deep-learning models, such as UNet and Cellos, have been established to 'fill in the gaps' with predictive interpretations to assess and visualise organoids (Bai *et al.*, 2024; Kok *et al.*, 2025; Mukashyaka *et al.*, 2023; Park *et al.*, 2023). Existing open-source models can be trained on follicle datasets to detect true fluorescent signal and other morphological structures. By combining brightfield and fluorescence data, these trained analysis pipelines could discriminate genuine follicles with debris and autofluorescence. These pipelines would also further reduce inter-observer bias and improve segmentation accuracy. It should be noted that software-led adaptive organoid tracing and automated analytical workflows through ImageJ have already been implemented for FolliTracker. Expanding this method through artificial intelligence integration could open the door for further advancement as technology develops.

6.6 Future directions and translational potential

The principal translational value of the FolliTracker workflow lies in its ability to repeatedly measure follicle-associated features in the same intact tissue over time, under controlled experimental conditions, without destroying the sample through fixation. It is well-established that gonadotoxic

agents, such as platinum-based chemotherapies, can result in atresia, accelerated primordial follicle activation, and stromal damage (Lopes *et al.*, 2014, 2019; Morgan *et al.*, 2013; Rossi *et al.*, 2016; Sonmezer *et al.*, 2025; Spears *et al.*, 2019). However, most studies on gonadotoxic and fertility-preserving agents must rely on static histology-based methodologies to infer follicle number and activation versus loss via statistical reconstructions and representative samples (Lopes *et al.*, 2014, 2019; Morgan *et al.*, 2013; Rossi *et al.*, 2016; Soleimani *et al.*, 2011). Thus, the timing of damage relative to exposure and heterogeneity of follicle response within the same ovary cannot be directly measured with existing methods. As a result, primordial follicle trajectories, such as direct atresia versus activation then atresia, must be inferred as opposed to observed. By facilitating within-tissue, dynamic analysis, FolliTracker could support mechanistic interrogation of how gonadotoxic or fertility-preserving agents influence follicles, including distinguishing between suppression of activation and preservation through survival. However, further optimisation of detection thresholds and analytical sensitivity is required to maximise quantitative accuracy.

The adaptive nature of FolliTracker, enabled by cell-specific targeting via AAV-delivery and the CRISPR/Cas9 system, could support a wide range of experimental applications. An example of the substitution of a fluorescent reporter to a therapeutic agent to restore fertility has already been discussed in Chapter 6.4, thus will not be explored further here (Yoshida *et al.*, 2025). However, applying the FolliTracker workflow to rare and endangered animals, such as the declining white rhinoceros species, could improve the identification and visualisation of sparse follicles in ovarian tissue; supporting efforts to optimise *in vitro* follicle growth for species preservation (Appeltant *et al.*, 2023; Williams, 2025). Together, by supporting dynamic analysis within intact ovarian tissues, FolliTracker offers a workflow to interrogate fertility-preserving interventions and aid endangered species research by enabling analysis of follicle dynamics over time, complementing histological approaches that require static, terminal assessment.

6.7 Final remarks and overarching conclusions

This thesis aimed to establish techniques capable of supporting and monitoring early follicle growth in culture. Through the investigation of the RO model in culture, targeted AAV-based fluorescent labelling, and live quantitative imaging, the FolliTracker analytical workflow provided a new means of observing real-time follicle growth dynamically and in three-dimensions. These findings confirmed that transduction, live imaging, and prolonged culture of ROs could be completed without significantly compromising follicular health or tissue structure, which validates this multimodal approach as both safe and biologically relevant. The system generated novel, quantitative datasets that captured continuous measures of follicles in culture.

More broadly, FolliTracker demonstrated that converging biological, microscopy, and technologically-advanced tools can modernise and support reproductive research. By enabling continuous, three-dimensional, and data-rich analyses of ovarian tissue, it could further promote cross-discipline research within the ovarian landscape. Ultimately, the work presented here contributes to the growing movement toward dynamic, high-content biological systems that bridge the gap between traditional methods and modern dataset-focused science. FolliTracker represents a step toward integrative, data-driven approaches in ovarian research.

7. REFERENCES

"I hate writing, I love having written."

— **Dorothy Parker**, 'The Paris Review' (1969)

Abercrombie M. Estimation of nuclear population from microtome sections. *Anat Rec* 1946;**94**:239–247. Available at: /doi/pdf/10.1002/ar.1090940210. Accessed September 27, 2025.

Adeniran B V., Bjarkadottir BD, Appeltant R, Lane S, Williams SA. Improved preservation of ovarian tissue morphology that is compatible with antigen detection using a fixative mixture of formalin and acetic acid. *Human Reproduction* 2021;**36**:1871–1890. Available at: https://dx.doi.org/10.1093/humrep/deab075. Accessed May 29, 2025.

Adhikari D, Liu K. Molecular mechanisms underlying the activation of mammalian primordial follicles. *Endocr Rev* 2009;**30**:438–464. Available at: https://pubmed.ncbi.nlm.nih.gov/19589950/. Accessed September 27, 2025.

Ahmadi SE, Soleymani M, Shahriyary F, Amirzargar MR, Ofoghi M, Fattahi MD, Safa M. Viral vectors and extracellular vesicles: innate delivery systems utilized in CRISPR/Cas-mediated cancer therapy. *Cancer Gene Therapy 2023 30:7* 2023;**30**:936–954. Available at: https://www.nature.com/articles/s41417-023-00597-z. Accessed July 13, 2025.

Alam MH, Miyano T. Interaction between growing oocytes and granulosa cells in vitro. *Reprod Med Biol* 2019;**19**:13–23. Available at: https://pubmed.ncbi.nlm.nih.gov/31956281/. Accessed September 27, 2025.

Albertini DF, Combelles CMH, Benecchi E, Carabatsos MJ. Cellular basis for paracrine regulation of ovarian follicle development. *Reproduction* 2001;**121**:647–653. Available at: https://pubmed.ncbi.nlm.nih.gov/11427152/. Accessed September 27, 2025.

American College of Obstetricians and Gynecologists. Committee opinion no. 605: Primary ovarian insufficiency in adolescents and young women. *Obstetrics and Gynecology* 2014;**124**:193–197. Available at: https://journals.lww.com/greenjournal/fulltext/2014/07000/committee_opinion_no__605__primary_ovarian.36.aspx. Accessed December 11, 2025.

Anchundia D, Huyvaert KP, Anderson DJ. Chronic lack of breeding by Galápagos Blue-footed Boobies and associated population decline. *Avian Conservation and Ecology, Published online: Apr 17, 2014 | doi:105751/ACE-00650-090106* 2014;**9**. Available at: http://dx.doi.org/10.5751/ACE-00650-090106. Accessed December 10, 2025.

Anderson RA, Brewster DH, Wood R, Nowell S, Fischbacher C, Kelsey TW, Hamish W, Wallace B. The impact of cancer on subsequent chance of pregnancy: a population-based analysis. *Human Reproduction* 2018:1–10. Available at: https://academic.oup.com/humrep/advance-article-abstract/doi/10.1093/humrep/dey216/5038415. Accessed December 11, 2025.

Anderson RA, Wallace WHB, Telfer EE. Ovarian tissue cryopreservation for fertility preservation: clinical and research perspectives. *Hum Reprod Open* 2017;**2017**:1–9. Available at: https://dx.doi.org/10.1093/hropen/hox001. Accessed December 11, 2025.

Antonouli S, Di Nisio V, Messini C, Daponte A, Rajender S, Anifandis G. A comprehensive review and update on human fertility cryopreservation methods and tools. *Front Vet Sci* 2023;**10**:1151254.

Appeltant R, Hermes R, Holtze S, Modina SC, Galli C, Bjarkadottir BD, Adeniran B V., Wei X, Swegen A, Hildebrandt TB, *et al.* The neonatal southern white rhinoceros ovary contains oogonia in germ cell nests. *Communications Biology 2023 6:1* 2023;**6**:1049-. Available at: https://www.nature.com/articles/s42003-023-05256-5. Accessed December 29, 2025.

Arango NA, Lovell-Badge R, Behringer RR. Targeted mutagenesis of the endogenous mouse Mis gene promoter: In vivo definition of genetic pathways of vertebrate sexual development. *Cell* 1999;**99**:409–419. Available at: https://www.cell.com/action/showFullText?pii=S0092867400815275. Accessed July 10, 2025.

Arjomandnejad M, Dasgupta I, Flotte TR, Keeler AM. Immunogenicity of Recombinant Adeno-Associated Virus (AAV) Vectors for Gene Transfer. *Biodrugs* 2023;**37**:311. Available at: https://pmc.ncbi.nlm.nih.gov/articles/PMC9979149/. Accessed August 3, 2025.

Armbruster N, Lattanzi A, Jeavons M, Van Wittenberghe L, Gjata B, Marais T, Martin S, Vignaud A, Voit T, Mavilio F, *et al.* Efficacy and biodistribution analysis of intracerebroventricular administration of an optimized scAAV9-SMN1 vector in a mouse model of spinal muscular atrophy. *Mol Ther Methods Clin Dev* 2016;**3**:16060. Available at: https://www.cell.com/action/showFullText?pii=S2329050116301899. Accessed July 10, 2025.

Asmamaw Mengstie M. Viral Vectors for the in Vivo Delivery of CRISPR Components: Advances and Challenges. *Front Bioeng Biotechnol* 2022;**10**.

Auersperg N, Wong AST, Choi K-C, Kang SK, Leung PCK. Ovarian Surface Epithelium: Biology, Endocrinology, and Pathology. *Endocr Rev* 2001;**22**:255–288. Available at: https://dx.doi.org/10.1210/edrv.22.2.0422. Accessed May 4, 2026.

Baca M, Zamboni L. The fine structure of human follicular oocytes. *J Ultrastruct Res* 1967;**19**:354–381. Available at: https://www.sciencedirect.com/science/article/pii/S0022532067802259?via%3Dihub. Accessed May 4, 2026.

Baek JK, Lee J, Chung YS, Seo S. Identification of Adeno-Associate Virus (AAV) Serotype for Endometriosis Therapy and Effect of AAV-Mediated RNAi Delivery on Gene Expression and Cell Proliferation in In Vitro Endometrial Cell Culture. *Microorganisms* 2025;**13**:2144. Available at: https://pmc.ncbi.nlm.nih.gov/articles/PMC12472493/. Accessed November 8, 2025.

Bagheri MJ, Valojerdi MR, Salehnia M. Formation of ovarian organoid by co-culture of human endometrial mesenchymal stem cells and mouse oocyte in 3-dimensional culture system. *Cytotechnology* 2024;**76**:571–584. Available at: https://link.springer.com/article/10.1007/s10616-024-00639-w. Accessed September 21, 2025.

Bai L, Wu Y, Li G, Zhang W, Zhang H, Su J. AI-enabled organoids: Construction, analysis, and application. *Bioact Mater* 2024;**31**:525–548. Available at: https://www.sciencedirect.com/science/article/pii/S2452199X23002761. Accessed November 13, 2025.

Baker TG. A QUANTITATIVE AND CYTOLOGICAL STUDY OF GERM CELLS IN HUMAN OVARIES. *Proc R Soc Lond B Biol Sci* 1963;**158**:417–433. Available at: https://pubmed.ncbi.nlm.nih.gov/14070052/. Accessed December 14, 2025.

Barbato V, Genovese V, De Gregorio V, Di Nardo M, Travaglione A, De Napoli L, Fragomeni G, Zanetti EM, Adiga SK, Mondrone G, *et al.* Dynamic in vitro culture of bovine and human ovarian tissue enhances follicle progression and health. *Scientific Reports 2023 13:1* 2023;**13**:1–15. Available at: https://www.nature.com/articles/s41598-023-37086-0. Accessed November 8, 2025.

Barroso M, Monaghan MG, Niesner R, Dmitriev RI. Probing organoid metabolism using fluorescence lifetime imaging microscopy (FLIM): The next frontier of drug discovery and disease understanding. *Adv Drug Deliv Rev* 2023;**201**:115081. Available at: https://www.sciencedirect.com/science/article/pii/S0169409X23003964. Accessed November 8, 2025.

Bastings L, Beerendonk CCM, Westphal JR, Massuger LFAG, Kaal SEJ, van Leeuwen FE, Braat DDM, Peek R. Autotransplantation of cryopreserved ovarian tissue in cancer survivors and the risk of reintroducing malignancy: a systematic review. *Hum Reprod Update* 2013;**19**:483–506. Available at: https://dx.doi.org/10.1093/humupd/dmt020. Accessed December 11, 2025.

Becker CM, Bokor A, Heikinheimo O, Horne A, Jansen F, Kiesel L, King K, Kvaskoff M, Nap A, Petersen K, *et al.* ESHRE guideline: endometriosis. *Hum Reprod Open* 2022;**2022**. Available at: https://dx.doi.org/10.1093/hropen/hoac009. Accessed December 29, 2025.

Benayoun BA, Kochersberger A, Garrison JL. Studying ovarian aging and its health impacts: modern tools and approaches. *Genes Dev* 2025;**39**:975. Available at: https://pmc.ncbi.nlm.nih.gov/articles/PMC12315883/. Accessed December 10, 2025.

Bjarkadottir BD, Walker CA, Fatum M, Lane S, Williams SA. Analysing culture methods of frozen human ovarian tissue to improve follicle survival. *Reproduction & fertility* 2021;**2**:59–68. Available at: https://pubmed.ncbi.nlm.nih.gov/35128433/. Accessed September 27, 2025.

Blevins GM, Flanagan CL, Kallakuri SS, Meyer OM, Nimmagadda L, Hatch JD, Shea SA, Padmanabhan V, Shikanov A. Quantification of follicles in human ovarian tissue using image processing software and trained artificial intelligence†. *Biol Reprod* 2024;**110**:1086–1099. Available at: https://pubmed.ncbi.nlm.nih.gov/38537569/. Accessed November 8, 2025.

Bochner F, Fellus-Alyagor L, Kalchenko V, Shinar S, Neeman M. A Novel Intravital Imaging Window for Longitudinal Microscopy of the Mouse Ovary. *Scientific Reports 2015 5:1* 2015;**5**:1–12. Available at: https://www.nature.com/articles/srep12446. Accessed November 8, 2025.

Booth MJ. Adaptive optics in microscopy. *Philosophical Transactions of the Royal Society A: Mathematical, Physical and Engineering Sciences* 2007;**365**:2829–2843. Available at: /doi/pdf/10.1098/rsta.2007.0013. Accessed November 9, 2025.

Bristol-Gould SK, Hutten CG, Sturgis C, Kilen SM, Mayo KE, Woodruff TK. The Development of a Mouse Model of Ovarian Endosalpingiosis. *Endocrinology* 2005;**146**:5228–5236. Available at: https://dx.doi.org/10.1210/en.2005-0697. Accessed July 10, 2025.

Bristol-Gould SK, Kreeger PK, Selkirk CG, Kilen SM, Mayo KE, Shea LD, Woodruff TK. Fate of the initial follicle pool: Empirical and mathematical evidence supporting its sufficiency for adult fertility. *Dev Biol* 2006;**298**:149–154. Available at: https://pubmed.ncbi.nlm.nih.gov/16925987/. Accessed September 27, 2025.

De Bruin JP, Dorland M, Spek ER, Posthuma G, Van Haaften M, Looman CWN, Te Velde ER. Ultrastructure of the Resting Ovarian Follicle Pool in Healthy Young Women. *Biol Reprod*

2002;**66**:1151–1160. Available at: https://dx.doi.org/10.1095/biolreprod66.4.1151. Accessed June 6, 2024.

Bueno-Sánchez L, Alhambra-Borrás T, Gallego-Valadés A, Garcés-Ferrer J. Psychosocial Impact of Infertility Diagnosis and Conformity to Gender Norms on the Quality of Life of Infertile Spanish Couples. *Int J Environ Res Public Health* 2024;**21**:158. Available at: https://pmc.ncbi.nlm.nih.gov/articles/PMC10888361/. Accessed December 10, 2025.

Burton RAB, Lee P, Casero R, Garny A, Siedlecka U, Schneider JE, Kohl P, Grau V. Three-dimensional histology: tools and application to quantitative assessment of cell-type distribution in rabbit heart. *Europace* 2014;**16**:iv86. Available at: https://pmc.ncbi.nlm.nih.gov/articles/PMC4217519/. Accessed November 9, 2025.

Cable JK, Grider MH. Physiology, Progesterone. *StatPearls* 2023. Available at: https://www.ncbi.nlm.nih.gov/books/NBK558960/. Accessed December 14, 2025.

Cai X, Dou R, Guo C, Tang J, Li X, Chen J, Zhang J. Cationic Polymers as Transfection Reagents for Nucleic Acid Delivery. *Pharmaceutics* 2023;**15**:1502.

Campbell JM, Mahbub SB, Bertoldo MJ, Habibalahi A, Goss DM, Ledger WL, Gilchrist RB, Wu LE, Goldys EM. Multispectral autofluorescence characteristics of reproductive aging in old and young mouse oocytes. *Biogerontology* 2022;**23**:237. Available at: https://pmc.ncbi.nlm.nih.gov/articles/PMC9023381/. Accessed November 11, 2025.

Chang HM, Qiao J, Leung PCK. Oocyte–somatic cell interactions in the human ovary—novel role of bone morphogenetic proteins and growth differentiation factors. *Hum Reprod Update* 2016;**23**:1. Available at: https://pmc.ncbi.nlm.nih.gov/articles/PMC5155571/. Accessed September 27, 2025.

Chen H, Fang H-Q, Liu J-T, Chang S-Y, Cheng L-B, Sun M-X, Feng J-R, Liu Z-M, Zhang Y-H, Rosen CJ, *et al.* Atlas of Fshr expression from novel reporter mice. *Elife* 2025;**13**.

Cheng H, Wei F, Del Valle JS, Stolk THR, Huirne JA, Asseler JD, Pilgram GSK, Van Der Westerlaken LAJ, Van Mello NM, Chuva De Sousa Lopes SM. In vitro growth of secondary follicles from cryopreserved-thawed ovarian cortex. *Hum Reprod* 2024;**39**:2743–2753.

Cheng Y, Kim J, Li XX, Hsueh AJ. Promotion of Ovarian Follicle Growth following mTOR Activation: Synergistic Effects of AKT Stimulators. *PLoS One* 2015;**10**:e0117769. Available at: https://journals.plos.org/plosone/article?id=10.1371/journal.pone.0117769. Accessed December 14, 2025.

Chon SJ, Umair Z, Yoon MS. Premature Ovarian Insufficiency: Past, Present, and Future. *Front Cell Dev Biol* 2021;**9**. Available at: https://pubmed.ncbi.nlm.nih.gov/34041247/. Accessed December 11, 2025.

Christenson LK, Gunewardena S, Hong X, Spitschak M, Baufeld A, Vanselow J. Research Resource: Preovulatory LH Surge Effects on Follicular Theca and Granulosa Transcriptomes. *Molecular Endocrinology* 2013;**27**:1153. Available at: https://pmc.ncbi.nlm.nih.gov/articles/PMC3706842/. Accessed May 4, 2026.

Chu VT, Weber T, Graf R, Sommermann T, Petsch K, Sack U, Volchkov P, Rajewsky K, Kühn R. Efficient generation of Rosa26 knock-in mice using CRISPR/Cas9 in C57BL/6 zygotes. *BMC Biotechnol* 2016;**16**:1–15. Available at: https://bmcbiotechnol.biomedcentral.com/articles/10.1186/s12896-016-0234-4. Accessed July 10, 2025.

Clarkson YL, McLaughlin M, Waterfall M, Dunlop CE, Skehel PA, Anderson RA, Telfer EE. Initial characterisation of adult human ovarian cell populations isolated by DDX4 expression and

aldehyde dehydrogenase activity. *Scientific Reports 2018 8:1* 2018;**8**:6953-. Available at: https://www.nature.com/articles/s41598-018-25116-1. Accessed December 14, 2025.

Cobo A, García-Velasco JA, Coello A, Domingo J, Pellicer A, Remohí J. Oocyte vitrification as an efficient option for elective fertility preservation. *Fertil Steril* 2016;**105**:755-764.e8. Available at: https://pubmed.ncbi.nlm.nih.gov/26688429/. Accessed December 11, 2025.

Conchello JA, Lichtman JW. Optical sectioning microscopy. *Nature Methods 2005 2:12* 2005;**2**:920–931. Available at: https://www.nature.com/articles/nmeth815. Accessed June 6, 2024.

Cooper GM. Heredity, Genes, and DNA. 2000. Available at: https://www.ncbi.nlm.nih.gov/books/NBK9944/. Accessed December 10, 2025.

Cordeiro MH, Kim SY, Ebbert K, Duncan FE, Ramalho-Santos J, Woodruff TK. Geography of follicle formation in the embryonic mouse ovary impacts activation pattern during the first wave of folliculogenesis. *Biol Reprod* 2015;**93**. Available at: https://dx.doi.org/10.1095/biolreprod.115.131227. Accessed July 10, 2025.

Costa-Verdera H, Meneghini V, Fitzpatrick Z, Abou Alezz M, Fabyanic E, Huang X, Dzhashiashvili Y, Ahiya A, Mangiameli E, Valeri E, *et al.* AAV vectors trigger DNA damage response-dependent pro-inflammatory signalling in human iPSC-derived CNS models and mouse brain. *Nature Communications 2025 16:1* 2025;**16**:1–20. Available at: https://www.nature.com/articles/s41467-025-58778-3. Accessed July 10, 2025.

Coulam CB, Adamson SC, Annegers JF. Incidence of premature ovarian failure. *Obstetrics and Gynecology* 1986;**67**:604–606. Available at: https://europepmc.org/article/med/3960433. Accessed December 11, 2025.

Cranfill PJ, Sell BR, Baird MA, Allen JR, Lavagnino Z, De Gruiter HM, Kremers GJ, Davidson MW, Ustione A, Piston DW. Quantitative Assessment of Fluorescent Proteins. *Nat Methods* 2016;**13**:557. Available at: https://pmc.ncbi.nlm.nih.gov/articles/PMC4927352/. Accessed November 13, 2025.

Dan L, Kang-Zheng L. Optimizing viral transduction in immune cell therapy manufacturing: key process design considerations. *Journal of Translational Medicine 2025 23:1* 2025;**23**:1–17. Available at: https://translational-medicine.biomedcentral.com/articles/10.1186/s12967-025-06524-0. Accessed November 13, 2025.

Dekkers JF, Alieva M, Wellens LM, Ariese HCR, Jamieson PR, Vonk AM, Amatngalim GD, Hu H, Oost KC, Snippert HJG, *et al.* High-resolution 3D imaging of fixed and cleared organoids. *Nature Protocols 2019 14:6* 2019;**14**:1756–1771. Available at: https://www.nature.com/articles/s41596-019-0160-8. Accessed November 9, 2025.

Demır MB, Çopuroğlu M, Çevik Kaya F, Yüksek Ş. Correlation between serum AMH, AFC, AND histologically quantified primordial follicles: a prospective study in premenopausal women. *Journal of Ovarian Research 2025 18:1* 2025;**18**:1–9. Available at: https://ovarianresearch.biomedcentral.com/articles/10.1186/s13048-025-01807-y. Accessed November 9, 2025.

Dhalwani NN, Fiaschi L, West J, Tata LJ. Occurrence of fertility problems presenting to primary care: population-level estimates of clinical burden and socioeconomic inequalities across the UK. *Hum Reprod* 2013;**28**:960–968. Available at: https://pubmed.ncbi.nlm.nih.gov/23315065/. Accessed December 11, 2025.

Dharma SJ, Modi DN, Nandedkar TD. Gene expression profiling during early folliculogenesis in the mouse ovary. *Fertil Steril* 2009;**91**:2025–2036. Available at: https://www.sciencedirect.com/science/article/pii/S0015028208002471. Accessed September 27, 2025.

Dhungel BP, Bailey CG, Rasko JEJ. Journey to the Center of the Cell: Tracing the Path of AAV Transduction. *Trends Mol Med* 2021;**27**:172–184. Available at: https://www.cell.com/action/showFullText?pii=S1471491420302574. Accessed April 26, 2026.

Dipali SS, Gowett MQ, Kamat P, Converse A, Zaniker EJ, Fennell A, Chou T, Pritchard MT, Zelinski M, Phillip JM, *et al.* Self-organizing ovarian somatic organoids preserve cellular heterogeneity and reveal cellular contributions to ovarian aging. *bioRxiv* 2024:2024.08.10.607456. Available at: https://www.biorxiv.org/content/10.1101/2024.08.10.607456v1. Accessed September 21, 2025.

Dittmar R, Potier E, Van Zandvoort M, Ito K. Assessment of Cell Viability in Three-Dimensional Scaffolds Using Cellular Auto-Fluorescence. *Tissue Eng Part C Methods* 2011;**18**:198. Available at: https://pmc.ncbi.nlm.nih.gov/articles/PMC3285599/. Accessed November 9, 2025.

Doherty GP, Bailey K, Lewis PJ. Stage-specific fluorescence intensity of GFP and mCherry during sporulation In Bacillus Subtilis. *BMC Res Notes* 2010;**3**:303. Available at: https://pmc.ncbi.nlm.nih.gov/articles/PMC2994887/. Accessed November 13, 2025.

Donnez J, Dolmans MM. Fertility preservation in women. *Nat Rev Endocrinol* 2013;**9**:735–749. Available at: https://pubmed.ncbi.nlm.nih.gov/24166000/. Accessed December 11, 2025.

Doshi S, Agarwal A. The role of oxidative stress in menopause. *J Midlife Health* 2013;**4**:140. Available at: https://journals.lww.com/jomh/fulltext/2013/04030/the_role_of_oxidative_stress_in_menopause.2.aspx. Accessed December 14, 2025.

Duan D. Lethal immunotoxicity in high-dose systemic AAV therapy. *Molecular Therapy* 2023;**31**:3123–3126. Available at: https://www.sciencedirect.com/science/article/pii/S1525001623005567. Accessed July 10, 2025.

Dupont J, Reverchon M, Cloix L, Froment P, Rame C, Ramé C. Involvement of adipokines, AMPK, PI3K and the PPAR signaling pathways in ovarian follicle development and cancer. *International Journal of Developmental Biology* 2012;**56**:959–967. Available at: https://hal.science/hal-01129696v1. Accessed September 27, 2025.

Eliyahu H, Barenholz Y, Domb AJ. Polymers for DNA Delivery. *Molecules* 2005;**10**:34–64.

Ellis BL, Hirsch ML, Barker JC, Connelly JP, Steininger RJ, Porteus MH. A survey of ex vivo/in vitro transduction efficiency of mammalian primary cells and cell lines with Nine natural adeno-associated virus (AAV1-9) and one engineered adeno-associated virus serotype. *Virol J* 2013;**10**:74. Available at: https://pmc.ncbi.nlm.nih.gov/articles/PMC3607841/. Accessed July 10, 2025.

Epifano O, Liang LF, Familari M, Moos MC, Dean J. Coordinate expression of the three zona pellucida genes during mouse oogenesis. *Development* 1995;**121**:1947–1956. Available at: https://dx.doi.org/10.1242/dev.121.7.1947. Accessed May 4, 2026.

Eppig JJ. Intercommunication between mammalian oocytes and companion somatic cells. *BioEssays* 1991;**13**:569–574. Available at: /doi/pdf/10.1002/bies.950131105. Accessed September 27, 2025.

Eppig JJ, Wigglesworth K. Development of Mouse and Rat Oocytes in Chimeric Reaggregated Ovaries after Interspecific Exchange of Somatic and Germ Cell Components. *Biol Reprod* 2000;**63**:1014–1023. Available at: https://dx.doi.org/10.1095/biolreprod63.4.1014. Accessed November 2, 2024.

Eppig JJ, Wigglesworth K, Pendola FL. The mammalian oocyte orchestrates the rate of ovarian follicular development. *Proc Natl Acad Sci U S A* 2002;**99**:2890–2894. Available at: https://www.pnas.org/doi/pdf/10.1073/pnas.052658699. Accessed September 27, 2025.

Faddy MJ, Gosden RG. A model conforming the decline in follicle numbers to the age of menopause in women. *Hum Reprod* 1996;**11**:1484–1486. Available at: https://pubmed.ncbi.nlm.nih.gov/8671489/. Accessed December 10, 2025.

Faddy MJ, Gosden RG, Gougeon A, Richardson SJ, Nelson JF. Accelerated disappearance of ovarian follicles in mid-life: implications for forecasting menopause. *Hum Reprod* 1992;**7**:1342–1346. Available at: https://pubmed.ncbi.nlm.nih.gov/1291557/. Accessed December 10, 2025.

Fages-Lartaud M, Tietze L, Elie F, Lale R, Hohmann-Marriott MF. mCherry contains a fluorescent protein isoform that interferes with its reporter function. *Front Bioeng Biotechnol* 2022;**10**:892138.

Faire M, Skillern A, Arora R, Nguyen DH, Wang J, Chamberlain C, German MS, Fung JC, Laird DJ. Follicle dynamics and global organization in the intact mouse ovary. *Dev Biol* 2015;**403**:69–79.

Fauser BCJM, van Heusden AM. Manipulation of human ovarian function: physiological concepts and clinical consequences. *Endocr Rev* 1997;**18**:71–106. Available at: https://pubmed.ncbi.nlm.nih.gov/9034787/. Accessed December 14, 2025.

Fehrman RL, Chern KJ, Stoltz KP, Lipinski DM. The vectors went in two-by-two: Transduction efficiency and tolerability of dual and triple rAAV vector delivery following intravitreal injection for genome-editing applications. *Exp Eye Res* 2025;**251**:110223. Available at: https://www.sciencedirect.com/science/article/pii/S0014483524004457. Accessed November 10, 2025.

Feng J, Wu Q, Liang Y, Liang Y, Bin Q. Epidemiological characteristics of infertility, 1990–2021, and 15-year forecasts: an analysis based on the global burden of disease study 2021. *Reprod Health* 2025;**22**:26. Available at: https://pmc.ncbi.nlm.nih.gov/articles/PMC11841318/. Accessed December 10, 2025.

Feng Y, Cui P, Lu X, Hsueh B, Möller Billig F, Zarnescu Yanez L, Tomer R, Boerboom D, Carmeliet P, Deisseroth K, *et al.* CLARITY reveals dynamics of ovarian follicular architecture and vasculature in three-dimensions. *Scientific Reports 2017 7:1* 2017;**7**:1–13. Available at: https://www.nature.com/articles/srep44810. Accessed June 6, 2024.

Fink D, Wohrer S, Pfeffer M, Tombe T, Ong CJ, Sorensen PHB. Ubiquitous expression of the monomeric red fluorescent protein mcherry in transgenic mice. *genesis* 2010;**48**:723–729. Available at: /doi/pdf/10.1002/dvg.20677. Accessed November 13, 2025.

Folts L, Martinez AS, McKey J. Tissue clearing and imaging approaches for in toto analysis of the reproductive system. *Biol Reprod* 2023. Available at: https://dx.doi.org/10.1093/biolre/ioad182. Accessed May 27, 2024.

Folts L, Martinez AS, Williams JA, Bunce C, Capel B, McKey J. OoCount: a machine-learning-based approach to mouse ovarian follicle counting and classification. *Biol Reprod* 2025. Available at: https://dx.doi.org/10.1093/biolre/ioaf023. Accessed November 9, 2025.

Forabosco A, Sforza C. Establishment of ovarian reserve: a quantitative morphometric study of the developing human ovary. *Fertil Steril* 2007;**88**:675–683. Available at: https://www.sciencedirect.com/science/article/pii/S0015028206047285?utm_source=chatgpt.com#bib36. Accessed November 15, 2025.

Fortune JE, Rivera GM, Yang MY. Follicular development: the role of the follicular microenvironment in selection of the dominant follicle. *Anim Reprod Sci* 2004;**82–83**:109–126. Available at:

https://www.sciencedirect.com/science/article/pii/S0378432004000867?via%3Dihub. Accessed December 14, 2025.

Francés-Herrero E, Lopez R, Campo H, de Miguel-Gómez L, Rodríguez-Eguren A, Faus A, Pellicer A, Cervelló I. Advances of xenogeneic ovarian extracellular matrix hydrogels for in vitro follicle development and oocyte maturation. *Biomaterials Advances* 2023;**151**:213480. Available at: https://www.sciencedirect.com/science/article/pii/S2772950823002030. Accessed December 30, 2025.

Gaj T, Staahl BT, Rodrigues GMC, Limsirichai P, Ekman FK, Doudna JA, Schaffer D V. Targeted gene knock-in by homology-directed genome editing using Cas9 ribonucleoprotein and AAV donor delivery. *Nucleic Acids Res* 2017;**45**:e98–e98. Available at: https://dx.doi.org/10.1093/nar/gkx154. Accessed July 10, 2025.

Ge X, Xi H, Yang F, Zhi X, Fu Y, Chen D, Xu RH, Lin G, Qu J, Zhao J, *et al.* CRISPR/Cas9-AAV Mediated Knock-in at NRL Locus in Human Embryonic Stem Cells. *Mol Ther Nucleic Acids* 2016;**5**:e393. Available at: https://www.cell.com/action/showFullText?pii=S2162253117300161. Accessed July 10, 2025.

Gellert SE, Pors SE, Kristensen SG, Bay-Bjørn AM, Ernst E, Yding Andersen C. Transplantation of frozen-thawed ovarian tissue: an update on worldwide activity published in peer-reviewed papers and on the Danish cohort. *J Assist Reprod Genet* 2018;**35**:561–570. Available at: https://pubmed.ncbi.nlm.nih.gov/29497953/. Accessed December 11, 2025.

Gibson E, Mahdy H. Anatomy, Abdomen and Pelvis, Ovary. *StatPearls* 2023. Available at: https://www.ncbi.nlm.nih.gov/books/NBK545187/. Accessed December 11, 2025.

Gilchrist RB, Ritter LJ, Armstrong DT. Oocyte-somatic cell interactions during follicle development in mammals. *Anim Reprod Sci* 2004;**82–83**:431–446. Available at: https://pubmed.ncbi.nlm.nih.gov/15271471/. Accessed September 27, 2025.

Gittens JEI, Barr KJ, Vanderhyden BC, Kidder GM. Interplay between paracrine signaling and gap junctional communication in ovarian follicles. *J Cell Sci* 2005;**118**:113–122. Available at: https://pubmed.ncbi.nlm.nih.gov/15585573/. Accessed September 27, 2025.

Gittens JEI, Kidder GM. Differential contributions of connexin37 and connexin43 to oogenesis revealed in chimeric reaggregated mouse ovaries. *J Cell Sci* 2005;**118**:5071–5078. Available at: https://dx.doi.org/10.1242/jcs.02624. Accessed September 27, 2025.

Golezar S, Ramezani Tehrani F, Khazaei S, Ebadi A, Keshavarz Z. The global prevalence of primary ovarian insufficiency and early menopause: a meta-analysis. *Climacteric* 2019;**22**:403–411. Available at: https://pubmed.ncbi.nlm.nih.gov/30829083/. Accessed December 11, 2025.

Gougeon A. Dynamics of follicular growth in the human: a model from preliminary results. *Hum Reprod* 1986;**1**:81–87. Available at: https://pubmed.ncbi.nlm.nih.gov/3558758/. Accessed September 27, 2025.

Grasa P, Ploutarchou P, Williams SA. Oocytes lacking O-glycans alter follicle development and increase fertility by increasing follicle FSH sensitivity, decreasing apoptosis, and modifying GDF9:BMP15 expression. *FASEB J* 2015;**29**:525–539. Available at: https://pubmed.ncbi.nlm.nih.gov/25416550/. Accessed September 27, 2025.

Grasa P, Sheikh S, Krzys N, Millar K, Janjua S, Nawaggi P, Williams SA. Dysregulation of follicle development in a mouse model of premature ovarian insufficiency. *Reproduction* 2016;**152**:591–601.

Gromoll J, Simoni M. Genetic complexity of FSH receptor function. *Trends in Endocrinology and Metabolism* 2005;**16**:368–373. Available at: https://www.cell.com/action/showFullText?pii=S1043276005001827. Accessed July 10, 2025.

Grosbois J, Demeestere I. Dynamics of PI3K and Hippo signaling pathways during in vitro human follicle activation. *Hum Reprod* 2018;**33**:1705–1714. Available at: https://pubmed.ncbi.nlm.nih.gov/30032281/. Accessed September 27, 2025.

Gruijters MJG, Visser JA, Durlinger ALL, Themmen APN. Anti-Müllerian hormone and its role in ovarian function. *Mol Cell Endocrinol* 2003;**211**:85–90. Available at: https://www.sciencedirect.com/science/article/pii/S0303720703003265. Accessed July 10, 2025.

Gundersen HJG, Jensen EB. The efficiency of systematic sampling in stereology and its prediction*. *J Microsc* 1987;**147**:229–263. Available at: /doi/pdf/10.1111/j.1365-2818.1987.tb02837.x. Accessed November 15, 2025.

Guo Z, Peng H, Kang J, Sun D. Cell-penetrating peptides: Possible transduction mechanisms and therapeutic applications. *Biomed Rep* 2016;**4**:528–534.

Guo Z, Yu Q. Role of mTOR Signaling in Female Reproduction. *Front Endocrinol (Lausanne)* 2019;**10**:479357. Available at: www.frontiersin.org. Accessed September 27, 2025.

Haery L, Deverman BE, Matho KS, Cetin A, Woodard K, Cepko C, Guerin KI, Rego MA, Ersing I, Bachle SM, *et al.* Adeno-Associated Virus Technologies and Methods for Targeted Neuronal Manipulation. *Front Neuroanat* 2019;**13**:493120. Available at: www.frontiersin.org. Accessed November 13, 2025.

Halbert CL, Alexander IE, Wolgamot GM, Miller AD. Adeno-associated virus vectors transduce primary cells much less efficiently than immortalized cells. *J Virol* 1995;**69**:1473–1479. Available at: https://pubmed.ncbi.nlm.nih.gov/7853479/. Accessed July 10, 2025.

Hansen KR, Knowlton NS, Thyer AC, Charleston JS, Soules MR, Klein NA. A new model of reproductive aging: the decline in ovarian non-growing follicle number from birth to menopause. *Human Reproduction* 2008;**23**:699–708. Available at: https://dx.doi.org/10.1093/humrep/dem408. Accessed April 29, 2026.

Hao E ying, Liu X lu, Chang L yun, Xue H, Su B fei, Chen Y fan, Wang D he, Shi L, Chen H. Melatonin alleviates endoplasmic reticulum stress to improve ovarian function by regulating the mTOR pathway in aged laying hens. *Poult Sci* 2024;**103**:103703. Available at: https://www.sciencedirect.com/science/article/pii/S0032579124002840. Accessed December 14, 2025.

Hao J, Li T, Heinzelmann M, Moussaud-Lamodière E, Lebre F, Krjutškov K, Damdimopoulos A, Arnelo C, Pettersson K, Alfaro-Moreno E, *et al.* Effects of chemical in vitro activation versus fragmentation on human ovarian tissue and follicle growth in culture. *Hum Reprod Open* 2024;**2024**. Available at: https://dx.doi.org/10.1093/hropen/hoae028. Accessed December 14, 2025.

Harrison AS, Bjarkadottir BD, Kuscu N, Davies J, Lane S, Williams SA, Harrison S. Three-dimensional visualisation of human ovarian follicles using a whole-mount immunolabelling and optical tissue clearing method. *Reproduction and Fertility* 2025;**6**. Available at: https://raf.bioscientifica.com/view/journals/raf/6/4/RAF-25-0096.xml. Accessed November 8, 2025.

Hassan MH, Reiter E, Razzaq M. Automatic ovarian follicle detection using object detection models. *Scientific Reports 2024 14:1* 2024;**14**:1–15. Available at: https://www.nature.com/articles/s41598-024-82904-8. Accessed November 9, 2025.

He X, Zhang Z, Xue J, Wang Y, Zhang S, Wei J, Zhang C, Wang J, Urip BA, Ngan CC, *et al.* Low-dose AAV-CRISPR-mediated liver-specific knock-in restored hemostasis in neonatal hemophilia B mice with subtle antibody response. *Nature Communications 2022 13:1*

2022;**13**:7275-. Available at: https://www.nature.com/articles/s41467-022-34898-y. Accessed December 8, 2025.

Heckert LL, Daggett MAF, Chen J. Multiple promoter elements contribute to activity of the follicle-stimulating hormone receptor (FSHR) gene in testicular Sertoli cells. *Mol Endocrinol* 1998;**12**:1499–1512. Available at: https://pubmed.ncbi.nlm.nih.gov/9773974/. Accessed December 8, 2025.

Heeren AM, Van Iperen L, Klootwijk DB, De Melo Bernardo A, Roost MS, Fernandes MMG, Louwe LA, Hilders CG, Helmerhorst FM, Van Der Westerlaken LAJ, *et al.* Development of the follicular basement membrane during human gametogenesis and early folliculogenesis. *BMC Dev Biol* 2015;**15**. Available at: https://pubmed.ncbi.nlm.nih.gov/25605128/. Accessed September 27, 2025.

Hennet ML, Combelles CMH. The antral follicle: a microenvironment for oocyte differentiation. *Int J Dev Biol* 2012;**56**:819–831. Available at: https://pubmed.ncbi.nlm.nih.gov/23417404/. Accessed December 14, 2025.

Hickey SM, Ung B, Bader C, Brooks R, Lazniewska J, Johnson IRD, Sorvina A, Logan J, Martini C, Moore CR, *et al.* Fluorescence microscopy—an outline of hardware, biological handling, and fluorophore considerations. *Cells* 2022;**11**:35. Available at: https://www.mdpi.com/2073-4409/11/1/35/htm. Accessed November 9, 2025.

Hikabe O, Hamazaki N, Nagamatsu G, Obata Y, Hirao Y, Hamada N, Shimamoto S, Imamura T, Nakashima K, Saitou M, *et al.* Reconstitution in vitro of the entire cycle of the mouse female germ line. *Nature* 2016;**539**:299–303. Available at: https://www.nature.com/articles/nature20104. Accessed September 27, 2025.

Holesh JE, Bass AN, Lord M. Physiology, Ovulation. *StatPearls* 2023. Available at: https://www.ncbi.nlm.nih.gov/books/NBK441996/. Accessed December 14, 2025.

Honda A, Hirose M, Hara K, Matoba S, Inoue K, Miki H, Hiura H, Kanatsu-Shinohara M, Kanai Y, Kono T, *et al.* Isolation, characterization, and in vitro and in vivo differentiation of putative thecal stem cells. *Proceedings of the National Academy of Sciences* 2007;**104**:12389–12394. Available at: /doi/pdf/10.1073/pnas.0703787104?download=true. Accessed September 27, 2025.

Hu X, Meister R, Tode J, Framme C, Fuchs H. Long-term in vitro monitoring of AAV-transduction efficiencies in real-time with Hoechst 33342. *PLoS One* 2024;**19**:e0298173. Available at: https://journals.plos.org/plosone/article?id=10.1371/journal.pone.0298173. Accessed November 8, 2025.

İnik Ö, Ceyhan A, Balcıoğlu E, Ülker E. A new method for automatic counting of ovarian follicles on whole slide histological images based on convolutional neural network. *Comput Biol Med* 2019;**112**:103350. Available at: https://www.sciencedirect.com/science/article/pii/S0010482519302276?via%3Dihub. Accessed November 9, 2025.

Iyer S, Zhang S, Yucel S, Horn H, Smith SG, Reinhardt F, Hoefsmit E, Assatova B, Casado J, Meinsohn MC, *et al.* Genetically defined syngeneic mouse models of ovarian cancer as tools for the discovery of combination immunotherapy. *Cancer Discov* 2020;**11**:384. Available at: https://pmc.ncbi.nlm.nih.gov/articles/PMC8344888/. Accessed July 10, 2025.

Jang DE, Lee JY, Lee JH, Koo OJ, Bae HS, Jung MH, Bae JH, Hwang WS, Chang YJ, Lee YH, *et al.* Multiple sgRNAs with overlapping sequences enhance CRISPR/Cas9-mediated knock-in efficiency. *Experimental & Molecular Medicine 2018 50:4* 2018;**50**:1–9. Available at: https://www.nature.com/articles/s12276-018-0037-x. Accessed July 10, 2025.

Johnson J, Bagley J, Skaznik-Wikiel M, Lee HJ, Adams GB, Niikura Y, Tschudy KS, Tilly JC, Cortes ML, Forkert R, *et al.* Oocyte generation in adult mammalian ovaries by putative germ cells in bone marrow and peripheral blood. *Cell* 2005;**122**:303–315. Available at: https://www.cell.com/action/showFullText?pii=S0092867405006501. Accessed December 14, 2025.

Johnson J, Canning J, Kaneko T, Pru JK, Tilly JL. Germline stem cells and follicular renewal in the postnatal mammalian ovary. *Nature* 2004;**428**:145–150. Available at: https://pubmed.ncbi.nlm.nih.gov/15014492/. Accessed December 14, 2025.

Kagami K, Shinmyo Y, Ono M, Kawasaki H, Fujiwara H. Three-dimensional evaluation of murine ovarian follicles using a modified CUBIC tissue clearing method. *Reproductive Biology and Endocrinology* 2018;**16**:1–7. Available at: https://rbej.biomedcentral.com/articles/10.1186/s12958-018-0381-7. Accessed June 6, 2024.

Kanatsu-Shinohara M, Lee J, Miyazaki T, Morimoto H, Shinohara T. Adeno-associated-virus-mediated gene delivery to ovaries restores fertility in congenital infertile mice. *Cell Rep Med* 2022;**3**:100606. Available at: https://www.sciencedirect.com/science/article/pii/S2666379122001239. Accessed July 10, 2025.

Kashir J, Heindryckx B, Jones C, de Sutter P, Parrington J, Coward K. Oocyte activation, phospholipase C zeta and human infertility. *Hum Reprod Update* 2010;**16**:690–703. Available at: https://dx.doi.org/10.1093/humupd/dmq018. Accessed December 11, 2025.

Kato M, Yamanouchi K, Ikawa M, Okabe M, Naito K, Tojo H. Efficient selection of transgenic mouse embryos using EGFP as a marker gene. *Mol Reprod Dev* 1999;**54**:43–48. Available at: /doi/pdf/10.1002/%28SICI%291098-2795%28199909%2954%3A1%3C43%3A%3AAID-MRD6%3E3.0.CO%3B2-N. Accessed July 10, 2025.

Kawamura K, Cheng Y, Suzuki N, Deguchi M, Sato Y, Takae S, Ho CH, Kawamura N, Tamura M, Hashimoto S, *et al.* Hippo signaling disruption and Akt stimulation of ovarian follicles for infertility treatment. *Proc Natl Acad Sci U S A* 2013;**110**:17474–17479. Available at: https://pubmed.ncbi.nlm.nih.gov/24082083/. Accessed September 27, 2025.

Kemeny R. Blue-footed boogie isn't enough for booby babies . *New Sci (1956)* 2014. Available at: https://www.newscientist.com/article/dn25505-blue-footed-boogie-isnt-enough-for-booby-babies/. Accessed December 10, 2025.

Kerr JB, Myers M, Anderson RA. The dynamics of the primordial follicle reserve. *Reproduction* 2013;**146**:R205–R215. Available at: https://rep.bioscientifica.com/view/journals/rep/146/6/R205.xml. Accessed September 27, 2025.

Kinnear HM, Tomaszewski CE, Chang FL, Moravek MB, Xu M, Padmanabhan V, Shikanov A. The Ovarian Stroma as a New Frontier. *Reproduction* 2020;**160**:R25. Available at: https://pmc.ncbi.nlm.nih.gov/articles/PMC7453977/. Accessed December 11, 2025.

Kleeman B, Olsson A, Newkold T, Kofron M, DeLay M, Hildeman D, Grimes HL. A Guide to Choosing Fluorescent Protein Combinations for Flow Cytometric Analysis Based on Spectral Overlap. *Cytometry A* 2018;**93**:556. Available at: https://pmc.ncbi.nlm.nih.gov/articles/PMC8008483/. Accessed November 13, 2025.

Kok RNU, Spoelstra WK, Betjes MA, van Zon JS, Tans SJ. Label-free cell imaging and tracking in 3D organoids. *Cell Rep Phys Sci* 2025;**6**:102522. Available at: https://www.cell.com/action/showFullText?pii=S2666386425001213. Accessed November 13, 2025.

Komatsu K, Iwase A, Murase T, Masubuchi S. Ovarian Tissue Culture to Visualize Phenomena in Mouse Ovary. *J Vis Exp* 2018;**2018**:57794. Available at: https://pmc.ncbi.nlm.nih.gov/articles/PMC6101919/. Accessed July 10, 2025.

Komatsu K, Koya T, Wang J, Yamashita M, Kikkawa F, Iwase A. Analysis of the effect of leukemia inhibitory factor on follicular growth in cultured murine ovarian tissue. *Biol Reprod* 2015;**93**:1–8. Available at: https://dx.doi.org/10.1095/biolreprod.115.128421. Accessed November 8, 2025.

de Koning R, Blikkendaal MD, de Sousa Lopes SMC, van der Meeren LE, Cheng H, Jansen FW, Lashley EELO. Histological analysis of (antral) follicle density in ovarian cortex tissue attached to stripped endometriomas. *Journal of Assisted Reproduction and Genetics 2024 41:4* 2024;**41**:1067–1076. Available at: https://link.springer.com/article/10.1007/s10815-024-03058-0. Accessed November 9, 2025.

Kubo H, McCauley CJ, Zelinski MB, Laronda MM. Establishing the baseline: understanding follicle activation morphometrics in multiple mammalian species. *Biol Reprod* 2025;**XX**. Available at: https://dx.doi.org/10.1093/biolre/ioaf059. Accessed May 29, 2025.

Kuscu N, Abdul Kader S, Stephens ER, Adeniran B V., Ammar OF, Harrison AS, Lo BK, Williams SA. Ovarian culture with mouse serum improves follicle development compared with fetal bovine serum, showing the importance of as yet unidentified factors in follicle growth. *Reprod Fertil Dev* 2025;**37**. Available at: https://pubmed.ncbi.nlm.nih.gov/40577554/. Accessed September 21, 2025.

Lécureuil C, Fontaine I, Crepieux P, Guillou F. Sertoli and granulosa cell-specific Cre recombinase activity in transgenic mice. *Genesis (United States)* 2002;**33**:114–118.

Lei Y, Wang X, Zhou Y, Li Y, Wang L, Jia X, Ma Q, Lin C, Liao J, Li X, *et al.* The Impact of Social, Cultural, and Identity-Related Factors on Delayed Childbearing: A Multi-Center Study. *Risk Manag Healthc Policy* 2025;**18**:1959. Available at: https://pmc.ncbi.nlm.nih.gov/articles/PMC12182101/. Accessed December 11, 2025.

Levallet J, Koskimies P, Rahman N, Huhtaniemi I. The Promoter of Murine Follicle-Stimulating Hormone Receptor: Functional Characterization and Regulation by Transcription Factor Steroidogenic Factor 1. *Molecular Endocrinology* 2001;**15**:80–92. Available at: https://dx.doi.org/10.1210/mend.15.1.0583. Accessed December 8, 2025.

Leyser-Whalen O, Temple JR, Phelps JY. Ethical and Psychosocial Impact of Female Infertility. *Curr Obstet Gynecol Rep* 2012;**1**:153. Available at: https://pmc.ncbi.nlm.nih.gov/articles/PMC3547399/. Accessed December 10, 2025.

Li J, Fan H, Liu W, Zhang J, Xiao Y, Peng Y, Yang W, Liu W, He Y, Qin L, *et al.* Mesenchymal stem cells promote ovarian reconstruction in mice. *Stem Cell Res Ther* 2024;**15**:1–15. Available at: https://link.springer.com/articles/10.1186/s13287-024-03718-z. Accessed September 27, 2025.

Li X, Zheng M, Xu B, Li D, Shen Y, Nie Y, Ma L, Wu J. Generation of offspring-producing 3D ovarian organoids derived from female germline stem cells and their application in toxicological detection. *Biomaterials* 2021;**279**:121213. Available at: https://www.sciencedirect.com/science/article/pii/S0142961221005706. Accessed September 21, 2025.

Liang Q, Ren W, Jin B, Qiao L, Ge X, Fu Y, Lv X, Li M, Xi P. High-fidelity tissue super-resolution imaging achieved with confocal2 spinning-disk image scanning microscopy. *Light Sci Appl* 2025;**14**:260. Available at: https://pmc.ncbi.nlm.nih.gov/articles/PMC12319088/. Accessed November 9, 2025.

Liao H, Wu J, VanDusen NJ, Li Y, Zheng Y. CRISPR-Cas9-mediated homology-directed repair for precise gene editing. *Mol Ther Nucleic Acids* 2024;**35**:102344. Available at: https://pmc.ncbi.nlm.nih.gov/articles/PMC11531618/. Accessed July 13, 2025.

Lichtman JW, Conchello JA. Fluorescence microscopy. *Nature Methods 2005 2:12* 2005;**2**:910–919. Available at: https://www.nature.com/articles/nmeth817. Accessed November 9, 2025.

Lin HCA, Dutta R, Mandal S, Kind A, Schnieke A, Razansky D. Advancing ovarian folliculometry with selective plane illumination microscopy. *Scientific Reports 2016 6:1* 2016;**6**:1–7. Available at: https://www.nature.com/articles/srep38057. Accessed November 9, 2025.

Ling C, Yu C, Wang C, Yang M, Yang H, Yang K, He Y, Shen Y, Tang S, Yu X, *et al.* rAAV capsid mutants eliminate leaky expression from DNA donor template for homologous recombination. *Nucleic Acids Res* 2024;**52**:6518–6531. Available at: https://dx.doi.org/10.1093/nar/gkae401. Accessed November 13, 2025.

Lionis CD, Martellucci CA, Jerjes W, Harding D. Breaking barriers: enhancing cancer detection in younger patients by overcoming diagnostic bias in primary care. *Front Med (Lausanne)* 2025;**11**:1438402. Available at: https://pmc.ncbi.nlm.nih.gov/articles/PMC11794322/. Accessed December 11, 2025.

Liu C, Peng J, Matzuk MM, Yao HH-C. Lineage specification of ovarian theca cells requires multicellular interactions via oocyte and granulosa cells. *Nat Commun* 2015;**6**:6934.

Liu CF, Barsoum I, Gupta R, Hofmann MC, Yao HHC. Stem cell potential of the mammalian gonad. *Front Biosci (Elite Ed)* 2009;**1**:510. Available at: https://pmc.ncbi.nlm.nih.gov/articles/PMC2902374/. Accessed December 10, 2025.

Liu J, Qin Y, Liu H, Liu Y, Yang Y, Ning Y, Ye H. Global, regional, and national burden of female infertility and trends from 1990 to 2021 with projections to 2050 based on the GBD 2021 analysis. *Sci Rep* 2025;**15**. Available at: https://pubmed.ncbi.nlm.nih.gov/40394053/. Accessed December 11, 2025.

Lo BKM, Sheikh S, Williams SA. In vitro and in vivo mouse follicle development in ovaries and reaggregated ovaries. *Reproduction* 2019;**157**:135–148.

Longobardi S, Klinger FG, Zheng W, Campitiello MR, D'Hooghe T, La Marca A. Gonadotropin Activity during Early Folliculogenesis and Implications for Polycystic Ovarian Syndrome and Premature Ovarian Insufficiency: A Narrative Review. *Int J Mol Sci* 2024;**25**:7520. Available at: https://pmc.ncbi.nlm.nih.gov/articles/PMC11277126/. Accessed April 29, 2026.

Lopes F, Liu J, Morgan S, Matthews R, Nevin L, Anderson RA, Spears N. Single and combined effects of cisplatin and doxorubicin on the human and mouse ovary in vitro. *Reproduction* 2019;**159**:193. Available at: https://pmc.ncbi.nlm.nih.gov/articles/PMC6993208/. Accessed December 29, 2025.

Lopes F, Smith R, Anderson RA, Spears N. Docetaxel induces moderate ovarian toxicity in mice, primarily affecting granulosa cells of early growing follicles. *Mol Hum Reprod* 2014;**20**:948. Available at: https://pmc.ncbi.nlm.nih.gov/articles/PMC4172173/. Accessed December 29, 2025.

Luborsky JL, Meyer P, Sowers MF, Gold EB, Santoro N. Premature menopause in a multi-ethnic population study of the menopause transition*. *Human Reproduction* 2003;**18**:199–206. Available at: https://dx.doi.org/10.1093/humrep/deg005. Accessed December 11, 2025.

Lv X, He C, Huang C, Wang H, Hua G, Wang Z, Zhou J, Chen X, Ma B, Timm BK, *et al.* Timely expression and activation of YAP1 in granulosa cells is essential for ovarian follicle development. *The FASEB Journal* 2019;**33**:10049–10064. Available at: /doi/pdf/10.1096/fj.201900179RR. Accessed July 10, 2025.

La Marca A, Volpe A. Anti-Müllerian hormone (AMH) in female reproduction: is measurement of circulating AMH a useful tool? *Clin Endocrinol (Oxf)* 2006;**64**:603–610. Available at: /doi/pdf/10.1111/j.1365-2265.2006.02533.x. Accessed November 13, 2025.

Marchais M, Gilbert I, Bastien A, Macaulay A, Robert C. Mammalian cumulus-oocyte complex communication: a dialog through long and short distance messaging. *J Assist Reprod Genet* 2022;**39**:1011–1025. Available at: https://link.springer.com/article/10.1007/s10815-022-02438-8. Accessed September 27, 2025.

Maric-Bilkan C, Gilbert EL, Ryan MJ. Impact of ovarian function on cardiovascular health in women: focus on hypertension. *Int J Womens Health* 2014;**6**:131. Available at: https://pmc.ncbi.nlm.nih.gov/articles/PMC3908909/. Accessed December 10, 2025.

McGee EA, Hsueh AJW. Initial and cyclic recruitment of ovarian follicles. *Endocr Rev* 2000;**21**:200–214. Available at: https://pubmed.ncbi.nlm.nih.gov/10782364/. Accessed September 27, 2025.

McKey J, Cameron LA, Lewis D, Batchvarov IS, Capel B. Combined iDISCO and CUBIC tissue clearing and lightsheet microscopy for in toto analysis of the adult mouse ovary†. *Biol Reprod* 2020;**102**:1080. Available at: /pmc/articles/PMC7186783/. Accessed June 6, 2024.

McLaughlin EA, McIver SC. Awakening the oocyte: controlling primordial follicle development. *Reproduction* 2009;**137**:1–11. Available at: https://rep.bioscientifica.com/view/journals/rep/137/1/1.xml. Accessed May 29, 2025.

McLaughlin M, Albertini DF, Wallace WHB, Anderson RA, Telfer EE. Metaphase II oocytes from human unilaminar follicles grown in a multi-step culture system. *Mol Hum Reprod* 2018;**24**:135–142. Available at: https://pubmed.ncbi.nlm.nih.gov/29390119/. Accessed September 27, 2025.

Meng Y, Sun D, Qin Y, Dong X, Luo G, Liu Y. Cell-penetrating peptides enhance the transduction of adeno-associated virus serotype 9 in the central nervous system. *Mol Ther Methods Clin Dev* 2021;**21**:28. Available at: https://pmc.ncbi.nlm.nih.gov/articles/PMC7960505/. Accessed November 13, 2025.

Mihm M, Evans ACO. Mechanisms for dominant follicle selection in monovulatory species: a comparison of morphological, endocrine and intraovarian events in cows, mares and women. *Reprod Domest Anim* 2008;**43 Suppl 2**:48–56. Available at: https://pubmed.ncbi.nlm.nih.gov/18638104/. Accessed December 14, 2025.

Millier SG, Whitelaw PF, Smyth CD. Follicular oestrogen synthesis: the 'two-cell, two-gonadotrophin' model revisited. *Mol Cell Endocrinol* 1994;**100**:51–54. Available at: https://www.sciencedirect.com/science/article/abs/pii/030372079490278X?via%3Dihub. Accessed December 14, 2025.

Mishra GD, Pandeya N, Dobson AJ, Chung HF, Anderson D, Kuh D, Sandin S, Giles GG, Bruinsma F, Hayashi K, *et al.* Early menarche, nulliparity and the risk for premature and early natural menopause. *Hum Reprod* 2017;**32**:679–686. Available at: https://pubmed.ncbi.nlm.nih.gov/28119483/. Accessed December 11, 2025.

Mizuno N, Mizutani E, Sato H, Kasai M, Ogawa A, Suchy F, Yamaguchi T, Nakauchi H. Intra-embryo Gene Cassette Knockin by CRISPR/Cas9-Mediated Genome Editing with Adeno-Associated Viral Vector. *iScience* 2018;**9**:286–297. Available at: https://www.sciencedirect.com/science/article/pii/S2589004218301895. Accessed July 10, 2025.

Moolhuijsen LME, Visser JA. Anti-Müllerian Hormone and Ovarian Reserve: Update on Assessing Ovarian Function. *J Clin Endocrinol Metab* 2020;**105**:3361. Available at: https://pmc.ncbi.nlm.nih.gov/articles/PMC7486884/. Accessed November 13, 2025.

Morgan S, Lopes F, Gourley C, Anderson RA, Spears N. Cisplatin and Doxorubicin Induce Distinct Mechanisms of Ovarian Follicle Loss; Imatinib Provides Selective Protection Only against Cisplatin. *PLoS One* 2013;**8**:e70117. Available at: https://pmc.ncbi.nlm.nih.gov/articles/PMC3726485/. Accessed December 29, 2025.

Morgan S, Murray A, Spears N. Culture and Co-Culture of Mouse Ovaries and Ovarian Follicles. *J Vis Exp* 2015;**2015**:52458. Available at: https://pmc.ncbi.nlm.nih.gov/articles/PMC4401360/. Accessed December 8, 2025.

Mork L, Maatouk DM, McMahon JA, Guo JJ, Zhang P, McMahon AP, Capel B. Temporal differences in granulosa cell specification in the ovary reflect distinct follicle fates in mice. *Biol Reprod* 2012;**86**. Available at: https://pubmed.ncbi.nlm.nih.gov/21976597/. Accessed September 27, 2025.

Muhuri M, Levy DI, Schulz M, McCarty D, Gao G. Durability of transgene expression after rAAV gene therapy. *Molecular Therapy* 2022;**30**:1364–1380. Available at: https://www.sciencedirect.com/science/article/pii/S1525001622001617. Accessed July 13, 2025.

Mukashyaka P, Kumar P, Mellert DJ, Nicholas S, Noorbakhsh J, Brugiolo M, Courtois ET, Anczukow O, Liu ET, Chuang JH. High-throughput deconvolution of 3D organoid dynamics at cellular resolution for cancer pharmacology with Cellos. *Nature Communications 2023 14:1* 2023;**14**:1–17. Available at: https://www.nature.com/articles/s41467-023-44162-6. Accessed November 13, 2025.

Murase T, Iwase A, Komatsu K, Bayasula, Nakamura T, Osuka S, Takikawa S, Goto M, Kotani T, Kikkawa F. Follicle dynamics: visualization and analysis of follicle growth and maturation using murine ovarian tissue culture. *Journal of Assisted Reproduction and Genetics 2017 35:2* 2017;**35**:339–343. Available at: https://link.springer.com/article/10.1007/s10815-017-1073-5. Accessed November 8, 2025.

Nackenhorst MC, Kasiri M, Gollackner B, Regele H. Ex vivo fluorescence confocal microscopy: chances and changes in the analysis of breast tissue. *Diagnostic Pathology 2022 17:1* 2022;**17**:1–7. Available at: https://diagnosticpathology.biomedcentral.com/articles/10.1186/s13000-022-01240-5. Accessed November 9, 2025.

Najafi S, Rahimpour A, Ahmadieh H, Tehrani MM, Khalilzad MA, Suri F, Ranjbari J. The significance of chemical transfection/transduction enhancers in promoting the viral vectors-assisted gene delivery approaches: A focus on potentials for inherited retinal diseases. *Electronic Journal of Biotechnology* 2024;**72**:29–40. Available at: https://www.sciencedirect.com/science/article/pii/S0717345824000265. Accessed November 13, 2025.

National Academies of Sciences E and MH and MDB on PH and PHPC on the A of NR on WH, Geller A, Salganicoff A, Burke SP. The Need for Women's Health Research. *A New Vision for Women's Health Research: Transformative Change at the National Institutes of Health* 2025:1–507. Available at: https://www.ncbi.nlm.nih.gov/books/NBK612396/. Accessed December 10, 2025.

Nicol B, Rodriguez K, Yao HHC. Aberrant and constitutive expression of FOXL2 impairs ovarian development and functions in mice. *Biol Reprod* 2020;**103**:966. Available at: https://pmc.ncbi.nlm.nih.gov/articles/PMC7609876/. Accessed July 10, 2025.

Nie L, Wang X, Wang S, Hong Z, Wang M. Genetic insights into the complexity of premature ovarian insufficiency. *Reproductive Biology and Endocrinology 2024 22:1* 2024;**22**:94-. Available at: https://link.springer.com/article/10.1186/s12958-024-01254-2. Accessed December 11, 2025.

Nilsson NMP, Jameson MH, Clinton K. Thesmophoria. *Oxford Research Encyclopedia of Classics* 2016. Available at: https://oxfordre.com/classics/display/10.1093/acrefore/9780199381135.001.0001/acrefore-9780199381135-e-6391. Accessed December 10, 2025.

Niu W, Spradling AC. Two distinct pathways of pregranulosa cell differentiation support follicle formation in the mouse ovary. *Proc Natl Acad Sci U S A* 2020;**117**:20015–20026. Available at: /doi/pdf/10.1073/pnas.2005570117?download=true. Accessed July 13, 2025.

O'Connell JM, Pepling ME. Primordial Follicle Formation – Some Assembly Required. *Curr Opin Endocr Metab Res* 2021;**18**:118. Available at: https://pmc.ncbi.nlm.nih.gov/articles/PMC8133693/. Accessed September 27, 2025.

Office for National Statistics. Childbearing for women born in different years, England and Wales: 2023. *Office for National Statistics* 2025. Available at: https://www.ons.gov.uk/peoplepopulationandcommunity/birthsdeathsandmarriages/conceptionandfertilityrates/bulletins/childbearingforwomenbornindifferentyearsenglandandwales/2023. Accessed April 29, 2026.

Office for National Statistics UK. Milestones: journeying through modern life. 2024. Available at: https://www.ons.gov.uk/peoplepopulationandcommunity/populationandmigration/populationestimates/articles/milestonesjourneyingthroughmodernlife/2024-04-08. Accessed December 11, 2025.

Office for National Statistics UK. Population estimates for the UK, England, Wales, Scotland and Northern Ireland - Office for National Statistics. 2025. Available at: https://www.ons.gov.uk/peoplepopulationandcommunity/populationandmigration/populationestimates/bulletins/annualmidyearpopulationestimates/mid2024. Accessed December 11, 2025.

Oktem O, Oktay K. The ovary: Anatomy and function throughout human life. *Ann N Y Acad Sci* 2008;**1127**:1–9.

Oreopoulos J, Berman R, Browne M. Spinning-disk confocal microscopy: present technology and future trends. *Methods Cell Biol* 2014;**123**:153–175. Available at: https://www.sciencedirect.com/science/chapter/bookseries/pii/B9780124201385000094. Accessed November 9, 2025.

Orisaka M, Miyazaki Y, Shirafuji A, Tamamura C, Tsuyoshi H, Tsang BK, Yoshida Y. The role of pituitary gonadotropins and intraovarian regulators in follicle development: A mini-review. *Reprod Med Biol* 2021;**20**:169. Available at: https://pmc.ncbi.nlm.nih.gov/articles/PMC8022101/. Accessed April 29, 2026.

Ou Z, Duh YS, Rommelfanger NJ, Keck CHC, Jiang S, Brinson K, Zhao S, Schmidt EL, Wu X, Yang F, *et al.* Achieving optical transparency in live animals with absorbing molecules. *Science (1979)* 2024;**385**. Available at: /doi/pdf/10.1126/science.adm6869?download=true. Accessed November 13, 2025.

Ouni E, Vertommen D, Chiti MC, Dolmans MM, Amorim CA. A Draft Map of the Human Ovarian Proteome for Tissue Engineering and Clinical Applications. *Mol Cell Proteomics* 2018;**18**:S159. Available at: https://pmc.ncbi.nlm.nih.gov/articles/PMC6427241/. Accessed May 4, 2026.

Pacak CA, Sakai Y, Thattaliyath BD, Mah CS, Byrne BJ. Tissue specific promoters improve specificity of AAV9 mediated transgene expression following intra-vascular gene delivery in neonatal mice. *Genet Vaccines Ther* 2008;**6**:13.

Pankajakshan D, Makinde TO, Gaurav R, Del Core M, Hatzoudis G, Pipinos I, Agrawal DK. Successful Transfection of Genes Using AAV-2/9 Vector in Swine Coronary and Peripheral

Arteries. *J Surg Res* 2011;**175**:169. Available at: https://pmc.ncbi.nlm.nih.gov/articles/PMC3150285/. Accessed July 10, 2025.

Pankhurst MW, Kelley RL, Sanders RL, Woodcock SR, Oorschot DE, Batchelor NJ. Anti-Müllerian hormone overexpression restricts preantral ovarian follicle survival. *Journal of Endocrinology* 2018;**237**:153–163. Available at: https://joe.bioscientifica.com/view/journals/joe/237/2/JOE-18-0005.xml. Accessed November 13, 2025.

De Paola L, Napoletano G, Gullo G, Circosta F, Vergallo GM, Marinelli S. The era of increasing cancer survivorship: Trends in fertility preservation, medico-legal implications, and ethical challenges. *Open Medicine* 2025;**20**:20251144. Available at: https://pmc.ncbi.nlm.nih.gov/articles/PMC11826245/. Accessed December 11, 2025.

Park T, Kim TK, Han YD, Kim KA, Kim H, Kim HS. Development of a deep learning based image processing tool for enhanced organoid analysis. *Scientific Reports 2023 13:1* 2023;**13**:1–11. Available at: https://www.nature.com/articles/s41598-023-46485-2. Accessed November 13, 2025.

Paulino LRFM, de Assis EIT, Azevedo VAN, Silva BR, da Cunha E V., Silva JRV. Why Is It So Difficult To Have Competent Oocytes from In vitro Cultured Preantral Follicles? *Reproductive Sciences* 2022;**29**:3321–3334. Available at: https://link.springer.com/article/10.1007/s43032-021-00840-8. Accessed September 27, 2025.

Pedersen T, Peters H. Proposal for a classification of oocytes and follicles in the mouse ovary. *J Reprod Fertil* 1968;**17**:555–557. Available at: https://pubmed.ncbi.nlm.nih.gov/5715685/. Accessed September 27, 2025.

Pellatt L, Hanna L, Brincat M, Galea R, Brain H, Whitehead S, Mason H. Granulosa Cell Production of Anti-Müllerian Hormone Is Increased in Polycystic Ovaries. *J Clin Endocrinol Metab* 2007;**92**:240–245. Available at: https://dx.doi.org/10.1210/jc.2006-1582. Accessed November 13, 2025.

Peng J, Li Q, Wigglesworth K, Rangarajan A, Kattamuri C, Peterson RT, Eppig JJ, Thompson TB, Matzuk MM. Growth differentiation factor 9:bone morphogenetic protein 15 heterodimers are potent regulators of ovarian functions. *Proc Natl Acad Sci U S A* 2013;**110**:E776–E785. Available at: /doi/pdf/10.1073/pnas.1218020110?download=true. Accessed December 14, 2025.

Pépin D, Sosulski A, Zhang L, Wang D, Vathipadiekal V, Hendren K, Coletti CM, Yu A, Castro CM, Birrer MJ, *et al.* AAV9 delivering a modified human Mullerian inhibiting substance as a gene therapy in patient-derived xenografts of ovarian cancer. *Proc Natl Acad Sci U S A* 2015;**112**:E4418–E4427. Available at: /doi/pdf/10.1073/pnas.1510604112?download=true. Accessed November 10, 2025.

Pepling ME, Spradling AC. Mouse ovarian germ cell cysts undergo programmed breakdown to form primordial follicles. *Dev Biol* 2001;**234**:339–351. Available at: https://pubmed.ncbi.nlm.nih.gov/11397004/. Accessed September 27, 2025.

Picut CA, Swanson CL, Scully KL, Roseman VC, Parker RF, Remick AK. Ovarian follicle counts using proliferating cell nuclear antigen (PCNA) and semi-automated image analysis in rats. *Toxicol Pathol* 2008;**36**:674–679. Available at: https://scholar.google.com/scholar_url?url=https://journals.sagepub.com/doi/pdf/10.1177/0192623308317428&hl=en&sa=T&oi=ucasa&ct=ufr&ei=n6EQaZL7NoS6ieoP-o_w-Qg&scisig=ABGrvjKYt9jZoqFqmzRo4UyMwJ7N. Accessed November 9, 2025.

Porras-Gomez TJ, Moreno-Mendoza N. Interaction between oocytes, cortical germ cells and granulosa cells of the mouse and bat, following the dissociation-re-aggregation of adult ovaries.

Zygote 2020;**28**:223–232. Available at: https://pubmed.ncbi.nlm.nih.gov/32122435/. Accessed September 27, 2025.

Prasad S, Koch B, Chaube SK. RO-3306 prevents postovulatory aging-mediated spontaneous exit from M-II arrest in rat eggs cultured in vitro. *Biomedicine & Pharmacotherapy* 2016;**78**:216–225. Available at: https://www.sciencedirect.com/science/article/pii/S0753332215302134. Accessed December 14, 2025.

Preibisch S, Saalfeld S, Tomancak P. Globally optimal stitching of tiled 3D microscopic image acquisitions. *Bioinformatics* 2009;**25**:1463. Available at: https://pmc.ncbi.nlm.nih.gov/articles/PMC2682522/. Accessed November 15, 2025.

Rahman S, Sesenna V, Osorio Arce D, Maugeri E, Esposito S. From Survival to Parenthood: The Fertility Journey After Childhood Cancer. *Biomedicines* 2025;**13**. Available at: https://pubmed.ncbi.nlm.nih.gov/40868114/. Accessed December 11, 2025.

Ran FA, Cong L, Yan WX, Scott DA, Gootenberg JS, Kriz AJ, Zetsche B, Shalem O, Wu X, Makarova KS, *et al.* In vivo genome editing using Staphylococcus aureus Cas9. *Nature 2015 520:7546* 2015;**520**:186–191. Available at: https://www.nature.com/articles/nature14299. Accessed July 10, 2025.

Regensteiner JG, McNeil M, Faubion SS, Bairey-Merz CN, Gulati M, Joffe H, Redberg RF, Rosen SE, Reusch JE, Klein W. Barriers and solutions in women's health research and clinical care: a call to action. *Lancet Regional Health - Americas* 2025;**44**:101037. Available at: https://pmc.ncbi.nlm.nih.gov/articles/PMC11937288/. Accessed December 10, 2025.

Richards JS, Pangas SA. The ovary: basic biology and clinical implications. *J Clin Invest* 2010;**120**:963. Available at: https://pmc.ncbi.nlm.nih.gov/articles/PMC2846061/. Accessed December 10, 2025.

Richardson DS, Lichtman JW. Clarifying Tissue Clearing. *Cell* 2015;**162**:246–257. Available at: http://www.cell.com/article/S0092867415008375/fulltext. Accessed June 6, 2024.

Richardson SJ, Senikas V, Nelson JF. Follicular depletion during the menopausal transition: evidence for accelerated loss and ultimate exhaustion. *J Clin Endocrinol Metab* 1987;**65**:1231–1237. Available at: https://pubmed.ncbi.nlm.nih.gov/3119654/. Accessed December 10, 2025.

Rinaldi VD, Bloom JC, Schimenti JC. Whole Mount Immunofluorescence and Follicle Quantification of Cultured Mouse Ovaries. *JoVE (Journal of Visualized Experiments)* 2018;**2018**:e57593. Available at: https://www.jove.com/v/57593/whole-mount-immunofluorescence-follicle-quantification-cultured-mouse. Accessed June 6, 2024.

Rizzardi AE, Johnson AT, Vogel RI, Pambuccian SE, Henriksen J, Skubitz APN, Metzger GJ, Schmechel SC. Quantitative comparison of immunohistochemical staining measured by digital image analysis versus pathologist visual scoring. *Diagnostic Pathology 2012 7:1* 2012;**7**:1–10. Available at: https://diagnosticpathology.biomedcentral.com/articles/10.1186/1746-1596-7-42. Accessed November 9, 2025.

Roet JEG, Mikula AM, de Kok M, Chadick CH, Garcia Vallejo JJ, Roest HP, van der Laan LJW, de Winde CM, Mebius RE. Unbiased method for spectral analysis of cells with great diversity of autofluorescence spectra. *Cytometry Part A* 2024;**105**:595–606. Available at: /doi/pdf/10.1002/cyto.a.24856. Accessed November 11, 2025.

De Roo C, Lierman S, Tilleman K, De Sutter P. In-vitro fragmentation of ovarian tissue activates primordial follicles through the Hippo pathway. *Hum Reprod Open* 2020;**2020**. Available at: https://dx.doi.org/10.1093/hropen/hoaa048. Accessed December 14, 2025.

Rooda I, Méar L, Hassan J, Damdimopoulou P. The adult ovary at single cell resolution: an expert review. *Am J Obstet Gynecol* 2025;**232**:S94-S103.e6. Available at:

https://www.sciencedirect.com/science/article/pii/S0002937824006501. Accessed September 27, 2025.

Rossi V, Lispi M, Longobardi S, Mattei M, Rella F Di, Salustri A, De Felici M, Klinger FG. LH prevents cisplatin-induced apoptosis in oocytes and preserves female fertility in mouse. *Cell Death Differ* 2016;**24**:72. Available at: https://pmc.ncbi.nlm.nih.gov/articles/PMC5260508/. Accessed December 29, 2025.

Ruifrok AC, Johnston DA. Quantification of histochemical staining by color deconvolution. *Anal Quant Cytol Histol* 2001;**23**:291–299.

Sarraj MA, Drummond AE. Mammalian foetal ovarian development: consequences for health and disease. *Reproduction* 2012;**143**:151–163. Available at: https://pubmed.ncbi.nlm.nih.gov/22106406/. Accessed December 14, 2025.

Schallmoser A, Einenkel R, Färber C, Sänger N. In vitro growth (IVG) of human ovarian follicles in frozen thawed ovarian cortex tissue culture supplemented with follicular fluid under hypoxic conditions. *Arch Gynecol Obstet* 2022;**306**:1299. Available at: https://pmc.ncbi.nlm.nih.gov/articles/PMC9470640/. Accessed September 21, 2025.

Schneckenburger H, Richter V. Challenges in 3D Live Cell Imaging. *Photonics 2021, Vol 8, Page 275* 2021;**8**:275. Available at: https://www.mdpi.com/2304-6732/8/7/275/htm. Accessed November 9, 2025.

Scripps E, Webb L. Impacts of birthrate decline, POSTnote 745. *The Parliamentary Office of Science and Technology* 2025:1–30. Available at: https://doi.org/10.58248/PN745. Accessed December 10, 2025.

Shao T, Ke H, Liu R, Xu L, Han S, Zhang X, Dang Y, Jiao X, Li W, Chen ZJ, *et al.* Autophagy regulates differentiation of ovarian granulosa cells through degradation of WT1. *Autophagy* 2022;**18**:1864–1878. Available at: https://www.tandfonline.com/doi/pdf/10.1080/15548627.2021.2005415. Accessed July 13, 2025.

Sheikh S, Lo BKM, Kaune H, Bansal J, Deleva A, Williams SA. Rescue of follicle development after oocyte-induced ovary dysfunction and infertility in a model of POI. *Front Cell Dev Biol* 2023;**11**. Available at: https://pubmed.ncbi.nlm.nih.gov/37614224/. Accessed September 27, 2025.

Shirafuta Y, Tamura I, Shiroshita A, Fujimura T, Maekawa R, Taketani T, Sugino N. Analysis of cell–cell interaction between mural granulosa cells and cumulus granulosa cells during ovulation using single-cell RNA sequencing data of mouse ovary. *Reprod Med Biol* 2024;**23**:e12564. Available at: https://pmc.ncbi.nlm.nih.gov/articles/PMC10867398/. Accessed September 27, 2025.

Da Silva-Buttkus P, Marcelli G, Franks S, Stark J, Hardy K. Inferring biological mechanisms from spatial analysis: Prediction of a local inhibitor in the ovary. *Proc Natl Acad Sci U S A* 2009;**106**:456. Available at: https://pmc.ncbi.nlm.nih.gov/articles/PMC2626724/. Accessed April 30, 2026.

Soleimani R, Heytens E, Oktay K. Enhancement of neoangiogenesis and follicle survival by sphingosine-1-phosphate in human ovarian tissue xenotransplants. *PLoS One* 2011;**6**. Available at: https://pubmed.ncbi.nlm.nih.gov/21559342/. Accessed December 29, 2025.

Soleimani R, De Vos W, Van Oostveldt P, Lierman S, Van den Broecke R, De Sutter P, Dhont M, Van der Elst J. Two novel techniques to detect follicles in human ovarian cortical tissue. *Human Reproduction* 2006;**21**:1720–1724. Available at: https://dx.doi.org/10.1093/humrep/del057. Accessed May 27, 2024.

Sonmezer M, Sacinti KG, Oktay KH. Female fertility preservation: 25 years of progress, expanding indications and future prospects. *Hum Reprod Update* 2025. Available at: https://dx.doi.org/10.1093/humupd/dmaf026. Accessed December 29, 2025.

Soriano P. Generalized lacZ expression with the ROSA26 Cre reporter strain [1]. *Nat Genet* 1999a;**21**:70–71. Available at: https://www.nature.com/articles/ng0199_70. Accessed July 10, 2025.

Soriano P. Generalized lacZ expression with the ROSA26 Cre reporter strain. *Nature Genetics 1999 21:1* 1999b;**21**:70–71. Available at: https://www.nature.com/articles/ng0199_70. Accessed January 4, 2026.

Soygur B, Laird DJ. Ovary Development: Insights From a Three-Dimensional Imaging Revolution. *Front Cell Dev Biol* 2021;**9**:698315.

Spears N, Lopes F, Stefansdottir A, Rossi V, De Felici M, Anderson RA, Klinger FG. Ovarian damage from chemotherapy and current approaches to its protection. *Hum Reprod Update* 2019;**25**:673. Available at: https://pmc.ncbi.nlm.nih.gov/articles/PMC6847836/. Accessed December 29, 2025.

Stephens CJ, Kashentseva E, Everett W, Kaliberova L, Curiel DT. Targeted in vivo knock-in of human alpha-1-antitrypsin cDNA using adenoviral delivery of CRISPR/Cas9. *Gene Therapy 2018 25:2* 2018;**25**:139–156. Available at: https://www.nature.com/articles/s41434-018-0003-1. Accessed November 13, 2025.

Strauss JF, Williams CJ. Ovarian Life Cycle. *Yen & Jaffe's Reproductive Endocrinology: Physiology, Pathophysiology, and Clinical Management: Eighth Edition* 2019:167-205.e9. Available at: https://www.sciencedirect.com/science/article/abs/pii/B9780323479127000081. Accessed September 27, 2025.

Suoranta T, Laham-Karam N, Ylä-Herttuala S. Strategies to improve safety profile of AAV vectors. *Frontiers in Molecular Medicine* 2022;**2**:1054069.

Tanimoto R, Yoshida K, Ikeda S, Obata Y. Insights into in vivo follicle formation: a review of in vitro systems. *Histochemistry and Cell Biology 2021 157:3* 2021;**157**:333–345. Available at: https://link.springer.com/article/10.1007/s00418-021-02058-w. Accessed May 1, 2026.

Taylor CR, Levenson RM. Quantification of immunohistochemistry - Issues concerning methods, utility and semiquantitative assessment II. *Histopathology* 2006;**49**:411–424. Available at: /doi/pdf/10.1111/j.1365-2559.2006.02513.x. Accessed November 9, 2025.

Telfer EE, Andersen CY. In vitro growth and maturation of primordial follicles and immature oocytes. *Fertil Steril* 2021;**115**:1116–1125.

Telfer EE, Grosbois J, Odey YL, Rosario R, Anderson RA. Making a good egg: human oocyte health, aging, and in vitro development. *Physiol Rev* 2023;**103**:2623–2677. Available at: https://pubmed.ncbi.nlm.nih.gov/37171807/. Accessed December 29, 2025.

Telfer EE, McLaughlin M. Strategies to support human oocyte development in vitro. *International Journal of Developmental Biology* 2012;**56**:901–907.

Telfer EE, Zelinski MB. Ovarian follicle culture: advances and challenges for human and nonhuman primates. *Fertil Steril* 2013;**99**:1523–1533. Available at: https://www.sciencedirect.com/science/article/pii/S0015028213004597. Accessed November 13, 2025.

Thomas C, Marx TL, Penir SM, Schuh M. Ex vivo imaging reveals the spatiotemporal control of ovulation. *Nature Cell Biology 2024 26:11* 2024;**26**:1997–2008. Available at: https://www.nature.com/articles/s41556-024-01524-6. Accessed November 8, 2025.

Tilly JL. Ovarian follicle counts – not as simple as 1, 2, 3. *Reproductive Biology and Endocrinology 2003 1:1* 2003;**1**:1–4. Available at: https://rbej.biomedcentral.com/articles/10.1186/1477-7827-1-11. Accessed November 9, 2025.

Tingen C, Kim A, Woodruff TK. The primordial pool of follicles and nest breakdown in mammalian ovaries. *Mol Hum Reprod* 2009;**15**:795. Available at: https://pmc.ncbi.nlm.nih.gov/articles/PMC2776475/. Accessed September 27, 2025.

Tomic D, Brodie SG, Deng C, Hickey RJ, Babus JK, Malkas LH, Flaws JA. Smad 3 May Regulate Follicular Growth in the Mouse Ovary. *Biol Reprod* 2002;**66**:917–923. Available at: https://dx.doi.org/10.1095/biolreprod66.4.917. Accessed May 1, 2026.

Turathum B, Gao EM, Chian RC. The Function of Cumulus Cells in Oocyte Growth and Maturation and in Subsequent Ovulation and Fertilization. *Cells* 2021;**10**:2292. Available at: https://pmc.ncbi.nlm.nih.gov/articles/PMC8470117/. Accessed December 14, 2025.

UNFPA, (Denmark) I for M, Rights UNO of the HC for H. Reproductive rights are human rights :: a handbook for national human rights institutions. 2014. Available at: https://digitallibrary.un.org/record/3975325. Accessed December 10, 2025.

United Nations General Assembly. Convention on the Elimination of All Forms of Discrimination against Women New York, 18 December 1979 . *OHCHR* 1979. Available at: https://www.ohchr.org/en/instruments-mechanisms/instruments/convention-elimination-all-forms-discrimination-against-women. Accessed December 11, 2025.

Uslu B, Dioguardi CC, Haynes M, Miao DQ, Kurus M, Hoffman G, Johnson J. Quantifying growing versus non-growing ovarian follicles in the mouse. *J Ovarian Res* 2017;**10**:3. Available at: /pmc/articles/PMC5237173/. Accessed June 6, 2024.

Valeri C, Pappalardo S, De Felici M, Manna C. Correlation of oocyte morphometry parameters with woman's age. *J Assist Reprod Genet* 2011;**28**:545. Available at: https://pmc.ncbi.nlm.nih.gov/articles/PMC3158254/. Accessed December 11, 2025.

Varghese F, Bukhari AB, Malhotra R, De A. IHC Profiler: An Open Source Plugin for the Quantitative Evaluation and Automated Scoring of Immunohistochemistry Images of Human Tissue Samples. *PLoS One* 2014;**9**:e96801. Available at: https://pmc.ncbi.nlm.nih.gov/articles/PMC4011881/. Accessed October 18, 2025.

te Velde ER, Scheffer GJ, Dorland M, Broekmans FJ, Fauser BCJM. Developmental and endocrine aspects of normal ovarian aging. *Mol Cell Endocrinol* 1998;**145**:67–73. Available at: https://pubmed.ncbi.nlm.nih.gov/9922101/. Accessed December 14, 2025.

Visser JA, de Jong FH, Laven JSE, Themmen APN. Anti-Müllerian hormone: a new marker for ovarian function. *Reproduction* 2006;**131**:1–9. Available at: https://rep.bioscientifica.com/view/journals/rep/131/1/1310001.xml. Accessed November 13, 2025.

Walker CA, Bjarkadottir BD, Fatum M, Lane S, Williams SA. Variation in follicle health and development in cultured cryopreserved ovarian cortical tissue: a study of ovarian tissue from patients undergoing fertility preservation. *Hum Fertil (Camb)* 2021;**24**:188–198. Available at: https://pubmed.ncbi.nlm.nih.gov/31117847/. Accessed September 27, 2025.

Walkey CJ, Snow KJ, Bulcha J, Cox AR, Martinez AE, Ljungberg MC, Lanza DG, De Giorgi M, Chuecos MA, Alves-Bezerra M, *et al.* A comprehensive atlas of AAV tropism in the mouse. *Molecular Therapy* 2025;**33**:1282–1299. Available at: https://www.cell.com/action/showFullText?pii=S1525001625000437. Accessed November 10, 2025.

Wallace WHB, Kelsey TW. Human Ovarian Reserve from Conception to the Menopause. *PLoS One* 2010;**5**:e8772. Available at: https://pmc.ncbi.nlm.nih.gov/articles/PMC2811725/. Accessed April 29, 2026.

Wallace WHB, Thomson AB, Kelsey TW. The radiosensitivity of the human oocyte. *Hum Reprod* 2003;**18**:117–121. Available at: https://pubmed.ncbi.nlm.nih.gov/12525451/. Accessed December 10, 2025.

Wang JH, Gessler DJ, Zhan W, Gallagher TL, Gao G. Adeno-associated virus as a delivery vector for gene therapy of human diseases. *Signal Transduction and Targeted Therapy 2024 9:1* 2024;**9**:1–33. Available at: https://www.nature.com/articles/s41392-024-01780-w. Accessed July 13, 2025.

Wang S, Yang S, Lai Z, Ding T, Shen W, Shi L, Jiang J, Ma L, Tian Y, Du X, *et al.* Effects of culture and transplantation on follicle activation and early follicular growth in neonatal mouse ovaries. *Cell Tissue Res* 2013;**354**:609. Available at: https://pmc.ncbi.nlm.nih.gov/articles/PMC3836445/. Accessed November 13, 2025.

Wang X, Pepling ME. Regulation of Meiotic Prophase One in Mammalian Oocytes. *Front Cell Dev Biol* 2021;**9**:667306. Available at: www.frontiersin.org. Accessed September 26, 2025.

Wang X, Yang J, Jin C, Wang X, Contreras D, Devos M, Suh Y. Transcriptomic signatures of mouse ovarian aging and estropausal transition at single cell resolution. *bioRxiv* 2024:2024.08.12.607592. Available at: https://www.biorxiv.org/content/10.1101/2024.08.12.607592v1. Accessed July 10, 2025.

Warren A, Garrett K, Frame LA. Disparities in women's health and clinical considerations from a translational science perspective: A narrative review and framework for future directions. *Women's Health* 2025;**21**:17455057251399008. Available at: https://pmc.ncbi.nlm.nih.gov/articles/PMC12657800/. Accessed December 10, 2025.

Wear HM, McPike MJ, Watanabe KH. From primordial germ cells to primordial follicles: A review and visual representation of early ovarian development in mice. *J Ovarian Res* 2016;**9**:1–11. Available at: https://ovarianresearch.biomedcentral.com/articles/10.1186/s13048-016-0246-7. Accessed September 27, 2025.

Webb R, Campbell BK. Development of the dominant follicle: mechanisms of selection and maintenance of oocyte quality. *Soc Reprod Fertil Suppl* 2007;**64**:141–163. Available at: https://pubmed.ncbi.nlm.nih.gov/17491145/. Accessed December 14, 2025.

Weenen C, Laven JSE, von Bergh ARM, Cranfield M, Groome NP, Visser JA, Kramer P, Fauser BCJM, Themmen APN. Anti-Müllerian hormone expression pattern in the human ovary: potential implications for initial and cyclic follicle recruitment. *Mol Hum Reprod* 2004;**10**:77–83. Available at: https://dx.doi.org/10.1093/molehr/gah015. Accessed July 10, 2025.

Wei Y, Yu R, Cheng S, Zhou P, Mo S, He C, Deng C, Wu P, Liu H, Cao C. Single-cell profiling of mouse and primate ovaries identifies high levels of EGFR for stromal cells in ovarian aging. *Mol Ther Nucleic Acids* 2023;**31**:1–12. Available at: https://www.sciencedirect.com/science/article/pii/S2162253122003122. Accessed November 11, 2025.

West-Farrell ER, Xu M, Gomberg MA, Chow YH, Woodruff TK, Shea LD. The Mouse Follicle Microenvironment Regulates Antrum Formation and Steroid Production: Alterations in Gene Expression Profiles. *Biol Reprod* 2009;**80**:432–439. Available at: https://dx.doi.org/10.1095/biolreprod.108.071142. Accessed September 27, 2025.

Westhaus A, Cabanes-Creus M, Rybicki A, Baltazar G, Navarro RG, Zhu E, Drouyer M, Knight M, Albu RF, Ng BH, *et al.* High-Throughput In Vitro, Ex Vivo, and In Vivo Screen of Adeno-

Associated Virus Vectors Based on Physical and Functional Transduction. *Hum Gene Ther* 2020;**31**:575. Available at: https://pmc.ncbi.nlm.nih.gov/articles/PMC7232709/. Accessed July 10, 2025.

Van Wezel IL, Rodgers RJ. Morphological characterization of bovine primordial follicles and their environment in vivo. *Biol Reprod* 1996;**55**:1003–1011. Available at: https://pubmed.ncbi.nlm.nih.gov/8902210/. Accessed September 27, 2025.

Williams CJ, Erickson GF. Morphology and Physiology of the Ovary. *Endotext* 2012. Available at: https://www.ncbi.nlm.nih.gov/books/NBK278951/. Accessed December 11, 2025.

Williams SA. What do women and rhinos have in common? *F S Rep* 2025;**6**:19–23. Available at: https://www.sciencedirect.com/science/article/pii/S2666334125000108. Accessed December 29, 2025.

Winstanley YE, Stables JS, Gonzalez MB, Umehara T, Norman RJ, Robker RL. Emerging therapeutic strategies to mitigate female and male reproductive aging. *Nature Aging 2024 4:12* 2024;**4**:1682–1696. Available at: https://www.nature.com/articles/s43587-024-00771-4. Accessed December 11, 2025.

World Health Organisation. Infertility. 2025a. Available at: https://www.who.int/news-room/fact-sheets/detail/infertility. Accessed December 10, 2025.

World Health Organisation. Sexual and reproductive health and rights. 2025b. Available at: https://www.who.int/health-topics/sexual-and-reproductive-health-and-rights#tab=tab_1. Accessed December 11, 2025.

World Health Organisation Guideline Development Group for Infertility, Balen AH, Cohlen B, Huyser C, Kissin D, Mahajan N, Mansour R, Murage A, Reindollar R, Rizzo R, *et al.* Recommendations from the WHO guideline for the prevention, diagnosis, and treatment of infertility. *Human Reproduction* 2025. Available at: https://dx.doi.org/10.1093/humrep/deaf212. Accessed December 11, 2025.

Wu B, Chen Y, Müller JD. Fluorescence Fluctuation Spectroscopy of mCherry in Living Cells. *Biophys J* 2009;**96**:2391. Available at: https://pmc.ncbi.nlm.nih.gov/articles/PMC2907682/. Accessed November 13, 2025.

Wu GMJ, Chen ACH, Yeung WSB, Lee YL. Current progress on in vitro differentiation of ovarian follicles from pluripotent stem cells. *Front Cell Dev Biol* 2023;**11**:1166351.

Xiao C, Ji M, Lai D. The Incidence and 5-Years Relative Survival Rate of Cancer Among People Younger Than 25 Years in the US, 2000 to 2020: A SEER-Retrospective Study and Fertility Preservation Considerations. *Sage Open Pediatrics* 2025;**12**:30502225251370800. Available at: https://pmc.ncbi.nlm.nih.gov/articles/PMC12409066/. Accessed December 11, 2025.

Xiao Q, Chen S, Wang Q, Liu Z, Liu S, Deng H, Hou W, Wu D, Xiong Y, Li J, *et al.* CCR5 editing by Staphylococcus aureus Cas9 in human primary CD4+ T cells and hematopoietic stem/progenitor cells promotes HIV-1 resistance and CD4+ T cell enrichment in humanized mice. *Retrovirology* 2019;**16**:1–17. Available at: https://retrovirology.biomedcentral.com/articles/10.1186/s12977-019-0477-y. Accessed July 10, 2025.

Xiao S, Zhang J, Romero MM, Smith KN, Shea LD, Woodruff TK. In vitro follicle growth supports human oocyte meiotic maturation. *Sci Rep* 2015;**5**:1–5. Available at: https://www.nature.com/articles/srep17323. Accessed September 27, 2025.

Xie Y, Ren Y, Niu C, Zheng Y, Yu P, Li L. The impact of stigma on mental health and quality of life of infertile women: A systematic review. *Front Psychol* 2023;**13**:1093459. Available at: https://pmc.ncbi.nlm.nih.gov/articles/PMC9869765/. Accessed December 10, 2025.

Xu F, Lawson MS, Bean Y, Ting AY, Pejovic T, De Geest K, Moffitt M, Mitalipov SM, Xu J. Matrix-free 3D culture supports human follicular development from the unilaminar to the antral stage in vitro yielding morphologically normal metaphase II oocytes. *Human Reproduction* 2021;**36**:1326–1338.

Xu M, Banc A, Woodruff TK, Shea LD. Secondary follicle growth and oocyte maturation by culture in alginate hydrogel following cryopreservation of the ovary or individual follicles. *Biotechnol Bioeng* 2009;**103**:378. Available at: https://pmc.ncbi.nlm.nih.gov/articles/PMC2778231/. Accessed December 30, 2025.

Yaba A, Bianchi V, Borini A, Johnson J. A Putative Mitotic Checkpoint Dependent on mTOR Function Controls Cell Proliferation and Survival in Ovarian Granulosa Cells. *Reproductive Sciences 2008 15:2* 2008;**15**:128–138. Available at: https://link.springer.com/article/10.1177/1933719107312037. Accessed December 14, 2025.

Yang Q, Zhu L, Jin L. Human Follicle in vitro Culture Including Activation, Growth, and Maturation: A Review of Research Progress. *Front Endocrinol (Lausanne)* 2020;**11**:548. Available at: https://pmc.ncbi.nlm.nih.gov/articles/PMC7431469/. Accessed May 29, 2025.

Yang S, Liu Z, Wu S, Zou L, Cao Y, Xu H, Huang J, Tian Q, Wu F, Li P, *et al.* Meiosis resumption in human primordial germ cells from induced pluripotent stem cells by in vitro activation and reconstruction of ovarian nests. *Stem Cell Res Ther* 2022;**13**:1–11. Available at: https://link.springer.com/articles/10.1186/s13287-022-03019-3. Accessed September 27, 2025.

Yao S, Rong W, Yuan Y. Optimization of adeno-associated virus (AAV) gene delivery into human bone marrow stem cells (hBMSCs). *Stem Cell Investig* 2023;**10**:3. Available at: https://pmc.ncbi.nlm.nih.gov/articles/PMC9905037/. Accessed November 13, 2025.

Yin H, Feng R, Wang S, Rui X, Ye M, Hu Y, Zhong O, Huang J, Wang W, Huo R. Automated follicle counting system(AFCS) using YOLO-based object detection algorithm and its application in the POI model. *Biomed Signal Process Control* 2025;**103**:107423. Available at: https://www.sciencedirect.com/science/article/pii/S1746809424014812. Accessed November 9, 2025.

Yin O, Cayton K, Segars JH. In Vitro Activation: A Dip Into the Primordial Follicle Pool? *J Clin Endocrinol Metab* 2016;**101**:3568–3570. Available at: https://pubmed.ncbi.nlm.nih.gov/27702318/. Accessed December 14, 2025.

Yoshida K, Kimura S, Taguchi M, Morimoto H, Kanatsu-Shinohara M, Shinohara T, Obata Y. In vitro system completely restores oogenesis in congenitally infertile mice. *Human Reproduction* 2025. Available at: https://dx.doi.org/10.1093/humrep/deaf194. Accessed November 10, 2025.

Young JM, McNeilly AS. Theca: the forgotten cell of the ovarian follicle. *Reproduction* 2010;**140**:489–504. Available at: https://pubmed.ncbi.nlm.nih.gov/20628033/. Accessed September 27, 2025.

Zegers-Hochschild F, Adamson GD, De Mouzon J, Ishihara O, Mansour R, Nygren K, Sullivan E, Van Der Poel S. The International Committee for Monitoring Assisted Reproductive Technology (ICMART) and the World Health Organization (WHO) Revised Glossary on ART Terminology, 2009. *Human Reproduction* 2009;**24**:2683–2687. Available at: https://dx.doi.org/10.1093/humrep/dep343. Accessed December 11, 2025.

Zeleznik AJ. The physiology of follicle selection. *Reprod Biol Endocrinol* 2004;**2**:31. Available at: https://pmc.ncbi.nlm.nih.gov/articles/PMC442133/. Accessed December 14, 2025.

Zhang H, Liu K. Cellular and molecular regulation of the activation of mammalian primordial follicles: somatic cells initiate follicle activation in adulthood. *Hum Reprod Update*

2015;**21**:779–786. Available at: https://dx.doi.org/10.1093/humupd/dmv037. Accessed September 27, 2025.

Zhang T, He M, Zhang J, Tong Y, Chen T, Wang C, Pan W, Xiao Z. Mechanisms of primordial follicle activation and new pregnancy opportunity for premature ovarian failure patients. *Front Physiol* 2023;**14**:1113684. Available at: https://pmc.ncbi.nlm.nih.gov/articles/PMC10011087/. Accessed April 29, 2026.

Zhang T, Zhang M, Zhang S, Wang S. Research advances in the construction of stem cell-derived ovarian organoids. *Stem Cell Res Ther* 2024;**15**:505. Available at: https://pmc.ncbi.nlm.nih.gov/articles/PMC11687137/. Accessed September 27, 2025.

Zhang Y, Nishiyama T, Li H, Huang J, Atmanli A, Sanchez-Ortiz E, Wang Z, Mireault AA, Mammen PPA, Bassel-Duby R, *et al.* A consolidated AAV system for single-cut CRISPR correction of a common Duchenne muscular dystrophy mutation. *Mol Ther Methods Clin Dev* 2021;**22**:122–132. Available at: https://www.sciencedirect.com/science/article/pii/S232905012100098X. Accessed July 10, 2025.

Zhang Y, Shao L, Xu Y, Cui Y, Liu J, Chian RC. Effect of Anti-Mullerian Hormone in Culture Medium on Quality of Mouse Oocytes Matured In Vitro. *PLoS One* 2014;**9**:e99393. Available at: https://journals.plos.org/plosone/article?id=10.1371/journal.pone.0099393. Accessed November 13, 2025.

Zhang Y, Yan Z, Qin Q, Nisenblat V, Chang HM, Yu Y, Wang T, Lu C, Yang M, Yang S, *et al.* Transcriptome Landscape of Human Folliculogenesis Reveals Oocyte and Granulosa Cell Interactions. *Mol Cell* 2018;**72**:1021-1034.e4. Available at: https://www.sciencedirect.com/science/article/pii/S109727651830889X. Accessed May 29, 2025.

Zhao H, Wang Y, Yang Y. Follicular development and ovary aging: single-cell studies. *Biol Reprod* 2023;**109**:390–407. Available at: https://dx.doi.org/10.1093/biolre/ioad080. Accessed September 27, 2025.

Zhao J, Yue Y, Patel A, Wasala L, Karp JF, Zhang K, Duan D, Lai Y. High-Resolution Histological Landscape of AAV DNA Distribution in Cellular Compartments and Tissues following Local and Systemic Injection. *Mol Ther Methods Clin Dev* 2020;**18**:856–868. Available at: https://www.sciencedirect.com/science/article/pii/S2329050120301728. Accessed November 13, 2025.

Zhao Y, Feng H, Zhang Y, Zhang J V., Wang X, Liu D, Wang T, Li RHW, Ng EHY, Yeung WSB, *et al.* Current Understandings of Core Pathways for the Activation of Mammalian Primordial Follicles. *Cells 2021, Vol 10, Page 1491* 2021;**10**:1491. Available at: https://www.mdpi.com/2073-4409/10/6/1491/htm. Accessed September 27, 2025.

Zhu Y, Zhu H, Wu P. Gap junctions in polycystic ovary syndrome: Implications for follicular arrest. *Developmental Dynamics* 2024;**253**:882–894. Available at: /doi/pdf/10.1002/dvdy.706. Accessed December 14, 2025.

Zincarelli C, Soltys S, Rengo G, Rabinowitz JE. Analysis of AAV Serotypes 1–9 Mediated Gene Expression and Tropism in Mice After Systemic Injection. *Molecular Therapy* 2008;**16**:1073–1080. Available at: https://www.sciencedirect.com/science/article/pii/S1525001616317324. Accessed July 10, 2025.

Zwi-Dantsis L, Mohamed S, Massaro G, Moeendarbary E. Adeno-Associated Virus Vectors: Principles, Practices, and Prospects in Gene Therapy. *Viruses* 2025;**17**:239. Available at: https://pmc.ncbi.nlm.nih.gov/articles/PMC11861813/. Accessed July 10, 2025.

8. APPENDIX

8.1 Appendix I: Publications and awards

8.1.1 Publications

Harrison AS,* Bjarkadottir BD,* Kuscu N, Davies J, Lane S, Williams SA. Three-dimensional visualisation of human ovarian follicles using a whole-mount immunolabelling and optical tissue clearing method. *Reproduction and Fertility*. 2025;6. DOI: 10.1530/RAF-25-0096

*Equal contribution to work

Kuscu N, Abdul Kader S, Stephens ER, Adeniran BV, Ammar OF, Harrison AS, Lo BK, Williams SA. Ovarian culture with mouse serum improves follicle development compared with fetal bovine serum, showing the importance of as yet unidentified factors in follicle growth. *Reprod Fertil Dev.* 2025;37. DOI: 10.1071/RD24178

8.1.2 Conference abstracts

Harrison AS, Ammar OF, Williams SA. *Assessing the impact of human serum on adherence of frozen pre-pubertal human ovarian cortical tissue in culture*. Fertility Conference 2024. Edinburgh, Scotland, UK.

Harrison AS, Elorbany S, Berlato C, Gopinathan G, Balkwill F, Williams SA. *Application of a mouse model to investigate the effect of high-grade serous ovarian cancer on the ovaries*. Fertility Conference 2023. Belfast, Northern Ireland, UK.

Reproduction & Fertility

Reproduction & Fertility (2025) **6** e250096
https://doi.org/10.1530/RAF-25-0096

Received 16 July 2025
Accepted 23 September 2025
Available online 24 September 2025
Version of Record published 31 October 2025

RESEARCH

Three-dimensional visualisation of human ovarian follicles using a whole-mount immunolabelling and optical tissue clearing method

A S Harrison[1,*], B D Bjarkadottir[1,*], N Kuscu[1], J Davies[2], S Lane[1] and S A Williams[1]

[1]Nuffield Department of Women's & Reproductive Health, University of Oxford, Women's Centre, John Radcliffe Hospital, Oxford, United Kingdom
[2]Oxford Cell & Tissue Biobank, Oxford University Hospitals NHS Foundation Trust, Oxford, United Kingdom

Correspondence should be addressed to S A Williams: suzannah.williams@wrh.ox.ac.uk

*(A S Harrison and B D Bjarkadottir contributed equally to this work)

Abstract

To more accurately classify human ovarian follicles by developing a novel methodology with three-dimensional visualisation using whole-mount immunolabelling and optical tissue clearing techniques. A whole-mount immunolabelling protocol combined with optical tissue clearing was applied to human ovarian tissue for three-dimensional follicle analysis. Key markers, including DAPI for nuclear staining, DDX4 for oocyte-specific labelling, and LAMININ for basal membranes, were used to visualise follicular structures. The tissues underwent a clearing process to enable confocal z-stack imaging to obtain detailed three-dimensional data. Ovarian cortical tissue from three paediatric patients (aged 9–12 years) who had not undergone chemotherapy treatment was collected. The tissue was dissected into small fragments and stained to identify viable follicles. Follicle and oocyte size, as well as granulosa cell size and type, were assessed across multiple dimensions (XY, XZ, YZ planes). Follicles were classified as primordial or transitional based on granulosa cell characteristics. Three-dimensional analysis across XY, XZ, and YZ planes revealed that 58% of follicles, initially classified as primordial using conventional two-dimensional methods, were misidentified as transitional due to the presence of cuboidal granulosa cells that were only detectable in multi-plane analysis. Moreover, three-dimensional analyses revealed significant differences in the number and size of cuboidal granulosa cells detected on transitional follicles. This study presents a novel whole-mount immunolabelling and optical tissue clearing methodology for accurate three-dimensional visualisation and classification of human ovarian follicles. This technique improves the accuracy of follicle staging and provides a valuable tool for future research into ovarian function, reproductive health, and conditions impacting follicle development.

Lay Summary

In this study, we explored a new method for examining ovarian follicles – structures that contain the immature eggs – within human ovarian tissue. Traditional methods, which rely on two-dimensional imaging, can lead to mistakes in classifying the development of these follicles due to their spherical shape. To address this, we developed techniques to visualise the ovarian tissue in three dimensions. Using ovarian tissue from three patients, the tissue was processed using techniques called whole-mount immunolabelling (to detect structures) followed by optical clearing (to visualise the structures) and then analysed using microscopy. This enabled us to create detailed 3D images that showed the structures of the immature eggs and follicles across different planes of view. We discovered that conventional 2D

Published by Bioscientifica Ltd.
https://raf.bioscientifica.com
© 2025 the author(s)

This work is licensed under a Creative Commons Attribution 4.0 International License.

Downloaded from Bioscientifica.com at 12/29/2025 11:13:03PM
via Open Access. This work is licensed under a Creative Commons Attribution 4.0 International License.
https://creativecommons.org/licenses/by/4.0/

Reproduction & Fertility (2025) **6** e250096
https://doi.org/10.1530/RAF-25-0096

assessments misclassified nearly 60% of the follicles, as certain developmental characteristics were only visible in the 3D images. This innovative approach marks the first time such detailed 3D imaging has been applied to human ovarian follicles. It not only enhances the accuracy of classifying follicle stages but also holds potential for improving fertility preservation techniques in the future. Overall, the study highlights the benefits of using modern imaging methods to gain better insights into ovarian health and development.

Keywords: human; ovary; follicle; optical tissue clearing; three-dimensional imaging; immunolabelling

Introduction

The ovary is a heterogeneous organ, consisting of an outer cortex and an inner medulla, with follicles, blood vessels, and stroma. Ovarian follicles are the reproductive unit of the ovary, containing a single egg, herein referred to as the oocyte, surrounded by specialised somatic cells, including theca and granulosa cells (GCs) (Fig. 1A). Bidirectional communication between the oocyte and its neighbouring cells is vital for follicle development. Analysis of follicle development is reliant upon the intact morphology, location, and quantity of GCs surrounding the oocyte. Classification is important for understanding the stages of follicle maturation, which is crucial for reproductive health, managing fertility treatments, and conducting studies on ovarian function.

Histology and immunohistochemistry (IHC) are considered gold-standard methods to analyse early follicle development because they support the visualisation of structures within tissue. Methods that require cell digests or tissue lysates, such as Western blotting, can destroy cellular structures, preventing ovarian follicle visualisation. IHC enables the specific identification and localisation of proteins, providing valuable insights into the distribution and expression patterns of target molecules. Histology and IHC routinely involve the preparation of thin sections of tissue (typically 5 μm thick), which are then stained or immunolabelled and visualised under a brightfield microscope. A significant limitation is that a 5 μm section cannot encapsulate the three-dimensional follicle structure, which can range in size from ~40 μm for primordial follicles to over 18 mm for a pre-ovulatory follicle in humans (Griffin *et al.* 2006).

Rigorous distinction between follicles is important for accurate analysis. In standard practice, the largest cross-section of each follicle, identified by the presence of the oocyte nucleus, is used for assessment. Although time-efficient, the approach of assessing one section per follicle can lead to errors. First, only follicular cells within the chosen section are included for follicle analysis, while cells in neighbouring sections of the same follicle are excluded (Fig. 1B). Therefore, follicles could only be assessed as 'atretic' or 'growing' based on the presence or absence of pyknotic or mitotic GCs, due to the limited information provided by one section (Uslu *et al.* 2017). Second, follicles are classified into stages for subgroup analysis based on morphological data within the specific cross-section (Fig. 1C). There is no rationale to orient the tissue for optimal cross-section representation because follicles cannot be seen externally within intact tissue during the embedding process. There is potential for variable characteristics to be identified depending on the angle and orientation of the cross-section. Theoretically, a follicle classified as primordial due to the surrounding flattened pre-granulosa cells (fpGCs) in the analysed cross-section may contain concealed cuboidal cells at the opposite poles. Thus, the follicle would be more appropriately staged as transitional.

Accurate classification of early-stage follicles is essential for understanding ovarian reserve regulation. The transitional follicle stage marks the earliest morphological and molecular signs of activation from the dormant primordial stage (Maciel *et al.* 2004, McLaughlin & McIver 2009, Zhang *et al.* 2018, Rooda *et al.* 2024, Kubo *et al.* 2025). Follicular activation is tightly controlled, underpinning both the reproductive lifespan and fertility potential (Yang *et al.* 2020, Telfer & Andersen 2021). Improved methods for classifying early-stage follicles allow for more precise assessment of follicle dynamics, ovarian health, and the impact of clinical interventions such as chemotherapy (Titus *et al.* 2021, Erden & Oktay 2025).

Recent advancements in imaging and microscopy may assist in offering a solution for thorough follicle classification. Confocal microscopy enables high-resolution imaging at different focal planes in the z-plane through 'optical sectioning' without physically slicing the sample (Conchello & Lichtman 2005). Alternative non-invasive methods to visualise human ovarian follicles within tissue pieces include full-field optical coherence tomography (Peters *et al.* 2016) and laser-scanning confocal microscopy with rhodamine 123 staining of active mitochondria in follicles (Soleimani *et al.* 2006).

However, factors such as light scattering limit the imaging of whole tissue samples. Light scattering is characterised by light repeatedly reflecting of cellular structures, creating a milky appearance. This is due to the mismatch in refractive index, a measure describing the speed of light through a material, between the sample and

Downloaded from Bioscientifica.com at 12/29/2025 11:13:03PM
via Open Access. This work is licensed under a Creative Commons Attribution 4.0 International License.
https://creativecommons.org/licenses/by/4.0/

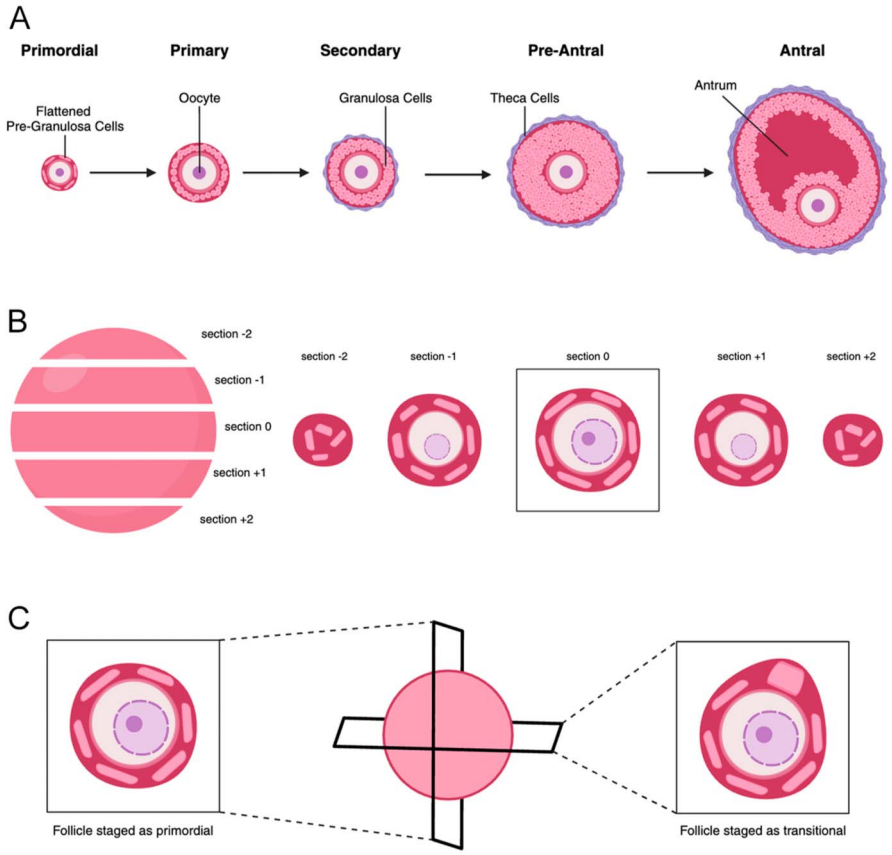

Figure 1

Overview of follicle development and standard histological analysis limitations. (A) The primordial follicle is the earliest stage of development, consisting of a single oocyte surrounded by a single layer of flattened pre-granulosa cells. Following follicle activation, the flattened pre-granulosa cells (fpGCs) begin to divide and become cuboidal granulosa cells (GCs). Once a full single layer of GCs is present, it is then considered a primary follicle. At this stage, the glycoprotein layer, called the zona pellucida, begins to form around the oocyte. A follicle is considered secondary when two full layers of GCs surround the oocyte; the theca cells form a layer around the follicular basal lamina. When three or more full layers of GCs surround the oocyte, the follicle is pre-antral. The antrum, a fluid-filled cavity, is a defining feature of the gonadotropin-dependent antral follicle. The follicle will continue to grow (~20 mm in humans) before ovulation. (B) Diagram of serial histological sections through a primordial follicle, shown as both a three-dimensional sphere and corresponding individual tissue sections. Only the largest follicle cross-section (represented by 'section 0') containing the oocyte nucleus is analysed. The sections before the largest follicle cross-section (represented by 'section −2' and 'section −1') and following the largest follicle cross-section (represented by 'section +1' and 'section +2') are not analysed. Thus, information is lost as the fpGCs contained in the neighbouring sections are disregarded. (C) As follicles cannot be visualised within ovarian tissue, the orientation of the follicle and the angle when sectioning cannot be controlled for. Thus, transitional follicles could be misclassified as primordial. For example, the largest resulting follicle cross-section when cut along the y-axis is staged as primordial (left). The largest cross-section of the same follicle when cut along the x-axis is staged as a transitional follicle due to the presence of a single cuboidal GC (right). Images are not to scale. Created with BioRender.com.

the immersion medium, causing light to bend as it passes through the material (Richardson & Lichtman 2015). For example, the mismatch of refractive index between air (1.00) and water (1.33) can be observed as light is refracted when moving through a glass of water, causing an object, such as a straw, to appear bent.

Optical clearing techniques have been developed to allow imaging of tissue at greater z-depths by mitigating factors such as light scattering (Richardson & Lichtman 2015). Solvent-based tissue clearing involves tissue dehydration to remove water and some lipids, followed by immersion in a clearing agent such as benzyl benzoate, which alters the sample's refractive index to match that of the immersion medium (Richardson & Lichtman 2015). Tissue-clearing methods have been implemented on mammalian reproductive organs (Soygur & Laird 2021, Folts *et al.* 2023), including the placenta (human and non-human primate; Merz *et al.* 2018, Sargent *et al.* 2019) and ovary (mouse; Faire *et al.* 2015, Feng *et al.* 2017, Kagami *et al.* 2018, Rinaldi *et al.* 2018, McKey *et al.* 2020, Tong *et al.* 2020, Boateng *et al.* 2021, Soygur *et al.* 2023) (fish; Lesage *et al.* 2020) (human; Biswas *et al.* 2021, Barbato *et al.* 2023). Tissue clearing has been implemented on developing

Downloaded from Bioscientifica.com at 12/29/2025 11:13:03PM
via Open Access. This work is licensed under a Creative Commons Attribution 4.0 International License.
https://creativecommons.org/licenses/by/4.0/

embryos (human and mouse; Belle *et al.* 2017, Bunce *et al.* 2020), as well as external genitalia (foetal human; Isaacson *et al.* 2020) and uterus (adult mouse and human; Arora *et al.* 2016). At the time of reporting, there have been no reports of optical tissue clearing of human ovarian tissue for classification of follicles.

In this study, we have developed a methodology that enables the three-dimensional visualisation and classification of ovarian follicles in human ovarian tissue for the first time. Follicles, as early as the primordial stage, can now be accurately analysed via the whole-mount immunolabelling and tissue clearing method.

Materials and methods

Ethics

The use of human ovarian tissue was approved by the Health Research Authority South Central – Oxford B Research Ethics Committee under REC licence (REC reference 19/NW/0526). Tissue was collected from the Oxford Cell and Tissue Biobank located at the John Radcliffe Hospital, Oxford, UK. All patients, or their legal guardians, provided informed consent before ovarian tissue collection.

Patient samples

Fresh ovarian cortical tissue was collected from three patients (A, B, and C) who were 9, 11, and 12 years of age at the time of donation, respectively. Patients were chemotherapy-naïve at the time of donation. Patient A received a diagnosis of osteosarcoma, patient B had a diagnosis of sickle cell disease, and patient C had received a diagnosis of localised synovial sarcoma. All three paediatric patients contributed ovarian cortical tissue for method development. Fragments from patient A and patient C were used for the purposes of protocol development and optimisation; follicles analysed and presented here were derived from patient B.

Ovarian tissue dissection

Human ovarian cortical strips were transferred to dissection medium, consisting of Leibovitz's L-15 (L5520, Sigma-Aldrich, UK) medium supplemented with 3 mg/mL human serum albumin (HSA; AI653, Sigma-Aldrich), 100 U/mL penicillin, 100 μg/mL streptomycin (Penicillin-Streptomycin; P0781, Sigma-Aldrich), 2 mM L-glutamine (25030024, Life Technologies, UK), and 2 mM sodium pyruvate (S8636, Sigma-Aldrich). The tissue was kept at 4°C until use (within 1 h) and processed into fragments. Cortical tissue strips in dissection medium were cut using scalpel blades (No. 15, 233-5366, and No. 24, 233-5529, VWR International, UK) into fragments ~0.25 mm thick (approximately 0.5 × 0.5 × 0.25 mm) under a stereomicroscope (M125, Leica Microsystems, UK).

Processed fragments were stained with 50 μg/mL neutral red (NR; N2889, Sigma-Aldrich) in minimal essential medium alpha (αMEM; 22561021, Thermo Fisher) containing the same supplements as the dissection medium to identify pieces containing viable follicles, as previously described (Walker *et al.* 2021). Stained fragments were incubated in a humidified incubator (5% CO_2) for 2 h at 37°C. Following incubation, fragments were visualised under a dissection microscope. Visible, red-stained follicles (NR-positive) were preferentially selected for culture. Tissue pieces were washed briefly in dissection medium before culture.

Ovarian tissue culture

All tissue fragments included in this study were cultured before fixation, clearing, and imaging. Ovarian tissue pieces were cultured individually in Corning Costar 24-well culture plates (3526, Scientific Laboratory Supplies, UK) in 300 μL culture medium, consisting of αMEM supplemented with 1 mg/mL HSA, 100 U/mL penicillin, 100 μg/mL streptomycin, 2 mM L-glutamine, 10 μg/mL insulin, 5.5 μg/mL transferrin, 5 ng/mL selenium (I3145, Sigma-Aldrich), 50 μg/mL ascorbic acid (10012011, Thermo Fisher, UK), and 12.5 IU/L recombinant human follicle-stimulating hormone (Gonal-f; Z1540, Merck Serono, UK). Sterile water supplemented with 100 U/mL penicillin and 100 μg/mL streptomycin was added to the inter-well space to prevent medium evaporation. All culture medium was equilibrated for at least 1 h in an incubator before use. Ovarian tissue was cultured for up to 48 h; culture was carried out before analysis to ensure that our method was compatible with cultured tissues.

Following culture, samples were fixed in 1% form-acetic, a fixative consisting of 10% neutral buffered formalin with 1% acetic acid, which reduces the formation of fixation-induced artefacts; form-acetic has been previously described (Adeniran *et al.* 2021). Tissue was fixed at room temperature (RT) on a rocker for 24 h, after which tissue was transferred to 70% ethanol and stored at 4°C until processing.

Whole-mount immunolabelling protocol

The protocol was developed to allow visualisation of human ovarian tissue fragments using a commercially available Tissue Clearing Kit (ab243298, Abcam, UK).

Washing and permeabilisation

Fixed tissue pieces were washed twice in phosphate-buffered saline (PBS; 20 mM phosphate, 150 mM NaCl, pH 7.4) and incubated for 15 min each. All incubations were completed at 4°C with gentle agitation unless

Downloaded from Bioscientifica.com at 12/29/2025 11:13:03PM
via Open Access. This work is licensed under a Creative Commons Attribution 4.0 International License.
https://creativecommons.org/licenses/by/4.0/

otherwise indicated. The tissue was dehydrated and incubated in an increasing series of methanol solutions: 50% methanol/PBS, 80% methanol, and 100% methanol. Tissue was permeabilised and incubated in 20% dimethyl sulfoxide (DMSO; D8418, Sigma) solution with methanol. Following permeabilisation, samples were rehydrated and incubated in 80% methanol, 50% methanol/PBS, then 100% PBS solution. Finally, samples were then incubated in a penetration buffer (PBS with 0.2% Triton X-100, 0.3 M glycine, and 20% DMSO) overnight at RT with gentle agitation.

Whole-mount immunolabelling

The next day, tissues were transferred to a 400 μL blocking solution (PBS with 0.2% Triton X-100, 6% donkey serum, and 10% DMSO) and incubated for 24 h. Tissues were labelled with rabbit anti-LAMININ polyclonal antibody (1.75 μg/mL, ab11575, Abcam) as a marker for the basal lamina and rabbit anti-DEAD-Box Helicase 4 (DDX4) polyclonal antibody (10 μg/mL, ab13840, Abcam) as an oocyte-specific marker. Both were diluted in antibody buffer (PBS with 0.2% Tween, heparin, 3% donkey serum, and 5% DMSO; total volume 400 μL) for 7 days at 4°C (the incubation time required was determined experimentally; data not shown). Following primary antibody incubation, tissues were washed five times for 20 min in washing buffer (PBS with 0.2% Tween and heparin), after which they were transferred to 400 μL of secondary antibody solution (Alexa Fluor 488 donkey anti-rabbit IgG; 1:100, 20 μg/mL, A21205, Thermo Fisher Scientific) to detect LAMININ and DDX4. A negative control was prepared using rabbit IgG (10 μg/mL, 3900S, Cell Signaling Technology, USA) and mouse IgG1 (14.2 μg/mL, 401401, BioLegend, USA). Nuclei were counterstained using 5 μg/mL 4′,6-diamidino-2-phenylindole (DAPI; D9542, Sigma-Aldrich) in antibody buffer. Tissues were incubated for 7 days at 4°C and protected from light.

Tissue clearing

All following steps were performed while protecting samples from light. Tissues were washed ten times in washing buffer for 10 min at RT with gentle agitation. Tissues were then dehydrated by washing in 50% methanol/PBS, 80% methanol, and three washes of 100% methanol for 15 min each at RT with gentle agitation. Tissues were removed from methanol and carefully dried (using lens paper and allowing the methanol to evaporate).

After dehydration in methanol, tissues were transferred to a glass embryo dish containing 1 mL Tissue Clearing Reagent 1 (refractive index of 1.50; mixture of benzyl alcohol and 2,2,2-trichloroethanol) and incubated for 1 h at RT with gentle agitation (Fig. 2A). Tissues were mounted in a prepared silicone isolator (approximately 13 mm diameter and 0.25 mm deep) on a glass coverslip (22 × 50 mm, #1.5) filled with Tissue Clearing Reagent 2 (refractive index 1.50; mixture of diphenyl ether, 2,2,2-trichloroethanol, and benzyl alcohol). Tissues were placed in the centre of the well and sealed with a square coverslip (22 × 22 mm, #1.5). Tissues were stored at 4°C away from light until imaged. Tissue clearing could be reversed by incubating cleared samples in 100% ethanol at RT until sample opacity was restored.

Imaging

Images were collected using a Zeiss 780 upright confocal microscope. Images of whole tissue fragments were obtained with a ×10/0.45 numerical aperture objective (working distance 2 mm) or ×25/0.8 numerical aperture oil immersion objective (working distance 570 μm). DAPI was excited using a 405 nm laser and detected at 380–480 nm. Alexa Fluor 488 was excited using a 488 nm laser and detected at 490–555 nm emission. Optimal pinhole size was determined for each channel and kept consistent for all samples. Gain settings for DAPI and Alexa Fluor 488 were adjusted individually for each sample to allow clear visualisation of cell nuclei (DAPI) and LAMININ and oocytes (Alexa Fluor 488), as these markers would not be quantified. Z-compensation with extrapolation was used to adjust for decreasing signal brightness at greater z-depths. Z-stacks were obtained by identifying the top and bottom of the sample. Samples were first imaged from one side and then flipped over and imaged again.

Image analysis

Follicles were enumerated across cleared fragments meeting inclusion criteria; per-fragment counts were not prospectively recorded for the final analysis set, and results are therefore reported at patient level. Images of cleared tissue samples were analysed using ImageJ Fiji and Imaris (version 9.7.0) of patient B. Measurements across the XY, XZ, or YZ planes were performed in ImageJ Fiji using orthogonal views and the measurement tools to measure the size of follicles, oocytes, and GCs (Fig. 2B, C, D). GCs and fpGCs, with nuclear counterstaining, were visualised as the space between the LAMININ and DDX4 signal to account for variability in cellular expression across different follicular stages. Follicle health and incidence of atresia were not systematically assessed in this study. Oocyte and follicle volume (V) was calculated based on the oocyte or follicle radius (r) at the x, y, and z planes using the following formula for the volume of an ellipsoid:

$$V = \frac{4}{3}\pi r_x r_y r_z.$$

Statistical analysis

Data were analysed using GraphPad Prism (version 9.1). Data were tested for normality using the Shapiro–Wilk test. One-way ANOVA with Tukey's post-hoc testing was used to compare GC, oocyte, and follicle size measurements of

Downloaded from Bioscientifica.com at 12/29/2025 11:13:03PM
via Open Access. This work is licensed under a Creative Commons Attribution 4.0 International License.
https://creativecommons.org/licenses/by/4.0/

Reproduction & Fertility (2025) **6** e250096
https://doi.org/10.1530/RAF-25-0096

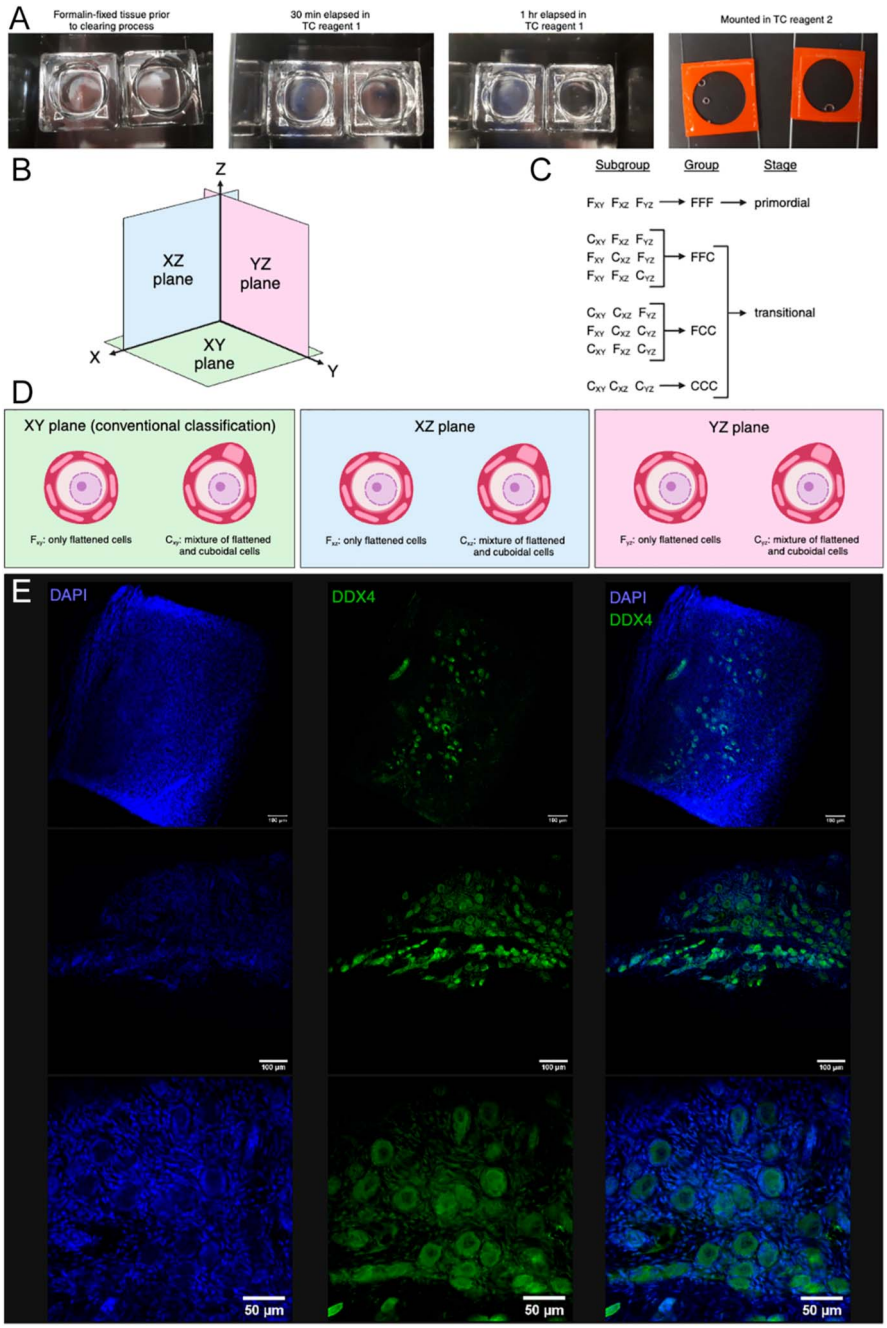

Figure 2

Establishment of a novel method to optically clear, whole-mount immunolabel, and three-dimensionally classify ovarian follicles in human tissue. (A) A fragment of human ovarian tissue stained with 5 µg/mL DAPI nuclear counterstain (L-R) in an embryo dish before optical clearing using Visikol® HISTO™ technology, after 30 min in tissue clearing (TC) reagent 1, after 1 h in TC reagent 1, and the tissue near-invisible after mounting on glass coverslips in TC reagent 2. Arrowheads denote the fragment. (B) Diagram of the three coordinate planes: XY (green), YZ (pink), and XZ (blue). (C) Each follicle could be classified into one of eight subgroups (left column) based on morphological classification across each of the three planes. Follicles were grouped based on having flattened pre-granulosa cells across all three planes (FFF), or as having cuboidal granulosa cells at one (FFC), two (FCC), or all three planes (CCC). Follicles in the FFF group were classified as primordial, while follicles in the FFC, FCC, or CCC groups were considered transitional stage. (D) Each follicle was assessed across three planes and categorised based on morphology as having only flattened pre-granulosa cells (F) or a mixture of flattened pre-granulosa cells and cuboidal granulosa cells (C). Subscript indicates the relevant plane. Histological analysis, conventional classification, is completed on the XY plane. (E) Whole-mount immunolabelling of DEAD-Box Helicase 4 (DDX4) (1:100) antibody as a follicular marker (oocyte) in optically cleared human ovarian tissue (<250 µm thickness), as seen in green. Samples were counterstained with DAPI (blue). A single human ovarian tissue sample is shown with DAPI, DDX4, and merged at three distances. Optical sectioning (10 µm intervals) imaged with a 10× objective. Created with BioRender.com.

primordial and transitional follicles. Statistical significance was defined as $P < 0.05$. Descriptive statistics are presented as counts and percentages.

Results

Visualisation of follicles using tissue clearing method

By implementing the whole-mount immunolabelling and tissue clearing technique with DAPI and DDX4, follicles were successfully visualised in ovarian tissues (Fig. 2E). The resulting optical sectioning in z-stacks allows for the visualisation of follicles throughout the ovarian tissue (Supplementary Video 1 (see section on Supplementary materials given at the end of the article)). Follicular structures, including the oocyte and GCs, can be observed via magnification of z-stack images. The most optimal results for follicle assessment were achieved when utilising a combination of DAPI, DDX4, and LAMININ (a marker for the follicle basal membrane) (Fig. 3A; Supplementary Video 2).

Downloaded from Bioscientifica.com at 12/29/2025 11:13:03PM
via Open Access. This work is licensed under a Creative Commons Attribution 4.0 International License.
https://creativecommons.org/licenses/by/4.0/

Reproduction & Fertility (2025) **6** e250096
https://doi.org/10.1530/RAF-25-0096

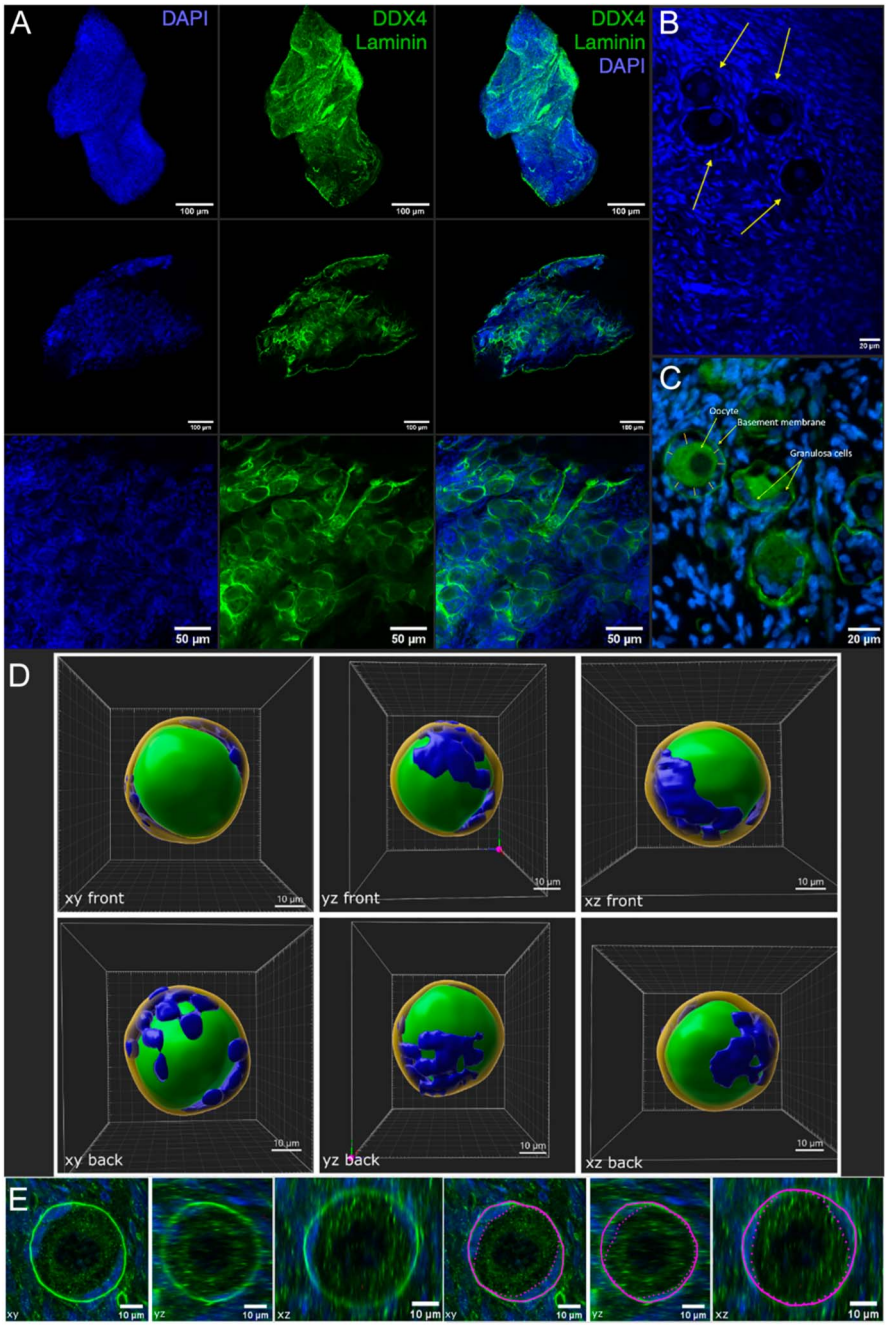

Figure 3

Visualisation and three-dimensional rendering of ovarian follicular structures in optically cleared human tissue. (A, C, E) Human ovarian tissue was labelled with LAMININ and DEAD-Box Helicase 4 (DDX4) to detect the follicle basement membrane and oocyte, respectively, in green. Samples were counterstained with DAPI (blue) and optically cleared. (A) Representative tissue following whole-mount immunolabelling and tissue clearing of a single human ovarian tissue sample labelled with DAPI, DDX4, and merged at three distances. (B) Identification of primordial and transitional follicles (yellow arrows) in a single slice through the centre of the tissue fragment counterstained with DAPI (blue) as a nuclear marker. Oocytes can be seen as black circles with the oocyte nucleus as the dimmer blue circle inside. (C) Follicles, labelled with DDX4 and LAMININ (green) with DAPI counterstain (blue), with structures identified (oocyte, basement membrane, granulosa cells) with yellow arrows. Orange lines represent the distance between the oocyte and the basement membrane wherein the (pre-)granulosa cells are present. (D) Three-dimensional reconstruction, using Imaris, of the same follicle as E. The basal lamina (yellow), oocyte (green), and granulosa cell nuclei (blue) were manually selected, allowing three-dimensional reconstruction. The follicle is shown from different angles (e.g. xy front) as indicated on each panel. (E) Representative follicle labelled with LAMININand DDX4 (green) and DAPI (blue) labelling demonstrating a central slice through the XY plane and orthogonal views through the XZ and YZ planes in three serial images. Granulosa cell (GC) visualisation is highlighted as the area between the basement membrane (magenta, unbroken line) and the oocyte (magenta, dotted line) in repeated images. Imaged with a 10× objective at 10 µm intervals (A) or using a 25× oil immersion objective to obtain z-stacks at 1 µm intervals (B, C, E). Created with BioRender.com.

Three-dimensional staging of follicles

A total of 52 follicles were included in the three-dimensional analysis. Follicles were visualised across three orthogonal planes (XY, XZ, and YZ) (Fig. 3B and C). At each plane, follicles were classified as having only fpGCs (F) or a mixture of fpGCs and cuboidal GCs (C). Based on this analysis, follicles were classified as primordial (only fpGCs across all three planes, FFF) or transitional (cuboidal GCs observed in at least one plane). Transitional follicles were further classified as having GCs at one (FFC), two (FCC), or all three planes (CCC). For each follicle and oocyte, the diameter (largest and perpendicular diameter on the XY plane) and depth (diameter across the z-axis) were measured, in addition to fpGC and GC height at each plane.

Presence of cuboidal granulosa cells

When viewed only across the XY plane (as in conventional analysis), 24 follicles were classified as primordial and 28 as transitional (Fig. 4A). However, when viewed across all three planes, only ten follicles were found to be

Downloaded from Bioscientifica.com at 12/29/2025 11:13:03PM
via Open Access. This work is licensed under a Creative Commons Attribution 4.0 International License.
https://creativecommons.org/licenses/by/4.0/

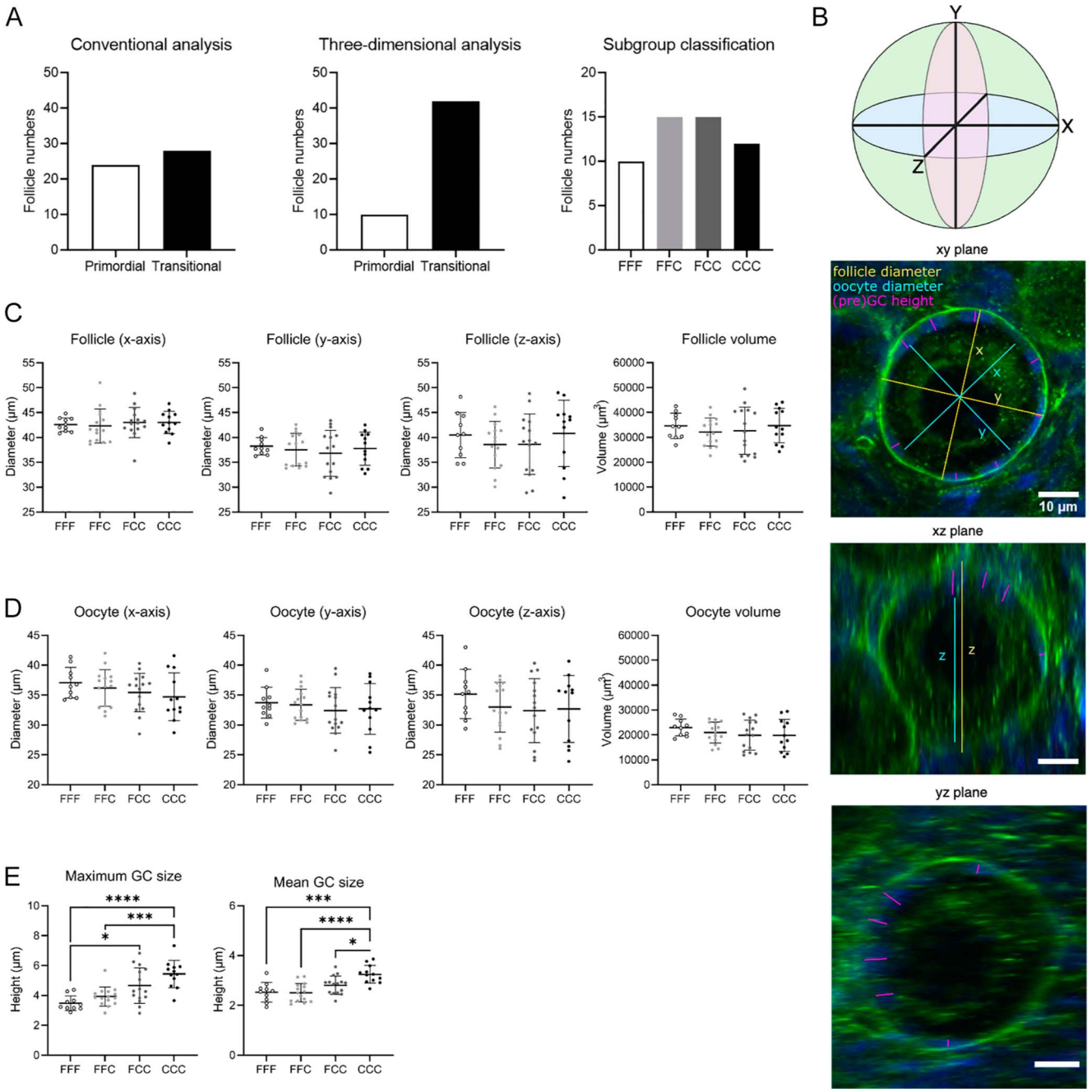

Figure 4

Three-dimensional analysis of primordial and transitional follicles. Fifty-two follicles were classified and analysed across three planes (XY, XZ, YZ). Follicles were further classified into subgroups based on whether only flattened pre-granulosa cells (fpGCs) were observed across all three planes (FFF, primordial) or a mixture of fpGCs and cuboidal granulosa cells (GCs) were observed at one (FFC, transitional), two (FCC, transitional), or all three planes (CCC, transitional), as described in the text. (A) Follicles were analysed and identified as primordial and transitional follicles based on the largest follicle cross-section across the XY plane (conventional analysis) or across three planes (three-dimensional analysis). (B) Diagram of an ellipsoid to represent a three-dimensional view of a follicle across three planes: X, Y, and Z. A representative image of a follicle (classified as FCC) is shown. For each follicle, the maximum follicle (yellow) and oocyte (blue) diameter was measured (defined as the x-axis), along with the corresponding perpendicular diameter (y-axis). The depth of the follicle was also measured across the z-axis. The height of (pre-)granulosa cells was measured (magenta lines) across all three planes (XY, XZ, and YZ). Scale bars represent 10 µm. (C) Follicle diameter (x- and y-axis; µm), follicle depth (z-axis; µm), and follicle volume (µm^3). (D) Oocyte diameter (x- and y-axis; µm), oocyte depth (z-axis; µm), and oocyte volume (µm^3). (E) Maximum and mean (pre-)GC height. *P < 0.05, ***P < 0.001, ****P < 0.0001. Created using BioRender.com.

Downloaded from Bioscientifica.com at 12/29/2025 11:13:03PM
via Open Access. This work is licensed under a Creative Commons Attribution 4.0 International License.
https://creativecommons.org/licenses/by/4.0/

Reproduction & Fertility (2025) **6** e250096
https://doi.org/10.1530/RAF-25-0096

primordial and 42 were transitional; therefore, 14 follicles were misclassified. Using the conventional staging method, 58% (14 of 24) of follicles initially classified as primordial contained cuboidal GCs that could not be observed across the XY plane and were therefore actually transitional follicles. Out of the 42 confirmed transitional follicles identified with our three-dimensional method, only 12 follicles contained one or more cuboidal cells at all three planes.

Follicle and oocyte diameter

Follicle and oocyte diameters were measured across three axes (X, Y, and Z) and volume calculated (Fig. 4B). There was no difference in follicle size (diameter across the X, Y, and Z axes) or volume between the four groups, and no difference in oocyte size or volume (Fig. 4C and D).

Granulosa cell size

There was a significant difference in both mean and maximum fpGC size between the different stages of follicle development (Fig. 4E). The maximum fpGC size was significantly smaller for FFF (primordial) follicles (3.5 ± 0.5 μm) compared to transitional follicles (FCC and CCC, 4.6 ± 1.2 μm with $P < 0.05$ and 5.4 ± 0.9 μm with $P < 0.0001$, respectively). Within transitional follicles, there was also a difference in maximum fpGC cell height between FFC and CCC follicles (3.9 ± 0.6 μm vs 5.4 ± 0.9 μm with $P < 0.001$). Furthermore, there was a significant difference in mean fpGC size between the groups. The mean fpGC size of FFF follicles was significantly smaller than transitional follicles (CCC group, 2.5 ± 0.4 μm compared to 3.2 ± 0.4 μm with $P < 0.001$). Within transitional follicles, there was a significant difference in mean fpGC size between FFC and CCC ($P < 0.0001$) and FCC and CCC ($P < 0.05$) follicles (FFC: 2.5 ± 0.4 μm, FCC: 2.8 ± 0.4 μm, and CCC: 3.2 ± 0.4 μm).

Discussion

The primary aim of this novel study was to develop a three-dimensional whole-mount immunolabelling and optical tissue clearing technique to comprehensively visualise human ovarian follicles for the purpose of improved classification at the primordial and transitional stages.

According to the results, our method enabled more accurate follicle classification, revealing that 58% of follicles initially classified as primordial using conventional two-dimensional (XY plane) analysis were reclassified as transitional when assessed with our three-dimensional (XY, XZ, and YZ planes) approach. This staggering discrepancy underscores the limitations of two-dimensional histology, which captures follicular features in a single plane and may miss key morphological features, such as the presence of cuboidal granulosa cells that define transitional follicles. GC size was determined by diameter measurement as opposed to volume to differentiate between fpGCs and cuboidal GCs. This measurement was selected as it applies in both conventional analysis and the three-dimensional technique provided here. In this study, primordial and transitional follicles did not differ in follicle nor oocyte diameter, yet there was a difference in fpGC and GC size. Thus, a comprehensive view of all follicular GCs across all three planes is required for accurate follicle classification and subgroup analysis.

This is the first study to describe three-dimensional analysis of human primordial and transitional follicles with optical tissue clearing. Previously, three-dimensional analysis of mouse and bovine follicle size has been reported using either serial histological sections (Van Wezel & Rodgers 1996) or tissue clearing (Feng *et al.* 2017), without measurements or detailed assessment of fpGCs. Methods to optically clear human ovarian tissue have been reported to identify follicle viability (Barbato *et al.* 2023) and assess protein expression (Biswas *et al.* 2021); however, follicle classification was not assessed. Previously described spatial analysis of growing human ovarian follicles was limited to the XY plane (Quan *et al.* 2020). The whole-mount immunolabelling and tissue clearing technique used in the present study enables the investigation of spatial effects across three dimensions using a combination of DAPI, DDX4, and laminin. Follicle health and incidence of atresia were not used as endpoints in this study; however, this methodology paves the way for future studies to investigate markers of follicle development.

The ability to distinguish between primordial and transitional follicles has important scientific and clinical implications. Biologically, this transition marks the earliest shift from dormancy (primordial stage) to activation, involving both significant transcriptomic and morphological changes (Maciel *et al.* 2004, McLaughlin & McIver 2009, Zhang *et al.* 2018, Rooda *et al.* 2024, Kubo *et al.* 2025). Follicle activation governs the rate of recruitment and depletion of the ovarian reserve, with accurate staging vital for investigating *in vitro* growth strategies for fertility preservation (Yang *et al.* 2020, Telfer & Andersen 2021). Clinically, assessing ovarian damage from chemotherapy depends on reliable classification of quiescent versus activated follicles, as current hypotheses suggest loss may occur either through premature activation ('burnout') (Erden & Oktay 2025) or direct apoptosis of dormant follicles (Titus *et al.* 2021). By preserving three-dimensional follicular architecture, our approach enables more precise and reproducible analysis of early-stage follicle development.

Human ovarian tissue fragments were successfully rendered transparent, with the tissue visualised up to ~250 μm depth by imaging each sample from both sides. This limitation in z-depth is likely due to the

Downloaded from Bioscientifica.com at 12/29/2025 11:13:03PM
via Open Access. This work is licensed under a Creative Commons Attribution 4.0 International License.
https://creativecommons.org/licenses/by/4.0/

dense nature of the human ovarian cortex (Richardson & Lichtman 2015). The Visikol® HISTO™ technique does not fully remove lipids from the tissue, a potential source of light scattering. Alternative clearing methods could improve this limitation. However, other tissue clearing methods can cause tissue shrinkage or swelling, which may affect follicle morphology (Richardson & Lichtman 2015). Furthermore, mechanical sectioning of paraffin-embedded tissue would no longer be required, mitigating variability of user ability. Data collection could be expedited as tissue sections would not have to be imaged and analysed individually, but in one instance using z-stacks. Visikol® HISTO™ has previously been used to generate three-dimensional renderings of immunolabelled non-human primate and human placental tissue (Merz *et al.* 2018, Sargent *et al.* 2019); other tissue clearing methods have been applied to investigate human ovaries (Biswas *et al.* 2021, Barbato *et al.* 2023). However, there are no reports of this technology being used to classify human ovarian follicles.

In the present study, most follicles analysed in tissue fragments cultured for 2 days were at the transitional stage. This is in line with reports from both our own group (Bjarkadottir *et al.* 2021, Walker *et al.* 2021) and others (Pampanini *et al.* 2019, Lopes *et al.* 2020, De Bruin *et al.* 2002). Follicular analysis was restricted to primordial and transitional follicles, but this method could more accurately classify other follicles, such as those at the primary, secondary, and pre-antral stages. Follicle stage distributions should not be extrapolated to uncultured ('day 0') tissue without direct comparison. Short-term culture (up to 8 days) of human ovarian cortex, and even the act of fragmenting cortical tissue, has been reported to promote activation of dormant primordial follicles, which would result in shifting the distribution between stages (Anderson *et al.* 2018, Kagami *et al.* 2018, McLaughlin *et al.* 2018, Bjarkadottir *et al.* 2021, Walker *et al.* 2021, Barbato *et al.* 2023). Accordingly, the ratio of primordial to transitional follicles observed here in cultured fragments is likely to differ from that of fresh ('day 0') tissue (Anderson *et al.* 2018, Bjarkadottir *et al.* 2021, Walker *et al.* 2021, Barbato *et al.* 2023). We also note that the supporting literature uses conventional histology, which may call into question the true recorded number of follicles at each stage (Bjarkadottir *et al.* 2021, Walker *et al.* 2021, Barbato *et al.* 2023). Further investigation with a larger number of patients analysing cultured and uncultured tissues would be required to confirm follicle proportions.

While we appreciate that histology is considered the gold standard for assessing ovarian follicle development, our study was specifically designed to evaluate the contribution of three-dimensional visualisation using confocal imaging. We did this by comparing two-dimensional and three-dimensional views within the same immunolabelled tissue block, thus preserving tissue architecture and avoiding artefacts introduced by the fixation, embedding, and sectioning processes. Utilising optical sectioning via confocal microscopy enabled a controlled assessment of dimensional influences on follicle classification. It is important to note that a direct comparison with standard histology of the same tissues and finding the same primordial follicles would be impossible; moreover, we do not consider this to be as accurate as comparison using the same method.

Shrinkage of tissue during preparation for analysis is a well-known occurrence. The standard histological workflow of formalin-fixed, paraffin-embedded processing can cause tissue shrinkage of up to 15%, and solvent-based dehydration has also been reported to cause shrinkage (Jali *et al.* 2015, Richardson & Lichtman 2015, Tran *et al.* 2015). Shrinkage due to clearing was not quantified in this study; however, shrinkage would not change the morphology of the primordial and transitional follicles and thus would not change the results of this study.

In this study, we focused on pre-pubertal ovarian cortical tissue due to its high density of early-stage follicles, particularly primordial and transitional stages, which are the primary targets of our classification method (Overland *et al.* 2023). While older tissue is indeed important for studying broader ovarian physiology, early-stage follicles are present across both pre- and post-pubertal tissues (Hansen *et al.* 2011, Overland *et al.* 2023). Paediatric and adolescent cortical tissues represent a growing proportion (approximately 15–40%) of cryopreserved samples, likely due to increased uptake of fertility preservation (Jadoul *et al.* 2017, Poirot *et al.* 2019, Emrich *et al.* 2025). Further studies including larger numbers of tissues and follicles from individuals with different histories and ages are required to validate the robustness of our protocol. For example, it will be important to assess potential age-related differences in tissue characteristics, such as antibody penetration or stromal density, which may affect protocol performance (Amargant *et al.* 2020).

In summary, the focus of this study was to demonstrate the potential of our novel protocol for identifying and quantifying primordial and transitional follicles in whole human tissue. Visualisation of follicular structures across all three dimensions is vital when distinguishing between primordial and transitional follicles. While the size of fpGCs differed between primordial and transitional follicles and within transitional follicle subgroups, there was no difference in follicle or oocyte size or volume. Histological analysis remains fundamental in studying ovarian tissue, yet recent advancements enable three-dimensional visualisation and analysis, offering significant potential for advancing ovarian research.

Supplementary materials

This is linked to the online version of the paper at https://doi.org/10.1530/RAF-25-0096.

Downloaded from Bioscientifica.com at 12/29/2025 11:13:03PM
via Open Access. This work is licensed under a Creative Commons Attribution 4.0 International License.
https://creativecommons.org/licenses/by/4.0/

Declaration of interest

The authors declare that there is no conflict of interest that could be perceived as prejudicing the impartiality of the work reported.

Funding

This project was supported by the Oxford Medical Research Council Doctoral Training Programme (Oxford MRC-DTP) grant (MR/N013468/1) awarded to BDB, and the Iceland Chamber of Commerce to BDB, the Icelandic Cancer Society to SAW and BDB. This project has also been made possible in part by grant number 2021-238038 from the Chan Zuckerberg Initiative DAF, an advised fund of the Silicon Valley Community Foundation.

Author contribution statement

ASH was responsible for writing the original draft, writing review and editing, and data curation. BDB was responsible for writing the original draft, conceptualisation, formal analysis, investigation, methodology, and funding acquisition. NK was responsible for writing review and editing, and writing the original draft. JD and SL helped in sample acquisition. SAW was responsible for resources, supervision, conceptualisation, project administration, and funding acquisition.

Acknowledgements

The authors express their gratitude to the Oxford Cell and Tissue Biobank for their support in acquiring patient samples, and the patients who generously contributed tissue for research purposes. Thanks to Dr Chris Largerholm and Dr Jana Koth at the Wolfson Imaging Facility for technical advice and access to equipment. The authors would also like to thank Kate Fowler, Nicole Moosbrugger, Tiya Ministry, Callum Tromans-Coia, and Virginie Uhlmann for reading and commenting.

References

Adeniran BV, Bjarkadottir BD, Appeltant R, *et al.* 2021 Improved preservation of ovarian tissue morphology that is compatible with antigen detection using a fixative mixture of formalin and acetic acid. *Hum Reprod* **36** 1871–1890. (https://doi.org/10.1093/humrep/deab075)

Amargant F, Manuel SL, Tu Q, *et al.* 2020 Ovarian stiffness increases with age in the mammalian ovary and depends on collagen and hyaluronan matrices. *Aging Cell* **19** e13259. (https://doi.org/10.1111/acel.13259)

Anderson RA, Brewster DH, Wood R, *et al.* 2018 The impact of cancer on subsequent chance of pregnancy: a population-based analysis. *Hum Reprod* **33** 1281–1290. (https://doi.org/10.1093/humrep/dey216)

Arora R, Fries A, Oelerich K, *et al.* 2016 Insights from imaging the implanting embryo and the uterine environment in three dimensions. *Development* **143** 4749–4754. (https://doi.org/10.1242/dev.144386)

Barbato V, Genovese V, De Gregorio V, *et al.* 2023 Dynamic in vitro culture of bovine and human ovarian tissue enhances follicle progression and health. *Sci Rep* **13** 1–15. (https://doi.org/10.1038/s41598-023-37086-0)

Belle M, Godefroy D, Couly G, *et al.* 2017 Tridimensional visualization and analysis of early human development. *Cell* **169** 161–173.e12. (https://doi.org/10.1016/j.cell.2017.03.008)

Biswas L, Chen J, Angelis JD, *et al.* 2021 SUMIC: a simple ultrafast multicolor immunolabelling and clearing approach for whole-organ and large tissue 3D imaging. *bioRxiv* 2021.01.20.427385. (https://doi.org/10.1101/2021.01.20.427385)

Bjarkadottir BD, Walker CA, Fatum M, *et al.* 2021 Analysing culture methods of frozen human ovarian tissue to improve follicle survival. *Reprod Fertil* **2** 59. (https://doi.org/10.1530/raf-20-0058)

Boateng R, Boechat N, Henrich PP, *et al.* 2021 Whole ovary immunofluorescence, clearing, and multiphoton microscopy for quantitative 3D analysis of the developing ovarian reserve in mouse. *J Vis Exp* **175** e62972. (https://doi.org/10.3791/62972)

De Bruin JP, Dorland M, Spek ER, *et al.* 2002 Ultrastructure of the resting ovarian follicle pool in healthy young women. *Biol Reprod* **66** 1151–1160. (https://doi.org/10.1095/biolreprod66.4.1151)

Bunce C, McKey J & Capel B 2020 Concerted morphogenesis of genital ridges and nephric ducts in the mouse captured through whole-embryo imaging. *Development* **148** dev199208. (https://doi.org/10.1242/dev.199208)

Conchello JA & Lichtman JW 2005 Optical sectioning microscopy. *Nat Methods* **2** 920–931. (https://doi.org/10.1038/nmeth815)

Emrich NLA, Einenkel R, Färber CM, *et al.* 2025 Ovarian tissue cryopreservation for fertility preservation: a two-decade single-center experience with 451 children and adolescents. *Reprod Biol Endocrinol* **23** 1–17. (https://doi.org/10.1186/s12958-025-01388-x)

Erden M & Oktay KH 2025 Does gonadotoxic chemotherapy deplete the ovarian reserve through activation of primordial follicles? *Hum Reprod* **40** 571–579. (https://doi.org/10.1093/humrep/deaf024)

Faire M, Skillern A, Arora R, *et al.* 2015 Follicle dynamics and global organization in the intact mouse ovary. *Dev Biol* **403** 69–79. (https://doi.org/10.1016/j.ydbio.2015.04.006)

Feng Y, Cui P, Lu X, *et al.* 2017 CLARITY reveals dynamics of ovarian follicular architecture and vasculature in three-dimensions. *Sci Rep* **7** 1–13. (https://doi.org/10.1038/srep44810)

Folts L, Martinez AS & McKey J 2023 Tissue clearing and imaging approaches for in toto analysis of the reproductive system. *Biol Reprod* **110** 1041–1054. (https://doi.org/10.1093/biolre/ioad182)

Griffin J, Emery BR, Huang I, *et al.* 2006 Comparative analysis of follicle morphology and oocyte diameter in four mammalian species (mouse, hamster, pig, and human). *J Exp Clin Assist Reprod* **3** 1–9. (https://doi.org/10.1186/1743-1050-3-2)

Hansen KR, Hodnett GM, Knowlton N, *et al.* 2011 Correlation of ovarian reserve tests with histologically determined primordial follicle number. *Fertil Steril* **95** 170–175. (https://doi.org/10.1016/j.fertnstert.2010.04.006)

Isaacson D, McCreedy D, Calvert M, *et al.* 2020 Imaging the developing human external and internal urogenital organs with light sheet fluorescence microscopy. *Differentiation* **111** 12–21. (https://doi.org/10.1016/j.diff.2019.09.006)

Jadoul P, Guilmain A, Squifflet J, *et al.* 2017 Efficacy of ovarian tissue cryopreservation for fertility preservation: lessons learned from 545 cases. *Hum Reprod* **32** 1046–1054. (https://doi.org/10.1093/humrep/dex040)

Jali P, Donoghue M & Gadiwan M 2015 A rapid manual processing technique for resource-limited small laboratories. *J Oral Maxillofac Pathol* **19** 306. (https://doi.org/10.4103/0973-029x.174616)

Kagami K, Shinmyo Y, Ono M, *et al.* 2018 Three-dimensional evaluation of murine ovarian follicles using a modified CUBIC tissue clearing method. *Reprod Biol Endocrinol* **16** 1–7. (https://doi.org/10.1186/s12958-018-0381-7)

Kubo H, McCauley CJ, Zelinski MB, *et al.* 2025 Establishing the baseline: understanding follicle activation morphometrics in multiple mammalian species. *Biol Reprod* **112** 1123–1133. (https://doi.org/10.1093/biolre/ioaf059)

Downloaded from Bioscientifica.com at 12/29/2025 11:13:03PM
via Open Access. This work is licensed under a Creative Commons Attribution 4.0 International License.
https://creativecommons.org/licenses/by/4.0/

Lesage M, Thomas M, Bugeon J, *et al.* 2020 C-ECi: a CUBIC-ECi combined clearing method for three-dimensional follicular content analysis in the fish ovary. *Biol Reprod* **103** 1099–1109. (https://doi.org/10.1093/biolre/ioaa142)

Lopes F, Liu J, Morgan S, *et al.* 2020 Single and combined effects of cisplatin and doxorubicin on the human and mouse ovary in vitro. *Reproduction* **159** 193–204. (https://doi.org/10.1530/rep-19-0279)

Maciel GAR, Baracat EC, Benda JOA, *et al.* 2004 Stockpiling of transitional and classic primary follicles in ovaries of women with polycystic ovary syndrome. *J Clin Endocrinol Metab* **89** 5321–5327. (https://doi.org/10.1210/jc.2004-0643)

McKey J, Cameron LA, Lewis D, *et al*. 2020 Combined iDISCO and CUBIC tissue clearing and lightsheet microscopy for in toto analysis of the adult mouse ovary. *Biol Reprod* **102** 1080. (https://doi.org/10.1093/biolre/ioaa012)

McLaughlin EA & McIver SC 2009 Awakening the oocyte: controlling primordial follicle development. *Reproduction* **137** 1–11. (https://doi.org/10.1530/rep-08-0118)

McLaughlin M, Albertini DF, Wallace WHB, *et al.* 2018 Metaphase II oocytes from human unilaminar follicles grown in a multi-step culture system. *Mol Hum Reprod* **24** 135–142. (https://doi.org/10.1093/molehr/gay002)

Merz G, Schwenk V, Shah R, *et al.* 2018 Three-dimensional rendering and analysis of immunolabeled, clarified human placental villous vascular networks. *J Vis Exp* **133** 57099. (https://doi.org/10.3791/57099)

Overland MR, Li Y, Derpinghaus A, *et al.* 2023 Development of the human ovary: fetal through pubertal ovarian morphology, folliculogenesis and expression of cellular differentiation markers. *Differentiation* **129** 37–59. (https://doi.org/10.1016/j.diff.2022.10.005)

Pampanini V, Wagner M, Asadi-Azarbaijani B, *et al.* 2019 Impact of first-line cancer treatment on the follicle quality in cryopreserved ovarian samples from girls and young women. *Hum Reprod* **34** 1674. (https://doi.org/10.1093/humrep/dez125)

Peters ITA, Stegehuis PL, Peek R, *et al.* 2016 Noninvasive detection of metastases and follicle density in ovarian tissue using full-field optical coherence tomography. *Clin Cancer Res* **22** 5506–5513. (https://doi.org/10.1158/1078-0432.ccr-16-0288)

Poirot C, Brugieres L, Yakouben K, *et al.* 2019 Ovarian tissue cryopreservation for fertility preservation in 418 girls and adolescents up to 15 years of age facing highly gonadotoxic treatment. Twenty years of experience at a single center. *Acta Obstet Gynecol Scand* **98** 630–637. (https://doi.org/10.1111/aogs.13616)

Quan N, Mara JN, Grover AR, *et al.* 2020 Spatial analysis of growing follicles in the human ovary to inform tissue engineering strategies. *Tissue Eng Part A* **26** 733–746. (https://doi.org/10.1089/ten.tea.2020.0051)

Richardson DS & Lichtman JW 2015 Clarifying tissue clearing. *Cell* **162** 246–257. (https://doi.org/10.1016/j.cell.2015.06.067)

Rinaldi VD, Bloom JC & Schimenti JC 2018 Whole mount immunofluorescence and follicle quantification of cultured mouse ovaries. *J Vis Exp* **135** e57593. (https://doi.org/10.3791/57593)

Rooda I, Hassan J, Hao J, *et al.* 2024 In-depth analysis of transcriptomes in ovarian cortical follicles from children and adults reveals interfollicular heterogeneity. *Nat Commun* **15** 1–18. (https://doi.org/10.1038/s41467-024-51185-0)

Sargent JA, Roberts VHJ, Gaffney JE, *et al.* 2019 Clarification and confocal imaging of the nonhuman primate placental micro-anatomy. *Biotechniques* **66** 79–84. (https://doi.org/10.2144/btn-2018-0110)

Soleimani R, De Vos W, Van Oostveldt P, *et al.* 2006 Two novel techniques to detect follicles in human ovarian cortical tissue. *Hum Reprod* **21** 1720–1724. (https://doi.org/10.1093/humrep/del057)

Soygur B & Laird DJ 2021 Ovary development: insights from a three-dimensional imaging revolution. *Front Cell Dev Biol* **9** 698315. (https://doi.org/10.3389/fcell.2021.698315)

Soygur B, Foecke MH, Gaylord EA, *et al.* 2023 A roadmap for three-dimensional analysis of the intact mouse ovary. *Methods Mol Biol* **2677** 203. (https://doi.org/10.1007/978-1-0716-3259-8_12)

Telfer EE & Andersen CY 2021 In vitro growth and maturation of primordial follicles and immature oocytes. *Fertil Steril* **115** 1116–1125. (https://doi.org/10.1016/j.fertnstert.2021.03.004)

Titus S, Szymanska KJ, Musul B, *et al.* 2021 Individual-oocyte transcriptomic analysis shows that genotoxic chemotherapy depletes human primordial follicle reserve in vivo by triggering proapoptotic pathways without growth activation. *Sci Rep* **11** 1–11. (https://doi.org/10.1038/s41598-020-79643-x)

Tong X, Liu Y, Xu X, *et al.* 2020 Ovarian innervation coupling with vascularity: the role of electro-acupuncture in follicular maturation in a rat model of polycystic ovary syndrome. *Front Physiol* **11** 526285. (https://doi.org/10.3389/fphys.2020.00474)

Tran T, Sundaram CP, Bahler CD, *et al.* 2015 Correcting the shrinkage effects of formalin fixation and tissue processing for renal tumors: toward standardization of pathological reporting of tumor size. *J Cancer* **6** 759. (https://doi.org/10.7150/jca.12094)

Uslu B, Dioguardi CC, Haynes M, *et al.* 2017 Quantifying growing versus non-growing ovarian follicles in the mouse. *J Ovarian Res* **10** 3. (https://doi.org/10.1186/s13048-016-0296-x)

Walker CA, Bjarkadottir BD, Fatum M, *et al.* 2021 Variation in follicle health and development in cultured cryopreserved ovarian cortical tissue: a study of ovarian tissue from patients undergoing fertility preservation. *Hum Fertil* **24** 188–198. (https://doi.org/10.1080/14647273.2019.1616118)

Van Wezel IL & Rodgers RJ 1996 Morphological characterization of bovine primordial follicles and their environment in vivo. *Biol Reprod* **55** 1003–1011. (https://doi.org/10.1095/biolreprod55.5.1003)

Yang Q, Zhu L & Jin L 2020 Human follicle in vitro culture including activation, growth, and maturation: a review of research progress. *Front Endocrinol* **11** 548. (https://doi.org/10.3389/fendo.2020.00548)

Zhang Y, Yan Z, Qin Q, *et al.* 2018 Transcriptome landscape of human folliculogenesis reveals oocyte and granulosa cell interactions. *Mol Cell* **72** 1021–1034.e4. (https://doi.org/10.1016/j.molcel.2018.10.029)

Downloaded from Bioscientifica.com at 12/29/2025 11:13:03PM
via Open Access. This work is licensed under a Creative Commons Attribution 4.0 International License.
https://creativecommons.org/licenses/by/4.0/

CSIRO PUBLISHING

COLLECTION | RESEARCH PAPER
https://doi.org/10.1071/RD24178

Reproduction, Fertility and Development

Ovarian culture with mouse serum improves follicle development compared with fetal bovine serum, showing the importance of as yet unidentified factors in follicle growth

Nilay Kuscu[A,#], Sabriya Abdul Kader[A,#], Eleanor R. Stephens[A,#], Babatomisin V. Adeniran[A], Omar F. Ammar[A], Ava S. Harrison[A], Belinda KM Lo[A] and Suzannah A. Williams[A,*]

For full list of author affiliations and declarations see end of paper

***Correspondence to:**
Suzannah A. Williams
Nuffield Department of Women's and Reproductive Health, University of Oxford, Women's Centre, Level 3, John Radcliffe Hospital, Oxford OX3 9DU, UK
Email: suzannah.williams@wrh.ox.ac.uk

[#]These authors contributed equally to this paper

Handling Editor:
Jennifer Juengel

Received: 21 October 2024
Accepted: 22 May 2025
Published: 27 June 2025

Cite this: Kuscu N *et al.* (2025) Ovarian culture with mouse serum improves follicle development compared with fetal bovine serum, showing the importance of as yet unidentified factors in follicle growth. *Reproduction, Fertility and Development* **37**, RD24178. doi:10.1071/RD24178

© 2025 The Author(s) (or their employer(s)). Published by CSIRO Publishing.
This is an open access article distributed under the Creative Commons Attribution 4.0 International License (CC BY).

OPEN ACCESS

ABSTRACT

Context. For survivors of childhood blood cancer, fertility preservation through ovarian tissue cryopreservation (OTC) and reimplantation is not recommended because of the risk of reintroducing malignant cells. Since a robust *in vitro* ovarian tissue culture system does not exist for humans, new approaches are needed. **Aims.** To investigate new approaches to *in vitro* follicle growth, our aim was to determine whether mouse serum (MS) could support follicle development better in mouse ovaries *in vitro* compared to fetal bovine serum (FBS). **Methods.** Neonatal ovaries were cultured for 14 days in either MS or FBS. Follicle development and health were assessed by histological and molecular analyses. Anti-Müllerian hormone (AMH) and laminin were analysed using immunohistochemistry. **Key results.** MS supported the development of primordial follicles to preantral follicles, whereas those in FBS did not develop beyond primary. Ovaries cultured in MS had fewer atretic follicles than those in FBS. There were more AMH-positive follicles in MS-cultured than in FBS-cultured ovaries, more primary follicles that were AMH-positive and, AMH-positive primary follicles contained more AMH-positive granulosa cells than those cultured in FBS. Finally, ovaries cultured in either MS or FBS contained laminin; however, the follicle basal lamina (FBL) in MS ovaries were more defined. **Conclusions.** MS better supported follicle development, health, and function than did BS, indicating that MS contains additional factors important for follicle development in mice. **Implications.** These findings demonstrated that as-yet-unknown factors exist that are important for *in vitro* follicle development, and we need to define them, and explore the role of these molecules in human studies.

Keywords: culture, culture media, culture methodologies, fetal bovine serum, follicle, follicle development, histology, immunohistochemistry, mouse serum, ovarian tissue culture, ovary, serum.

Introduction

Developing methods to generate follicles and eggs *in vitro* is crucial as a method of fertility preservation for survivors of childhood blood cancer. For young patients who need to undertake gonadotoxic treatment regimes, ovarian tissue is cryopreserved to preserve their fertility. However, for patients with blood cancer, this tissue cannot be reimplanted because of the risk of reintroducing cancerous cells (Dolmans *et al.* 2013; Rosendahl *et al.* 2013; Moravek *et al.* 2023). Therefore, *in vitro* follicle culture techniques are being developed to produce mature oocytes from the ovarian cortex of pre-pubertal girls. This technique, although established in mice, has proven much more challenging for human ovarian tissues. At present, only two groups have generated mature human oocytes from primordial follicles in ovarian tissue, but these results have not been replicated (McLaughlin *et al.* 2018; Xu *et al* 2021). The lack of widespread success in follicle development using

Collection: The biology of the ovary – Honouring the contributions of Ken P McNatty and Rex J Scaramuzzi

Downloaded from http://connectsci.au/rd/article-pdf/doi/10.1071/RD24178/1361716/rd24178.pdf by guest on 29 December 2025

human tissues in culture led us to consider what might be missing in culture media because follicle development is fully supported in the human body.

The aim of tissue culture media is to mimic the *in vivo* environment by providing nutrients, growth factors, and hormones to support cell survival, proliferation, and function. The basic composition of culture media for ovarian tissue culture in a variety of species includes a base medium such as alpha minimal essential medium (α-MEM), McCoy bicarbonate, Waymouth's media or Earle's balanced salt solution (EBSS) plus pyruvate (Ghezelayagh *et al.* 2022) and the addition of fetal bovine serum (FBS). However, when developing a clinical treatment for humans, it is not ideal to use FBS and thus serum-free systems have been established by adding insulin–transferrin–selenium (ITS) and human serum albumin (HSA) (Bjarkadottir *et al.* 2021).

Although serum-free cultures are valuable for studying the effects of specific hormones or growth factors on follicle development, they may overlook synergistic interactions or factors that are active at very low concentrations, which remain unexplored or unidentified. Additionally, species-specific differences are often neglected, with FBS being commonly used in cultures without considering its compatibility with human tissues.

In mouse follicle development, follicles in cultured ovaries do not grow as well as those grown *in vivo* (Lo *et al.* 2019). In comparison to the complex array of molecules that follicles are exposed to *in vivo*, *in vitro* culture systems are simplistic and may well lack important molecules required for follicle growth. Therefore, alternatives need to be investigated to improve follicle growth in ovarian tissue culture. MS has previously been used in the culture of isolated mouse follicles and shown to support follicle growth and development, whereas FBS has been observed to inconsistently support follicle development and reduce development to the preovulatory stage (Morgan *et al.* 2015). However, MS has not been added to ovarian tissue culture, and comparisons have not been made with alternatives such as FBS. Therefore, the aim of this study was to investigate the effect of MS and FBS on mouse follicle development, survival, and function, as well as extracellular matrix (ECM) development in an *in vitro* ovarian tissue culture system. By using a Day 3 neonatal mouse model, which contains a high proportion of primordial follicles known to activate readily in culture, we were able to assess the impact of different culture conditions on early follicle development. Anti-Müllerian hormone (AMH), produced by granulosa cells (GCs) of functioning follicles, was detected to visualise GCs, count growing follicles and assess the stage of follicle development. AMH is a glycoprotein produced by GCs of preantral and early antral follicles and serves as a key regulator of follicular recruitment and growth. High AMH concentrations are typically observed in healthy, growing follicles, whereas reduced expression is associated with diminished GC activity, the onset of atresia, or cellular stress (Visser and Themmen 2005; Knight and Glister 2006; Van Houten *et al.* 2010). By assessing AMH expression, we gain critical insight into the functional status of early follicles and the impact of MS treatment on ovarian development.

Materials and methods

Collection of ovaries

Mouse pups were sacrificed by cervical dislocation at postnatal Day 3 (P3) and the ovaries and associated tissues were removed. The ovaries were dissected and isolated in Dulbecco's phosphate-buffered saline (DPBS; Sigma-Aldrich, UK) containing 1 mg/mL bovine serum albumin (BSA; Fisher Scientific, UK), by using a stereomicroscope. Each ovary used in the study was collected from a different mouse.

Ovarian tissue culture

P3 ovary culture was performed as previously described (Lo *et al.* 2019). Briefly, whole ovaries were cultured in 300 μL of media (Waymouth-based culture media (Merck, Germany) supplemented with 1% insulin–transferrin–selenium (ITS-G; Sigma-Aldrich, UK); 100 IU/mL penicillin and 0.1 mg/mL streptomycin (Sigma-Aldrich, UK), 2.5 IU/mL recombinant follicle-stimulating hormone (FSH; Gonal-F; Merck-Serono, Feltham, UK), 10 μg/mL BSA (Factor V heat-shock treated; Fisher Scientific, UK), and 25 μg/mL ascorbic acid (Acros Organics, Belgium) in a 24-well tissue culture treated plate (Corning CoStar, Fisher Scientific, UK) on a polycarbonate Transwell membrane (6.5 mm diameter, 0.4 mm pore size; Corning Incorporated, USA). Media was supplemented with either 5% fetal bovine serum (FBS; Biosera, USA) or 5% mouse serum (MS; Biosera). All cultures used serum from a single manufacturing lot for both FBS and MS to minimise batch-to-batch variability. The culture media were replaced every 2 days during the 14-day culture period. The plates were incubated at 37°C with 5% carbon dioxide and 95% air.

Tissue processing

Fixation

Whole ovaries were fixed in form-acetic (neutral buffered formalin (NBF; VWR International, UK) and 5% acetic acid (Merck, Germany); Adeniran *et al.* 2021) for 24 h, with gentle agitation at room temperature, then stored in 70% ethanol.

Tissue processing, embedding and sectioning

Fixed ovarian tissue samples were dehydrated in increasing concentrations of ethanol solution (70%, 80%, 95% and 3 × 100%) for 15 min each at room temperature, then cleared in three washes of xylene for 20 min each at room temperature. The whole ovary samples were then embedded in paraffin wax (Histoplast; Thermo Scientific). The embedded whole ovaries

Downloaded from http://connectsci.au/rd/article-pdf/doi/10.1071/RD24178/1361716/rd24178.pdf by guest on 29 December 2025

were serially sectioned at 5 μm. Every 20th section was collected and stained with PAS and haematoxylin for histological analysis, and the remaining tissue sections were used for immunohistochemistry.

Histological staining with periodic acid schiff (PAS) and haematoxylin

Every 20th section was stained with periodic acid schiff (PAS) and haematoxylin. Sections were dewaxed in three washes of xylene for 20 min and rehydrated in graded concentrations of ethanol (100% × 2, 90%, 70%, 50%), and then placed in tap water. Sections were then incubated in periodic acid stock (Sigma-Aldrich, UK) for 5 min, rinsed in dH^2O, immersed in Schiff's reagent (Merck, Germany) for 15 min, followed by washing in tap water for 5 mins, and then immersion in haematoxylin (Gills no2 Haematoxylin; Sigma-Aldrich, UK) for 90s. Sections were then dehydrated in 80%, 95% and 100% ethanol, cleared in xylene and then mounted using DPX mounting media (Sigma-Aldrich).

Immunohistochemistry

Immunohistochemistry was performed to detect AMH as a marker of follicular function and laminin to assess extracellular matrix (ECM) integrity as previously described (Adeniran *et al.* 2021). We define functional follicles as those with intact GC layers and detectable AMH, indicative of active growth and developmental potential. In contrast, atretic follicles show disrupted morphology with no detectable AMH. In brief, sections were dewaxed in xylene and rehydrated in graded concentrations of ethanol (100%, 90%, 70%, 50%) then washed in double-distilled water (ddH_2O). Antigen retrieval was performed by placing the slides in a 1:10 dilution of 100 × Vector® antigen unmasking solution (Vector Labs, UK; according to manufacturer's instructions) in dH_2O, and microwaving for 1 min on full power and 9 min at low power. To block endogenous peroxidase activity, sections were treated with 3% hydrogen peroxide (Sigma-Aldrich, 31642) in phosphate-buffered saline (PBS; Sigma-Aldrich) for 5 min, then washed in ddH_20 for 3 min, then PBS with 0.05% Tween 20 (Fisher Scientific, Loughborough, UK) (PBS-T) for 3 min. To prevent non-specific antibody binding, sections were blocked with 5% normal goat serum (NGS; Vector Laboratories, PK-6101) in PBS-T for 1 h at room temperature in a humidifying chamber. To detect AMH, sections were incubated with mouse monoclonal anti-human AMH (5 μg/mL, MCA2246, Bio-Rad UK) in a 1:50 dilution in 5% NGS in PBS-T. For laminin detection, sections were incubated with rabbit anti-laminin (1:30; Sigma-Aldrich UK, 030M4798). Negative control sections were incubated in 5% NGS in PBS-T, with the primary antibody being omitted. For both antibodies, sections were then incubated at 4°C overnight. Sections were then washed in PBS-T and all sections (including negative controls) were incubated with secondary antibodies for 1 h at room temperature: biotinylated goat anti-mouse immunoglobulin G (IgG) (1:100; Vector Laboratories, UK, BA-9200) for AMH and goat anti-rabbit IgG (1:100; Vector Laboratories, BA-1000) for laminin. Sections were washed and incubated in Vectastain Elite ABC kit (Vector Laboratories, PK-6101; according to manufacturer's instructions) in a humidifying chamber at room temperature for 30 min. Sections were then washed in PBS-T followed by exposure to 3,3′-diaminobenzidine (DAB) peroxidase (Vector Laboratories, SK-4100; prepared according to manufacturer's instructions). All slides in each experiment were exposed to DAB for the same amount of time. The sections were then dehydrated in graded concentrations of ethanol (50%, 70%, 90%, 2 × 100%) and cleared in xylene. Slides were mounted using DPX mounting media (Sigma-Aldrich). Slides were examined and imaged using a Leica DM2500 light microscope (Microscope Services Ltd., Woodstock, UK) and MicroPublisher 5.0 RTV camera (Qimaging; Microscope Service Ltd.). Images were captured using the Infinity analyse software (ver. 6.5.5; see https://www.teledynevisionsolutions.com/products/infinity-analyze/?model=infinityanalyze&vertical=tvs-lumenera&segment=tvs; Lumenera Corporation (now part of Teledyne Lumenera), Canada) to obtain pre-counterstained images. Following imaging, the AMH immunohistochemistry slides were counterstained with haematoxylin. First, the slides were transferred to xylene to loosen and remove the coverslips, followed by graded concentrations of ethanol before counterstaining with haematoxylin as described above.

Follicle analysis

Every 20th section stained with PAS and haematoxylin was used for follicle analyses. Images were obtained using a Leica DM2500 light microscope (Microscope Services Ltd., Woodstock, UK), and a MicroPublisher 5.0 RTV camera (Qimaging; Microscope Services Ltd.). Follicles with a visible oocyte were classified as primordial, transitional, primary, secondary, and preantral according to established criteria (Pedersen and Peters 1968; Lo *et al.* 2019; Adeniran *et al.* 2021). Follicles were classed as atretic if they had a pyknotic nucleus, shrunken oocyte or ≥10% pyknotic granulosa cells, or a combination of the above factors (Winship *et al.* 2019; Walker *et al.* 2021). Ovarian follicles as well as their components were analysed, namely, oocyte, nucleus, follicle basal lamina (FBL), granulosa cells (GCs), and theca cells (TCs). All image analysis measurements were performed blind in ImageJ with the FIJI® software (ver. 2.1.0/1.53c; National Institute of Health), with 4.39 pixels/μm as a scale. The total number of ovarian follicles at each follicle stage was calculated using the Abercrombie correction factor (Abercrombie 1946), by using the nuclear diameter (assessed using ImageJ in these ovaries). GC and TC numbers were manually counted; GCs were identified as cuboidal cells found within the FBL, whereas TCs were identified by their squamous appearance and their extension from the outer wall of the FBL to the visibly different stromal

Downloaded from http://connectsci.au/rd/article-pdf/doi/10.1071/RD24178/1361716/rd24178.pdf by guest on 29 December 2025

cells (Chiti *et al.* 2017). Follicle area (μm^2) was determined by measuring the area from the outer edge of the FBL or the outer wall of the TCs by using ImageJ. Oocyte diameter (μm) was determined by averaging two measurements at the widest cross-section of follicles (Griffin *et al.* 2006). To analyse AMH-positive follicles, the counterstained IHC images were analysed in ImageJ to assess the number of primary, secondary and preantral follicles and cells that were AMH-positive (AMH+ve; i.e. stained brown with DAB); all other cells and follicles were considered AMH-negative. The number of AMH+ve follicles is expressed as a percentage of all follicles counted in the section, this is then broken down into follicle stages. To determine the percentage of GCs that were AMH+ve, the non-counterstained IHC images were used.

Statistical analysis

GraphPad Prism (ver. 9.2.0; GraphPad Software Inc., USA) was used for statistical analysis and creating graphs. For all results, a Shapiro–Wilk test and the associated Q–Q plot was used to determine whether data were normally or abnormally distributed. Normally distributed data were compared using two-sample Student's *t*-tests; this was performed for atretic counts and AMH+ve follicle counts. Abnormally distributed data were analysed using the non-parametric Mann–Whitney test; this was performed for total follicle counts, somatic cell counts, and proportions including follicles without a defined FBL and AMH+ve GCs. Linear regressions were also performed and plotted to correlate follicle area and oocyte diameter to GC number. Results are presented as mean ± standard deviation (STDEV), with $P < 0.05$ being considered statistically significant.

Ethical approval

All animal studies and experimental procedures using mice were conducted with approval from the Local Ethical Review Panel at the University of Oxford, in accordance with the UK Animals (Scientific Procedures) Act 1986, under a project licence held by Professor Suzannah Williams (Project Licence number: PP1638762). Male C57BL/6J mice, purchased from the Biomedical Services at the University of Oxford, UK, were mated in-house with female CD-1 mice purchased from Charles River, UK.

Results

Follicle health and development is improved in mouse ovarian tissue cultured in MS versus FBS

Follicles were analysed in PAS and haematoxylin-stained sections (FBS, $n = 3$; MS, $n = 3$). Follicles at different stages of development were found in ovarian tissue cultured in both FBS-supplemented media and MS-supplemented media (Fig. 1*a*); however, there was no difference in the total number of follicles between the two groups (Fig. 1*b*; $P = 0.700$).

To evaluate the development and growth of follicles in FBS- versus MS-supplemented media, the number of follicles at each stage of development was determined. Ovaries cultured with FBS-supplemented media were present only at the early stages of development, with no secondary or preantral follicles present, whereas ovaries cultured with MS-supplemented media contained follicles at all stages of development; primordial to preantral (Fig. 1*c*). Therefore, although there was a clear difference in the more developed follicles, there were no differences in earlier-stage follicles ($P > 0.05$) (Fig. 1*d*). Focusing on later follicle development, all three MS-treated ovaries contained secondary follicles, whereas none of the FBS-treated ovaries contained secondary follicles. Moreover, although preantral follicles were found only in the MS-treated group, these were restricted to one individual.

To compare follicle health of mouse ovaries cultured in FBS- and MS-supplemented media, the number of atretic follicles was determined; follicle atresia was defined as follicles exhibiting a pyknotic nucleus, a notably shrunken oocyte, or ≥10% pyknotic granulosa cells. The proportion of atretic follicles in the MS group was significantly lower than in the FBS group ($P < 0.02$; Fig. 1*e*). However, of the atretic follicles, there was no difference in the number of atretic follicles at each stage of development between the two culture media supplement groups (Fig. 1*f*). Because no secondary or preantral follicles were observed in the FBS group, the percentage of atresia for these stages could not be compared with the MS group.

Analysis of follicular cells and follicle size in mouse ovaries cultured in FBS- versus MS-supplemented culture media

The number of GCs and TCs were determined to assess how MS affected somatic cells (Fig. 2*a*). However, since ovaries cultured in FBS did not contain any secondary (FBS, $n = 0$; MS, $n = 11$) or preantral (FBS, $n = 0$; MS, $n = 5$) follicles, only primary follicles were compared (FBS, $n = 39$; MS, $n = 58$). Despite MS clearly supporting later stages of development evidenced by the presence of secondary and preantral follicles, there was no difference in the number of GCs and TCs in primary follicles, although this is unsurprising because primary follicles are categorised on the basis of the number of GCs (Fig. 2*b*, *c*).

Another parameter measured to compare follicle development between ovaries cultured in FBS and those cultured in MS-supplemented media was the growth rate of follicles and oocytes. As the number of GCs increases, it is expected that the GC area, and thus follicle area, will also increase (Lo *et al.* 2019). Therefore, the rate of area increase per GC can reflect follicle growth rate. To investigate this, follicle area and oocyte diameter were assessed relative to GC

Downloaded from http://connectsci.au/rd/article-pdf/doi/10.1071/RD24178/1361716/rd24178.pdf by guest on 29 December 2025

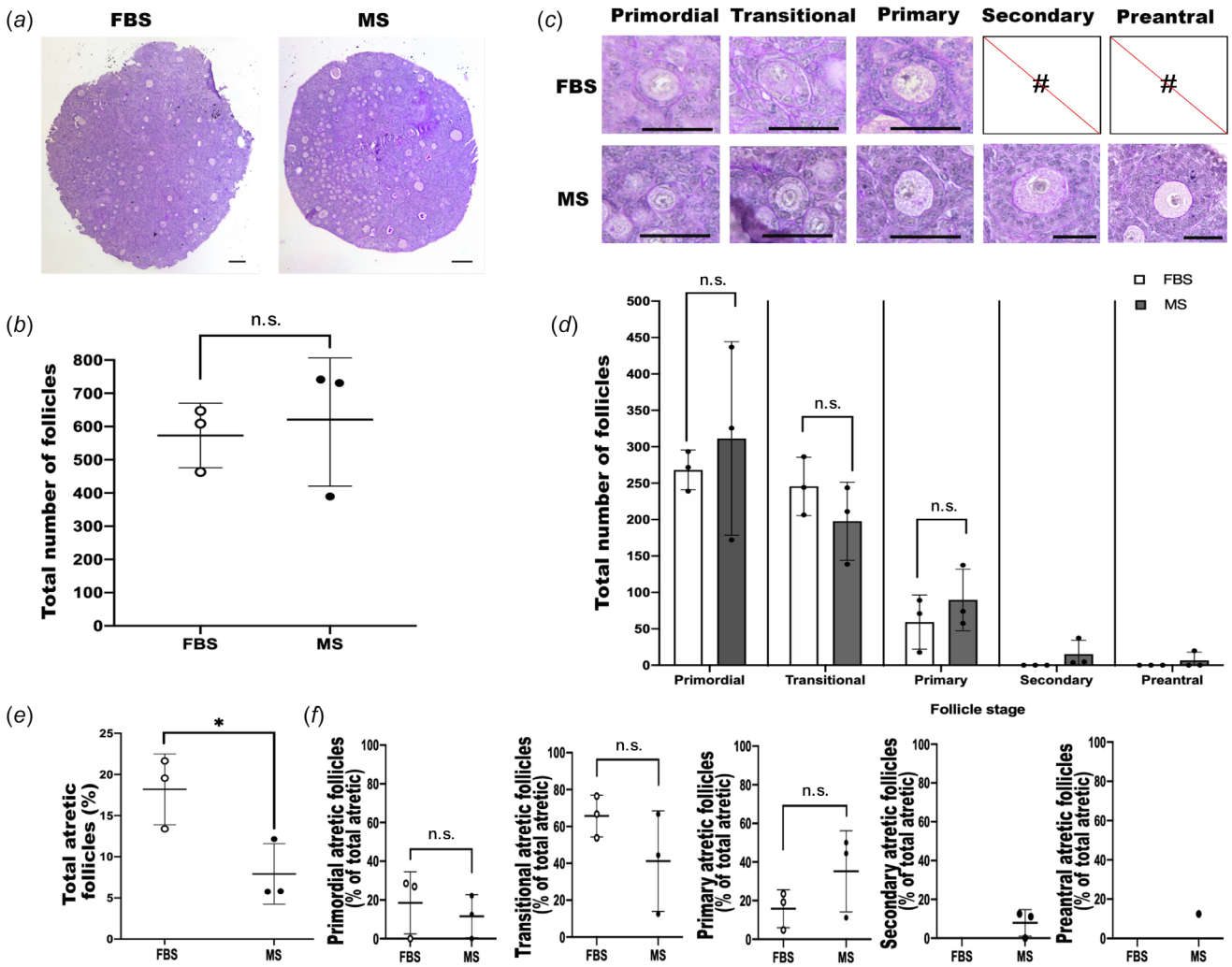

Fig. 1. Analysis of follicle number, follicular somatic cells, and atretic follicles in neonatal mouse ovaries cultured in fetal bovine serum (FBS)- and mouse serum (MS)-supplemented culture media. (*a*) P3 mice ovaries were cultured for 14 days in Waymouth's media supplemented with either FBS ($n = 3$) or MS ($n = 3$), and sections were stained in PAS and haematoxylin. Scale bar = 100 µm. (*b*) The total number of follicles in FBS- and MS-cultured ovaries was not significantly ($P > 0.05$) different; n.s., non-significant. (*c*) Representative images of each follicle type. No secondary or preantral follicles were found in the FBS group. Scale bar = 50 µm. (*d*) The number of follicles at each developmental stage did not differ although secondary and preantral follicles were only in the MS group. (*e*) The proportion of atretic follicles was lower in the MS-supplemented culture group (*$P < 0.05$); however, the stage of follicle development when atresia occurred did not differ (*f*). Data are means ± std.

number for primary follicles in both groups. Primary follicles were chosen because they represent the initial stage of follicle development where a rapid increase in follicle area, GC count, and oocyte size occurs; secondary and preantral follicles were not assessed as none were observed in the FBS group. Linear regression lines were plotted (Fig. 2*d*, *e*) to analyse the relationships between follicle area and GC count, as well as oocyte diameter and GC count in both groups. The linear regressions showed weak but positive correlations between follicle area and GC count, as well as oocyte diameter and GC count (follicle area: MS vs FBS, $r^2 = 0.314$ and $r^2 = 0.185$; Oocyte diameter: MS vs FBS, $r^2 = 0.02$ and $r^2 = 0.135$). No significant difference was found in the slope gradient, and thus growth trajectories, between the MS and FBS groups for either follicle area or oocyte diameter.

Analysis of follicle basal lamina in mouse ovaries cultured in FBS- versus MS-supplemented culture media

During follicle analysis, some follicles were found that lacked a well-defined FBL and thus the stage of development could not be classified according to established follicle classification criteria (Fig. 3*a*). To investigate whether the occurrence of these was improved by the addition of MS, we analysed the proportion of these in the two conditions. Although there was

Downloaded from http://connectsci.au/rd/article-pdf/doi/10.1071/RD24178/1361716/rd24178.pdf by guest on 29 December 2025

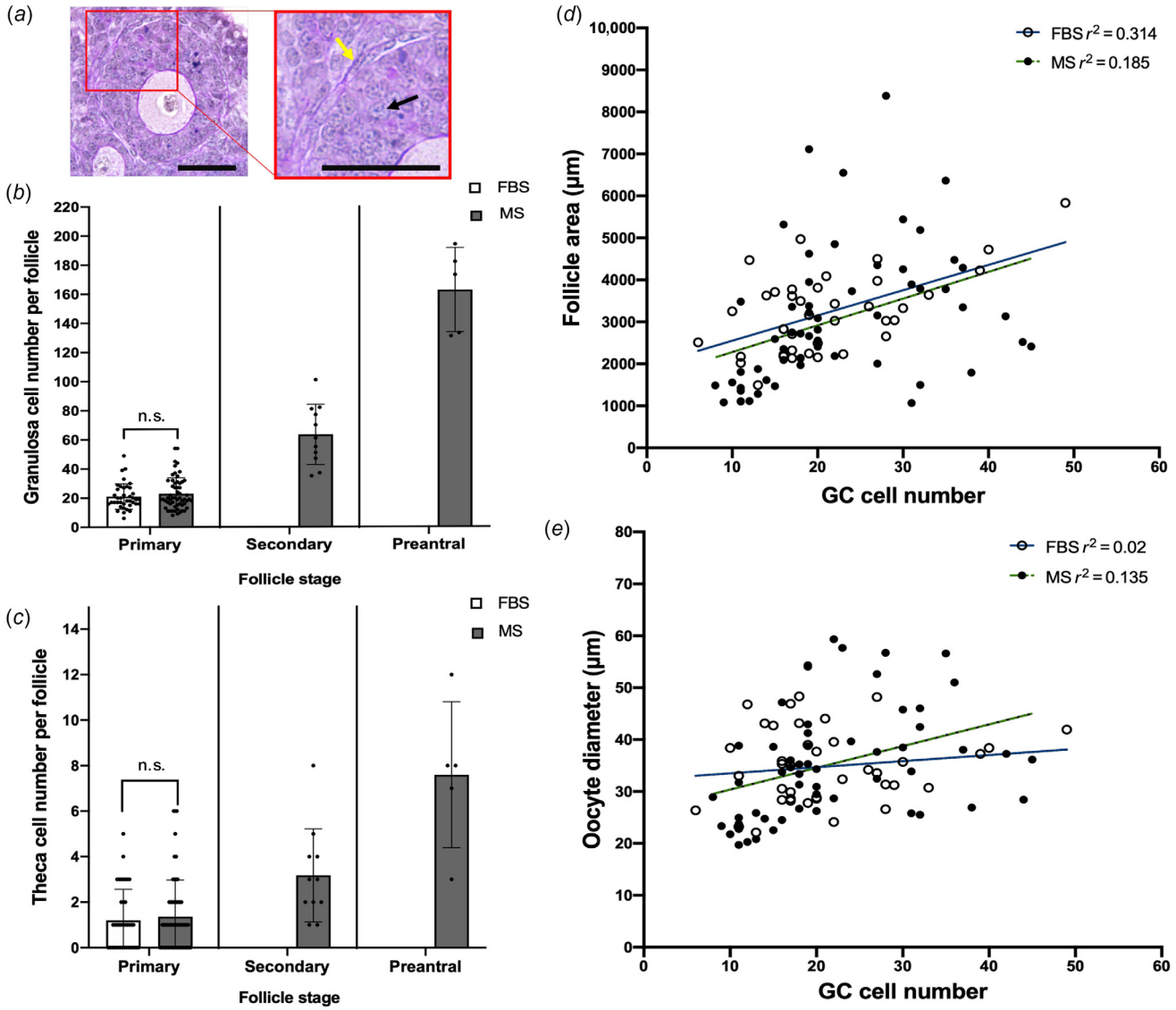

Fig. 2. Evaluation of follicular somatic cells and follicle development in mouse ovaries cultured in FBS- versus MS-supplemented culture media. (*a*) Representative images of the granulosa and theca cells in a late-stage follicle. Sections were stained in PAS and haematoxylin. The black arrow indicates GCs, and the yellow arrow indicates TCs. Scale bar = 50 µm. The number of (*b*) granulosa and (*c*) theca cells around follicles from the primary stage onwards were counted. n.s., non-significant. Primary follicles: FBS, $n = 39$; MS, $n = 58$. Secondary follicles: MS, $n = 11$. Preantral follicles: MS, $n = 5$. Data are means ± std. (*d*) Follicle area and (*e*) oocyte diameter were plotted against GC number for primary follicles and linear regressions were performed: FBS, $n = 39$ follicles, and MS, $n = 58$ follicles. No significant difference was found between the gradient of the slopes for either analysis.

no significant difference in the incidence of follicles with an undefined FBL (FBS vs MS, $P = 0.100$), the mean proportion in MS was half the proportion found in FBS-supplemented media (Fig. 3*b*).

Assessment of follicle function in ovaries cultured in FBS-supplemented media compared with MS-supplemented media

To assess follicle function, we detected AMH by using immunohistochemistry. Ovaries cultured in either FBS or MS both contained follicles that were clearly positive for AMH (AMH+ve; Fig. 4*a*). However, ovaries cultured in media supplemented with MS had more AMH+ve follicles than did those in FBS-supplemented media ($P < 0.05$; Fig. 4*b*). To determine whether this reflected the increased number of later-stage follicles in MS or a difference in AMH at a specific stage of development, the percentage of AMH+ve follicles per stage was analysed (Fig. 4*c*, *d*). Interestingly, the proportion of AMH+ve primary follicles was higher in the MS-supplemented group compared with the FBS-supplemented group ($P < 0.05$). Since no secondary or preantral follicles

Downloaded from http://connectsci.au/rd/article-pdf/doi/10.1071/RD24178/1361716/rd24178.pdf by guest on 29 December 2025

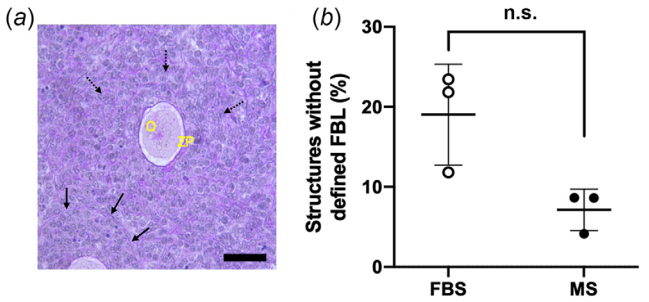

Fig. 3. Analysis of follicle basal lamina in mouse ovaries cultured for 14 days in FBS- and MS-supplemented culture media. (*a*) A representative image of a follicle-like structure with a defined FBL and an indistinguishable FBL; black solid arrows indicate a clear FBL surrounding the follicle, and broken black arrows indicate follicles without a defined FBL. O, oocyte; ZP, zona pellucida. Sections were stained in PAS and haematoxylin. (*b*) The percentage of follicles without a defined FBL ($P = 0.1$). n.s., non-significant. Data are means ± std.

were detected in ovaries cultured with FBS-supplemented media, no comparison could be made at the later stages of development. All GCs within AMH-positive (AMH+ve) follicles were not equally stained (Fig. 4*e*). With the aim of distinguishing between them, the percentage of GCs that were AMH+ve was calculated for each AMH+ve follicle to determine whether ovaries cultured in MS-supplemented media had a higher proportion of AMH+ve GCs than those in FBS-supplemented media (Fig. 4*f*). This analysis showed that a higher percentage of GCs was AMH+ve in the primary follicles of ovaries cultured in MS-supplemented media compared to those in FBS-supplemented media ($P < 0.05$).

ECM evaluation via laminin in MS- and FBS-cultured mouse ovarian tissue

With the aim of identifying the FBL, TCs and exploring the composition of the ECM, laminin was detected in ovarian sections by immunohistochemistry (Fig. 5). In ovarian tissue cultured within both FBS- and MS-supplemented media, the majority of the section was positive for laminin, with the exception of the GCs within follicles. Visible laminin staining suggests the presence of the FBL around follicles in both conditions, appearing more prominent in later-stage follicles that were cultured in MS. Thus, both MS- and FBS-supplemented culture media supported the expression of laminin in ovarian tissue, indicating their potential to maintain essential ECM integrity for follicle development.

Discussion

Optimising the culture of ovarian tissue to develop mature follicles *in vitro* is a crucial technique with significant clinical implications, such as providing new fertility preservation options for prepubertal girls undergoing gonadotoxic therapies and advancing reproductive biology research. Because there is no clinical method to develop mature eggs from primordial follicles by using human ovarian tissue, we hypothesised that by not adding serum from the species in question, crucial components that support follicle development are lacking. Therefore, using a mouse model, we investigated whether mouse serum (MS) improved early *in vitro* follicle development in mouse ovaries compared with the standard fetal bovine serum (FBS). Our study yielded the following key findings: (1) media supplemented with mouse serum resulted in follicles at later stages of development (secondary and preantral) (2) follicles in MS media had better survival and fewer atretic follicles compared to those in FBS; (3) primary follicles developed in MS media contained more AMH-positive GCs, indicating better follicle function than in FBS; and (4) although both MS and FBS media maintained similar laminin staining patterns throughout the ovary, the FBL was also clearly visible around the more developed follicles in MS-cultured ovaries.

Follicle development in cultured ovaries was assessed using histological analysis. Both FBS and MS supported follicle development in neonatal ovaries during the 2-week culture period, as evidenced by the development of growing follicles. However, although the number of primordial, transitional, and primary follicles did not differ in the different culture conditions, FBS-supplemented media failed to support the development of secondary and preantral follicles, because these were observed exclusively in the MS group. The presence of secondary follicles in all three MS-treated ovaries clearly demonstrated consistent enhanced support of follicle development by MS as opposed to FBS, because no secondary follicles were observed in any of the FBS-treated ovaries. However, although preantral follicles were found in the MS-treated group, they were observed in only one ovary. Such variability in follicle development in different individuals could result from a mild difference in ovary age. Although ovaries were all collected on P3, a difference in time of birth (for example, 6 am vs 6 pm Day 0) would mean that some ovaries were from older animals, thus containing slightly more developed follicles (Pedersen 1969; Peters 1969), which could result in the observed variability in follicle development after culture. While the current study has provided preliminary evidence that MS better supports later follicle development, larger studies are needed to fully elucidate the underlying mechanisms and also to determine the broader applicability of these observations.

Follicle health was also improved by the addition of MS compared with FBS, with approximately half the number of atretic follicles in the MS group. Although there is currently no literature specifically investigating the effects of MS-supplemented media on mouse follicle health and comparing it to the commonly used FBS (Eppig and O'Brien 1996), MS obtained from whole mouse blood has been shown to support isolated mouse follicle growth and development (Morgan *et al.* 2015). Even though FBS is standard for various mouse ovarian

Downloaded from http://connectsci.au/rd/article-pdf/doi/10.1071/RD24178/1361716/rd24178.pdf by guest on 29 December 2025

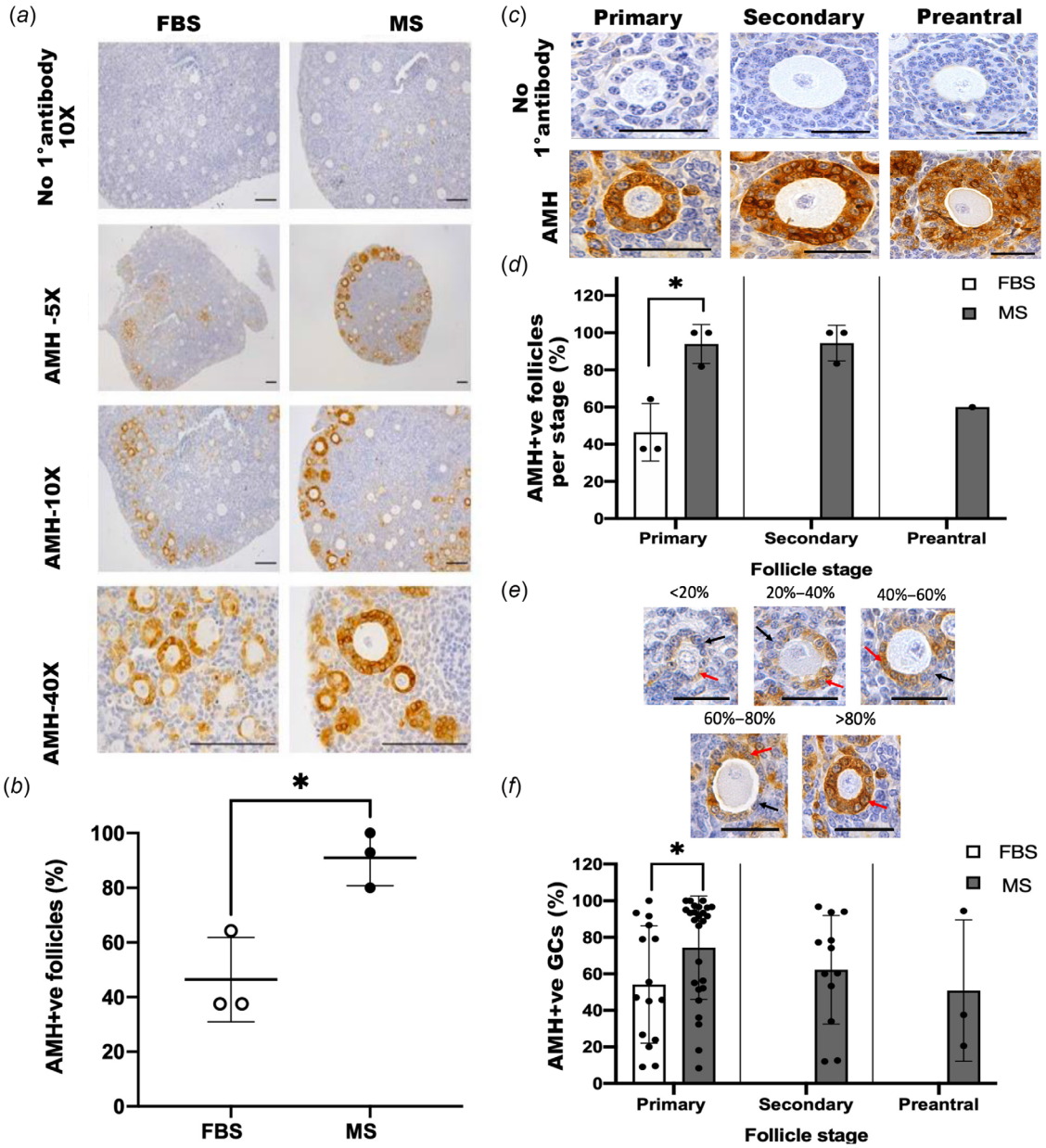

Fig. 4. Analysis of anti-Müllerian hormone in mouse ovaries cultured in fetal bovine serum (FBS)- or mouse serum (MS)-supplemented media for 14 days. (*a*) Representative images of ovarian sections using immunohistochemistry to detect anti-Müllerian hormone (AMH). Images are from the same experiment with the same DAB exposure to allow for direct comparison. Scale bar = 100 μm. (*b*) The percentage of AMH+ve follicles in the MS group was higher than in the FBS group ($P < 0.05$). (*c*) Representative images of AMH+ve primary, secondary and preantral follicles detected using immunohistochemistry with a DAB chromogen. Scale bar = 50 μm. (*d*) The percentage of AMH+ve follicles per stage was analysed and the proportion of primary AMH+ve follicles was higher in the MS group at the primary stage than in the FBS group ($P < 0.05$). There were no secondary and preantral follicles in the FBS group and thus no comparisons could be made. (*e*) Representative sections of AMH+ve follicles with varying proportions of AMH +ve GCs. The red arrows point to an example of AMH+ve GCs, whereas the black arrows point to AMH-negative GCs. Scale bar = 50 μm. (*f*) The percentage of AMH+ve per follicle at each stage of development. (Primary follicles: FBS, $n = 15$; MS, $n = 26$; secondary follicles: FBS, $n = 0$; MS, $n = 12$; preantral follicles: FBS, $n = 0$; MS, $n = 3$). There was a higher proportion of AMH+ve in primary follicles in the MS group than in the FBS group (*$P < 0.05$). There were no secondary and preantral follicles in the FBS group and thus no comparison could be made. Data are means ± std.

Downloaded from http://connectsci.au/rd/article-pdf/doi/10.1071/RD24178/1361716/rd24178.pdf by guest on 29 December 2025

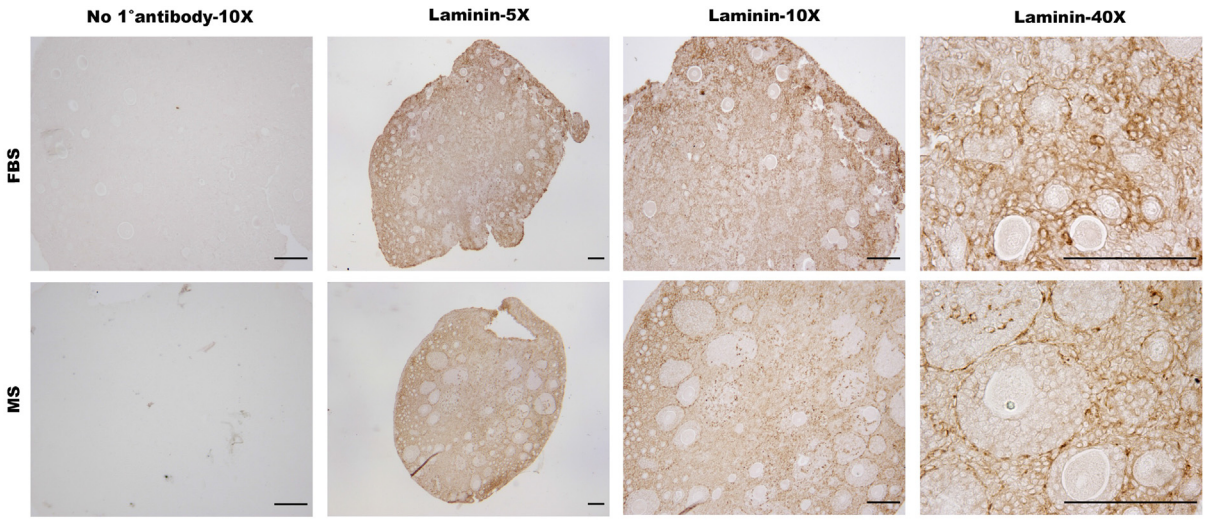

Fig. 5. Detection of laminin using immunohistochemistry in mouse ovarian tissue cultured in FBS- versus MS-supplemented culture media. P3 mice ovaries were cultured for 14 days in Waymouth's media supplemented with either FBS or MS. Control sections were not exposed to the primary antibody. Images are representative of the same experiment with the same DAB exposure to allow for direct comparison. Scale bar = 100 μm.

culture systems, using serum from the same species as the ovarian tissue might be more beneficial.

The impact of varying MS concentrations on mouse embryo viability suggested potential benefits of higher MS concentrations by improving overall embryo health (Saito *et al.* 1984). Future research directions could explore the use of elevated MS concentrations to further enhance follicle health during culture and also determine the molecular mechanisms of the apoptotic pathways involved.

FBS is widely used in cell culture studies and is routinely used in the culture of mouse ovaries and mouse follicles (Kaune *et al* 2017; Lo *et al.* 2019). However, FBS is not used when culturing human ovarian tissues because relying on a reagent to develop follicles and eggs *in vitro* that would not be suitable for a clinical treatment seems counterintuitive. Crucially, this stripped-back approach may be the reason why a robust technique for culturing ovarian human tissues to develop mature eggs from primordial follicles has proved elusive, because perhaps there are other molecules that are also required.

Since primary follicles appear to develop similarly in both conditions but did not progress further in the FBS, we sought to examine follicle development in more depth. Interestingly, the number of GCs and TCs in primary follicles did not differ in FBS- versus MS-supplemented media, indicating that MS did not affect the development of somatic cells in these very early follicles compared with FBS supplementation. However, analysis of AMH, as a marker of follicle function, showed that ovaries cultured in MS were more likely to be AMH+ve. Moreover, the proportion of GCs that were AMH+ve was also higher in primary follicles and, thus, despite the fact that the number of primary follicles did not differ between the groups, their functionality did. These results are likely to suggest improved granulosa cell functionality and overall follicle function in MS media. However, the assessment was limited to granulosa cells, and future studies could include markers such as c-Kit receptor expression to assess the functionality of TCs (Thomas and Vanderhyden 2006) or GDF-9 for oocytes (Hreinsson *et al.* 2002) to obtain more insight into the molecular modifications of follicle development.

The FBL plays a critical role in regulating molecular exchange within the follicle, creating an optimal environment for oocyte development, and supporting the proliferation and differentiation of GCs (Irving-Rodgers and Rodgers 2000). GCs also produce factors that recruit TCs, which reciprocally support GCs, influencing overall follicle quality (Young and McNeilly 2010). An underdeveloped FBL may disrupt these interactions between GCs and TCs, potentially resulting in follicles of poorer quality. Follicles lacking a distinct FBL occurred twice as often in the FBS group as in the MS group; however, this was not statistically significant likely because of the small sample size. In similar culture conditions, the absence of a distinct FBL was routinely observed in ovaries cultured *in vitro* compared with their *in vivo* counterparts (Lo *et al* 2019), and, thus, if the inclusion of mouse serum can improve FBL development, this indicates that something is missing precluding robust FBL development when culturing in FBS alone. There is a close relationship between the number of GCs and the formation of the FBL; however, whether this is a direct effect owing to missing factor(s) in the media, or indirect owing to a lack of factor(s) usually produced by other ovarian or follicular cells, is unknown. For example, GDF-9, a member of the TGF-β superfamily generated by mammalian oocytes, could potentially improve

Downloaded from http://connectsci.au/rd/article-pdf/doi/10.1071/RD24178/3617716/rd24178.pdf by guest on 29 December 2025

TC development and subsequently enhance GC count and FBL formation (Elvin *et al.* 1999).

Considering that the FBL was improved in MS, we explored the presence of laminin as a crucial ECM molecule (Irving-Rodgers and Rodgers 2000). Both MS and FBS media preserved laminin distribution within the ECM of cultured ovarian tissue, indicating preserved ECM integrity, a crucial component for follicle development and function (Berkholtz *et al.* 2006; Grosbois *et al.* 2023). However, detection of laminin in the MS ovaries clearly outlined the follicles readily defining the granulosa–FBL border. The role of other ECM components such as collagen and elastin should be explored in future studies to fully understand ECM dynamics under different culture conditions.

Conclusions

In conclusion, we have provided preliminary evidence that MS supports the growth of mouse primordial follicles to preantral follicles *in vitro* more effectively than does standard FBS, offering new insights into follicle development. These findings suggest potential advantages of MS over FBS in supporting follicle development, health, and function, as well as maintaining crucial ECM components in mice. Further research is required to identify the specific components in MS responsible for these benefits and to explore their applicability to human systems. Although further studies need to be performed in humans, these findings may ultimately aid in the establishment of the *in vitro* ovarian tissue culture system and provide female childhood cancer survivors, particularly those with blood cancers, a safe fertility preservation option.

References

Abercrombie M (1946) Estimation of nuclear population from microtome sections. *The Anatomical Record* **94**(2), 239–247. doi:10.1002/ar.1090940210

Adeniran BV, Bjarkadottir BD, Appeltant R, Lane S, Williams SA (2021) Improved preservation of ovarian tissue morphology that is compatible with antigen detection using a fixative mixture of formalin and acetic acid. *Human Reproduction* **36**(7), 1871–1890. doi:10.1093/humrep/deab075

Berkholtz CB, Shea LD, Woodruff TK (2006) Extracellular matrix functions in follicle maturation. *Seminars in Reproductive Medicine* **24**(4), 262–269. doi:10.1055/s-2006-948555

Bjarkadottir BD, Walker CA, Fatum M, Lane S, Williams SA (2021) Analysing culture methods of frozen human ovarian tissue to improve follicle survival. *Reproduction and Fertility* **2**(1), 59–68. doi:10.1530/RAF-20-0058

Chiti MC, Dolmans MM, Lucci CM, Paulini F, Donnez J, Amorim CA (2017) Further insights into the impact of mouse follicle stage on graft outcome in an artificial ovary environment. *Molecular Human Reproduction* **23**(6), 381–392. doi:10.1093/molehr/gax016

Dolmans M-M, Luyckx V, Donnez J, Andersen CY, Greve T (2013) Risk of transferring malignant cells with transplanted frozen-thawed ovarian tissue. *Fertility and Sterility* **99**(6), 1514–1522. doi:10.1016/j.fertnstert.2013.03.027

Elvin JA, Yan C, Wang P, Nishimori K, Matzuk MM (1999) Molecular characterization of the follicle defects in the growth differentiation factor 9-deficient ovary. *Molecular Endocrinology* **13**(6), 1018–1034. doi:10.1210/mend.13.6.0309

Eppig JJ, O'Brien MJ (1996) Development *in vitro* of mouse oocytes from primordial follicles. *Biology of Reproduction* **54**(1), 197–207. doi:10.1095/biolreprod54.1.197

Ghezelayagh Z, Khoshdel-Rad N, Ebrahimi B (2022) Human ovarian tissue *in-vitro* culture: primordial follicle activation as a new strategy for female fertility preservation. *Cytotechnology* **74**, 1–15. doi:10.1007/s10616-021-00510-2

Griffin J, Emery BR, Huang I, Peterson CM, Carrell DT (2006) Comparative analysis of follicle morphology and oocyte diameter in four mammalian species (mouse, hamster, pig, and human). *Journal of Experimental & Clinical Assisted Reproduction* **3**, 2. doi:10.1186/1743-1050-3-2

Grosbois J, Bailie EC, Kelsey TW, Anderson RA, Telfer EE (2023) Spatio-temporal remodelling of the composition and architecture of the human ovarian cortical extracellular matrix during *in vitro* culture. *Human Reproduction* **38**(3), 444–458. doi:10.1093/humrep/dead008

Hreinsson JG, Scott JE, Rasmussen C, Swahn ML, Hsueh AJ, Hovatta O (2002) Growth differentiation factor-9 promotes the growth, development, and survival of human ovarian follicles in organ culture. *The Journal of Clinical Endocrinology & Metabolism* **87**(1), 316–321. doi:10.1210/jcem.87.1.8185

Irving-Rodgers HF, Rodgers RJ (2000) Ultrastructure of the basal lamina of bovine ovarian follicles and its relationship to the membrana granulosa. *Reproduction* **118**(2), 221–228. doi:10.1530/reprod/118.2.221

Kaune H, Sheikh S, Williams SA (2017) Analysis of *in vitro* follicle development during the onset of premature ovarian insufficiency in a mouse model. *Reproduction, Fertility and Development* **29**(8), 1538–1544. doi:10.1071/RD15524

Knight PG, Glister C (2006) TGF-β superfamily members and ovarian follicle development. *Reproduction* **132**(2), 191–206. doi:10.1530/rep.1.01074

Lo BKM, Sheikh S, Williams SA (2019) *In vitro* and *in vivo* mouse follicle development in ovaries and reaggregated ovaries. *Reproduction* **157**(2), 135–148. doi:10.1530/REP-18-0115

McLaughlin M, Albertini DF, Wallace WHB, Anderson RA, Telfer EE (2018) Metaphase II oocytes from human unilaminar follicles grown in a multi-step culture system. *Molecular Human Reproduction* **24**(3), 135–142. doi:10.1093/molehr/gay002

Moravek MB, Pavone ME, Burns K, Kashanian JA, Anderson RA, Klosky JL, Rotz SJ, Stern CJ, Rodriguez-Wallberg KA, Levine JM, Meacham LR (2023) Fertility assessment and treatment in adolescent and young adult cancer survivors. *Pediatric Blood & Cancer* **70**, e28854. doi:10.1002/pbc.28854

Morgan S, Campbell L, Allison V, Murray A, Spears N (2015) Culture and co-culture of mouse ovaries and ovarian follicles. *Journal of Visualized Experiments* **97**, e52458. doi:10.3791/52458

Pedersen T (1969) Follicle growth in the immature mouse ovary. *Acta Endocrinologica* **62**(1), 117–132. doi:10.1530/acta.0.0620117

Pedersen T, Peters H (1968) Proposal for a classification of oocytes and follicles in the mouse ovary. *Reproduction* **17**(3), 555–557. doi:10.1530/jrf.0.0170555

Peters H (1969) The development of the mouse ovary from birth to maturity. *Acta Endocrinologica* **62**(1), 98–116.

Rosendahl M, Greve T, Andersen CY (2013) The safety of transplanting cryopreserved ovarian tissue in cancer patients: a review of the literature. *Journal of Assisted Reproduction and Genetics* **30**, 11–24. doi:10.1007/s10815-012-9912-x

Saito H, Berger T, Mishell D, Marrs RP (1984) Effect of variable concentration of serum on mouse embryo development. *Fertility and Sterility* **41**(3), 460–464. doi:10.1016/S0015-0282(16)47728-9

Thomas FH, Vanderhyden BC (2006) Oocyte–granulosa cell interactions during mouse follicular development: regulation of kit ligand expression and its role in oocyte growth. *Reproductive Biology and Endocrinology* **4**, 19. doi:10.1186/1477-7827-4-19

Van Houten ELAF, Themmen AP, Visser JA (2010) Anti-Müllerian hormone (AMH): regulator and marker of ovarian function. *Annales d'Endocrinologie* **71**(3), 191–197. doi:10.1016/j.ando.2010.02.016

Visser JA, Themmen APN (2005) Anti-Müllerian hormone and folliculogenesis. *Molecular and Cellular Endocrinology* **234**(1–2), 81–86. doi:10.1016/j.mce.2004.09.008

Downloaded from http://connectsci.au/rd/article-pdf/doi/10.1071/RD24178/13617116/rd24178.pdf by guest on 29 December 2025

Walker CA, Bjarkadottir BD, Fatum M, Lane S, Williams S (2021) Variation in follicle health and development in cultured cryopreserved ovarian cortical tissue: a study of ovarian tissue from patients undergoing fertility preservation. *Human Fertility* **24**(3), 188–198. doi:10.1080/14647273.2019.1616118

Winship AL, Carpenter M, Griffiths M, Hutt KJ (2019) Vincristine chemotherapy induces atresia of growing ovarian follicles in mice. *Toxicological Sciences* **169**(1), 43–53. doi:10.1093/toxsci/kfz022

Xu F, Lawson MS, Bean Y, Ting AY, Pejovic T, De Geest K, Moffitt M, Mitalipov SM, Xu J (2021) Matrix-free 3D culture supports human follicular development from the unilaminar to the antral stage *in vitro* yielding morphologically normal metaphase II oocytes. *Human Reproduction* **36**, 1326–1338. doi:10.1093/humrep/deab003

Young JM, McNeilly AS (2010) Theca: the forgotten cell of the ovarian follicle. *Reproduction* **140**(4), 489–504. doi:10.1530/REP-10-0094

Data availability. The data of this study are available from the corresponding author upon reasonable request.

Conflicts of interest. The authors declare that they have no conflicts of interest.

Declaration of funding. This work was supported by a Clarendon Fund Scholarship to B. K. M. Lo, Nuffield Department of Women's and Reproductive Health funding to B. K. M. Lo, S. A. Kader, E. R. Stephens and John Fell OUP to S. A. Williams to fund O. F. Ammar. This project has also been made possible in part by Grant number 2021-238038 from the Chan Zuckerberg Initiative DAF, an advised fund of Silicon Valley Community Foundation, to S. A. Williams to fund N. Kuscu.

Acknowledgements. The authors acknowledge assistance by the BMS facilities.

Author contributions. S. A. Williams conceived the study, S. A. Williams, B. K. M. Lo, B. V. Adeniran designed the study, samples were generated and analysed by B. V. Adeniran, S. A. Kader, E. R. Stephens, O. F. Ammar, A. S. Harrison, and N. Kuscu. The manuscript draft and figures were generated by N. Kuscu on the basis of MSc dissertations generated by S. A. Kader and E. R. Stephens. All authors edited and approved the final draft.

Author affiliation

[A]Nuffield Department of Women's and Reproductive Health, University of Oxford, Women's Centre, Level 3, John Radcliffe Hospital, Oxford OX3 9DU, UK.

Downloaded from http://connectsci.au/rd/article-pdf/doi/10.1071/RD24178/1361716/rd24178.pdf by guest on 29 December 2025

Assessing the impact of human serum on adherence of frozen pre-pubertal human ovarian cortical tissue in culture

Ava Harrison[1]; Omar Ammar[1]; Suzannah A Williams[1]
[1] *Nuffield Department of Women's & Reproductive Health, University of Oxford*

Introduction

Ovarian tissue cryopreservation is a fertility preservation strategy for pre-pubescent girls, and women requiring immediate gonadotoxic treatment (1,2). Patients with blood-based cancers risk reintroducing malignant cells if re-implanted and thus culture methods need to be established (3,4). For accurate follicle imaging in culture, tissue must remain stationary. One approach is to promote adherence of ovarian tissue to the dish. We investigated the impact of human serum (HS), either untreated (uHS) or inactivated HS (iHS), on the initial adherence, and maintenance of adherence, of cryopreserved human cortical tissue during 14-day culture.

Methods

Cryopreserved ovarian cortical tissue from chemotherapy-naïve pre-pubertal patients (n = 3) was obtained (Table 1). Tissues were thawed, cut into fragments, and cultured for 14-days with human serum albumin (HSA; control), uHS, or iHS. On day 8 (d8), two groups receiving uHS or iHS were switched to HSA supplementation. Adherence and cellular outgrowth were assessed on d8 and d14. The two-sided Chi-square with Yates' correction was used for all statistical analysis.

Table 1. Patient characteristics at time of donation of ovarian cortical tissue for culture following freezing.

Patient	Pubertal status	Age	Condition	Chemotherapy	Tissue type	Fresh or frozen
A	Pre-pubertal	7 years	Osteosarcoma	Naïve	Ovarian Cortex	Frozen
B	Pre-pubertal	1 month	Osteoporosis	Naïve	Ovarian Cortex	Frozen
C	Pre-pubertal	12 years	Osteosarcoma	Naïve	Ovarian Cortex	Frozen

Discussion

Interestingly, both uHS and iHS promoted human ovary adherence equally during culture thus enabling accurate monitoring of potential follicle development. Moreover, HS removal on d8 did not affect tissue adherence illustrating that once adhered, continued supplementation of serum was not required to maintain adherence. Despite the small sample size, tissues from all three patients were consistent in their adherence in the presence of HS. However, post-pubertal patients may respond differently. The specific factor(s) promoting adherence in HS are unknown and further investigation could allow for more targeted in vitro supplementation.

The authors declare that there is no conflict of interest.

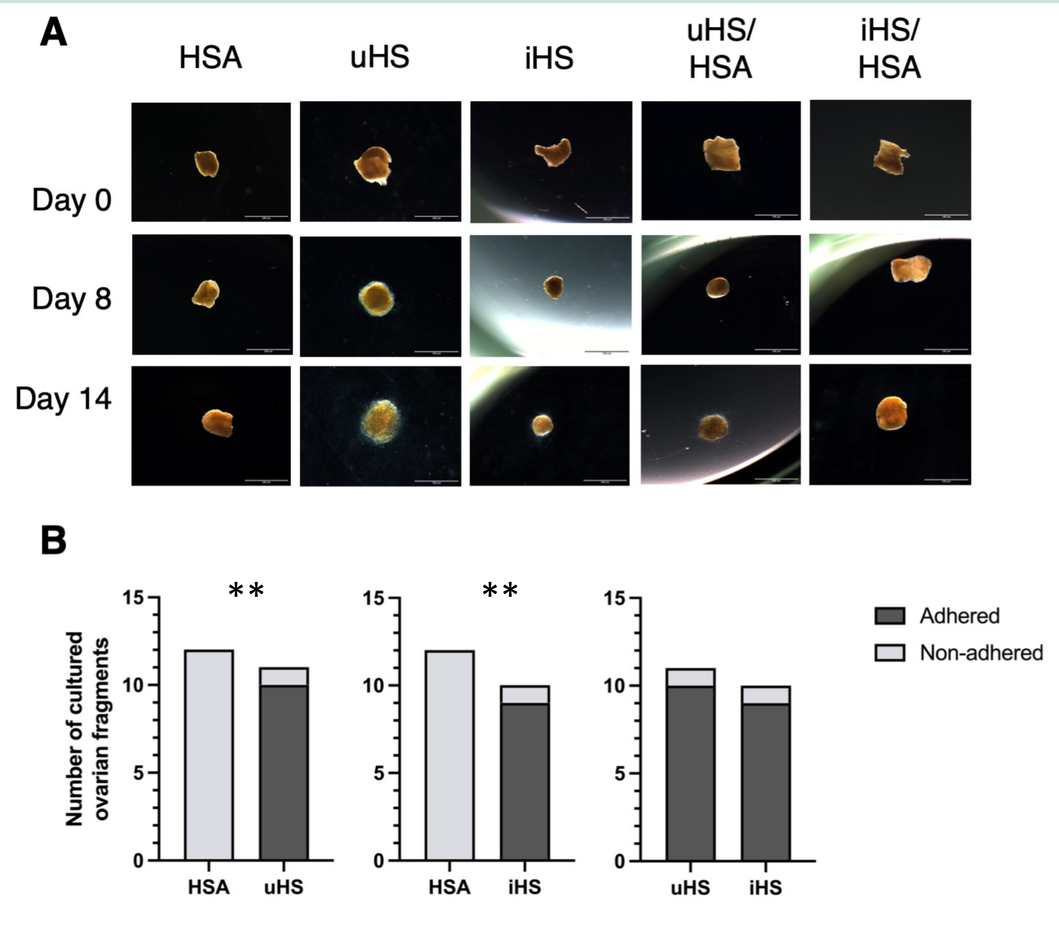

Figure 1. Adherence data of human ovarian cortical tissue fragments cultured with human serum albumin (HSA), untreated human serum (uHS), or inactivated HS (iHS). A) Representative images of fragments cultured in HSA, uHS, iHS, as well as uHS and iHS fragments switched to HSA culture supplement on d8 (uHS/HSA and iHS/HSA, respectively) over the 14-day culture period. **B**) Contingency bars representing the number of fragments that adhered or did not adhere after 14-days cultured with HSA, uHS, or iHS. Fragments cultured with uHS or iHS were more likely to adhere than those cultured in HSA, respectively (both $p < 0.01$). No difference was found between adherence on day 14 (d14) between fragments cultured in uHS vs iHS ($p > 0.05$).

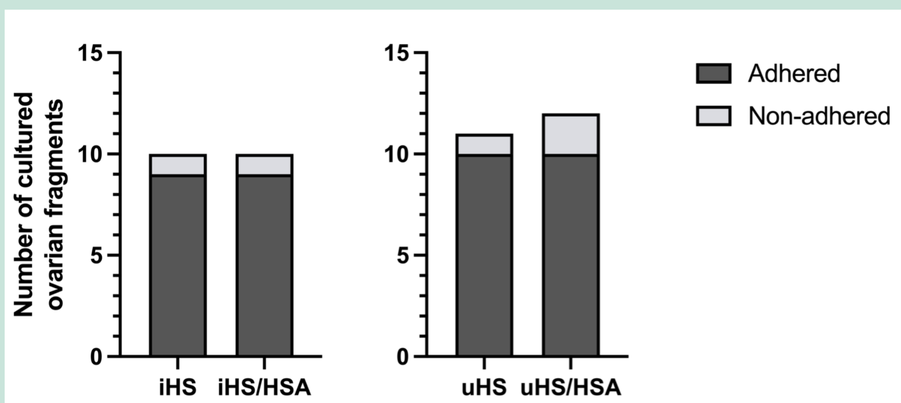

Figure 2. Adherence was maintained on day 14 (d14) when untreated human serum (uHS) or inactivated HS (iHS) was removed on d8 and switched with human serum albumin (HSA). No difference in number of adhered and non-adhered fragments were found in iHS vs iHS/HSA nor uHS vs uHS/HSA (both $p > 0.05$).

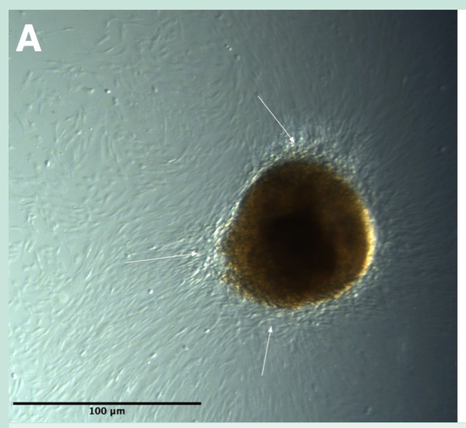

B ****

	Adherence	Non-Adherence	Total
Cellular Growth	32	0	32
No Cellular Growth	7	17	24
Total	39	17	56

Figure 3. Cellular outgrowth on day 8 (d8) was associated with tissue adherence on d14. A) Cellular outgrowth from human tissue fragment cultured in untreated human serum (uHS) on d8 (white arrows pointing to cells growth from the fragment). **B**) A contingency table demonstrating cellular outgrowth on d8 was associated with continued adherence on d14 ($p < 0.0001$) with data from tissue fragments across all five groups.

Results

Fragments cultured with uHS or iHS for 14-days were more often adhered compared to control ($p < 0.01$ for both) (Figure 1). No difference in adherence was found between uHS vs iHS. Where either uHS or iHS were removed on d8, adherence was maintained until d14 (Figure 2). The presence of cellular outgrowth on d8 was associated with tissue adherence on d14 ($p < 0.01$) (Figure 3).

References

(**1**) Donnez J, Dolmans M, Demylle D, Jadoul P, Pirard C, Squifflet J, et al. Livebirth after orthotopic transplantation of cryopreserved ovarian tissue. The Lancet. 2004;364(9443):1405–10. doi:10.1016/s0140-6736(04)17222-x. (**2**) Practice Committee of the American Society for Reproductive Medicine. Fertility preservation in patients undergoing gonadotoxic therapy or gonadectomy: A committee opinion. Fertility and Sterility. 2019 Dec 13;112(6):1022–33. doi:10.1016/j.fertnstert.2019.09.013. (**3**) Dolmans M-M, Luyckx V, Donnez J, Andersen CY, Greve T. Risk of transferring malignant cells with transplanted frozen-thawed ovarian tissue. Fertility and Sterility. 2013 May 6;99(6):1514–22. doi:10.1016/j.fertnstert.2013.03.027. (**4**) Shapira M, Raanani H, Barshack I, Amariglio N, Derech-Haim S, Marciano MN, et al. First Delivery in a leukemia survivor after transplantation of cryopreserved ovarian tissue, evaluated for leukemia cells contamination. Fertility and Sterility. 2018;109(1):48–53. doi:10.1016/j.fertnstert.2017.09.001.

NUFFIELD DEPARTMENT OF WOMEN'S & REPRODUCTIVE HEALTH
Medical Sciences Division

UNIVERSITY OF OXFORD

Application of a mouse model to investigate the effect of high-grade serous ovarian cancer on the ovaries

Ava Harrison[1]; Samar Elorbany[2]; Chiara Berlato[2]; Ganga Gopinathan[2]; Frances Balkwill[2]; Suzannah Williams[1]
[1] Nuffield Department of Women's & Reproductive Health, University of Oxford; [2]Barts Cancer Institute, Queen Mary University of London

Barts Cancer Institute
Queen Mary University of London

Introduction

- It is estimated that 1 in 50 women will be diagnosed with ovarian cancer in their lifetime, of which 12% will be within their reproductive years (1).
- A routine treatment of ovarian cancer involves the surgical removal of the ovaries and fallopian tubes, as the latter may be the major site of origin of this cancer (2,3).
- Novel mouse models have been designed to investigate ovarian cancer and the mechanisms involved (4).
- We investigated the incidence of ovarian cancer in a high-grade serous ovarian cancer (HGSOC) mouse model for future application for ovary-focused fertility research.

Aims & Objectives

- The current study sought to determine the proportion of tumours present on the HGSOC mouse model ovaries.
- This was assessed through gross anatomical evaluation of excised murine ovaries.

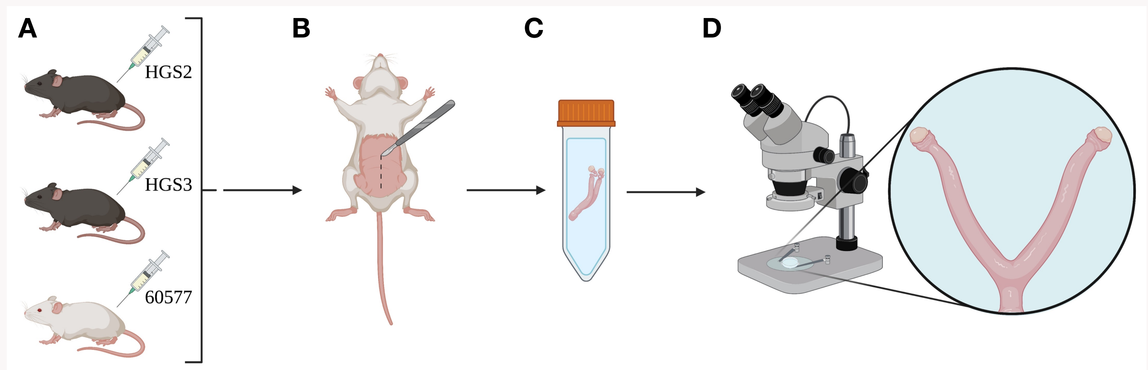

Figure 1. Schematic outlining the methodological steps to investigate ovarian tumour presence in mouse models of high-grade serous ovarian cancer (HGSOC). A) C57BL/6 or FVB female mice were administered with one of three HGSOC cell lines (HGS2, HGS3, or 60577) via intraperitoneal injection. **B, C)** At the natural end point, the ovaries and accompanying reproductive tract were dissected and fixed in formalin for 24 hours. **D)** Tumour presence was assessed by gross anatomical evaluation using a stereomicroscope. Objects in figure are not to scale. Created using BioRender.com.

Methods

- Ovaries were collected from C57BL/6 or FVB mouse models of HGSOC, previously described by the Balkwill group (4) (Figure 1).
- Intraperitoneal injection (IP) was administered to female mice with a cell line (HGS2, HGS3, or 60577) (4).
- Once natural end point was reached, the reproductive tract was dissected and fixed in formalin for 24 hours.
- Gross anatomical evaluation was performed to identify suspected ovarian tumours and potential necrosis via stereomicroscopy.

Results

- A total of 76 excised ovaries were examined (n = 38) (Table 1).
- Ovarian-specific tumours were identified in 20.98% (13/62) of ovaries from the HGSOC-model mice injected with the HGS2 cell line (n = 31) (Figure 2). No tumours were present on ovaries of HGS3 (n = 3) nor 60577 (n = 4) cell line injected mice.
- Necrosis was observed in 7.89% (6/76) of total ovaries (Figure 3). Of the six ovaries with necrosis, 5 were attributed to mice injected with the HGS2 cell line (n = 4) and 1 from mice injected with HGS3 cell line (n = 1). It is important to note, however, that no necrosis was found within or near any of the ovarian tumours.

Table 1. High-grade serous ovarian cancer model mice used in this study.

	***n* (%)**
C56BL/6 (*n* = 34)	
HGS2	31 (91.18%)
HGS3	3 (8.82%)
FVB (*n* = 4)	
60577	4 (100.00%)

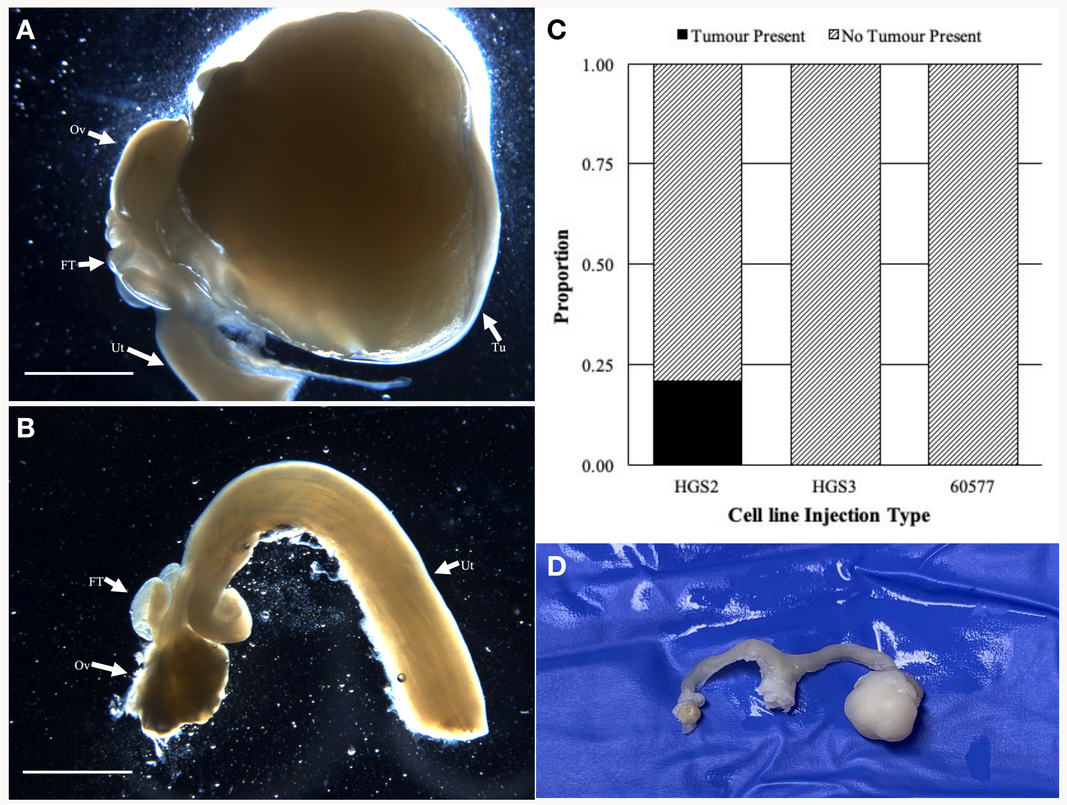

Figure 2. Investigation of tumour presence on the ovary of high-grade serous ovarian cancer (HGSOC) mouse models. A) Dissected reproductive tract with a tumour on the ovary of a C57BL/6 mouse following intraperitoneal (IP) injection of the HGS2 cell line (Ovary, Ov; Oviduct/ fallopian tube, FT; Uterus, Ut; Tumour, Tu). **B)** Dissected reproductive tract of C57BL/6 mouse injected with HGS2 with no tumour present on the ovary. **C)** Proportion of total ovaries with an ovarian tumour following IP injection of HGS2 (n = 31), HGS3 (n = 3), or 60577 (n = 4) cell lines and investigated via gross anatomical evaluation. **D)** Intact reproductive tract of C57BL/6 mouse injected with HGS2 with a unilateral HGSOC ovarian tumour present on the right ovary. Scale bar = 750 µm.

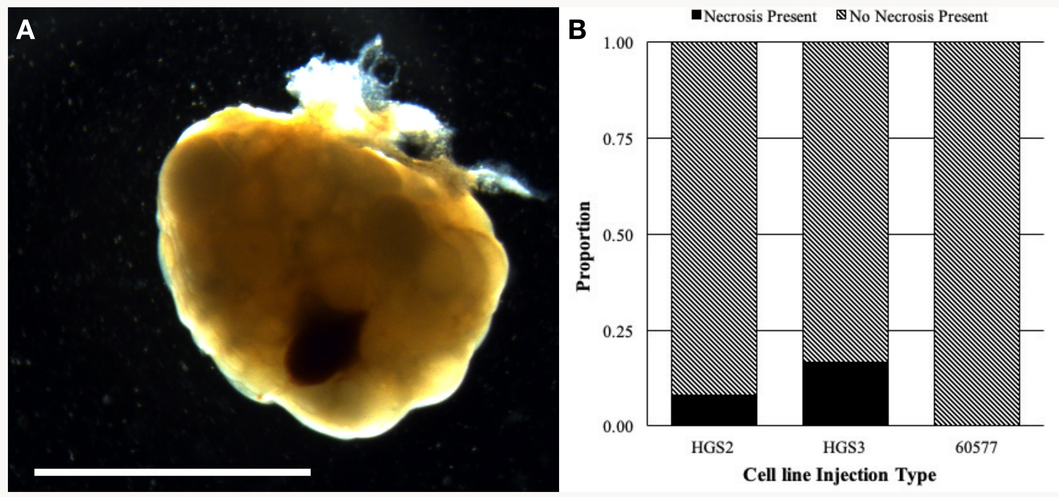

Figure 3. Potential necrotic tissue present on the ovary of high-grade serous ovarian cancer (HGSOC) mouse models. A) Dissected ovary of a C57BL/6 mouse following intraperitoneal (IP) injection of the HGS3 cell line with potential necrotic tissue present. Scale bar = 750 µm. **B)** Proportion of total ovaries with potential necrosis on the ovary following IP injection of HGS2 (n = 31), HGS3 (n = 3), or 60577 (n = 4) cell lines and investigated via gross anatomical evaluation.

Discussion

- Despite the nomenclature and being a well described model of ovarian cancer, few of the total HGSOC-model ovaries appeared cancerous even with a significant tumour burden elsewhere at time of culling. This was likely because the bursa acts as an anatomical barrier following IP injection. Furthermore, it is thought that HGSOC may originate from serous tubal intraepithelial carcinomas in the fallopian tube (3). Thus, growth in the ovary could be a metastases.
- As this study aimed to investigate the application of this HGSOC mouse model for future fertility research, the ovaries needed to be cancerous, intact, and viable. Gross anatomical evaluation was implemented to assess ovarian tumour and necrosis presence due to its non-invasiveness. Other methods, such as immunohistochemistry to assess p53 expression, have been utilised to assess and characterise HGSOC tumours in other studies, but were not selected due to invasiveness (3, 5).
- Ovarian dissection and investigation only occurred following the natural end point of each individual mouse. No necrosis was seen on ovaries where a tumour was present. Thus, necrosis presence in the ovary was not likely attributed to cancer within the ovaries.

Conclusion

This model is valuable, however it was not ideal for investigating fertility within cancerous ovaries following IP injection.

Contributions

S.E., C.B., G.G., & F.B. developed the HGSOC mouse model, administered the cell line IP injection, & dissected the reproductive tract upon natural end point. A.H. assessed tumour & necrosis presence to generate results. S.W. provided A.H. support generating results & necessary training handling murine ovarian tissue.

References

1) Office for National Statistics. Cancer registration statistics, England: 2017. https://www.ons.gov.uk/releases/cancerregistrationstatisticsengland2017 (31 August 2022, date last accessed). **2)** Colombo N, Sessa C, Bois AD, Ledermann J, McCluggage WG, McNeish I, et al. ESMO-ESGO consensus conference recommendations on ovarian cancer: pathology and molecular biology, early and advanced stages, borderline tumours and recurrent disease. Int J Gynecol Cancer. 2019. **3)** Labidi-Galy SI, Papp E, Hallberg D, Niknafs N, Adleff V, Noe M, et al. High grade serous ovarian carcinomas originate in the fallopian tube. Nat Commun. 2017;8(1):1093. **4)** Maniati E, Berlato C, Gopinathan G, Heath O, Kotantaki P, Lakhani A, et al. Mouse Ovarian Cancer Models Recapitulate the Human Tumor Microenvironment and Patient Response to Treatment. Cell Rep. 2020;30(2):525-40 e7.S. **5)** Cole AJ, Dwight T, Gill AJ, Dickson K-A, Zhu Y, Clarkson A, et al. Assessing mutant p53 in primary high-grade serous ovarian cancer using immunohistochemistry and massively parallel sequencing. Scientific Reports. 2016;6(1).

8.1.3 Awards

Lady Margaret Hall Graduate Scholarship Award (2022)

Lady Margaret Hall, University of Oxford

Award of £6,000 to support graduate students on the basis of academic merit and college community contributions.

Sir Alec Turnbull Travelling Scholarship Award (2022)

Nuffield Department of Women's and Reproductive Health, University of Oxford

Award of £750 to support travel for academic and research purposes.

Lady Margaret Hall Academic Development Fund (2021, 2022, 2023)

Lady Margaret Hall, University of Oxford

A series of small grants (maximum £300) received to complete academic pursuits, including conference attendance.

8.2 Appendix II: Supplementary results for Chapter 5

Table AII.5.2.6) Traceability of reaggregated ovary inclusion across experimental batches and analytical modalities, as used in Chapter 5.

Experiment	RO ID	Type	Histogel embedding	FolliTracker	H&E	IHC: AMH	IHC: mCherry	Notes
E1	Con A	Control	Yes	Yes	Yes	Yes	Yes	
	Con B	Control	Yes	Yes	Yes	Yes	Yes	
	Viral	Viral	Yes	Yes	Yes	Yes	Yes	
E2	Con	Control	No	Yes	Yes	Yes	Yes	
	Viral	Viral	No	Yes	Yes	Yes	Yes	
E3	Con A	Control	Yes	Yes	Yes	Yes	Yes	
	Con B	Control	Yes	Yes	Yes	Yes	Yes	
	Viral	Viral	Yes	Yes	Yes	Yes	Yes	
E4	Con	Control	No	Yes	No	Yes	No	Processing & sectioning artefacts
	Viral	Viral	No	Yes	No	Yes	Yes	Processing & sectioning artefacts
E5	Con A	Control	Yes	Yes	Yes	Yes	Yes	
	Con B	Control	Yes	Yes	Yes	Yes	Yes	
	Viral	Viral	Yes	Yes	Yes	Yes	Yes	

AMH, anti-Müllerian hormone; E(1/2/3/4/5), experiment (1/2/3/4/5); H&E, haematoxylin and eosin; IHC, immunohistochemistry; RO, reaggregated ovary.

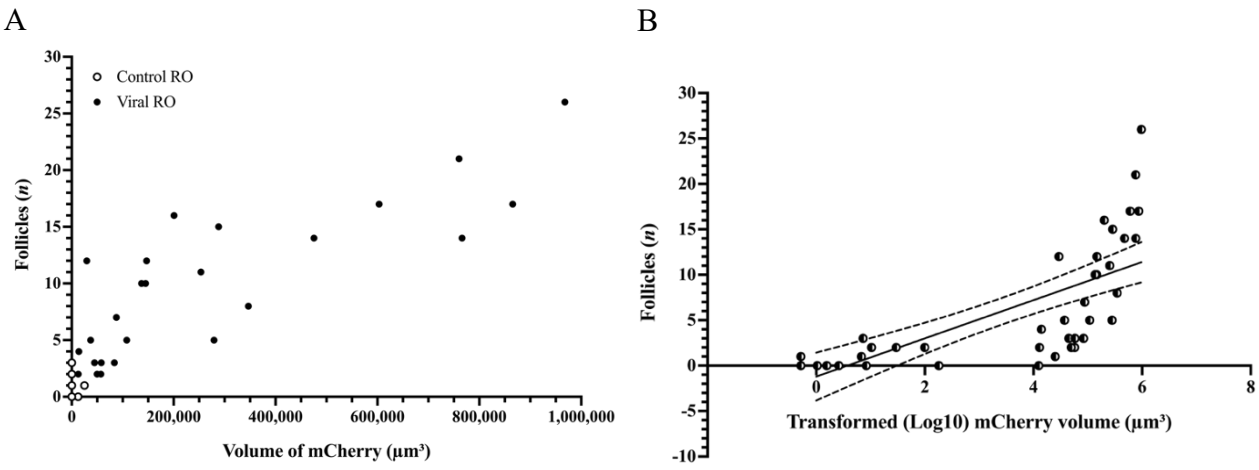

Figure AII.5.3.4) Quantitative correlation assessment of mCherry signal and follicle number via FolliTracker in reaggregated ovaries. Viral ROs underwent sequential transduction of AAVs prior to reaggregation, whereas control ROs were not exposed to virus-containing media. mCherry fluorescence represented successful transduction of somatic cells. **A)** Subgroup analysis of Spearman's correlation between mCherry volume (μm^3) and follicle number in control (r=0.5885; $p<0.0001$) and viral ROs (r=0.8079; $p<0.0001$), shown on a linear scale. **B)** Spearman's correlation (r=0.9069; $p<0.0001$) between Log_{10}-transformed mCherry signal volume (μm^3) and number of follicles detected by FolliTracker in a pooled analysis, with simple linear regression applied ($r^2=0.5155$; $p<0.0001$). Data are presented as individual ROs. Solid line represents best-fit regression line, shown with dashed line representing the 95% CI (B). AAV, adeno-associated virus; CI, confidence interval; RO, reaggregated ovary.

AII.5.3.12 Normalised DAB intensity for anti-Müllerian hormone

Pooled follicle-level data were used for analysis of AMH outcomes owing to low follicle numbers per RO in the control group (n=7; 29 follicles assessed) and viral group (n=4; 18 follicles assessed). Homogeneity of variance was confirmed by a non-significant F-test (p=0.4758). The coefficient of variation for the control group was 97.41% and 47.78% in the viral group. The unpaired, two-tailed t-test demonstrated a significant difference in mean normalised AMH intensity between groups (p=0.0118), supporting a difference between groups and justifying the pooling approach.

Table AII.5.3.12) Traceability of normalised DAB intensity of anti-Müllerian hormone across all assessed follicles in reaggregated ovaries across experimental batches, as used in Chapter 5.

		Control		Viral
Mean normalised DAB intensity for AMH, AU/µm² ± SD (min, max)		0.1754 ± 0.1708 (-0.0009718, 0.7558)		0.3025 ± 0.1445 (0.02214, 0.5542)
Normalised DAB intensity of all follicles, AU/µm²				
E1	**Control A**	0.109748422 0.41361595 0.182143516 0.070972079	**Viral**	0.446740427 0.421395114 0.193310393 0.346546199
	Control B	0.755784255		0.387197585 0.357516702 0.311735202
E2	**Control**	0.068564372	**Viral**	0.162581643 0.251960519
E3	**Control A**	-0.000198046 -0.00017898 0.047894525 0.154391405 0.029987619 0.155169655	**Viral**	0.554166861 0.358704382 0.390595434
	Control B	0.001654572 0.236251148 -0.000971752 0.028732079 0.132264656 0.040659849		
E5	**Control A**	0.337485971 0.339854715 0.030148248	**Viral**	0.022141793 0.104687174 0.449775571 0.060978523 0.283587795 0.340869573
	Control B	0.316674622 0.398061327 0.088135645 0.137849402 0.244303098 0.347509831 0.228232172 0.190863327		

AMH, anti-Müllerian hormone; AU, arbitrary unit; DAB, 3,3′-diaminobenzidine; E(1/2/3/4/5), experiment (1/2/3/4/5); RO, reaggregated ovary; SD, standard deviation.

Table AII.5.3.13) Immunohistochemical assessment of mCherry-positive area via DAB staining in reaggregated ovaries following 14 days in culture with all data shown. Viral ROs underwent sequential transduction with AAVs prior to reaggregation, whereas control ROs were not exposed to virus-containing media. Sections were stained for mCherry expression using DAB chromogenic detection to visualise transduction of somatic cell populations within the tissue.

		Control	Viral	
Mean area positive for mCherry, μm^2 ± SD (%)		301.5 ± 646.8* (0.16%)†	16,851 ± 13,792* (20.1%)†	
Area of mCherry per reaggregated ovary section, μm^2 (%)				
E1	**Control A**	48.5 (0.03%)	**Viral**	7,722.9 (9.6%)
	Control B	0.0 (0.00%)		
E2	**Control**	92.8 (0.07%)	**Viral**	27,519.6 (44.7%)
E3	**Control A**	5.3 (0.004%)	**Viral**	15,195.5 (16.0%)
	Control B	1,765.1 (0.82%)		
E4	**Control‡**	–	**Viral**	33,657.4 (30.2%)
E5	**Control A**	115.8 (0.12%)	**Viral**	160.0 (0.26%)
	Control B	83.4 (0.06%)		

AAV, adeno-associated virus; DAB, 3,3′-diaminobenzidine; E(1/2/3/4/5), experiment (1/2/3/4/5); RO, reaggregated ovary; SD, standard deviation. *$p<0.01$ (Mann-Whitney U test); †$p<0.01$ (Unpaired t-test with Welch's correction); ‡mCherry-positive area could not be quantified due to processing artefacts that may have affected data integrity.

AII.5.3.14 Outlier identification and stratified background analysis for immunohistochemical assessment of mCherry

Normalised mCherry DAB intensity was calculated relative to the mean background intensity of corresponding control sections. One control section from experiment 3 (E3) exhibited markedly elevated background staining (means ~212–221 AU vs. ~254–255 AU in all other controls). It should be noted that 255 AU represents complete saturation (no staining signal). As this value represented an artefact rather than biological variability, its inclusion would have inflated the normalisation denominator and underestimated the mCherry signal in the paired viral reaggregated ovary.

To ensure analytical integrity, two versions of the dataset were generated:

1. Stratified background analysis (including all control sections): maintained experimental pairing but included the artefactual high-intensity control
2. Sensitivity analysis (excluding the single E3 artefactual control B): used mean background intensity from remaining paired controls

Both analyses demonstrated consistent trends in relative mCherry signal between viral and control reaggregated ovaries, confirming that exclusion of the artefactual section did not alter interpretation of results. The exclusion was therefore applied to the final normalisation step to avoid skewing the viral dataset. The outlier was only removed for the normalised DAB intensity analyses. The outlier was included for area positive for mCherry, proportion of mCherry-positive area, and grade of staining intensity distribution for follicles.

Table AII.5.3.14) Distribution of oocyte mCherry staining intensity grades in reaggregated ovaries following 14 days in culture in the stratified background analysis. Viral ROs underwent sequential transduction with AAV-SaCas9 and AAV-DS vectors prior to reaggregation, whereas control ROs were not exposed to virus-containing media. Expression of mCherry, driven by the ubiquitous SFFV promoter, indicated successful viral transduction of somatic cells within the tissue. ROs were fixed at the end of culture and processed for IHC using DAB (brown) chromogenic staining to detect mCherry expression. Oocytes were graded (0–3) based on normalised DAB intensity for mCherry signal (grade 0, < 0.1; grade 1, 0.1 ≤ x < 0.2; grade 2, 0.2 ≤ x < 0.3; grade 3, ≥ 0.3). Statistical comparison between experimental conditions was performed using Fisher's exact test (p<0.0001). Data are presented as oocytes (n) per staining grade.

	Control	Viral
Grade 0	25	18
Grade 1	0	2
Grade 2	0	0
Grade 3	0	0

AAV, adeno-associated virus; Cas9, CRISPR-associated protein 9; DAB, 3,3′-diaminobenzidine; DS, donor strand; IHC, immunohistochemistry; NS, not significant; RO, reaggregated ovary.

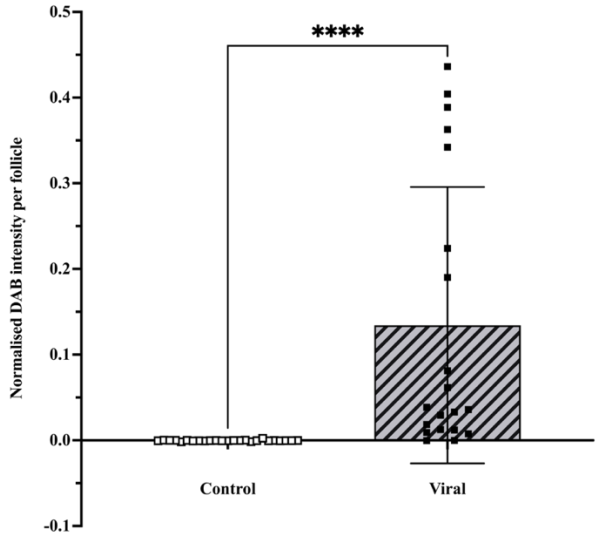

Figure AII.5.3.14) Immunohistochemical assessment of mCherry expression in reaggregated ovaries following 14 days in culture in the stratified background analysis. Viral ROs underwent sequential transduction with AAV-SaCas9 and AAV-DS vectors prior to reaggregation, whereas control ROs were not exposed to virus-containing media. Expression of mCherry, driven by the ubiquitous SFFV promoter, indicated successful viral transduction of somatic cells within the tissue. ROs were fixed at the end of culture and processed for IHC using DAB (brown) chromogenic staining to detect mCherry and haematoxylin to visualise nuclei. Normalised DAB intensity (AU) of mCherry staining per follicle in control and viral ROs. Statistical analysis was performed using Mann-Whitney U test. Data are presented as mean ± SD. AAV, adeno-associated virus; AU, arbitrary units; Cas9, CRISPR-associated protein 9; DAB, 3,3′-diaminobenzidine; DS, donor strand; IHC, immunohistochemistry; RO, reaggregated ovary; SD, standard deviation; SFFV, spleen focus-forming virus. *p≤0.05; **p<0.01; ***p<0.001; ****p<0.0001.

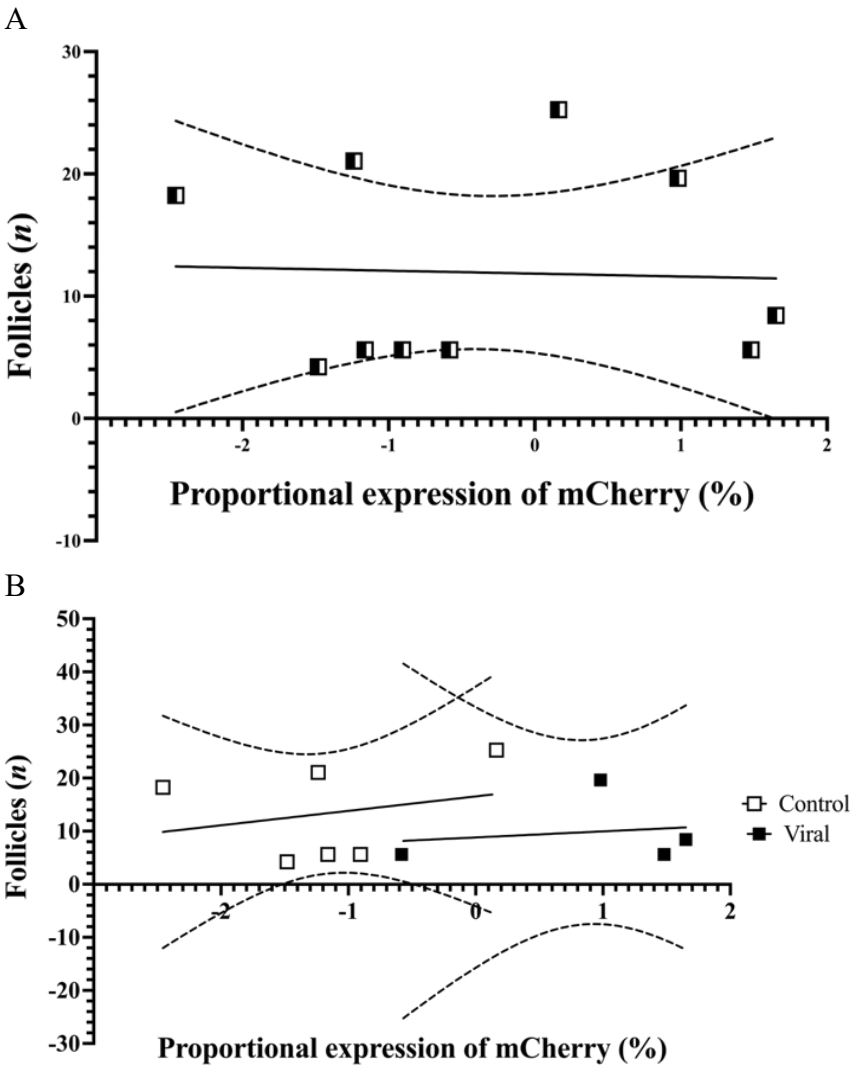

Figure AII.5.3.15) Correlation between proportion of mCherry-positive tissue area and total follicle number following 14 days in culture, as determined by histology-based analysis with stratified background data. Viral ROs underwent sequential transduction with AAV-SaCas9 and AAV-DS vectors prior to reaggregation, whereas control ROs were not exposed to virus-containing media. Expression of mCherry, driven by the ubiquitous SFFV promoter, indicated successful transduction of somatic cells within tissue. ROs were fixed at the end of culture and processed for histological analysis and IHC using DAB chromogenic staining to detect mCherry expression. Follicle number per RO was quantified using histological analysis of H&E-stained sections. Spearman's correlation and simple linear regression of Log_{10}-transformed proportional mCherry-positive area (%) and total follicle number in **A)** pooled ROs (r=0.1438; r^2=0.0016; slope, -0.2373) and **B)** separated control (r=0.3479; r^2=0.0624; slope, 2.722) and viral (r=0.2108; r^2=0.0301; slope, 1.140) ROs. In all analyses, the slope of regression did not differ significantly from zero, indicating no significant association between factors. Data are presented as individual ROs, with best-fit regression lines shown. Dashed lines represent 95% CIs. AAV, adeno-associated virus; Cas9, CRISPR-associated protein 9; CI, confidence interval; DAB, 3,3′-diaminobenzidine; DS, donor strand; IHC, immunohistochemistry; RO, reaggregated ovary; SFFV, spleen focus-forming virus.

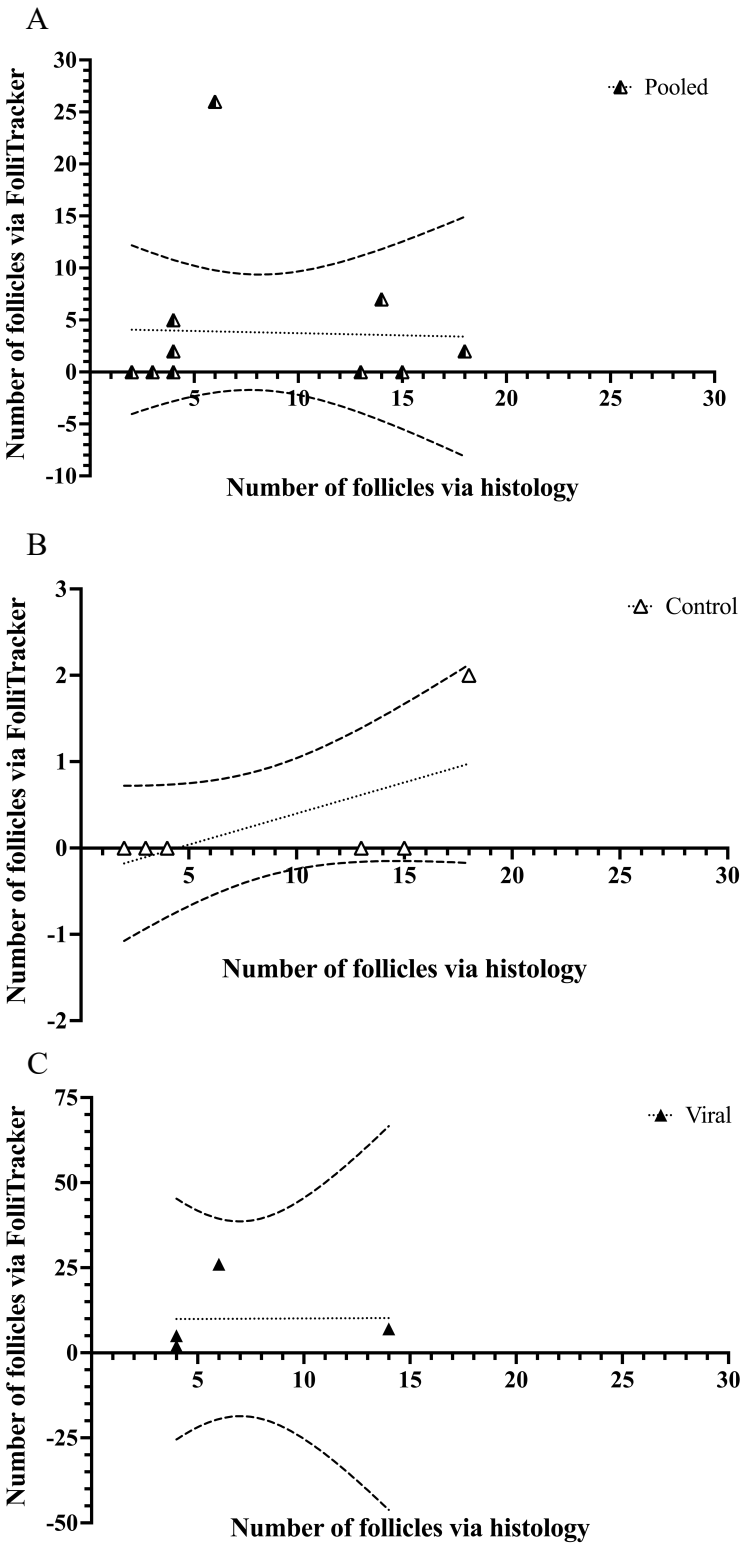

Figure AII.5.3.16) Correlation of follicle counts obtained via FolliTracker and raw follicle number determined by histological analysis in reaggregated ovaries following 14 days in culture. Follicle number per RO was quantified independently using histological analysis of H&E-stained sections and via FolliTracker, a live confocal-based imaging and analysis workflow that detects follicles by overlapping mCherry and EGFP fluorescence signals. Viral ROs underwent sequential transduction with AAV-SaCas9 and AAV-DS vectors prior to reaggregation, whereas control ROs were not exposed to virus-containing media. mCherry signal was driven by the ubiquitous SFFV promoter and EGFP signal was driven by the mAMH promoter, a hormone expressed specifically in granulosa cells of developing follicles. Spearman's correlation between follicle counts quantified by histology and by FolliTracker across **A)** pooled data from all ROs (r=0.3332; r^2=0.0010; slope, -0.0419), **B)** control ROs only (r=0.6179; r^2=0. 4022; slope, 0.0393), and **C)** viral ROs only (r=0.7379; r^2=0.0002; slope, 0.0294). Data are presented as individual ROs with best-fit regression lines shown. Dashed lines represent 95% CI. AAV, adeno-associated virus; AMH, anti-Müllerian hormone; Cas9, CRISPR-associated protein 9; CI, confidence interval; DS, donor strand; EGFP, enhanced green fluorescent protein; H&E, haematoxylin and eosin; RO, reaggregated ovary; SFFV, spleen focus-forming virus.

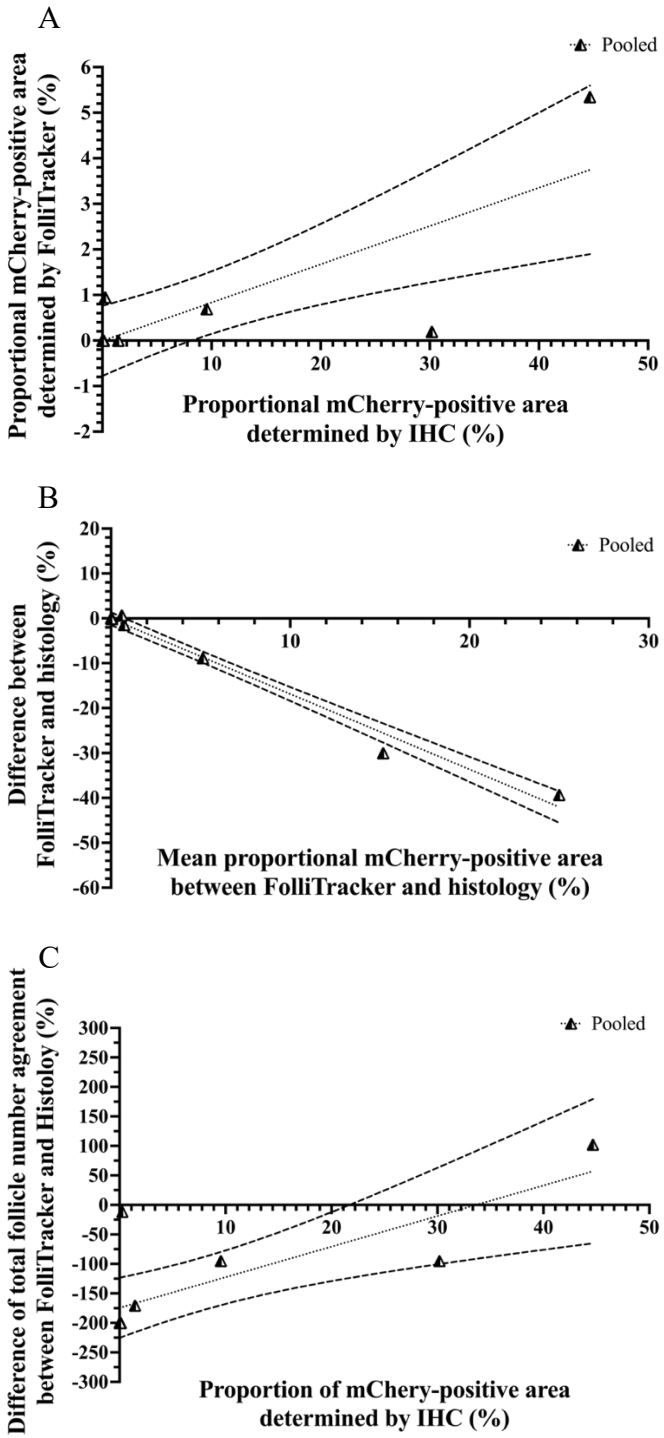

Figure AII.5.3.18) Correlation and agreement of proportional mCherry-positive area quantified via FolliTracker and histology-based methodologies, and its relationship with follicle detection concordance; visualised on a linear scale. Follicle number per RO was quantified independently using histological analysis of H&E-stained sections and via FolliTracker, a live confocal-based imaging and analysis workflow that detects follicles by overlapping mCherry and EGFP fluorescence signals. Viral ROs underwent sequential transduction with AAV-SaCas9 and AAV-DS vectors prior to reaggregation, whereas control ROs were not exposed to virus-containing media. mCherry signal was driven by the ubiquitous SFFV promoter and EGFP signal was driven by the mAMH promoter, a hormone expressed specifically in granulosa cells of developing follicles. ROs were cultured for 14 days, fixed, and processed for histological analysis and IHC using DAB chromogenic staining to detect mCherry expression. **A)** Spearman's correlation between proportional mCherry-positive area (%) determined by IHC and by FolliTracker (r=0.8349; p<0.01), with a significantly non-zero slope (r^2=0.6475; slope, 0.0840; p<0.01). **B)** Agreement between methods was evaluated using Bland-Altman analysis, which identified a mean bias of -7.2% ± 14.0% (95% LoA [-34.62, 20.21]). The slope of the regression line differed significantly from zero (r^2=0.9845; p<0.0001), indicating proportional bias. **C)** Spearman's correlation between proportional mCherry-positive area determined by IHC and follicle agreement (%) between both methodologies (r=0.8549; p<0.01), with a significantly non-zero slope (r^2=0.6155; slope, 5.182; p<0.01). Interception at the x-axis suggests that ~33.6% mCherry-positive area was associated with improved concordance in follicle identification between methodologies. All x-axes are displayed on a linear scale. Data are presented as individual ROs with best-fit regression lines shown. Dashed lines represent 95% CI; mean bias ± SD and 95% LoA are reported in the figure legend and accompanying text (Chapter 5.3.18). AAV, adeno-associated virus; Cas9, CRISPR-associated protein 9; CI, confidence interval; DAB, 3,3′-diaminobenzidine; DS, donor strand; H&E, haematoxylin and eosin; IHC, immunohistochemistry; LoA, limits of agreement; RO, reaggregated ovary; SD, standard deviation; SFFV, spleen focus-forming virus.